THE UNIVERSITY *of* EDINBURGH

MEASUREMENT OF SUBTLE BLOOD-BRAIN BARRIER DISRUPTION IN CEREBRAL SMALL VESSEL DISEASE USING DYNAMIC CONTRAST-ENHANCED MAGNETIC RESONANCE IMAGING

Anna Kathrin Heye

Doctor of Philosophy
The University of Edinburgh
2016

Declaration

I declare that this thesis was composed by myself and that the work contained herein is my own except where explicitly stated otherwise in the text. Where the work was done in collaboration with others, I have made significant contributions that are clearly indicated throughout the thesis. I further declare that this work has not been submitted for any other degree or professional qualification except as specified.

(Anna Kathrin Heye)

Abstract

Cerebral small vessel disease (SVD) is a common cause of strokes and dementia. The pathogenesis of SVD is poorly understood, but imaging and biochemical investigations suggest that subtle blood-brain barrier (BBB) leakage may contribute to tissue damage. The most widely-used imaging method for assessing BBB integrity and other microvascular properties is dynamic contrast-enhanced magnetic resonance imaging (DCE-MRI). DCE-MRI has primarily been applied in situations where contrast uptake in tissue is typically large and rapid (e.g. neuro-oncology); the optimal approach for quantifying BBB integrity in diseases where the BBB remains largely intact and the reliability of resulting measurements is unclear. The main purpose of this thesis was to assess and improve the reliability of quantitative assessment of subtle BBB disruption, in order to illuminate its potential role in cerebral SVD.

Firstly, a systematic literature review was performed in order to provide an overview of DCE-MRI methods in the brain. This review found large variations in MRI procedures and data analysis methods, resulting in widely varying estimates of tracer kinetic parameters. Secondly, this thesis focused on the analysis of DCE-MRI data acquired in an on-site clinical study of mild stroke patients. After performing basic DCE-MRI processing (e.g. selection of a vascular input function), this work aimed to determine the tracer kinetic modelling approach most suitable for assessing subtle BBB disruption in this cohort. Using data-driven model selection and computer simulations, the Patlak model was found to provide accurate estimates of blood plasma volume and low-level BBB leakage. Thirdly, this thesis aimed to investigate two potential pitfalls in the quantification of subtle BBB disruption. Contrast-free measurements in healthy volunteers revealed that a signal drift of approximately 0.1 %/min occurs during the DCE-MRI acquisition; computer simulations showed that this drift introduces significant systematic errors when estimating low-level tracer kinetic parameters. Furthermore, tracer kinetic analysis was performed in an external patient cohort in order to investigate the inter-study comparability of DCE-MRI measurements. Due to the nature of the acquisition protocol it proved difficult to obtain reliable estimates of BBB leakage, highlighting the importance of study design. Lastly, this thesis examined the relationship between quantitative MRI parameters and clinical measurements in cerebral SVD, with a focus on the estimates of blood volume and BBB leakage obtained in the internal SVD patient cohort. This work did not provide evidence that BBB leakage in normal-appearing tissue increases with SVD burden or predicts disease progression; however, increased BBB leakage was found in white matter hyperintensities. Furthermore, this work raises the possibility of a role for blood plasma volume and dietary salt intake in cerebral SVD.

The work described in this thesis has demonstrated that it is possible to estimate subtle BBB disruption using DCE-MRI, provided that the measurement and data analysis strategies are carefully optimised. However, absolute values of tracer kinetic parameters should be interpreted with caution, particularly when making comparisons between studies, and sources of error and their influence should be estimated where possible. The exact roles of BBB breakdown and other microvascular changes in SVD pathology remain to be defined; however, the work presented in this thesis contributes further insights and, together with technical advances, will facilitate improved study design in the future.

Lay summary

Small vessel disease is a condition in which the small blood vessels deep in the brain become damaged. This often happens as we become older and can lead to serious health problems such as stroke and dementia. At the moment, no one fully understands how and why these changes happen. Some researchers think that the lining of the tiny blood vessels in the brain becomes damaged and lets harmful material from the blood leak slowly into the surrounding brain tissue. This is known to happen in several other diseases, for example in brain tumours. In such diseases, the leakiness of the blood vessels is often measured using a particular magnetic resonance brain scanning technique. In small vessel disease, the blood vessel lining is only thought to be damaged very slightly, which makes taking exact measurements more difficult. The aim of this project was to find the best way of measuring these subtle changes to the blood vessels. Only if we can measure the degree of blood vessel leakage reliably, will we be able to better understand its importance in normal ageing, stroke and dementia.

At the beginning of this project, I created an overview of the different methods used by other research groups to measure the leakiness of vessels in the brain. This helped me to identify the challenges when measuring very minor leakage. In the second phase of the project, I focused on finding a suitable approach for analysing brain scans that we had collected in a large group of patients who had suffered a recent mild stroke. I have written computer software that applies several different analysis methods, selects the most appropriate method, provides estimates of the degree of damage to the vessels and tests how accurate these measurements are likely to be. In addition, I examined whether and to what degree the estimates of subtle vessel leakage are influenced by other factors. For this purpose, I scanned a group of healthy volunteers, which showed that measurement errors can be produced by the scanning machine. I also analysed brain scans that had been collected in a different research centre, so as to compare the measurements with our patient group. However, I found that the particular way in which these scans were taken made it difficult to measure subtle vessel leakage. Finally, I tested whether there are any connections between measurements from the brain scans and other medical measurements in our group of stroke patients. We found that blood vessels were leakier in visibly damaged brain tissue, but this particular investigation did not provide evidence that leakage of blood vessels in healthy-appearing tissues causes damage to the brain. However, we found other interesting connections – for example, people who eat a lot of salty food had more damaged tissue in their brains.

The work presented in this thesis has shown that it is possible to measure subtle damage to the blood vessel lining. However, it is very important to think carefully about which measurement techniques to apply and to be aware that there are several sources of error. Exactly what is happening in small vessel disease is still a fascinating puzzle, but the findings presented in this thesis, together with growing interest in the topic and improved brain scanning techniques will hopefully help to solve it in the future.

Acknowledgements

There are many people to whom I owe a great deal of thanks for their support throughout this PhD. First of all, I would like to express my deepest gratitude to my supervisors, Prof Joanna Wardlaw and Dr Michael Thrippleton, who have continuously provided invaluable guidance, advice and encouragement. The time, effort and thought that Michael has invested into this project have improved this work greatly. In addition, he has provided much appreciated emotional support that helped me through the harder times of this process. I am deeply thankful to Joanna for giving me the opportunity to pursue this degree. Her immense knowledge and experience are inspiring and have guided me through this project.

I was fortunate to have many knowledgeable and lovely colleagues, who have made me feel welcome in BRIC and helped me along the way. Special thanks go to Moira Henderson and Dr Duncan Martin for finding a solution for absolutely everything, to Dr Paul Armitage for the many helpful discussions on DCE-MRI, to Dr Francesca Chappell for patiently explaining statistics to me, to Dr Dominic Job for helping out with data questions and server issues, to Kirsten Shuler for her help with paper submissions and the MSSII database, to Dr Maria Valdés Hernández for her support with the literature review, to Dr Mark Bastin for answering my many random questions, to all the radiographers (Elaine Sandeman, Charlotte Jardine, Stewart Wiseman, Gayle Barclay and Iona Hamilton) for helping with my healthy volunteer study and to Jane Barr for nice tea breaks away from my computer. I would also like to thank my fellow lab mates (old and new), who have shared the highs and lows of this process with me: David, Andreas, Natalie, Shadia, Stewart, Xin, Jehill, Islem, Yulu, Daisy, Gordon, Marion, Yvonne and special thanks to Anna, whose company has made the last few months a lot more enjoyable.

I am very thankful to the Row Fogo Charitable Trust that has provided the funding for this project. Thank you to the SINAPSE Collaboration for providing the Postdoctoral and Early Career Researcher Exchange funding, which allowed me to visit other research groups. I would like to thank Dr Carlo Quattrocchi and his team at the Università Campus Bio-Medico in Rome for their hospitality and for kindly sharing data with me. My thanks also go to Prof Henrik Larsson and his group in the Functional Imaging Unit at Glostrup Hospital for their warm welcome in Copenhagen and the many helpful discussions. Moreover, I am thankful to all the participants in the MSSII and in my healthy volunteer study.

Finally, my thanks go to my family and friends without whose continuous encouragement this thesis would simply not exist. Thank you to my close friends from both school and Uni, who did not forget about me but spent hours on skype, sent amazing birthday post and came for visits despite the Scottish weather. Thank you also to my friends in Edinburgh, particularly Sarah and Natalie, who never failed to make me laugh and helped me to relax with a glass of wine (or two). Thank you to Jonathan for always being there for me and enduring my PhD-related moods. For their unwavering love and confidence in me, thanks to my parents.

Publications related to work presented in this thesis

Peer-reviewed journal articles

1. **Heye, A. K.**, *Thrippleton, M. J., Armitage, P. A., Valdés Hernández, M. D. C., Makin, S., Glatz, A., Sakka, E. and Wardlaw, J. M. (2016). Tracer kinetic modelling for DCE-MRI quantification of subtle blood-brain barrier permeability. *NeuroImage*, 125:446-455.

   Author's contributions: DCE-MRI analysis; computer simulations; design and execution of the healthy volunteer study (including recruitment, data collection, processing and analysis); manuscript preparation.
   Contribution by others: MJT supervised the project, provided advice regarding DCE-MRI analysis and computer simulations, assisted with design and execution of the healthy volunteer study and contributed to manuscript preparation. PAA designed the clinical MRI protocol, pre-processed DCE-MRI data, provided advice regarding DCE-MRI analysis and contributed to manuscript preparation. MVH processed and analysed the structural MRI data. AG assisted with the design and testing of the healthy volunteer MRI protocol and contributed to manuscript revision. SM recruited and assessed patients and collected demographic data. ES contributed to structural MRI analysis. JMW conceived the clinical study, obtained funding and provided supervision, performed diagnostic MRI assessment and contributed to manuscript preparation.

2. †**Heye, A. K.**, †Thrippleton, M. J., Chappell, F., Valdés Hernández, M. D. C., Armitage, P. A., Makin, S., Muñoz Maniega, S., Sakka, E., Flatman, P. W., Dennis, M. S. and *Wardlaw, J. M. (2016). Blood pressure and sodium: association with MRI markers in cerebral small vessel disease. *Journal of Cerebral Blood Flow and Metabolism*, 36(1):264-274.

   Author's contributions: DCE-MRI analysis; statistical analysis (in conjunction with MJT); manuscript preparation (in conjunction with MJT).
   Contribution by others: MJT performed the statistical analysis and prepared the manuscript (in conjunction with the author). FC contributed to manuscript preparation and statistical analysis. MVH processed and analysed the structural MRI data and contributed to DT-MRI analysis. PAA designed the imaging protocol, pre-processed the DT-MRI data and DCE-MRI data. SM recruited and assessed patients and collected demographic data. SMM contributed to DT-MRI analysis. ES contributed to structural MRI analysis. PWF provided advice regarding physiology and contributed to manuscript preparation. MSD oversaw patient clinical assessment and stroke subtyping. JMW conceived the study, obtained funding and provided supervision, performed diagnostic MRI assessment and contributed to manuscript preparation.

---

* Corresponding author
† The first two authors contributed equally to this work

3. **Heye, A. K.**, Culling, R. D., Valdés Hernández, M. D. C., Thrippleton, M. J. and *Wardlaw, J. M. (2014). Assessment of blood-brain barrier disruption using dynamic contrast-enhanced MRI. A systematic review. *NeuroImage Clinical*, 6:262–274.

   Author's contributions: Completion of the initial literature search; selection of articles for inclusion; data extraction and analysis; manuscript preparation.
   Contribution by others: RDC performed the initial literature search, removed duplicates and screened abstracts. MVH conceived the topic and helped with inclusion/exclusion decisions. MJT, MVH and JMW provided supervision, complemented the search and assisted with data analysis and manuscript preparation.

Conference abstracts

1. **Heye, A. K.**, Thrippleton, M. J., Glatz, A., Armitage, P. A. and Wardlaw, J. M. (2015). Influence of scanner drift on the accuracy of pharmacokinetic parameters in subtle leakage measured with DCE-MRI – a healthy volunteer and simulation study. ESMRMB Annual Scientific Meeting 2015, Edinburgh, UK.

2. [†]Thrippleton, M. J.,[†]**Heye, A. K.**, Chappell, F., Valdés Hernández, M. D. C., Armitage, P. A., Makin, S., Muñoz Maniega, S., Sakka, E., Flatman, P. W., Dennis, M. S. and Wardlaw, J. M. (2015). Added dietary salt is associated with increased white matter hyperintensity volume. European Stroke Organisation Conference 2015, Glasgow, UK.

3. **Heye, A. K.**, Thrippleton, M. J., Armitage, P. A., Valdés Hernández, M. D. C. and Wardlaw, J. M. (2014). Model selection for DCE-MRI applied to detect subtle blood-brain barrier disruption. ISMRM British Chapter Meeting 2014, Edinburgh, UK.

4. **Heye, A. K.**, Thrippleton, M. J., Valdés Hernández, M. D. C., Armitage, P. A. and Wardlaw, J. M. (2014). Quantification of subtle blood-brain barrier permeability in white matter using DCE-MRI. ISMRM Annual Scientific Meeting 2014, Milan, Italy.

5. **Heye, A. K.**, Thrippleton, M. J., Valdés Hernández, M. D. C., Armitage, P. A. and Wardlaw, J. M. (2013). Comparison of five quantitative analytic methods for the assessment of subtle blood-brain-barrier permeability using DCE-MRI. ESMRMB Annual Scientific Meeting 2013, Toulouse, France.

6. **Heye, A. K.**, Culling, R. D., Valdés Hernández, M. D. C. and Wardlaw, J. M. (2013). The use of dynamic contrast-enhanced MRI to study permeability of the blood-brain barrier – A systematic review. ESMRMB Annual Scientific Meeting 2013, Toulouse, France.

---

* Corresponding author
† The first two authors contributed equally to this work.

Contents

Part III Pitfalls in the quantification of subtle blood-brain barrier leakage

Part IV Quantitative magnetic resonance imaging markers in cerebral small vessel disease: associations with clinical and imaging variables in the Mild Stroke Study II cohort

Part V Conclusions and Perspectives

Appendix

Glossary

Abbreviations

AIC	Akaike information criterion
AUC	Area under the curve
AIF	Arterial input function
BBB	Blood-brain barrier
CBMS	Campus Bio-Medico Study
CSF	Cerebrospinal fluid
CT	Computed tomography
CI	Confidence interval
CNR	Contrast-to-noise ratio
DGM	Deep/subcortical grey matter
DT-MRI	Diffusion tensor magnetic resonance imaging
DWI	Diffusion-weighted imaging
DCE-MRI	Dynamic contrast-enhanced magnetic resonance imaging
DSC-MRI	Dynamic susceptibility contrast magnetic resonance imaging
EPI	Echo-planar imaging
EPVS	Enlarged perivascular spaces
EES	Extravascular extracellular space
FoV	Field of view
FLAIR	Fluid attenuated inversion recovery

FA	Fractional anisotropy
FID	Free induction decay
GRE	Gradient echo
GM	Grey matter
ICA	Internal carotid artery
ICV	Intracranial volume
IR	Inversion recovery
MRI	Magnetic resonance imaging
MR	Magnetic resonance
MAP	Mean arterial pressure
MD	Mean diffusivity
MSSII	Mild Stroke Study II
MS	Multiple sclerosis
NIHSS	National Institutes of Health stroke scale
NAWM	Normal-appearing white matter
NMR	Nuclear magnetic resonance
PP	Pulse pressure
RF	Radio frequency
RSL	Recent stroke lesion
ROI	Region of interest
SNR	Signal-to-noise ratio
SVD	Small vessel disease

SE	Spin echo
SSR	Sum of squared residuals
SSS	Superior sagittal sinus
SWI	Susceptibility-weighted imaging
T1W	T1-weighted
T2*W	T2*-weighted
T2W	T2-weighted
3D	Three-dimensional
TWIST	Time-resolved imaging with stochastic trajectories
TIA	Transient ischaemic attack
2CXM	Two-compartment exchange model
2CUM	Two-compartment uptake model
2D	Two-dimensional
VEGF	Vascular endothelial growth factor
VIF	Vascular input function
WMH	White matter hyperintensities
WM	White matter

Terms and symbols

AIC_m	Akaike information criterion associated with model m
$AICc_m$	Akaike information criterion corrected for small sample sizes associated with model m
AW_m	Akaike weight associated with model m

AUC_E^{bn}	Blood-normalised area under the signal enhancement curve
%BTV	Brain tissue volume as percentage of intracranial volume
F	Clearance
$c_a(t)$	Contrast agent concentration in arterial blood plasma over time
$c_p(t)$	Contrast agent concentration in capillary blood plasma over time
$c_e(t)$	Contrast agent concentration in EES over time
$C(t)$	Contrast agent concentration in tissue over time
R	Correlation coefficient
$\%B$	Density of sampling of region B in TWIST sequence
b	Diffusion weighting factor
TE	Echo time
T2*	Effective transverse relaxation time
$\mathbf{M}_0$	Equilibrium net magnetisation
α_{Ernst}	Ernst angle
E	Extraction fraction
α_a	Flip angle of the first pre-contrast acquisition
α_b	Flip angle of the second pre-contrast acquisition
α	Flip angle
J	Flux
v_e	Fractional interstitial volume
v_p	Fractional plasma volume
G_F	Frequency-encoding gradient

G_x	Gradient in x-direction
G_y	Gradient in y-direction
G_z	Gradient in z-direction
γ	Gyromagnetic ratio
Hct	Haematocrit
$I(t)$	Impulse response function
TI	Inversion time
ω_0	Larmor frequency
slope_E	Late phase slope of the signal enhancement curve
r_1	Longitudinal contrast agent relaxivity
T1	Longitudinal relaxation time
$\mathbf{m}$	Magnetic moment
M_z	Net magnetisation in longitudinal direction
M_{xy}	Net magnetisation in transverse direction
$\mathbf{M}$	Net magnetisation
K_m	Number of free parameters associated with model m
PS	Permeability-surface area product
G_P	Phase-encoding gradient
F_p	Plasma flow
$T1_0$	Pre-contrast longitudinal relaxation time
S_0	Pre-contrast signal intensity
$\%A$	Proportion of the central region A in TWIST sequence

ρ	Proton density
TR	Repetition time
$R(t)$	Residue function
$E(t)$	Signal enhancement at time point t
$S(t)$	Signal intensity at time point t
S_a	Signal intensity of the first pre-contrast acquisitions with flip angle α_a
S_b	Signal intensity of the second pre-contrast acquisitions with flip angle α_b
S	Signal
G_S	Slice-selective gradient
$\mathbf{B}_0$	Static magnetic field
SSR_m	Sum of squared residuals associated with model m
Δt	Temporal resolution
t	Time
r_2	Transverse contrast agent relaxivity
T2	Transverse relaxation time
$c_p(t)$	Vascular contrast agent concentration over time (blood plasma only)
$c_b(t)$	Vascular contrast agent concentration over time (whole blood)
K^{Trans}	Volume transfer constant
%WMHV	White matter hyperintensity volume as percentage of intracranial volume

Units

g	Gram
kg	Kilogram

l	Litre
MHz	Megahertz
ml	Millilitre
mm	Millimetre
mM	Millimolar
mmol	Millimole
ms	Millisecond
min	Minute
s	Second
T	Tesla

List of Figures

List of Tables

Part I.

Cerebral small vessel disease and dynamic contrast-enhanced magnetic resonance imaging

Contents

1. Introduction

This thesis focuses on the measurement of subtle blood-brain barrier (BBB) disruption in cerebral small vessel disease (SVD) using dynamic contrast-enhanced magnetic resonance imaging (DCE-MRI). The purpose of this chapter is to provide a general background of cerebral SVD (section 1.1) and DCE-MRI (section 1.2). Furthermore, this chapter presents the challenges related to measuring subtle BBB disruption (section 1.3). It concludes with an outline of the resulting aims and the structure of this thesis (section 1.4). Parts of this chapter have been published in the background section of Heye et al. (2014).

1.1. Cerebral SVD

The term cerebral SVD refers to various pathological processes affecting the small vascular structures (mainly small arterioles, capillaries and venules) that penetrate into the brain parenchyma or in the subarachnoid space. Because small vessels cannot currently be visualised in vivo using standard neuroimaging techniques, the term cerebral SVD usually refers to the consequences of small vessel changes seen in the brain parenchyma rather than the underlying vessel pathology itself (Wardlaw et al., 2013c). Consequently, the term cerebral SVD is commonly used to describe a variety of clinical, cognitive, neuroimaging and neuropathological findings.

1.1.1. Clinical aspects

In the past years, cerebral SVD has been recognised as a serious problem. The clinical manifestations are diverse and can range from stroke to subtle neurological symptoms to severe cognitive deficits including dementia and physical disabilities. Cerebral SVD plays a crucial role in at least three fields: stroke, normal ageing and dementia.

In developed countries, the proportion of elderly people is rapidly increasing. Ageing is commonly accompanied by cognitive decline, which significantly affects ability to live independently and, thus, causes huge costs to society. The prevalence of cerebral SVD increases with age (de Leeuw et al., 2001). It has been shown in several large studies that imaging markers of SVD are associated with general cognitive deficits in non-demented elderly subjects (Debette and Markus, 2010; de Groot et al., 2000; Garde et al., 2000; Longstreth et al., 1996; van der Flier et al., 2005). Furthermore, there is evidence that cerebral SVD correlates with gait

disturbances (Baezner et al., 2008), mood disorders (O'Brien et al., 1998) and urinary problems (Poggesi et al., 2008), all of which contribute to general age-related disability. In addition to subtle cognitive decline with normal ageing, 5% to 7% of people older than 60 years are affected by dementia (Prince et al., 2013). The prevalence increases to about 30% for people older than 80 years (Lobo et al., 2000), invoking large costs to the health system. Cerebral SVD has been recognised as the most common cause of vascular dementia (Dichgans and Zietemann, 2012) and also often occurs in Alzheimer's patients (Kalaria, 2002). Overall, it is estimated that cerebral SVD contributes to up to 45% of dementias (Gorelick et al., 2011).

Cerebral SVD is responsible for about a fifth of all strokes worldwide and about a quarter of ischaemic strokes (Sudlow and Warlow, 1997), placing an immense burden on society. Behind ischaemic heart disease, stroke is the second most common cause of death worldwide and also represents the leading neurological cause of disability in adults (Murray and Lopez, 1997, 2013). The number of global deaths from stroke is predicted to increase from an estimated 5.7 million in 2005 to 7.8 million in 2030 (Strong et al., 2007). Once a clinical diagnosis of stroke has been made, it is important to determine the cause of the stroke in order to initiate appropriate treatment. About 20% of all strokes are due to haemorrhage, which can be either parenchymal (15%) or subarachnoid (5%) (Feigin et al., 2003). With a proportion of 80%, the vast majority of strokes are ischaemic strokes. In ischaemic stroke, the underlying cause can be sub-classified in large artery atheroma (50%), SVD (25%), cardio-embolism (20%) and other ischaemic types (5%) (Sudlow and Warlow, 1997). Lacunar stroke, i.e. ischaemic stroke caused by SVD, has long been considered the most benign type of stroke and, therefore, has been neglected by research with most attention being given to the more disabling large artery stroke. Consequently, little is known about the exact mechanisms underlying SVD and lacunar stroke, as well as prevention and treatment options (Wardlaw et al., 2013b). Although the symptoms of lacunar stroke rarely cause death in the acute phase, they are associated with an increased risk of late recurrence, cognitive decline and dementia (Jackson and Sudlow, 2005; Norrving, 2003). SVD is often clinically silent and detected in late stage. The focus on lacunar stroke as a discrete form of cerebral SVD is useful because the discrete, sudden-onset symptoms give an inception point, from which it is easier to track subsequent disease progression (Wardlaw et al., 2013b).

1.1.2. Neuroimaging

Although the small vessels of the brain are hard to image in vivo, the consequences of their malfunction can be studied with brain imaging. Consequently, neuroimaging offers considerable insight into the disease and helps the clinical diagnosis. In the 1970s, the invention of x-ray computed tomography (CT) by Sir Godfrey N Hounsfield revolutionised brain imaging

by providing high contrast, cross-sectional images. Up to the present day, CT remains widely used in routine clinical brain imaging because it is quick and accurate in detecting various pathologies such as brain tumours and haemorrhagic strokes. However, the contrast between brain tissues in CT images is somewhat limited. In the early 1980s, magnetic resonance imaging (MRI) was introduced as an additional diagnostic tool for clinical practice (for more detailed information on MRI see section 1.2.1). Although the scanning time is longer than in CT, MRI does not use ionising radiation and produces superior image quality for the display of anatomical structures in the soft tissues of the brain. In SVD, MRI is particularly useful compared to CT due to its greater sensitivity in detecting small lesions and subtle tissue differences. A routine MRI brain examination for SVD consists of multiple sequences, commonly including: T1-weighted (T1W) imaging, T2-weighted (T2W) imaging, $T2^*$-weighted (T2*W) gradient echo (GRE) imaging, fluid attenuated inversion recovery (FLAIR) imaging and diffusion-weighted imaging (DWI). There are several signs of SVD that can be detected with conventional MRI; however, the terminology and definitions used vary widely. This lack of consistency inhibits inter-study comparisons and hinders research progress. In order to develop definitions and define imaging standards for research into SVD, an international working group of the Centres of Excellence in Neurodegeneration was assigned with the task to provide 'standards for reporting vascular changes on neuroimaging' (STRIVE). The main outcomes of this international effort have recently been published by Wardlaw et al. (2013c) and provide recommendations to standardise image acquisition, interpretation and reporting. Following the proposed standard terminology, the most common manifestations of SVD on MRI are:

i) recent small subcortical infarcts,
ii) lacunes of presumed vacular origin,
iii) white matter hyperintensities (WMH) of presumed vacular origin,
iv) enlarged perivascular spaces (EPVS),
v) cerebral microbleeds,
vi) brain atrophy.

These neuroimaging features are depicted in Figure 1.1 and will be discussed in detail below.

Recent small subcortical infarcts are a common sign of SVD and usually cause clinical symptoms of a lacunar stroke. The infarcts occur in the territory of one perforating arteriole in the deep parts of the brain; they are often seen in locations such as the basal ganglia, thalamus, internal capsule and pons (Pantoni, 2010; Gattringer et al., 2015). The imaging features or clinical symptoms of recent small subcortical infarcts must be consistent with a lesion occurring in the previous few weeks; the word 'small' refers to a lesion that is less than 20 mm in its maximum diameter in the axial plane (Wardlaw et al., 2013c). On MRI, they appear hypointense on T1W images, and hyperintense on DWI, T2W and FLAIR images

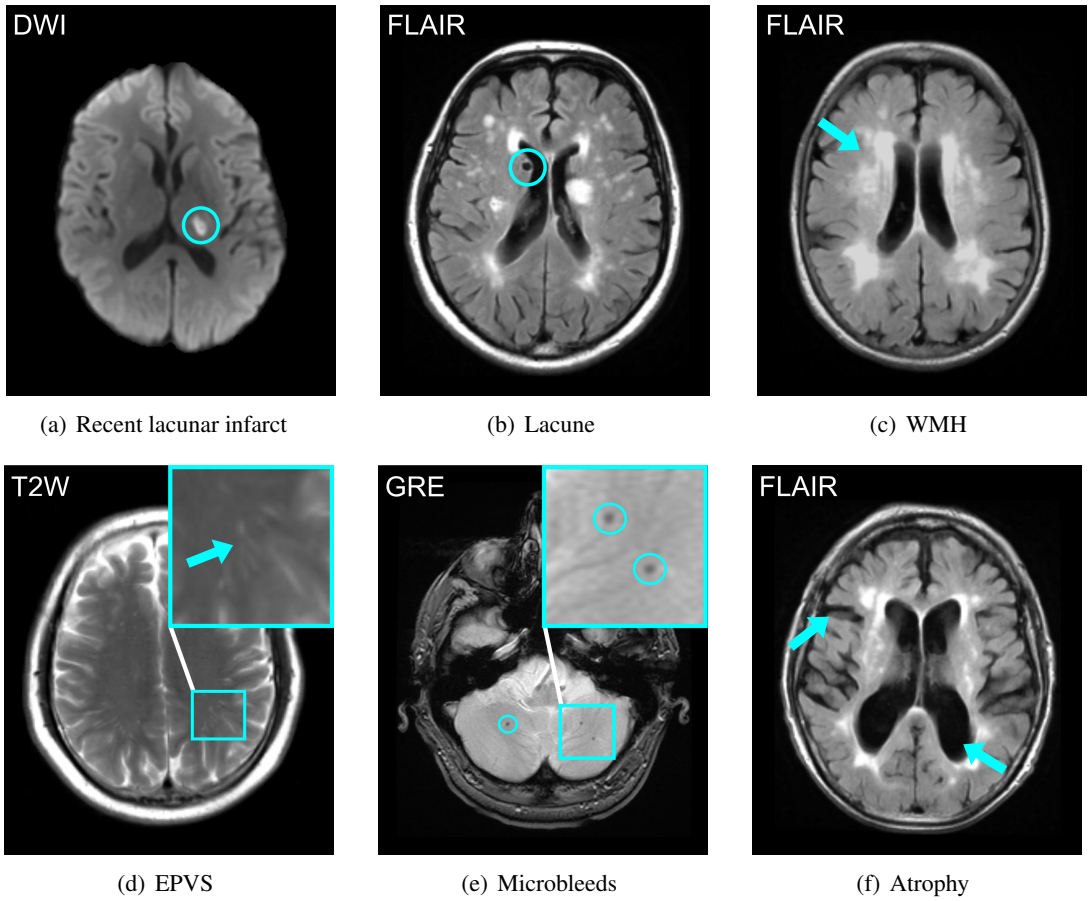

(a) Recent lacunar infarct (b) Lacune (c) WMH

(d) EPVS (e) Microbleeds (f) Atrophy

Figure 1.1.: Main MRI findings of cerebral SVD. Example images showing SVD imaging features on different MRI sequences. (a) The circle highlights a recent small subcortical infarct, (b) the circle highlights a fluid filled lacune, (c) the arrow points to a region with WMH characteristics (WMH are diffuse lesions which include all regions of similar hyperintense signal), (d) the square contains several linear EPVS, which are also visible on the contralateral side, (e) the circles highlight cerebral microbleeds, (f) the arrows point to the enlarged ventricles and enlarged sulci respectively, representing cerebral atrophy.

(see Figure 1.1(a)). The DWI sequence is particularly important for the identification of recent infarcts, as increased DWI signal or a reduced apparent diffusion coefficient help to discriminate them from old lesions (Wardlaw et al., 2013b). Recent small subcortical infarcts can have different long term fates: they often cavitate and become lacunes (estimates of cavitating proportion range from 28% to 94% (Potter et al., 2010; Moreau et al., 2012)), but can also appear like WMH or disappear completely (Wardlaw et al., 2013c). While small subcortical infarcts can occasionally be clinically silent (Kang et al., 2012), i.e. present as lesions on imaging but are asymptomatic, about 30% of patients show clinical symptoms of lacunar stroke but do not have visible lesions (Doubal et al., 2011). Lacunar infarcts are associated with cognitive decline (Samuelsson et al., 1996).

Lacunes are round or ovoid, subcortical, fluid filled cavities of presumed vascular origin and between 3 mm and 15 mm in diameter (Wardlaw et al., 2013c). Most lacunes are presumed to be caused by small subcortical infarcts, although they might also result from small deep haemorrhages (Franke et al., 1991). On MRI, lacunes have a similar signal to cerebrospinal fluid (CSF), usually with a hyperintense rim around the hypointense cavity on FLAIR images (see Figure 1.1(b)). Many lacunes appear silently in the brain without causing symptoms (Vermeer et al., 2007); however, it has been shown that lacunes are implicated in higher risk of recurrent stroke and dementia (Loeb et al., 1992; Vermeer et al., 2003). Moreover, the number of lacunes was found to be a predictor of speed and motor control among non-demented elderly subjects (Benisty et al., 2009).

WMH are signal abnormalities of presumed vascular origin and variable size in the white matter (WM). They are usually symmetrically distributed in both cerebral hemispheres. WMH appear hyperintense on T2W and FLAIR images (see Figure 1.1(c)) and can be isointense or slightly hypointense on T1W images. Such hyperintensities can also occur in grey matter (GM) and the brain stem; however, these should not be included in the term WMH unless explicitly stated (Wardlaw et al., 2013c). Several methods are available to measure the presence, size and progression of WMH, including qualitative rating scales (Breteler et al., 1994; Fazekas et al., 1987; Longstreth et al., 1996; Mäntylä et al., 1999; Scheltens et al., 1993) and automatic or semi-automatic quantitative methods (Enzinger et al., 2006; Valdés Hernández et al., 2010; Jeerakathil et al., 2004; Prins et al., 2004; van Straaten et al., 2006). WMH are strongly associated with increased risk of strokes, cognitive decline, dementia and death (Debette and Markus, 2010).

EPVS, previously commonly called enlarged Virchow-Robin spaces (Kwee and Kwee, 2007), are fluid filled spaces that surround the small deep perforating vessels as they pass through GM or WM (Wardlaw et al., 2013c). As EPVS contain fluid, they appear similar to CSF on MRI (see Figure 1.1(d)). Following the course of vessels, visible EPVS are linear when parallel to the imaging plane (e.g. in the lateral subcortical WM of the temporal, parietal and frontal lobes with axial imaging), and round or ovoid when perpendicular to the imaging plane (e.g. in the basal ganglia with axial imaging). Due to their similar appearance on MRI, EPVS must be discriminated from lacunes. As a general rule, EPVS are usually smaller than 3 mm in diameter (Bokura et al., 1998). Although the presence of a few visible EPVS can be normal at any age, they become increasingly frequent with older age (Groeschel et al., 2006). The clinical significance of EPVS remains controversial; however, a higher number of visible EPVS has been associated with active inflammation in multiple sclerosis (Wuerfel et al., 2008) and cognitive decline (Maclullich et al., 2004).

Cerebral microbleeds are small punctate areas that appear hypointense on T2*W GRE imaging (see Figure 1.1(e)), but are not visible on other MRI sequences. They are generally 2 mm to 5 mm in diameter, but some authors have considered lesions as large as 10 mm to be microbleeds (Cordonnier et al., 2007) . Microbleeds most commonly occur in the cortico-subcortical junction, and subcortical/deep GM (DGM) or WM in the cerebral hemispheres, brainstem and cerebellum (Wardlaw et al., 2013c). Histopathologically, microbleeds have been shown to correspond to small collections of haemosiderin-laden macrophages around small perforating vessels (Gouw et al., 2011; Shoamanesh et al., 2011). Microbleeds are associated with dementia in the form of Alzheimer's disease (Vernooij et al., 2008) as well as cerebral amyloid angiopathy (Knudsen et al., 2001) and, although originally thought to be asymptomatic, are now considered to be associated with transient neurological symptoms, especially in the presence of superficial siderosis (Lummel et al., 2015).

Brain atrophy describes a decrease in brain volume, which can be caused by several pathological processes, such as neuronal loss, cortical thinning and vascular infarcts. In the context of SVD, atrophy is defined as a reduced brain volume that is not related to a specific macroscopic focal injury (Wardlaw et al., 2013c). Hence, focal tissue loss from infarctions should not be included in this term unless explicitly stated. Atrophy can be either general and affect the whole brain, or focal (only affecting specific brain regions or lobes), or selective (only affecting a particular tissue type). On MRI, atrophy presents itself as tissue loss from enlargement of peripheral or central CSF spaces, i.e. increased ventricular volume and/or enlarged superficial sulci (see Figure 1.1(f)). The amount of tissue loss can be quantified as brain volume or CSF volume in relation to intracranial volume; however, brain atrophy should ideally be observed in longitudinal studies. Cerebral atrophy occurs to some degree with normal ageing, but a high atrophy rate has been associated with cognitive decline in Alzheimer's disease and vascular dementia (Fox and Schott, 2004; Jagust et al., 2008).

Several studies have shown that all these common neuroimaging features of SVD are interrelated. WMH presence, severity or progression are associated with lacunar strokes (Rost et al., 2010), lacunes (Gouw et al., 2008), microbleeds (Cordonnier et al., 2007), EPVS in patients with lacunar stroke (Doubal et al., 2010; Potter et al., 2013) and atrophy (Aribisala et al., 2013; de Leeuw et al., 2006). Similarly, studies reported correlations between EPVS and lacunar infarcts (Rouhl et al., 2008), lacunes (Zhu et al., 2010) and microbleeds (Martinez-Ramirez et al., 2013). Furthermore, several features share vascular risk factors, such as increased age and hypertension (Debette and Markus, 2010; Dufouil et al., 2001; Vermeer et al., 2007). As highlighted in Wardlaw et al. (2013c), lesions with different causes can often have a similar long term appearance on MRI; for instance, both small subcortical infarcts and stroke symptoms without acute visible lesion might appear as WMH or normal-appearing tissue in their chronic stages.

1.1.3. Pathophysiology and the proposed role of the BBB

Despite the increasing research interest in cerebral SVD, the underlying pathological processes are still largely unknown. Since the symptoms of SVD are rarely fatal in the acute phase, the human specimens usually reflect late stage pathology. Further difficulties are caused by the lack of suitable animal models (Bailey et al., 2009) and the inadequate scanning resolution of current in vivo imaging techniques.

Many perceptions of SVD aetiology arise from the seminal pathological studies by C Miller Fisher, in which he studied the appearance of lacunar infarcts, lacunes and perforating small arteries in about 20 deceased patients (Fisher, 1968, 1979, 1982, 1991, 1998). The commonest pathological findings described by Fisher are abnormalities of the small arterioles (40 μm to 200 μm). These vessel wall changes are characterised by arterial wall disorganisation and collagenous sclerosis, leading to narrowing and, in some cases, occlusion and sometimes dilation of the perforating artery. This process has been attributed to diffuse deposition of lipid in the arteriolar walls, and is sometimes referred to as lipohyalinosis. The size and severity of a lacunar infarct was thought to depend on the size of the pathologic vessels, with larger infarcts being caused by atherosclerosis or embolism in larger perforating arteries (200 μm to 850 μm). Although Fisher's work offers an intriguing insight into the pathology of lacunar stroke, there has been little further research to confirm his hypotheses (Pantoni, 2010; Wardlaw et al., 2013b). Furthermore, while microatheroma and emboli might account for some SVD features such as lacunar stroke and WMH, they cannot necessarily explain other SVD manifestations, for instance, EPVS or microbleeds. Consequently, it is now believed that other mechanisms such as inflammation (Rosenberg, 2009), oligodendrocytes apoptosis (Brown et al., 2000), endothelial dysfunction (Markus, 2008) and BBB impairment (Wardlaw et al., 2003) could be involved in the aetiology of SVD.

There is increasing evidence that endothelial failure plays an initiating role in the development of SVD. Endothelial cells form a key part of the BBB; they line capillaries and are sealed by tight junctions, which are unique to the brain microvasculature. The endothelium of the BBB interacts with several cellular and non-cellular elements, such as astrocytes, pericytes, microglial cells and basement membranes, that provide both functional and structural support to the BBB (see Figure 1.2). Together they form an interactive cellular complex: the neurovascular unit. The BBB regulates the passage of essential molecules such as glucose, while restricting the diffusion of potentially harmful substances. There are many mechanisms that can cause a disruption of the BBB, ranging from extrinsic systemic factors, such as infections and autoimmune processes, to intrinsic cellular mechanisms secondary to neuroinflammatory injury. Several comprehensive reviews provide detailed information on the molecular biology of BBB disruption with disease (Abbott and Friedman, 2012; Obermeier et al., 2013; Rosenberg,

2012). Failure of the BBB can explain many of the imaging and pathological observations related to SVD (Lammie et al., 1998; Wardlaw et al., 2001, 2003; Wardlaw, 2010; Wardlaw et al., 2013c). Disruption of the BBB caused by endothelial dysfunction leads to leakage of substances through the vessel wall, e.g. proteins, inflammatory markers and red cells. These substances can result in damage to the small vessel wall, ischaemia and oedema (Wardlaw et al., 2003), which affect the neuronal and glial cells and damage the brain parenchyma.

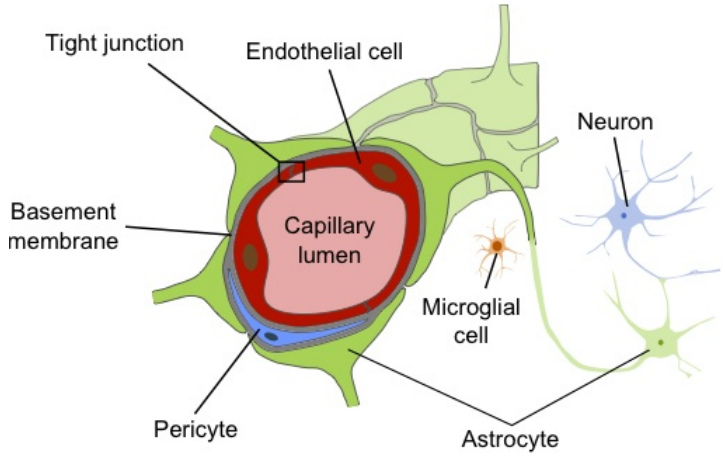

Figure 1.2.: Schematic drawing of the neurovascular unit. Reprinted from Heye et al. (2014).

Since the hypothesis that early endothelial failure precipitates SVD was first proposed, it has been supported by several studies. Several research groups have examined changes of the BBB with normal ageing, dementia and WMH; a comprehensive systematic literature review of available published human studies and meta-analysis found that increased BBB permeability is associated with (i) increasing age, (ii) diagnosis of dementia compared to healthy age-matched controls, (iii) diagnosis of vascular dementia compared to a diagnosis of Alzheimer's disease and (iv) increasing amount of WMH (Farrall and Wardlaw, 2009; Wardlaw, 2010). Furthermore, studies reported that BBB permeability in WM is increased in patients with lacunar stroke compared to cortical stroke (Wardlaw et al., 2008, 2009) or healthy age-matched controls (Topakian et al., 2010). Increased BBB permeability in normal-appearing tissues has also been reported to correlate with EPVS (Wardlaw et al., 2009) and increased risk of poor outcome and disability at long term follow-up after stroke (Wardlaw et al., 2013a).

Most of the studies reported in Farrall and Wardlaw (2009) used biochemical tests to assess BBB permeability, such as the CSF:plasma albumin ratio. Albumin is a medium-sized protein that is mainly produced on the plasma side of the BBB. Hence, any increase of albumin in the CSF can indicate a general disruption of the BBB. However, elevated CSF:plasma albumin ratios can also represent other processes and should be interpreted cautiously (Chen, 2011).

Moreover, CSF is obtained by lumbar puncture, which is not acceptable to many people. More recently, contrast-enhanced neuroimaging methods have become the standard method for in vivo assessment of BBB integrity, most of which are MRI based (Chassidim et al., 2013).

1.2. Assessment of BBB integrity with MRI

This section provides an introduction to MRI and the specific imaging method (DCE-MRI) that this research focuses on. Moreover, this section will explain how the resulting data can be analysed in order to obtain measurements of BBB integrity.

1.2.1. Introduction to MRI

MRI is based on the phenomenon of nuclear magnetic resonance (NMR), which was independently discovered by Bloch (1946) and Purcell et al. (1946). NMR refers to the interaction between atomic nuclei with a non-zero magnetic moment and an external magnetic field. Although the potential of NMR was recognised early on, it took more than two decades to implement NMR-based imaging. In the early 1970s, Paul C Lauterbur demonstrated that the NMR signal can be used to obtain images (Lauterbur, 1973) and implemented the first MRI scanner. During the following years, the development and refinement of processing techniques and hardware ultimately led to a clinical tool that can provide high-quality images of the human brain. The following sections will provide a brief introduction to the physics of MRI; for further information, the interested reader is referred to the detailed literature, e.g. McRobbie et al. (2006).

Nuclear spins and magnetic fields

Subatomic particles have the quantum mechanical property of spin. Certain nuclei have a non–zero spin and therefore a magnetic moment. In MRI, the magnetic properties of hydrogen nuclei $\left({}^{1}\mathrm{H}\right)$ are of particular interest, because hydrogen is a substantial component of water and lipids, which make up 75% to 80% of the human body. Without an external magnetic field, nuclei are randomly oriented (see Figure 1.3(a)) and their non-zero magnetic moments $\mathbf{m}$ cancel each other out, resulting in a zero net magnetisation $\mathbf{M}$. When spinning nuclei are subjected to a static magnetic field $\mathbf{B}_0$, their non-zero magnetic moments tend to align with the field (see Figure 1.3(b)). Some spins will align parallel and some anti-parallel to the orientation of the magnetic field, with a slight excess of parallel spins because this is a lower energy state (following the laws of quantum mechanics that, for simplicity, will not be discussed here). The

alignment of the spins and their magnetic moments produces a bulk magnetisation $\mathbf{M}_0$ in the direction of the static field. However, the nuclear spins do not align exactly with the external field, and therefore precess around the direction of the field (see Figure 1.3(c)). The frequency of this precessional movement is called the Larmor frequency ω_0 and is directly proportional to the strength B_0 of the external magnetic field:

$$\omega_0 = \gamma B_0, \tag{1.1}$$

where γ is the gyromagnetic ratio that, for hydrogen, is equal to 42.57 MHz T^{-1}. While all spins have the same frequency, they are of random phase orientation. Consequently, their magnetic moments in the transverse (xy) plane cancel to zero and the net magnetisation $\mathbf{M}_0$ is non-zero in the direction of the static field (z) only.

As the net magnetisation of the nuclei is very small compared to the external magnetic field, it cannot be easily measured in its equilibrium state. In order to measure the magnetisation, it has to be tipped into the transverse plane. This can be achieved by exposing the nuclei to an oscillating magnetic field in the transverse direction (usually referred to as a radio frequency (RF) pulse) that has to be applied at the Larmor frequency, i.e. be in resonance with the nuclear spins. The duration and strength of the RF pulse determine the flip angle α, which describes how far the magnetisation has been tipped away from its original orientation. A 90° pulse moves the magnetisation exactly into the transverse plane, whereas a 180° pulse flips it into the opposite direction of the static field. After the RF pulse, all spins are phase-coherent and $\mathbf{M}$ is in the transverse plane; consequently, $\mathbf{M}$ precesses, creating an oscillating magnetic field in the transverse plane (see Figure 1.3(d)), which can be detected as a voltage with an electromagnetic coil.

Spin relaxation

The precessing field in the transverse plane induces a voltage in an electromagnetic receive coil, creating the magnetic resonance (MR) signal. Once the RF field is turned off, the amplitude of the measured signal decays quickly. This typical MR signal is called the free induction decay (FID) and is depicted in Figure 1.4(a). The decay of the signal is caused by the nuclei returning to their equilibrium state. This process is called relaxation and consists of two main mechanisms: longitudinal relaxation and transverse relaxation. Nuclear relaxation is formally described by the Bloch equations, whose solutions are given in equations 1.2 and 1.3 below.

Longitudinal relaxation describes the recovery of the longitudinal component of the net magnetisation towards its equilibrium value. During the RF pulse, the nuclei absorb energy; longitudinal relaxation is caused by the loss of this additional energy by interaction with the

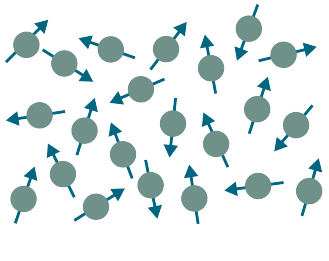

(a) Spin ensemble in a field-free space

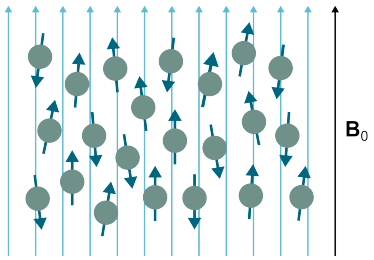

(b) Spin ensemble in a static magnetic field

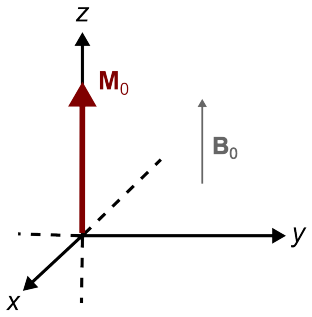

(c) Spin precession and net magnetisation in the equilibrium state

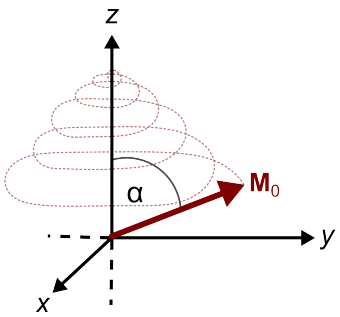

(d) Effect of a RF pulse on the net magnetisation

Figure 1.3.: Behaviour of nuclear spins in external magnetic fields. (a) Without an external magnetic field, spinning nuclei are randomly oriented and their non-zero magnetic moments cancel each other out, (b) when subjected to a static magnetic field $\mathbf{B}_0$, nuclear spins tend to align with the field, (c) precessing nuclear spins produce a net magnetisation $\mathbf{M}_0$ in direction of the static $\mathbf{B}_0$ field, (d) during a RF pulse with flip angle α, $\mathbf{M}_0$ is tipped into the transverse plane.

surrounding tissue, or lattice. Consequently, the process is also known as spin-lattice relaxation. In addition to the external static field, the nuclei are subjected to the magnetic moments of neighbouring particles and their fluctuations due to molecular motion. By interacting with these magnetic fields, especially the ones that fluctuate close to the Larmor frequency, the nuclei emit energy and the net magnetisation vector returns to the equilibrium state. This recovery of magnetisation in the longitudinal direction (M_z) is typically an exponential process with time constant T1 (longitudinal relaxation time) and can be described as follows:

$$\mathrm{M}_z(t) = \mathrm{M}_0[1 - \exp(-t/\mathrm{T1})], \tag{1.2}$$

where t is the time after the (90°) RF pulse is switched off, and M_0 is the amplitude of the net magnetisation $\mathbf{M}_0$ at equilibrium. The rate of decay depends on the molecular environment of the nuclei and is therefore tissue-specific; for instance, large molecules such as lipids and proteins fluctuate at a rate close to the Larmor frequency and are, thus, subject to quick

relaxation, while smaller molecules such as free fluids fluctuate much faster, resulting in slower relaxation. Consequently, T1 is short in fatty tissue, but relatively long in CSF.

Transverse relaxation describes the decay of the transverse magnetisation due to dephasing of the spins. As mentioned before, the spins are phase-coherent in the transverse plane directly after the RF pulse. However, the magnetic moments of the spins interact with each other, causing transient field inhomogeneities that lead to small differences in the precessional frequencies of the spins. Due to these spin-spin interactions, the spins quickly dephase and the transverse magnetisation decays. Consequently, this mechanism is also known as spin-spin relaxation. The decay of the transverse magnetisation M_{xy} is characterised by the time constant T2 (transverse relaxation time) and can be described by

$$M_{xy}(t) = M_0 \exp(i\omega_0 t) \exp(-t/T2). \tag{1.3}$$

Similar to longitudinal relaxation, transverse relaxation is an exponential process; however, it tends to happen much more rapidly (see Figure 1.4(b)) and T2 values are therefore generally smaller than T1 values. As with T1, T2 is tissue-specific; typical T1 and T2 values for human brain tissues are displayed in Table 1.1.

As transverse relaxation is much quicker than longitudinal relaxation, one could expect that the FID decays with the time constant T2. However, the MR signal decays with a shorter effective time constant T2*. This is due to extrinsic field inhomogeneities, for instance variations in the static magnetic field, which lead to further dephasing of spins and, hence, to a quicker decay of the signal.

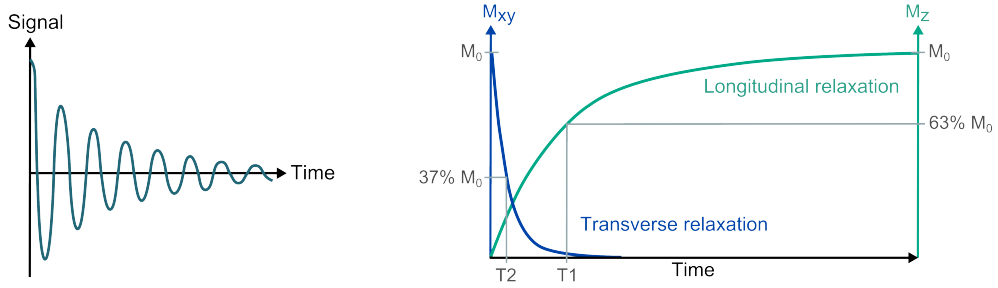

(a) FID (b) Longitudinal and transverse relaxation

Figure 1.4.: MR signal and spin relaxation after the RF pulse. (a) Oscillating signal induced in the electromagnetic receive coil (FID), (b) relaxation mechanisms: decay of the transverse magnetisation M_{xy} with time constant T2 (transverse relaxation) and recovery of the longitudinal magnetisation M_z with time constant T1 (longitudinal relaxation).

Table 1.1.: Typical longitudinal (T1) and transverse (T2) relaxation times for healthy brain tissues. Values are given for a magnetic field strength of 1.5 T (Warntjes et al., 2008).

Tissue type	T1 (ms)	T2 (ms)
WM	576	77
DGM	829	78
Cortical GM	1048	94
CSF	3940	1910

Generating echoes

In MRI, the FID is rarely measured directly; instead, pulse sequences are used in order to generate echoes. There are two basic methods for echo generation: spin echo and gradient echo (GRE). The GRE is particularly important for DCE-MRI acquisition and, thus, will be focused on in the following sections.

The principle of a GRE sequence is schematically depicted in Figure 1.5. The sequence starts with an RF pulse that creates the FID as described previously. Immediately after this excitation pulse, a negative gradient is applied. The term gradient refers to an additional magnetic field with linearly increasing field strength that is superimposed on the static magnetic field. As the precession frequency ω_0 is directly proportional to the magnetic field strength, the Larmor frequency of the spins varies along the direction of the gradient. Consequently, the applied gradient causes the spins to dephase, which results in a much faster decay of the FID. The polarity of the gradient is then reversed and the spins begin to rephase; the time after which the spins are fully phase-coherent is called the echo time TE. The amplitude of the GRE decays with T2*, as the positive gradient does not reverse dephasing due to spin-spin interactions or local magnetic field inhomogeneity.

Spatial encoding

During a simple MR experiment as described previously, the measured echo is the sum of all NMR effects in the entire body. In order to generate an image, it is necessary to spatially allocate individual MR signals. This is achieved by imposing additional gradient fields. As the resulting spatial variations in the magnetic field lead to different Larmor frequencies at different positions, this allows one to distinguish between MR signal at different positions in space. Three separate gradients, G_x, G_y and G_z, are used in an MRI scanner in order to encode each spatial dimension.

For slice selection, a gradient is applied simultaneously to the RF pulse. This gradient is called the slice-selective gradient (G_S). When the gradient is applied, the Larmor frequency becomes

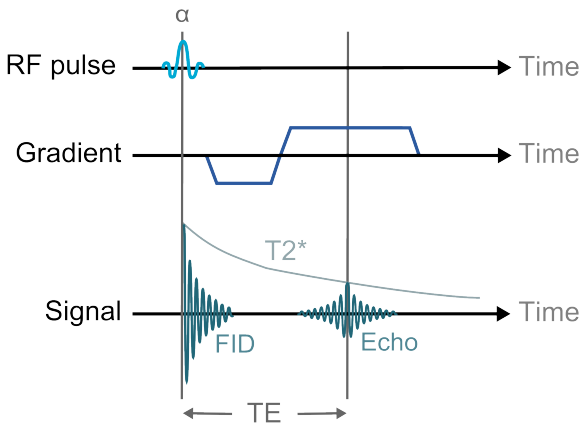

Figure 1.5.: Schematic principle of GRE generation. A negative gradient after the RF pulse dephases the spins, which are then rephased by applying a positive gradient. The echo occurs after echo time TE and its amplitude decays with the effective transverse relaxation time T2*.

spatially dependent, e.g. for a gradient in z-direction the frequency at position z is given by $\omega = \gamma(B_0 + z \cdot G_z)$. Consequently, the frequency of the RF pulse (ω_{RF}) can be chosen to excite only nuclei in a specific position along the gradient axis (see Figure 1.6(a)). The slice thickness can be controlled by altering the bandwidth of the RF pulse or the strength of the gradient. The three separate gradients G_x, G_y and G_z or combinations of these allow for flexible slice orientation.

For in-plane localisation of the MR signal, two concepts are used: frequency encoding and phase encoding (see Figure 1.6(b)). Frequency encoding involves the application of a gradient in a direction orthogonal to the slice selection simultaneously with the echo measurement. This gradient is called the readout or frequency-encoding gradient (G_F). As a result, nuclei at different positions along the frequency encoding direction precess with different frequencies. The measured MR signal is a combination of all signals along the frequency-encoding axis. In case of a simple one-dimensional image, the spatial information could then be extracted by applying a one-dimensional Fourier transform, which decomposes the frequency spectrum into its component signals in the frequency-encoding direction.

For the second in-plane resolution, an additional gradient (known as phase-encoding gradient G_P) is applied between the RF pulse and echo. This gradient causes the spins to precess at different speeds for a short time and, consequently, to dephase. After the gradient is switched off, the nuclei will return to their original frequency but show phase differences depending on their position along the phase-encoding direction. The degree of this phase shift is determined by the duration and amplitude of G_P.

In combination with frequency encoding, the phase distribution within each frequency provides information on the spatial origin along the phase-encoding axis. However, the phases of the individual spins cannot be encoded from a single signal. Consequently, in order to create unique phase- and frequency-encoded MR signals, the phase-encoding step has to be repeated after repetition time TR with different gradient strengths for each line of the plane. All measured signals are recorded in the frequency domain, known as k-space. A two-dimensional (2D) Fourier transform can then be applied to convert the raw data to a 2D MR image.

Sometimes it is desirable to acquire three-dimensional (3D) images for a whole volume rather than multiple 2D slices. This can be achieved by applying an additional phase-encoding gradient along the third direction. The in-plane spatial encoding procedure as described above must then be repeated for each phase-encoding step along the third dimension.

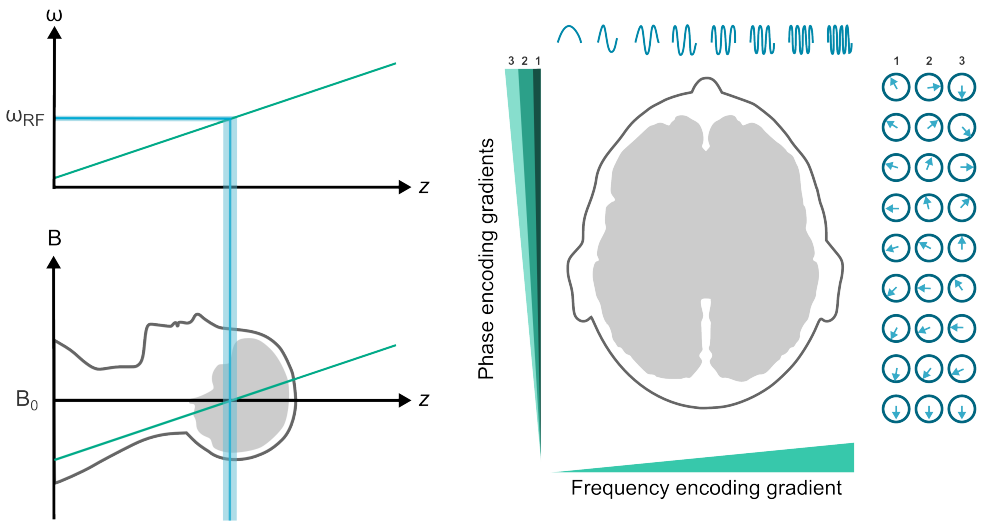

(a) Slice selection (b) Frequency and phase encoding

Figure 1.6.: Spatial encoding of the MR signal. (a) Selective excitation of a single slice by applying a gradient at the same time as the RF pulse (schematic illustration for $\omega_{RF} = \omega_0$), (b) in-plane locations are encoded by giving the spins a unique frequency in one direction and a unique phase in the second direction. In order to create unique phase- and frequency-encoded signals, the phase encoding step has to repeated with different gradient strengths for each line of the plane.

The GRE pulse sequence and tissue contrast

A full MRI pulse sequence includes three main components: RF excitation, spatial encoding and echo readout. Figure 1.7 illustrates a general GRE pulse sequence, which is repeated

with different phase-encoding steps until k-space is fully sampled. The repetition time TR can be reduced significantly by using RF pulses with small flip angles ($\alpha < 90°$). After several RF pulses, the magnetisation reaches a steady state where the longitudinal recovery during TR is equal to the loss of longitudinal magnetisation during the RF pulse; consequently, the magnetisation remains the same after each RF pulse. If TR is very short ($<$ T2), some transverse magnetisation remains when the next RF pulse is applied. In this case, the next RF pulse leads to rephasing of the spins and generates a spin echo. In a regularly spaced train of RF pulses, this echo occurs at exactly the same time as the next RF pulse, so that it coincides with the new FID signal. Since the spin echo arose from previous excitations, it may have different spatial encoding. Consequently, remaining transverse magnetisation may cause artefacts if left unattended. GRE sequences can generate different types of contrast, in particular images with T1, T2*, proton density and, in some instances, T2 weighting. The contrast behaviour is mainly determined by how the residual transverse magnetisation is dealt with, i.e. whether the coherences between the FID and spin echoes are utilised or eliminated.

For T1W GRE imaging, which is of particular interest for DCE-MRI, the residual transverse magnetisation is removed by gradient or RF spoiling. Hence, this technique is called incoherent GRE or spoiled GRE. As a result of spoiling the transverse magnetisation, the signal mainly depends on the effect of the RF pulse on the longitudinal magnetisation. The signal S measured with a spoiled GRE sequence is given by

$$S = \rho \frac{\sin(\alpha) \cdot [1 - \exp(-\mathrm{TR}/\mathrm{T1})] \cdot \exp(-\mathrm{TE}/\mathrm{T2}^*)}{1 - \cos(\alpha) \cdot \exp(-\mathrm{TR}/\mathrm{T1})}, \tag{1.4}$$

where ρ denotes the proton density. The signal is highly dependent on the flip angle; the angle that results in the highest signal for a specific T1 is called the Ernst angle and given by $\alpha_{\mathrm{Ernst}} = \cos^{-1}[\exp(-\mathrm{TR}/\mathrm{T1})]$. While T1 weighting generally occurs at flip angles greater than α_{Ernst}, it is possible to obtain proton density weighted images with smaller flip angles.

Technical components of the MRI system

The MRI system consists of three main components that are necessary for creating and measuring a spatially encoded signal: (i) the main magnet, (ii) the gradient system and (iii) the RF system. The basic setup of these components in an MRI scanner is shown in Figure 1.8.

The main magnet generates the static magnetic field in z-direction. Modern clinical MRI systems typically use superconducting magnets with field strengths between 0.5 T and 3.0 T. These magnets consist of superconducting wires, which have zero electrical resistance at very low temperatures close to absolute zero. Consequently, once a current is established in the coil, it will circulate indefinitely and no additional electrical power is required to maintain the

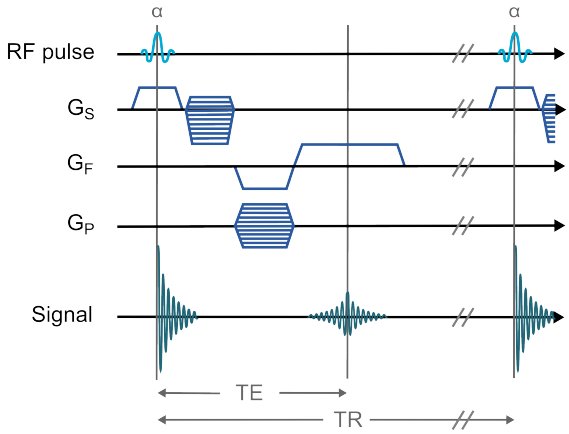

Figure 1.7.: Schematic principle of a general GRE pulse sequence. A positive slice-selective gradient G_S is applied simultaneously to the RF pulse with flip angle α. The echo is generated by the frequency-encoding gradient G_F at echo time TE. A phase-encoding gradient G_P is applied between the RF pulse and echo. The sequence is repeated with a different phase-encoding gradient after repetition time TR. A 3D volume acquisition can be achieved by applying an additional phase-encoding gradient after the slice-selective gradient and repeating the whole acquisition for each slice.

magnetic field. Liquid helium is used as a coolant to keep the temperature of the magnet consistently low. As all magnets suffer from some non-uniformity, a process known as shimming is used to optimise the field homogeneity by incorporating electrical coils and/or steel into the system. Furthermore, the system is shielded in order to reduce the magnetic effect outside the scanner as well as to prevent interference with external magnetic fields.

The gradient system includes three gradient coil arrangements for the *x*-, *y*- and *z*-direction. The *z*-gradient is typically generated via a pair of coils with counter-rotating currents; this is known as a Maxwell pair. In contrast, *x*- and *y*-gradients are generated through an arrangement of four coils each (known as Golay configuration). Large electrical currents are needed for operating the gradient coils. Hence, high-power RF amplifiers are used to supply the necessary currents.

The RF system consists of transmit and receive coils. The transmit coil produces the RF field; the same coil can often also act as a receive coil and detect the MR signal. A whole-body RF coil is usually built into the scanner. However, depending on the body region to examine, special local coils are often used in order to maximise the signal-to-noise ratio (SNR). The transmitter generates RF pulses of specific centre frequency, bandwidth, amplitude and phase, which need to be amplified before application. The receiver measures the MR signal, filters and amplifies it.

In order to control the three sub-systems and evaluate the measured signals, a high-performance computer system is needed. In a typical MRI system, a host computer controls and monitors the whole system. The operator defines the scan parameters on the host computer; they are then converted into commands for hardware control by a microprocessor system. A processing unit allows for real time signal post-processing and image reconstruction.

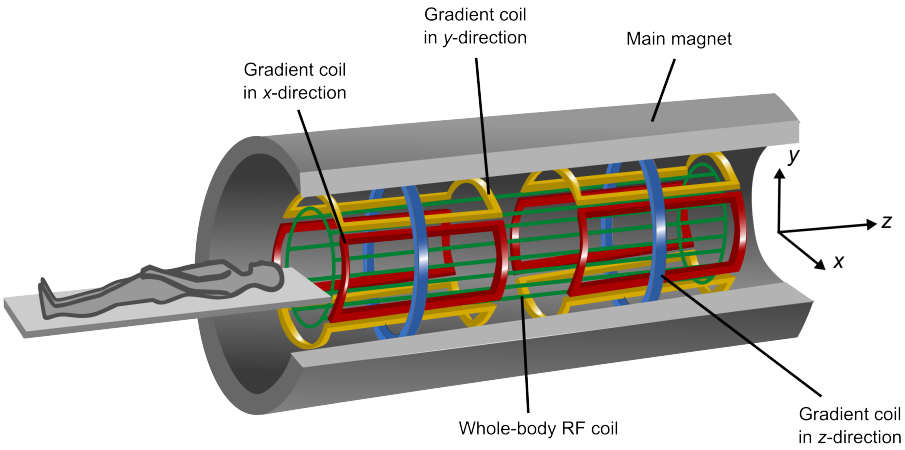

Figure 1.8.: Schematic illustration of a tunnel-shaped MRI system. An MRI scanner consists of three main components: the main magnet, the gradient system and the RF system. The gradient system consists of three gradient coil arrangements for the *x*-, *y*- and *z*-directions. The system includes a whole-body RF coil; a special local (usually receive-only) coil is usually used for imaging of the brain.

1.2.2. Principles of DCE-MRI

Disruption of the BBB can enable the extravasation of low-molecular weight contrast agents, which can be detected using contrast-enhanced MRI. MRI signal changes caused by contrast agent extravasation are determined by several factors, including tissue perfusion and capillary permeability. In the brain, T1W DCE-MRI is considered to be the standard MRI approach for assessing permeability, while T2*W dynamic susceptibility contrast MRI (DSC-MRI) is the method of choice for perfusion imaging (Sourbron and Buckley, 2013). However, it has been shown that DCE-MRI can combine perfusion and leakage measurements by using a sufficiently long acquisition time with high temporal resolution early on (Larsson et al., 2009; Li et al., 2000, 2012a; Sourbron et al., 2009).

The most commonly used agents for contrast-enhanced MRI are based on complexes of gad-

olinium(III), an ion with strong paramagnetic susceptibility. The molecule is too large to cross through the healthy BBB and does not enter brain cells. However, where the BBB is disrupted, gadolinium leaks into the extravascular extracellular space (EES). A gadolinium(III) complex has seven unpaired electrons with non-zero spin, which interact with the surrounding tissue and cause changes in its relaxation time. Firstly, the paramagnetic ions can directly interact with protons of water molecules in close proximity by formation or dissociation of covalent bonds. This accelerates the transition to lower energy states (spin-lattice relaxation) and, hence, leads to reduced T1. Secondly, the unpaired electrons create field inhomogeneities that decrease T2. At low doses as generally used in clinical practice, T1 shortening is the dominant effect. As a result, extravasation of contrast agent leads to reduced T1 and, hence, increased signal intensity in T1W images. DCE-MRI exploits this T1 enhancement in order to detect and evaluate regions of BBB disruption. The DCE-MRI procedure typically consists of intravenous injection of contrast agent followed by the repeated acquisition of T1W images (see Figure 1.9), providing measurements of signal enhancement as a function of time.

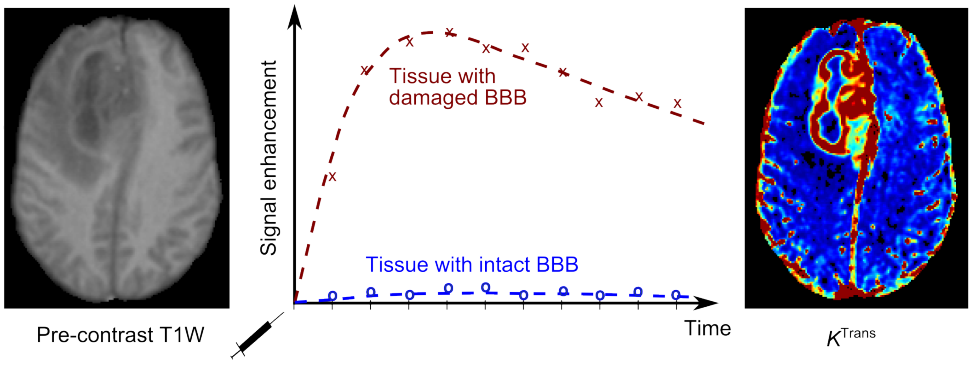

Figure 1.9.: Illustration of DCE-MRI in a patient with a glioma. The repeated acquisition of T1W images after contrast agent injection allows the calculation of signal enhancement as a function of time (middle) when compared to the pre-contrast signal intensity (left). These curves can be used to calculate maps of quantitative tracer kinetic parameters (e.g. K^{Trans}, right). DCE-MRI images by courtesy of Paul Armitage; reprinted from Heye et al. (2014).

Different approaches have been used to analyse DCE-MRI data, ranging from relatively simple visual assessment of signal enhancement curves to more complex fitting of tracer kinetic models (see section 1.2.3). Semi-quantitative analysis usually aims at describing general characteristics of the signal enhancement curve. Established measurements include, for instance, the area under the curve and the time to maximum enhancement. Such measurements are easy to obtain but difficult to interpret (Budde et al., 2012).

More advanced analysis often involves relating the measured signal enhancement to the contrast agent concentration, which requires an appropriate signal model. While early DCE-

MRI studies assumed a linear relationship between signal enhancement and contrast uptake, it is well known that the signal enhancement is non-linear and highly dependent on intrinsic tissue and acquisition parameters (Armitage et al., 2005, 2011). Consequently, more complex approaches were developed in order to control for the effect of tissue characteristics, such as the longitudinal and transverse contrast agent relaxivities r_1 and r_2 and the pre-contrast longitudinal relaxation time $T1_0$ (Armitage et al., 2005). The gold standard method for measuring T1 is a series of inversion recovery sequences with variable inversion time TI (Larsson et al., 1988). While this method has been shown to be very exact (Zhang et al., 1998), it requires long imaging times to achieve a sufficient SNR, spatial resolution and coverage. Consequently, it usually only allows for single-slice coverage. Several more time-efficient methods have been introduced for clinical practice, for instance the Look-Locker approach (Look and Locker, 1970) and the commonly used 3D T1W spoiled GRE sequence repeated with different flip angles (Brookes et al., 1999). While these methods allow for large spatial coverage and high spatial resolution, they often suffer from a low SNR. Furthermore, there are several factors that can compromise the accuracy of T1 measurements, such as blood flow artefacts and flip angle uncertainty (Tofts, 2005). Every method for T1 measurement involves a compromise between spatial resolution/coverage, accuracy and acquisition time; thus, the optimal method will depend on the requirements of the specific application. Since intrinsic tissue properties such as T1 and r_1 affect the relationship between signal enhancement and contrast agent concentration, uncertainties in these parameters propagate through to quantitative estimates of BBB functionality. Consequently, measurement errors or the use of assumed values can introduce significant bias in the analysis of DCE-MRI data (Armitage et al., 2011; Schabel and Parker, 2008).

1.2.3. Quantitative analysis of DCE-MRI data

Quantitative analysis aims to provide a link between the tissue signal enhancement and physiologically relevant parameters, such as microvascular permeability, blood flow, blood volume fraction and interstitial volume fraction. Tracer kinetic modelling was first introduced for the analysis of DCE-MRI in the early 1990s by Brix et al. (1991), Larsson et al. (1990) and Tofts and Kermode (1991), followed by a consensus paper on the notation (Tofts et al., 1999). Since then, improvement of the imaging techniques (e.g. higher temporal resolution and contrast-to-noise ratio) and a better understanding of the underlying physiology have promoted the development of several more complex tracer kinetic models. The following sections will provide a brief introduction to tracer kinetic modelling in DCE-MRI; detailed reviews have been published by Sourbron and Buckley (2012, 2013) and Koh et al. (2011). A summary of the main notations and parameters is provided in Table 1.2.

Table 1.2.: List of the main quantities and target parameters in tracer kinetic modelling. The parameters are generally normalised by either tissue volume or tissue mass, resulting in different possible units.

Symbol	Description	Units
$C(t)$	Contrast agent concentration in tissue	mM
$c_a(t)$	Contrast agent concentration in arterial blood plasma	mM
$c_p(t)$	Contrast agent concentration in capillary blood plasma	mM
$c_e(t)$	Contrast agent concentration in EES	mM
v	Distribution volume	dimensionless (ml/ml) or ml/g
J	Flux	mmol/min/ml or mmol/min/ml
F	Clearance	1/min (ml/min/ml) or ml/min/g
$R(t)$	Residue function	dimensionless
$I(t)$	Impulse response function	1/min (ml/min/ml) or ml/min/g
F_p	Plasma flow	1/min (ml/min/ml) or ml/min/g
PS	Permeability-surface area product	1/min (ml/min/ml) or ml/min/g
E	Extraction fraction	dimensionless (mM/mM)
$K^{\mathbf{Trans}}$	Volume transfer constant	1/min (ml/min/ml) or ml/min/g
v_p	Fractional plasma volume	dimensionless (ml/ml) or ml/g
v_e	Fractional interstitial volume	dimensionless (ml/ml) or ml/g

General tracer kinetic theory

All tracer kinetic models are based on the general tracer kinetic theory of linear and stationary systems (Lassen and Perl, 1979). Tracer kinetic theory describes the transport of an indicator, such as a gadolinium based contrast agent, in a tissue sample. The tissue sample is considered to have at least one inlet and one outlet, through which indicator is delivered and extracted. The tissue concentration $C(t)$ (in mM) is the amount of indicator in the tissue sample at time t relative to the tissue volume. While $C(t)$ is of interest in DCE-MRI because it is related to the signal enhancement and can, thus, be measured directly, the concepts of tracer kinetic theory are most naturally defined in terms of the local concentration $c(t)$ (Sourbron, 2014). The concentration $c(t)$ is defined as the amount of indicator within the distribution volume v, i.e. the fraction of tissue that is accessible to the indicator:

$$c(t) = \frac{C(t)}{v}. \tag{1.5}$$

The amount of indicator that passes through an inlet per unit of time and tissue volume is referred to as flux J. The clearance F is defined as the ratio of the flux and the concentration at the inlet or outlet (Sourbron and Buckley, 2013), so that

$$J(t) = Fc(t). \tag{1.6}$$

The volume of distribution, flux and clearance are usually normalised to either the volume (in ml) or the mass (in g) of tissue. As a result, different units can be found in the DCE-MRI literature (both notations for all parameters are given in Table 1.2). However, brain tissue has a density close to 1 g/ml (Barber et al., 1970), which generally makes the units interchangeable. If not stated otherwise, all tracer kinetic parameters in this thesis will be normalised to tissue volume; a normal tissue density of 1 g/ml is assumed when converting parameters reported elsewhere.

According to the principle of conservation of mass, no indicator can be created or destroyed inside the tissue. Consequently, the change of indicator inside the tissue sample can be expressed as the difference between the total influx J_{in} through inlets i and total outflux J_{out} through outlets o:

$$\frac{dC}{dt}(t) = \sum_i J_{in} - \sum_o J_{out} = \sum_i F_i c_i(t) - \sum_o F_o c_o(t). \tag{1.7}$$

If the clearances F are independent of concentration c, the system is called linear; it is called stationary if F does not depend on t. In a linear and stationary system, a solution of the differential equation is given by

$$C(t) = \sum_i R_i(t) * F_i c_i(t), \tag{1.8}$$

where $*$ denotes the convolution product and $R_i(t)$ is the residue function (Sourbron and Buckley, 2013). The residue function describes the fraction of indicator particles that entered an inlet i at $t = 0$ and are still present at time t.

In most applications, the system is considered to have a single inlet, i.e. the indicator enters the tissue sample through a single arterial vessel. In this case, the total influx is given by the product of the blood plasma flow F_p and the indicator concentration in the inflowing arterial blood plasma $c_a(t)$:

$$\sum_i J_{in} = \sum_i F_i c_i(t) = F_p c_a(t). \tag{1.9}$$

$c_a(t)$ is called the arterial input function (AIF) and generally has to be known for tracer kinetic modelling. There are several strategies for determining the AIF (Calamante, 2013), including the use of experimentally derived population-averaged AIFs (Parker et al., 2006; Weinmann et al., 1984) and the simultaneous individual measurement of the AIF in a feeding vessel close to the tissue of interest (Sourbron et al., 2009). Applying this single inlet to equation 1.8 leads to the following expression for the tissue concentration:

$$C(t) = F_p R(t) * c_a(t) = I(t) * c_a(t), \tag{1.10}$$

where $I(t)$ is the tissue-characteristic impulse response function. The aim of tracer kinetic

modelling is to extract physiological information from the measured impulse response function. In order to achieve this, assumptions on the distribution of indicator inside the tissue have to be made.

Figure 1.10 displays a general tissue model with exchange of contrast agent between blood plasma and the EES. Target parameters of tracer kinetic modelling in DCE-MRI are the fractional plasma volume v_p, the fractional interstitial volume v_e, the plasma flow F_p and the permeability-surface area product PS, which measures the rate at which contrast agent particles leak out of the plasma and into the EES over an assumed surface area per unit tissue volume and plasma concentration. An important physiological parameter that is widely reported in DCE-MRI studies is the volume transfer constant K^{Trans}, which is the rate at which contrast agent is delivered to the EES per volume of tissue and contrast agent concentration in the arterial blood plasma. While the terms PS and K^{Trans} are sometimes used interchangeably in the literature, PS represents the clearance for contrast agent leaking from the capillary plasma into the EES, i.e. the flux of contrast agent across an assumed surface area of the BBB normalised to the tissue plasma concentration and tissue volume. In contrast, K^{Trans} (as implicitly defined by Tofts et al., 1999), is the contrast clearance normalised to the arterial plasma concentration and therefore depends on the plasma flow F_p supplying the capillaries in addition to PS (the mathematical form of this relationship is model-dependent). K^{Trans} is necessarily equal to the product of plasma flow F_p and the extraction fraction E (i.e. the fraction of contrast agent molecules that leak into the EES).

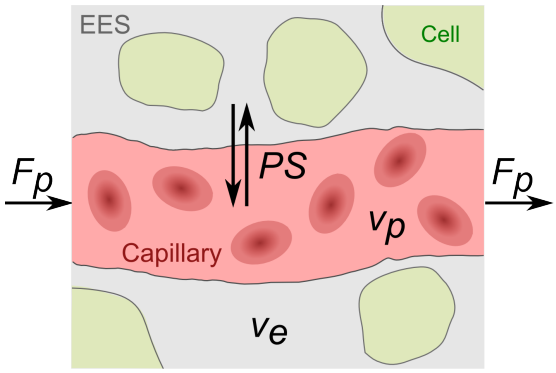

Figure 1.10.: Schematic illustration of a generic tissue model. The exchange between the EES (volume fraction v_e) and capillary blood plasma (volume fraction v_p) is determined by the plasma flow F_p and the permeability-surface area product PS. Reprinted from Heye et al. (2014).

Compartment models

The general tissue architecture presented in Figure 1.10 is usually modelled as a single space or a system of several spaces. A complete model for vascular-interstitial exchange can be formed with two spaces: the blood plasma and the EES. There are different approaches to modelling each of these two spaces: the blood plasma can be modelled as a well-mixed compartment, i.e. a region where the contrast agent concentration is spatially uniform, or as a plug-flow system, i.e. a region of flow with a constant velocity. Similarly, the interstitium can be modelled as well-mixed compartment or a distributed system, which assumes instant contrast transport perpendicular to the capillary. A complete model for vascular-interstitial exchange can be formed by combining two models for the blood plasma and the EES, leading to four different possible models. A detailed overview of the different tissue models has been provided by Sourbron and Buckley (2013); this thesis will focus on models that consider both the blood-plasma and the EES to be well-mixed compartments, because they are the most commonly used in DCE-MRI of the brain.

In multi-compartment models, the total tissue concentration consists of contributions of each subspace, so that the tissue concentration $C(t)$ is given by

$$C(t) = v_p c_p(t) + v_e c_e(t), \tag{1.11}$$

where $c_p(t)$ is the concentration of indicator in the capillary plasma space and $c_e(t)$ the interstitial indicator concentration. The principle of conservation of indicator mass (equation 1.7) must be fulfilled for each subspace, resulting in a system of differential equations. The only well-mixed compartment model that allows for the estimation of all four target parameters (F_p, PS, v_p and v_e) and has been applied in brain DCE-MRI is the two-compartment exchange model (2CXM) (Sourbron and Buckley, 2013). In many situations, it is not possible to measure all four parameters reliably. Hence, several simpler models have been proposed, which constrain the general four-parameter model to specific situations. Figure 1.11 shows an overview of the constrained models that can be derived from the 2CXM. The following section will present the compartment models most commonly used for DCE-MRI of the brain.

The conventional Tofts model (Tofts and Kermode, 1991) considers bidirectional flux of tracer between the two blood plasma and EES compartments with the volume transfer constant K^{Trans}. The plasma compartment is assumed to have negligible volume ($v_p \approx 0$), which makes the conventional Tofts model a one-compartment model for weakly vascularised tissues. The impulse response function is given by

$$I(t) = K^{\text{Trans}} \exp(-tK^{\text{Trans}}/v_e), \tag{1.12}$$

resulting in the following solution for the tissue concentration:

$$C(t) = K^{\text{Trans}} \int_0^t c_a(\tau) \exp\left(-K^{\text{Trans}}/v_e(t-\tau)\right) d\tau. \tag{1.13}$$

In a permeability-limited situation, i.e. $F_p \gg PS$, K^{Trans} equals PS; in a flow-limited situation, i.e. $F_p \ll PS$, K^{Trans} represents F_p.

Tofts et al. extended their classic model by introducing the blood plasma as a second well-mixed compartment (Tofts et al., 1999); this model is known as the modified Tofts model. In addition to the two parameters K^{Trans} and v_e, the model allows for v_p to be estimated and, hence, aims to separate enhancement effects due to contrast leakage from those due to intravascular contrast:

$$C(t) = v_p c_a(t) + K^{\text{Trans}} \int_0^t c_a(\tau) \exp\left(-K^{\text{Trans}}/v_e(t-\tau)\right) d\tau. \tag{1.14}$$

The tissue is assumed to be highly perfused, i.e. $F_p = \infty$, which means that the entire blood pool is well-mixed so that $c_p(t) = c_a(t)$. If the model fits the data well with a non-negligible v_p value, then the system is permeability-limited with $K^{\text{Trans}} = PS$ (Sourbron and Buckley, 2013). The impulse response function is given by

$$I(t) = v_p \delta(t) + K^{\text{Trans}} \exp(-tK^{\text{Trans}}/v_e). \tag{1.15}$$

Finally, the Patlak model (Patlak et al., 1983) also describes a highly perfused two-compartment tissue but considers unidirectional transport from the blood plasma into the EES. It can be seen as a special case of the modified Tofts model that ignores backflux from the EES into the blood. The impulse response function is reduced to

$$I(t) = v_p \delta(t) + K^{\text{Trans}}. \tag{1.16}$$

Hence, the tracer concentration in tissue is given by:

$$C(t) = v_p c_a(t) + K^{\text{Trans}} \int_0^t c_a(\tau) d\tau. \tag{1.17}$$

When first introducing this approach, Patlak and colleagues proposed a linear graphical analysis method, which is often used as it permits simple and fast fitting. In this analysis, the ratio $C(t)/c_a(t)$ is regressed against $\int_0^t c_a(\tau) d\tau / c_a(t)$, yielding a straight line with slope K^{Trans} and y-intercept v_p.

It should be noted that all tracer kinetic models paint a significantly simplified picture of the true complex biological system. The simpler the model, the greater is the amount of assumptions

regarding tissue structure and the transport of blood plasma and contrast agent. This over-simplification can lead to bias in the estimated physiological parameters. For example, all models discussed here assume that the water exchange between the vascular, EES and intracellular compartments is in the fast-exchange limit, i.e. that the tissue relaxes with a single T1 (Sourbron and Buckley, 2011). However, transendothelial water exchange is likely to be limited in brain tissues with largely intact BBB. Violation of this assumption can lead to systematic errors in estimates of contrast agent concentrations and tracer kinetic parameters (Bains et al., 2010; Larsson et al., 2001). While it is tempting to apply a model accounting for as many biological processes as possible, the resulting high number of free parameters can lead to estimates with low accuracy and precision. Instead, the optimum model depends on both the nature of the tissue and the acquisition protocol employed (Sourbron and Buckley, 2013; Ewing and Bagher-Ebadian, 2013).

1.3. Challenges of DCE-MRI in cerebral SVD

Historically, DCE-MRI has been mainly applied in body tissues without BBB or the assessment of diseases that show relatively large abnormalities in BBB functionality, such as brain tumours and acute ischaemic strokes. Only recently has there been growing interest in the application of DCE-MRI to pathologies associated with subtle BBB disruption, such as diabetes and Alzheimer's disease (Starr et al., 2003, 2009). In cerebral SVD, observed signal enhancement in normal-appearing tissue and lesions is of the order of only a few percent. This subtle nature of the process poses various challenges for the imaging procedure and data analysis:

1. Although there is a variety of approaches for the analysis of DCE-MRI data, these have mostly been developed for oncology applications, where vessel density and permeability are typically high. The optimal approach for research in cerebral SVD is unclear. In addition to very low target levels of BBB dysfunction, DCE-MRI in SVD is likely to suffer from compromised temporal resolution, as the diffuse nature of the disease makes a high spatial coverage and resolution desirable. Hence, it needs to be examined whether tracer kinetic modelling is suitable and yields valid results in this situation.

2. The small DCE-MRI changes linked to subtle BBB breakdown are particularly susceptible to sources of error, such as uncertainty in relaxation times and contrast agent relaxivities. Moreover, low-level DCE-MRI measurements may be susceptible to influences by secondary processes, such as random noise, scanner drift or partial volume effect (Armitage et al., 2011). In order to enable reliable quantification of BBB integrity, it needs to be investigated to what extent the measured changes in DCE-MRI parameters are influenced by mechanisms other than BBB disruption.

3. Measurements of BBB disruption are most likely dependent on details of the acquisition protocol (e.g. type and dose of contrast agent, field strength, MRI pulse sequence), especially when looking at subtle abnormalities. Therefore, it is important to critically review clinical results and explore inter-study comparability.

Although there is growing interest in the application of DCE-MRI for the measurement of low-level BBB disruption as related to ageing and SVD, only very few groups have investigated the optimum methodology and reliability of resulting quantitative parameters. Consequently, there is a need for substantially more work to determine the optimum acquisition strategy and data analysis methods.

1.4. Aims and outline of the thesis

The work described in this thesis aims to assess and improve the methodology of DCE-MRI measurements in cerebral SVD and, thus, move closer towards reliable quantification of subtle BBB abnormalities. In addition to developing and assessing methods, this thesis also aims to investigate the role of BBB disruption and other MR imaging markers in cerebral SVD, by applying the methodology to a large clinical cohort of mild stroke patients. Reliable estimation of low-level BBB disruption can help to illuminate the role of endothelial failure in cerebral SVD, which may ultimately offer possibilities for early treatment and prevent severe outcomes such as strokes and dementia. This thesis is organised in five parts, which are further divided into different chapters. The following sections will present the specific aims and key contents of the subsequent eight chapters of this thesis.

Part I introduces the fundamental concepts that the work in this thesis is based on and gives a summary of DCE-MRI methods. This part has one further chapter:

Chapter 2 aims to provide an overview of applications, scanning protocols and data analysis methods used in DCE-MRI of the brain. A systematic literature review is performed, including all studies that assessed BBB integrity using T1W DCE-MRI techniques in animals and humans in normal or abnormal brain tissues.

Part II focuses on the analysis of DCE-MRI data acquired within the scope of an on-site clinical study of mild stroke patients.

Chapter 3 introduces the patient cohort, study procedures and image processing methods. Furthermore, this chapter aims to investigate some basic aspects of DCE-MRI analysis processes, such as AIF measurement and tracer concentration calculation.

Chapter 4 aims to determine the tracer kinetic model most suitable for analysis of the clinical data presented in chapter 3 and provides quantitative DCE-MRI parameters for normal-appearing tissues

and brain lesions. Moreover, this chapter tests the robustness of the model to its assumptions using simulations.

Part III investigates two potential pitfalls in the quantification of subtle BBB disruption.

Chapter 5 aims to investigate instrumental/physiological drift and its influence on tracer kinetic parameters. Signal drift is assessed in healthy volunteers, and its effect on quantitative parameters is modelled using computer simulations.

Chapter 6 aims to analyse an external DCE-MRI data set and to compare the results to the findings in the MSSII cohort. This chapter also discusses issues concerning inter-study comparability and study design, which arise from this work.

Part IV examines the relationship between MRI parameters and clinical measurements in the large cohort of mild stroke patients.

Chapter 7 focuses on statistical analyses of the DCE-MRI parameters obtained in chapter 4. The main purpose of this chapter is to investigate the relationship between measurements of BBB leakage and cerebral blood volume with clinical characteristics, SVD imaging markers and disease progression.

Chapter 8 presents work that was performed within the wider scope of our on-site clinical study of mild stroke patients; this work aims to investigate the association between MR imaging findings in cerebral SVD and blood pressure, dietary salt intake and plasma sodium concentration.

Part V provides final conclusions and perspectives.

Chapter 9 summarises the main findings and outlines the contributions that this work has made to the field. In addition, this chapter highlights limitations of the work presented in this thesis and suggests avenues for future research.

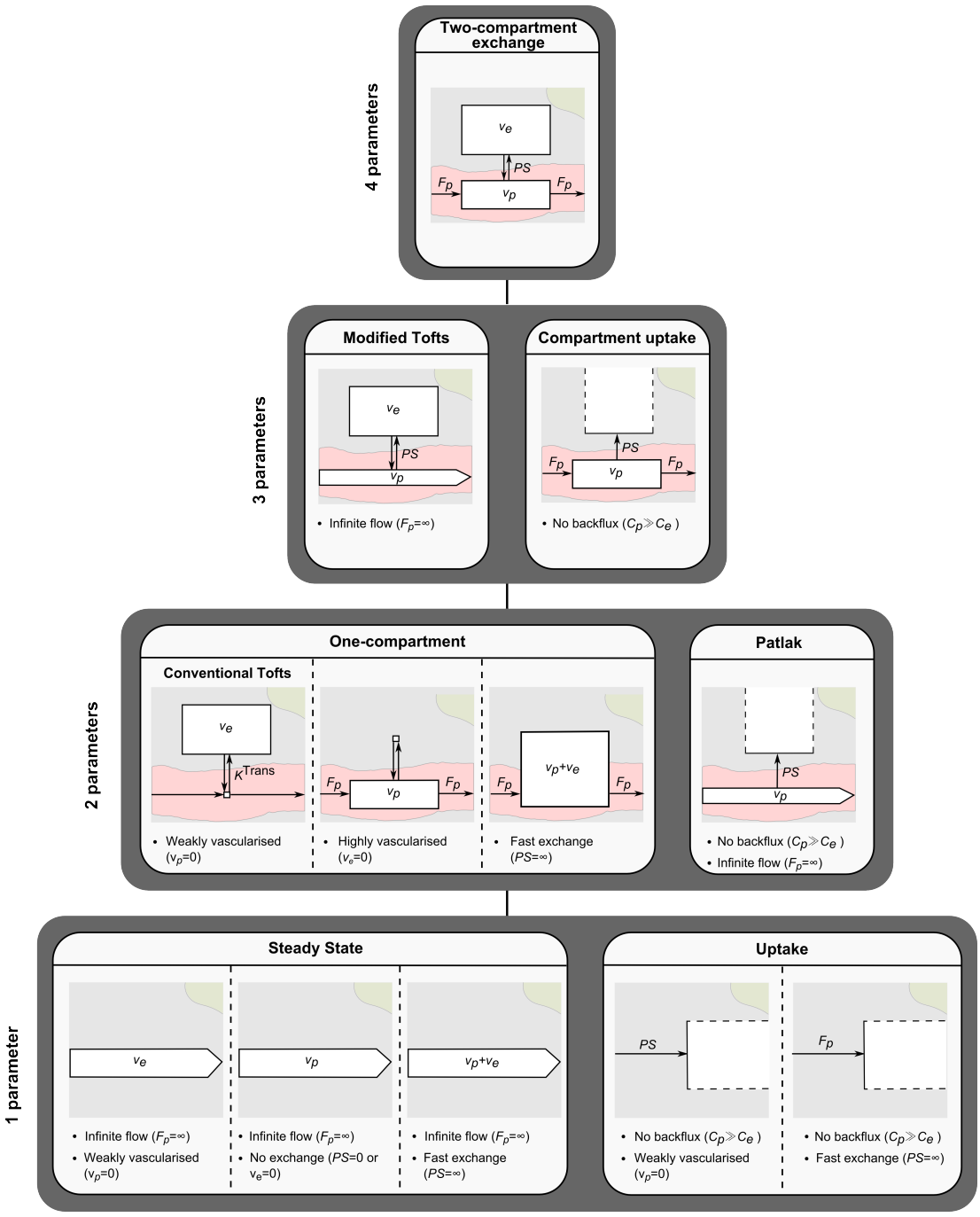

Figure 1.11.: Overview of compartment models for DCE-MRI. Schematic drawings of the 2CXM and derived simpler models with their assumptions (according to review by Sourbron and Buckley, 2013). Target parameters: plasma flow F_p, permeability-surface area product PS, volume-transfer constant K^{Trans}, interstitial volume fraction v_e, blood plasma volume fraction v_p.

2. Assessment of blood-brain barrier disruption using dynamic contrast-enhanced magnetic resonance imaging: a systematic literature review

This chapter aims to provide an overview of applications, scanning protocols and data analysis methods used in dynamic-contrast enhanced magnetic resonance imaging (DCE-MRI) of the brain. A previous version of this literature review has been published in Heye et al. (2014).

2.1. Introduction

DCE-MRI has been used to study pathological changes of blood-brain barrier (BBB) functionality in a large variety of diseases. However, there is no standard approach of measuring and analysing DCE-MRI data: studies differ widely in their MR imaging procedures and several methods for analysing the data are available, ranging from relatively simple non-model based methods to several tracer kinetic models. DCE-MRI has been mainly applied in body tissues without BBB and in diseases with large abnormalities in BBB functionality. Consequently, most previous literature reviews have focused on specific applications such as oncology (Barnes et al., 2012; Bergamino et al., 2014; Jain, 2013; Türkbey et al., 2010). Only recently has there been growing interest in the application of DCE-MRI to pathologies associated with subtle BBB disruption, and there are no literature reviews that cover the application of DCE-MRI in ageing, microvascular disease or dementia.

The aim of this systematic literature review was to provide an overview of all applications and imaging procedures used in DCE-MRI of the brain. Furthermore, the purpose of this work was to identify the most commonly used methods for data analysis and to provide an overview of the resulting parameter ranges for pathological and normal-appearing tissues. Finally, this review aimed to investigate studies that have attempted to measure subtle BBB changes and to assess whether their approaches differ from the ones used in other applications.

2.2. Methods

2.2.1. Search strategy

The existing literature was systematically reviewed up to May 2015 by performing an electronic search in PubMed, EMBASE, MEDLINE and Web of Knowledge databases. Multiple combinations of the following search terms were used: 'permeability', 'brain', 'blood-brain barrier', 'MRI', 'dynamic', 'DCE-MRI' and 'contrast enhancement'. English as well as non-English literature was sought. Ross D Culling, a medical student at the University of Edinburgh, performed the initial literature search, removed duplicates and screened all papers' titles and abstracts in order to identify those relevant for full assessment. The electronic search was supplemented by hand searching the reference lists of review papers. Before final inclusion or exclusion of studies, the full text of all selected articles was read and the relevant data extracted. Disagreements between reviewers about inclusion or exclusion of papers were resolved through discussion with Dr Maria del C Valdés Hernández. Dr Michael J Thrippleton, Dr Maria del C Valdés Hernández and Prof Joanna M Wardlaw complemented the search and assisted with the data analysis. The original systematic literature search included articles published up to February 2014; in order to update the review, an additional manual search was performed in May 2015.

2.2.2. Eligibility criteria

This literature review focuses on studies which assessed BBB integrity using DCE-MRI techniques. Studies on humans and animals were included in all diseases known or thought to affect BBB function. Consequently, other applications of DCE-MRI such as breast or prostate cancer as well as publications that focus on theoretical aspects of image processing or modelling without testing them in a clinical setting (e.g. Gal et al., 2008) were excluded. Furthermore, only primary research articles available as full-text were accepted; however, review articles were checked for additional primary references.

Studies using dynamic susceptibility contrast magnetic resonance imaging (DSC-MRI), non-MRI methods or non-dynamic MRI methods, which are not generally quantitative, were excluded from this review. The literature search yielded several papers that focused on therapeutic BBB disruption for novel anti-cancer drugs. Since these mainly addressed pharmaceutical or technical aspects of the disruption method on a molecular level, these studies were rejected. An excellent review on DCE-MRI in clinical trials of antivascular therapies has been published by O'Connor et al. (2012). However, studies that focused on the clinical effect of treatment strategies and its link with BBB disruption were included if they provided baseline DCE-MRI

parameters. Moreover, single case reports and articles in which substantial information about the MRI procedure or the data analysis was lacking were rejected.

2.2.3. Data extraction and analysis

Relevant data were extracted from each included study. Information was cross-checked with preliminary data that had previously been extracted by Ross D Culling. Extracted data included the studied disease or pathology, sample size and subjects' ages (in the case of human studies). Moreover, details of the DCE-MRI protocol were extracted, including scanner field strength, MRI sequence with repetition time TR, echo time TE, flip angle, field of view (FoV), matrix size, slice thickness, overall duration and temporal resolution. Extracted data also included the type and dose of contrast agent. Furthermore, it was noted whether post-processing techniques were applied prior to data analysis, the analysis method used and the tissues/locations analysed. Where given, quantitative measurements were extracted. Additionally, the main study purpose and the overall conclusion of the study were summarised.

2.3. Results

2.3.1. Systematic literature search results

The electronic search yielded 829 results, 31 of which were in non-English languages. After removing duplicates, 352 publications were further analysed for inclusion. After scanning abstracts and titles, studies using non-dynamic and non-MRI methods were excluded ($n = 179$). In addition, review papers ($n = 46$), technical protocols ($n = 2$) and DSC-MRI studies ($n = 38$) were rejected, leaving 87 articles for full-text assessment. At this stage, 29 studies were identified as not being relevant to the focus of this review. Moreover, conference abstracts that were not detailed enough for full data extraction and that had not subsequently been published in full ($n = 8$), single-case reports and publications with missing information on the imaging methodology ($n = 2$) and publications that were based on previously published data ($n = 1$) were excluded. In addition to the resulting 47 relevant DCE-MRI studies, 23 relevant articles were identified by hand searching the bibliographies of review papers. Overall, the full literature search to February 2014 provided 70 DCE-MRI studies that were eligible for inclusion in this review. The search was manually updated in May 2015, yielding 10 relevant publications that had been missed previously and 15 relevant papers published between February 2014 and May 2015 (see Figure 2.1).

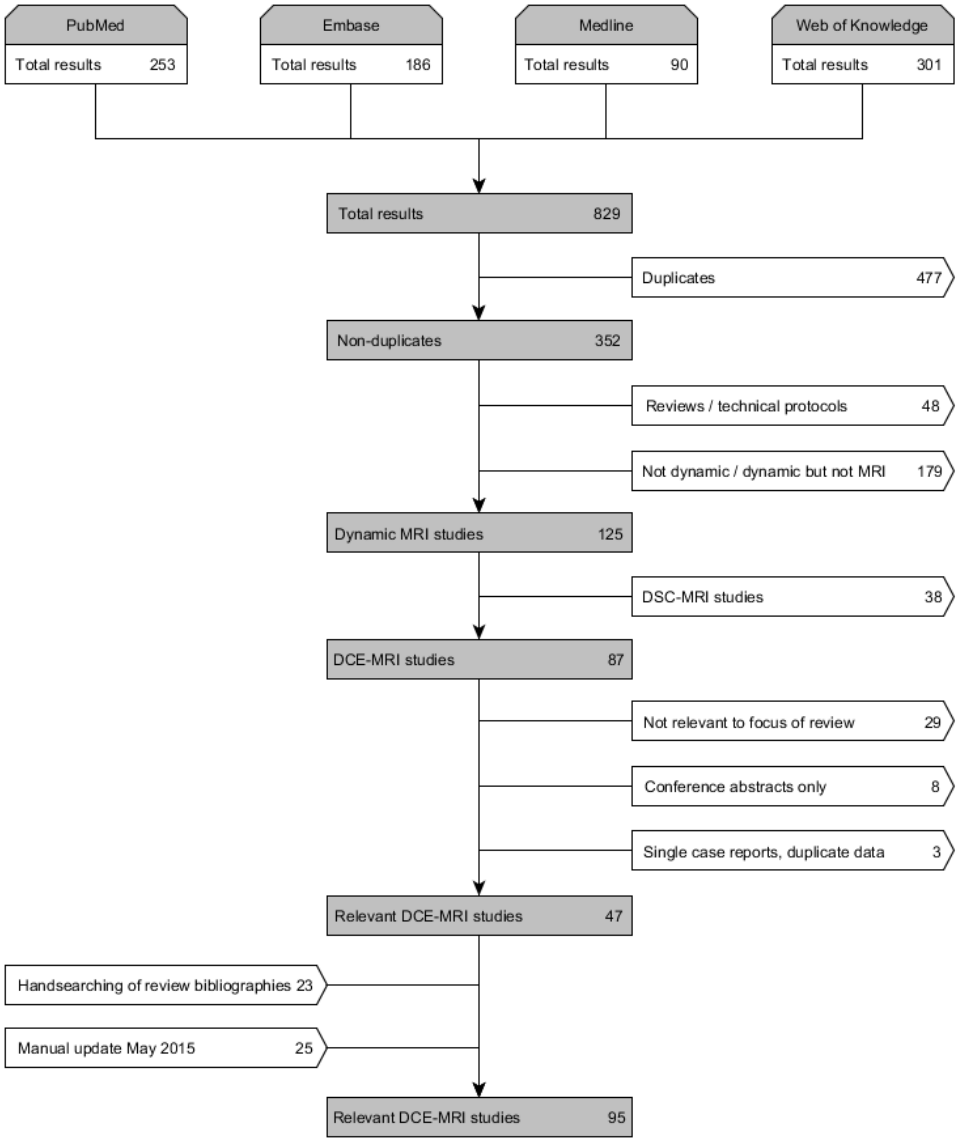

Figure 2.1.: Flow diagram summarising the literature search and inclusion process. Previous version published in Heye et al. (2014).

2.3.2. Study characteristics

Subjects and sample sizes

Table 2.1 summarises the main study sample characteristics and scanning protocols related to each pathology. Of the 95 included studies, 24 used animals (i.e. rodents, apart from two studies of dogs (Su et al., 1998; Li et al., 2014) and one of rabbits (Wei et al., 2011)). The sample size was not made available in one of these publications (Ewing et al., 2003). The mean sample size

of the remaining animal studies was 21 animals, with a total number of 495 animals (including 19 healthy controls; 447/495 were rodents). The largest included study involved 113 rats (Abo-Ramadan et al., 2009), whereas seven studies used a sample size smaller than 10 (Chwang et al., 2014; Ferrier et al., 2007; Hormuth et al., 2014; Lee et al., 2014; Li et al., 2010, 2014; Skinner et al., 2012).

The remaining 71 studies were in humans, including 2295 subjects in total (235 of which were healthy controls). Although duplicate publications that were undoubtedly based on the same data were excluded, it should be noted that some of the included studies were performed by the same research group and, thus, might share some patient data; consequently, the total number of individual patients is likely to be smaller than stated above. The mean sample size for human studies was 32. Only two studies involved more than 100 subjects (Haris et al., 2008a; Sahoo et al., 2013) and seven studies were based on fewer than 10 humans (Jelescu et al., 2011; Larsson et al., 1990; Kermode et al., 1990; Kleppestøet al., 2014; Li et al., 2012a; Thompson et al., 2012; Vidarsson et al., 2009). Information regarding patient age was not provided in eight of the 71 studies (Aksoy et al., 2013; Awasthi et al., 2012; Larsson et al., 1990, 2014; Li et al., 2000, 2012a; Miyati et al., 1997; Sourbron et al., 2009). A further eight publications stated only the age range of the study subjects (Bagher-Ebadian et al., 2012; Gupta et al., 2012; Haris et al., 2008b; Kassner et al., 2005; Manuchehri et al., 2007; Roberts et al., 2000; Vidarsson et al., 2009; Sahoo et al., 2013). Mean age as stated in the remaining 55 human studies was highly dependent on the studied pathology, ranging between 9 years (paediatric brain tumours, Thompson et al., 2012) and 74 years (mild cognitive impairment, Wang et al., 2006).

A complete list of included publications and their main characteristics is provided in the appendix (Table A.1).

Pathologies studied

The majority of animal studies concerned intracranial neoplasms (Ali et al., 2010; Aryal et al., 2014; Budde et al., 2012; Chwang et al., 2014; Engelhorn et al., 2013; Ferrier et al., 2007; Hoff et al., 2012; Hormuth et al., 2014; Krueck et al., 1994; Li et al., 2010; Nagaraja et al., 2013; Quarles et al., 2012; Skinner et al., 2012) including a total of 215/495 animals. Five publications investigated changes in the BBB caused by induced focal cerebral ischaemia in 154/495 animals overall (Abo-Ramadan et al., 2009; Ewing et al., 2003; Durukan et al., 2009; Nagaraja et al., 2010; Taheri et al., 2009). Moreover, two studies focused on traumatic head injuries (Li et al., 2014; Wei et al., 2011) and one study each investigated the influence of pneumococcal meningitis (Brandt et al., 2008), normal ageing (Su et al., 1998) or zinc deficiency (Noseworthy and Bray, 2000) on the BBB.

The pathology most studied in humans was intracranial neoplasms (43 publications, 1266/2295 subjects), including primary brain tumours and brain metastases. 12 studies investigated changes in BBB integrity caused by stroke and/or cerebrovascular disease (Aksoy et al., 2013; Armitage et al., 2011; Hanyu et al., 2002; Kassner et al., 2005, 2009; Taheri et al., 2011a,b; Thornhill et al., 2010; Topakian et al., 2010; Vidarsson et al., 2009; Wardlaw et al., 2008, 2009) with a total of 506/2295 subjects. 11 studies focused on multiple sclerosis (MS) (Cramer et al., 2014; Cramer and Larsson, 2014; Gaitán et al., 2011; Ingrisch et al., 2012; Jelescu et al., 2011; Kermode et al., 1990; Larsson et al., 1990; Leppert et al., 2014; Montagne et al., 2015; Shinohara et al., 2011; Taheri et al., 2011b) including a total of 270/2295 subjects. Six articles investigated changes of the BBB related to normal ageing (Montagne et al., 2015), mild cognitive impairment (Montagne et al., 2015; Wang et al., 2006) or dementia (Hanyu et al., 2002; Starr et al., 2009; Taheri et al., 2011b; Wahlund and Bronge, 2000). Other studied pathologies included brain tuberculomas (Haris et al., 2008b; Singh et al., 2007), optic neuritis (Cramer and Larsson, 2014), infective brain lesions (Haris et al., 2008a), multiple system atrophy (Song et al., 2011), diabetes (Starr et al., 2003) and neurocysticercosis (Gupta et al., 2012).

2.3.3. MRI procedures

Scanning techniques

The majority of human studies (41/71) were performed with a magnetic field strength of 1.5 T, while 29 studies used a 3 T scanner; one study each was performed using a 0.5 T (Kermode et al., 1990) and a 1.9 T scanner (Starr et al., 2003). A wider range of magnetic field strengths from 1.5 T (Krueck et al., 1994; Su et al., 1998) to 11.75 T (Li et al., 2010) were found in animal studies, with the majority of studies using 4.7 T or 7 T scanners. Two studies did not provide this information (Li et al., 2012a; Wei et al., 2011). Sahoo et al. (2013) compared DCE-MRI results from a 1.5 T and a 3 T scanner; while they found differences in the average tracer kinetic parameter values, the scanners performed equally well in classifying glioma grades.

The MRI pulse sequence types used are summarised in Figure 2.2(a). Most DCE-MRI acquisitions were based on gradient echo (GRE) sequences (79/95 studies), with spoiled GRE techniques being the most common. Further protocols include seven spin echo methods (Hanyu et al., 2002; Kermode et al., 1990; Krueck et al., 1994; Larsson et al., 1990; Su et al., 1998; Noseworthy and Bray, 2000; Wahlund and Bronge, 2000) and five unspecified T1-weighted (T1W) imaging sequences (Ahn et al., 2014; Choi et al., 2013; Farjam et al., 2014; Song et al., 2011; Starr et al., 2003). In addition, five studies used DCE-MRI methods that consist of repeated T1 measurements (Ewing et al., 2003; Nagaraja et al., 2010; Taheri et al., 2009, 2011a,b).

A complete list of the imaging procedures applied in the included studies is provided in the appendix (Table A.2), and also provides information about the spatial resolution and coverage. While some studies apply DCE-MRI methods with whole-brain coverage (e.g. Harrer et al., 2004; Ingrisch et al., 2012; Topakian et al., 2010; Wardlaw et al., 2009), most studies only image a limited FoV with a few slices (e.g. Cramer et al., 2014; Ewing et al., 2003; Larsen et al., 2013; Sourbron et al., 2009) or one single slice (e.g. Abo-Ramadan et al., 2009; Durukan et al., 2009; Lüdemann et al., 2000; Quarles et al., 2012), with slice thicknesses ranging from 1 mm to 8 mm.

Contrast agent and dose

The type and dose of contrast agents used in the included publications are shown in Figure 2.2(a). Information about the type and dose of contrast agent was not given in one study (Lee et al., 2014). In most studies, the contrast agent used was Gd-DTPA (gadopentetate dimeglumine, 53/95 studies) or its variants Gd-DTPA-BMA (gadodiamide, 19/95 studies), Gd-BT-DO3A (gadobutrol, 16/95 studies) or Gd-DOTA (gadoterate meglumine, 3/95 studies), given as an intravenous bolus injection. Single studies employed different gadolinium-based agents such as Gd-BOPTA (gadobentate-dimeglumine) (Montagne et al., 2015), gadoteridol (Thompson et al., 2012), gadofosveset (Chwang et al., 2014) and albumin-labelled Gd-DTPA (Ali et al., 2010). Chwang et al. (2014) compared two different contrast agents (Gd-DTPA and gadofosveset) in nine glioma-bearing rats; they found that the resulting mean estimates of K^{Trans} were significantly different, but highly correlated.

In 46/95 studies, the contrast agent was given in the standard dose (0.03 mmol/kg body weight for gadofosveset, 0.1 mmol/kg for all others). However, delivered doses ranged from a fifth (Awasthi et al., 2012) to fivefold (Abo-Ramadan et al., 2009; Brandt et al., 2008; Durukan et al., 2009) of the recommended dose. 10 studies delivered a fixed quantity of contrast agent, ranging between 7.5 mmol (Kassner et al., 2009; Thornhill et al., 2010; Vidarsson et al., 2009) and 20 mmol (Armitage et al., 2011; Wardlaw et al., 2008, 2009) in humans. We did not find any study that investigated the influence of different contrast agent concentrations, though Abo-Ramadan et al. state that different doses lead to an increase or decrease in signal-to-noise ratio (SNR) (Abo-Ramadan et al., 2009).

Duration and temporal resolution of DCE-MRI

The duration of data collection following contrast injection varied widely with values from 1.5 min (Shin et al., 2014) to 155 min (Shinohara et al., 2011). The median DCE-MRI imaging durations (not stated in seven publications, Bergamino et al., 2013; Brandt et al., 2008; Chu

Table 2.1.: Study sample characteristics and scanning protocols related to pathology. 'Mean age' displays the average of study mean ages for studies investigating the same pathology. '–' indicates that the information was not provided in the article. References are provided in the text of section 2.3.2.

Pathology	Sample				Scanning Protocol	
	Subjects	Number of studies	Number of subjects	Mean age (years)	Median imaging duration (min)	Median temporal resolution (s)
Intracranial neoplasms	Humans	43	1266	50.5	5.5	5.3
	Animals	13	215	n/a	15.0	8.7
Stroke / cerebrovascular disease	Humans	12	506	67.3	18.5	41.5
	Animals	5	154	n/a	25.0	150.0
MS	Humans	11	270	39.6	17.5	32.0
Dementia / mild cognitive impairment	Humans	6	165	73.1	25.3	219.5
Normal ageing	Humans	1	24	73.2	16	15.4
	Animals	1	15	n/a	12.0	15.0
Brain tuberculomas	Humans	2	18	23.2	2.8	5.3
Traumatic head injuries	Animals	2	33	n/a	9.8	11.5
Pneumococcal meningitis	Animals	1	42	n/a	–	–
Infective brain lesions	Humans	1	26	26.6	2.8	5.3
Diabetes	Humans	1	20	68.2	90.0	900.0
Multiple system atrophy	Humans	1	29	59.0	6.0	7.7
Neurocysticercosis	Humans	1	35	–	3.0	5.7
Zinc deficiency	Animals	1	36	n/a	36.0	240.0
Optic neuritis	Humans	1	1	–	15.7	1.3

et al., 2012; Engelhorn et al., 2013; Larsson et al., 1990; Li et al., 2010; Provenzale et al., 2006) according to pathology studied are shown in Table 2.1, together with the median temporal resolution (not stated in five publications, Bergamino et al., 2013; Brandt et al., 2008; Chu et al., 2012; Engelhorn et al., 2013; Provenzale et al., 2006). The highest temporal resolution of 1 s was found in tumour studies (Larsson et al., 2009; Quarles et al., 2012), whereas one study on diabetes used the longest intervals, in the range of 10 min to 30 min (Starr et al., 2003). Vidarsson et al. (2009), Larsson et al. (2013) and Cramer et al. (2014) investigated the influence of the temporal resolution and/or overall scan time on the quantification of BBB disruption. In both clinical data and simulation studies, they found that reducing the overall scanning time and sampling with a lower temporal resolution result in increased uncertainty of the tracer kinetic parameters.

As shown in Table 2.1, the overall scanning duration and the temporal resolution varied significantly between applications. In general, the highest temporal resolution was used in brain tumours. This is necessary to measure the fast kinetics typically seen in malignant neoplasms, but may limit spatial resolution and coverage. Conversely, studies that assess tissues with slow leakage rates (e.g. healthy appearing tissue in MS patients, ageing or dementia) often used lower temporal resolutions that allow for better spatial resolution and coverage. In order to combine the advantages of both approaches, Jelescu et al. (2011) and Li et al. (2012a) presented a dual temporal resolution scanning method with high temporal resolution during the bolus first pass and high spatial resolution during the later phase. A similar approach was later used by Leppert et al. (2014).

2.3.4. Data processing and analysis

Use of post-processing techniques

56 of the 95 included studies (59%) did not report the use or method of image post-processing. The most commonly used technique reported was image registration, aligning the DCE-MRI images to a pre-contrast acquisition and/or anatomic images, in order to remove patient movement (32/95 studies). Several studies reported a lack of precision of quantitative values due to limited spatial resolution or poor SNR (Cha et al., 2006; Ferrier et al., 2007; Gaitán et al., 2011; Kassner et al., 2009), but only five studies report the use of image processing techniques for noise reduction, including Gaussian smoothing (Lüdemann et al., 2009), Kalman filtering (Taheri et al., 2011a,b), unspecified smoothing of the signal enhancement curves (Ferl et al., 2010) and 'removing and compensation of noisy time points' (Artzi et al., 2015).

An additional confounding factor is signal drift, which was mentioned in four studies. Cramer et al. (2014) reported a signal drift of 1% to 3% over 15 min in healthy volunteers without

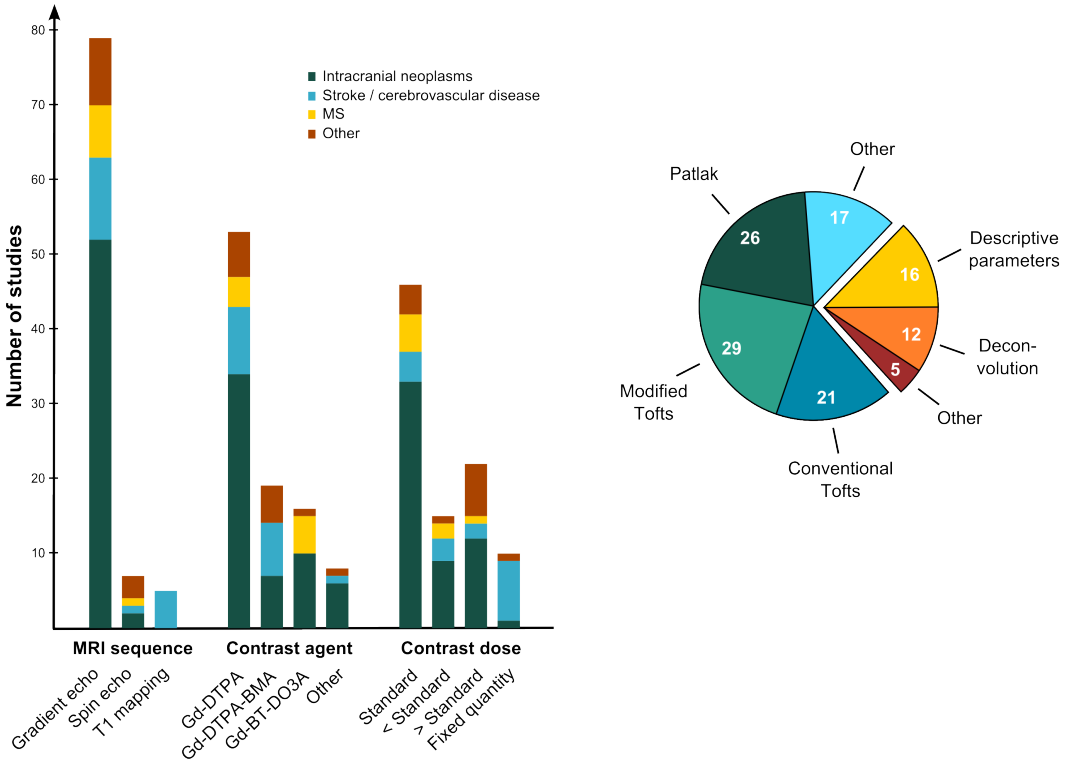

(a) MRI sequence and contrast agent/dose

(b) Data analysis methods

Figure 2.2.: Overview of methods used in the included studies. (a) MRI sequences, contrast agents and contrast doses used in the included studies. The bar height indicates the number of studies using a particular method, subdivided by pathology, (b) data analysis methods used in the included studies. Numbers indicate the count of studies using the particular tracer kinetic model (in blue-green colours) and model-free method (in yellow-red colours). Please note that some studies applied more than one approach and/or investigated more than one pathology; consequently, the numbers do not add up to the 95 included studies. Previous versions published in Heye et al. (2014).

contrast administration. Armitage et al. (2011) recommend that studies should investigate and if necessary correct for scanner drift in order to prevent systematic errors. However, only two studies corrected DCE-MRI data for scanner signal intensity drift using phantom or healthy volunteer measurements (Starr et al., 2003; Topakian et al., 2010).

Data analysis methods and tracer kinetic models

A wide variety of approaches to data analysis were used in the included studies (Figure 2.2(b)). The most simple analysis method was the visual assessment of spatiotemporal enhancement patterns in MS lesions (Gaitán et al., 2011; Kermode et al., 1990; Shinohara et al., 2011). Model-free analysis was most commonly based on the calculation of semi-quantitative para-

meters from the signal enhancement curves (Brandt et al., 2008; Mills et al., 2009; Miyati et al., 1997; Provenzale et al., 2006; Starr et al., 2003, 2009; Topakian et al., 2010; Wang et al., 2006; Wardlaw et al., 2008, 2009; Wilkinson et al., 2006), contrast agent concentration curves (Armitage et al., 2011; Budde et al., 2012; Shin et al., 2014) or T1 changes over time (Hanyu et al., 2002; Wahlund and Bronge, 2000). Further model-free analysis approaches included model-free deconvolution (Awasthi et al., 2012; Cramer et al., 2014; Cramer and Larsson, 2014; Ferl et al., 2010; Gupta et al., 2012; Haris et al., 2008a,b,c; Larsen et al., 2013; Larsson et al., 2009; Roy et al., 2013; Singh et al., 2007), principal component analysis (Farjam et al., 2014) and the fitting of empirical functions (i.e. mathematical functions that do not aim to model the tissue physiology, Bergamino et al., 2015).

The majority of included studies used tracer kinetic models for the DCE-MRI analysis. The most commonly used tracer kinetic models were the conventional Tofts model (21/95 studies), the modified Tofts model (29/95 studies) and the Patlak model (26/95 studies, including a simplified version of the Patlak model as introduced by Shames et al. (1993) and Iannotti et al. (1987). Table 2.2 summarises the range of K^{Trans} estimates for different tissue types and tracer kinetic models as reported in the included publications (a complete list can be found in Table A.3 in the appendix). Other modelling approaches included an arterial input function (AIF) free reference region model introduced by Yankeelov et al. (2005), which was applied to tumours in three studies (Lee et al., 2014; Quarles et al., 2012; Skinner et al., 2012). In addition, several studies aimed primarily at introducing a new method for data analysis or comparing different approaches; these will be briefly presented below.

A non-parametric method for evaluating DCE-MRI in $n = 16$ glioma patients was presented by Ferl et al. (2010), who showed that their resulting parameters closely approximate the conventional Tofts model parameters. Li et al. (2000) introduced a variant of the conventional Tofts model that only considers the first pass of the contrast bolus. They evaluated this method in $n = 11$ patients with primary brain neoplasms, finding that the results were visually comparable with those of the conventional Tofts model but less noisy and less susceptible to large vessel contributions. Harrer et al. (2004) evaluated the same model in $n = 18$ patients with high-grade gliomas, reporting a good correlation with the modified Tofts model but no correlation with the conventional Tofts method, though it should be noted that the AIF used differed between the models due to software limitations. Values obtained with the conventional Tofts model were considerably higher, indicating an overestimation of quantitative parameters due to vessel contributions. Sahoo et al. (2013) introduced a variant of the modified Tofts model, which includes an additional tissue uptake leakage compartment. When tested in $n = 184$ glioma patients, they found that the resulting parameter estimates were significantly different from the ones obtained with the modified Tofts model, and less sensitive to changes in the acquisition time. Li et al. (2010) considered the effect of water exchange, finding the Patlak model

to significantly underestimate the fractional blood volume when compared to their three-site equilibrium shutter-speed model. Lüdemann et al. (2000, 2002, 2009) introduced a modified two-compartment exchange model (2CXM), which includes two extravascular extracellular space (EES) compartments (one in slow and one in fast exchange with the blood compartment), but did not compare it to conventional models. Bergamino et al. (2013) compared the Patlak and modified Tofts model in $n = 25$ tumour patients. Although the two models resulted in significantly different parameter estimates in high-grade tumours, the authors did not investigate the model validity and/or accuracy but concluded that both methods are feasible (Bergamino et al., 2013).

Sourbron et al. (2009) used a set of two-compartment models for the analysis of DCE-MRI in the brain, including the 2CXM and two-compartment uptake model (2CUM). The approach was evaluated in $n = 15$ brain tumour patients, showing that the 2CXM provided accurate perfusion and permeability estimates in tumour tissue, while the 2CUM is sufficient to describe the tracer kinetics in healthy tissues. Larsson et al. (2009) used simulated data in order to investigate the accuracy of the 2CXM and the Patlak model. In agreement with Sourbron's results, they found that the 2CXM provides more accurate results for high K^{Trans} values, whereas the Patlak method is appropriate for low values of K^{Trans}. These findings were also confirmed by Cramer and Larsson (2014) and Barnes et al. (2015) in simulated data, suggesting the use of the Patlak model for measurement of low permeability and the 2CXM for high permeability.

Acknowledging the need for different models when investigating heterogeneous tissues, Bagher-Ebadian et al. (2012) presented a method for quantifying BBB disruption in glioma patients based on a voxel-by-voxel selection from a set of nested models: the most complex model with three parameters was required to fit the data in regions of aggressive tumour growth, while simpler models predominated in less aggressive tumour portions and in healthy tissues. This method has since been applied by several other groups (Artzi et al., 2015; Chwang et al., 2014; Li et al., 2014; Nagaraja et al., 2013). Similarly, Ingrisch et al. (2012) investigated BBB disruption in MS patients using automatic model selection from the modified Tofts model, 2CUM and 2CXM on a region of interest (ROI) level.

2.3.5. Clinical findings

Pronounced, localised BBB changes with disease

Most studies focused on diseases that cause brain lesions with pronounced BBB disruption, resulting in visible localised contrast enhancement on T1W images. For instance, studies showed significant differences in BBB integrity between healthy tissue and acute ischaemic

Table 2.2.: Overview of K^{Trans} values reported for different tissue types and tracer kinetic models. Given values are the range of cohort averages as reported in the included articles. Where necessary, units were converted assuming unity tissue density and values were transferred from whole blood to blood plasma notation assuming a haematocrit of 0.45. Please note that some subjects included in these studies (e.g. high grade glioma patients) underwent treatment before entering the study. Hence, the reported baseline parameters might be influenced by interventions that were not the focus in the study. It should also be noted that these values were obtained in different cohorts and with different methods and, hence, are difficult to compare directly; a complete list, including studies that compared different models in the same cohort, can be found in Table A.3 in the appendix.

Tissue type	K^{Trans} ($\cdot 10^{-2}$ min^{-1})			
	conventional Tofts	modified Tofts	Patlak	Other
Normal-appearing tissues				
White matter		0.04 to 16.00	0.04 to 0.44	−0.03 to 0.05
Grey matter		0.05	0.03 to 0.50	−0.01 to 0.06
Mixed tissue types	0.00 to 4.30	0.30 to 3.10	−0.24 to 6.20	
Tumour tissues				
Gliomas	−0.20 to 136.00	0.10 to 83.00	0.19 to 6.04	0.70 to 109.00
Brain metastases	13.00	38.00		
Brain lymphomas		44.00		
Meningeomas	27.80 to 47.00			
Schwannomas	22.80	8.30		
Mixed tumour types	25.00	34.00		
Stroke lesions				
Ischaemic strokes			−0.12 to 3.10	
Hemmorrhagic strokes			5.50	
MS lesions	9.24			3.53
Tuberculomas	204.00 to 281.00			
Traumatic injuries		0.40 to 4.90		
Infective lesions	210.00			
Neurocysticercosis	2.00 to 5.00			

stroke lesions (Abo-Ramadan et al., 2009), brain metastases (Budde et al., 2012) and enhancing MS lesions (Ingrisch et al., 2012). In such diseases, DCE-MRI has been shown to be useful for distinguishing between different types or grades of pathology. 13 studies showed with statistical significance that DCE-MRI derived parameters differentiate primary brain tumour types and grades (Abe et al., 2015; Ahn et al., 2014; Bergamino et al., 2013; Choi et al., 2013; Jia et al., 2013; Lüdemann et al., 2000, 2002; Mills et al., 2009; Roberts et al., 2000; Roy et al., 2013; Sahoo et al., 2013; Zhang et al., 2012; Zhu et al., 2000). Furthermore, significant differences were found between infective versus neoplastic brain lesions (Haris et al., 2008a), asymptomatic versus symptomatic neurocysticercosis (Gupta et al., 2012) and severe and moderate versus mild traumatic brain injuries (Wei et al., 2011). In addition, Aksoy et al. (2013) reported significantly different DCE-MRI parameters for haemorrhagic strokes depending on their size and location, and Kassner et al. (2005, 2009) found significantly

different permeability scores in ischaemic stroke lesions between patients who proceeded to haemorrhage and those who did not, with and without thrombolytic therapy.

Moreover, several studies focused on the effect of tumour treatments on BBB disruption and/or the potential of DCE-MRI derived parameters for predicting treatment response after radiotherapy. Krueck et al. (1994) showed significantly higher permeability in glioma-bearing animals following radiotherapy when compared to untreated controls. Moreover, two studies showed that DCE-MRI derived parameters can differentiate between tumour recurrence and radiation necrosis (Larsen et al., 2013; Shin et al., 2014), while Almeida-Freitas et al. (2014) reported that an increase in K^{Trans} after stereotactic radiosurgery was predictive of tumour progression. Similarly, Farjam et al. (2014) found that the subvolume of high K^{Trans} in brain metastases can predict the response to radiotherapy. Furthermore, Cao et al. (2009) found a correlation between BBB disruption in brain cancer patients during radiotherapy and the degree of radiation-induced dysfunction found six months after therapy.

Hoff et al. (2012) observed a significant decrease in tracer kinetic parameters in VEGF-Trap (a vascular endothelial growth factor inhibitor) treated gliomas versus controls. In contrast, Ali et al. (2010) made the unexpected, paradoxical observation that VEGF tyrosine kinase inhibitor treatment significantly increased BBB capillary permeability, microvessel density and glioma size. Furthermore, one publication each showed a significant change in BBB leakiness after dexamethasone treatment of cerebral mass lesions (Wilkinson et al., 2006), cilengitide treatment in glioma (Nagaraja et al., 2013) and after dopamine agonist treatment in prolactinoma (Manuchehri et al., 2007).

Subtle, diffuse BBB changes with disease

15/95 studies aimed to investigate the correlation between a particular disease and subtle BBB dysfunction in normal-appearing tissues. Significantly increased BBB dysfunction compared to healthy control subjects was found in the periventricular white matter (WM) but not basal ganglia of multiple system atrophy patients (Song et al., 2011), in the basal ganglia of patients with type-II diabetes (Starr et al., 2003), normal-appearing brain tissue of zinc-deficient rats (Noseworthy and Bray, 2000) and normal-appearing white matter (NAWM) in MS patients (Cramer et al., 2014; Taheri et al., 2011b).

There are a number of studies that applied DCE-MRI in elderly subjects with dementia and/or white matter hyperintensities (WMH), reflecting the recent interest in the role of BBB dysfunction in normal ageing, cognitive decline and cerebral small vessel disease. Su et al. (1998) showed a non-significant increase in BBB permeability with normal ageing in normal-appearing canine brain tissue, while Montagne et al. (2015) found a significant increase of BBB

permeability with age in the hippocampus of non-demented subjects. Moreover, Montagne et al. (2015) reported significantly increased BBB permeability in the hippocampus of patients with mild cognitive impairment when compared to the non-demented age-matched cohort and young controls. Increased BBB disruption in the hippocampus of patients with mild cognitive impairment compared to healthy elderly controls was also found by Wang et al. (2006); however, this did not reach the significance level. Furthermore, Starr et al. (2009) observed differences in signal intensity profiles over time between Alzheimer's disease patients and controls, but did not quantify BBB disruption. Taheri et al. (2011a,b) reported significantly increased BBB leakage in NAWM of patients with vascular cognitive impairment compared to healthy controls. Both Wahlund and Bronge (2000) and Hanyu et al. (2002) estimated BBB permeability in WMH by calculating T1 change during the DCE-MRI acquisition; while Wahlund and Bronge (2000) failed to detect T1 changes in WMH of demented subjects, Hanyu et al. (2002) found increased T1 changes in WMH of patients with Binswanger's disease when compared to WMH of patients with cerebrovascular events. Wardlaw et al. (2008, 2009) showed that post-contrast signal enhancement was higher in cerebrospinal fluid and WM in lacunar than in cortical stroke patients. Similar results were reported by Topakian et al. (2010), who found a significantly larger area under the signal enhancement curve in the NAWM of lacunar stroke patients compared to healthy controls.

2.4. Discussion

This systematic review of the available literature revealed 95 studies involving methods to assess BBB disruption in 18 pathologies in up to 495 animals and 2295 humans. These studies showed considerable heterogeneity with regard to image acquisition and analysis methods. This is partly a consequence of the wide range of tissues, pathologies and study objectives. However, it should be noted that only a minority of the articles explicitly justified the methodology used. The factors influencing inter-study comparability, implications for future studies and important considerations when assessing low-level BBB disruption are discussed in the following paragraphs.

2.4.1. Inter-study comparability of quantitative DCE-MRI parameters

Due to the wide range of analysis techniques used and their strong dependence on underlying assumptions and acquisition parameters, a lack of inter-study comparability represents a major problem. Care must be taken when comparing results from different studies as shown by the wide parameter ranges in Table 2.2. Some of this variability is inevitable due to the

heterogeneity of the study populations (e.g. subject age) and study designs. Several contrast agents are approved for the use in contrast-enhanced MRI; since they differ in their properties (e.g. molecular size and weight), they are likely to show different tracer kinetics in their extravasation from the microvasculature (Chwang et al., 2014). However, the exact extravasation dynamics are not fully understood; for instance, evidence is emerging of chronic gadolinium retention in the cerebral vascular endothelium and extracellular space (McDonald et al., 2015).

Since most articles did not explicitly justify the analytical method employed, differences in the choice of tracer kinetic model may account for some of the variation. Biased parameter estimates are likely to be obtained when the assumptions of the model are not met in the tissue or when the data acquired are inadequate to determine a unique solution. For example, several studies (e.g. Ali et al., 2010; Zhang et al., 2012) apply the same model to tumour tissue and contralateral healthy tissue, although the underlying tissue physiology is very different and one model is unlikely to be valid in both situations. The importance of appropriate model selection has been demonstrated both theoretically (Sourbron and Buckley, 2011) and experimentally in gliomas (Harrer et al., 2004) and low-permeability brain tissue (Cramer and Larsson, 2014; Larsson et al., 2009) and is discussed further in section 2.4.2. Several additional factors may also influence the results of DCE-MRI studies.

Firstly, the calculation of contrast agent concentration from signal enhancement requires reliable estimation of intrinsic tissue parameters such as the pre-contrast longitudinal relaxation time $T1_0$. As mentioned in section 1.2.2, there are several methods of estimating $T1_0$, with variable flip angle (Brookes et al., 1999) and variable inversion delay (Larsson et al., 1988) being the most common. The effect of uncertainty in $T1_0$ estimation on the calculation of contrast agent concentrations has been investigated by Schabel and Parker (2008). They demonstrate that $T1_0$ produces a significant concentration bias, which shows the importance of accounting for $T1_0$ when assessing BBB disruption in different tissue types (Armitage et al., 2011). It should also be noted that, unless T1 is measured at each time point, drifts in signal intensity may introduce further errors in tracer kinetic parameters; as noted above, the issue of scanner stability was seldom addressed in the included articles.

Secondly, most tracer kinetic models require the AIF to be known. Hence, determination of AIF represents a key issue in the reliable estimation of tracer kinetic parameters. As mentioned before, there are several strategies for AIF selection and the optimal method varies according to pathology, study aims and clinical requirements (Calamante, 2013). In most applications, direct measurement of the AIF is generally considered preferable to a standard or averaged AIF (Lavini and Verhoeff, 2010). However, this method is not always possible (Parker et al., 2006) and is susceptible to partial volume and inflow artefacts; uncertainty remains regarding which vessel should be sampled and how, with approaches ranging from

manual ROI selection to methods for automatic vessel detection (Chen et al., 2008). There is also disagreement on whether to describe the capillary bed in terms of blood concentration or plasma concentration by correcting for the haematocrit. In the latter case, the haematocrit should ideally be determined for every subject, but a standard value such as Hct = 0.45 is often assumed (Sourbron and Buckley, 2013). In theory, all model equations and resulting parameter values can easily be converted between conventions. However, most studies included in this literature review did not report this and other details, impeding reliable comparison of parameter values from different studies.

Other sources of uncertainty rarely considered in DCE-MRI studies may arise due to a lack of available data. For example, relaxivity values specific to a contrast agent, field strength and tissue/pathology are rarely known, with the consequence that uniform relaxivity across tissues and compartments is generally assumed. A further common assumption is that of fast water exchange between compartments; the influence of restricted water exchange has been described in the literature (see Ewing and Bagher-Ebadian, 2013, and references therein) but models accounting for this effect have received relatively little attention.

2.4.2. Implications for future DCE-MRI studies of BBB disruption

Given the diversity of DCE-MRI applications in the brain, it is impossible to prescribe a universal 'recipe' for future studies, though attempts have been made to better standardise methodology and reporting (DCE MRI Technical Committee, 2012; Leach et al., 2012; Tofts et al., 1999). Instead, it is essential to recognise that the optimal method is highly dependent on the specific application. An extensive body of primary DCE-MRI literature and a number of excellent review articles should help to facilitate optimal study design in the future. The following paragraphs will discuss some of the key aspects of acquisition protocol design and data analysis. In addition to these technical aspects, it should be noted that the overall design of a study (e.g. large sample size, appropriate control group) will be particularly important given the limitations of present DCE-MRI methods.

For most applications, changes in the longitudinal relaxation rate rather than signal intensity should be measured, since the former more accurately reflects contrast agent concentration, required for quantitative tracer kinetic analysis. A range of pulse sequences are available to obtain these data, and the optimal choice may be a compromise between speed, accuracy, spatial coverage and other factors. Two of the most critical acquisition parameters to determine are the temporal resolution and total duration of the scan, since the optimal values depend on the nature of the tissue being investigated and the quantities to be measured (Sourbron and Buckley, 2012). For example, temporal resolution of the order of a second is required to quantify tissue plasma flow. Temporal resolution must also be set against requirements for

spatial resolution and coverage, which differ markedly between applications (e.g. focal versus diffuse pathology). For accurate measurement of the permeability-surface area product *PS*, the scan duration should be long enough for significant contrast extravasation to occur: this may be of the order of a few minutes in tissues such as brain tumours, but longer scans are required in less permeable tissues such as normal-appearing brain. If the EES volume fraction v_e is to be accurately measured then imaging should continue well into the 'washout' phase, when the EES contrast agent concentration begins to fall.

A wide range of tracer kinetic models have been proposed for fitting DCE-MRI data, the most popular of which divide the tissue into well-mixed compartments. It is essential to recognise the assumptions built into these models and to assess their likely validity for a given application (Sourbron and Buckley, 2013). The original Tofts model, for example, is strictly valid only in weakly vascularised tissues, where contrast agent in the capillaries can be neglected; furthermore, the fitted K^{Trans} is equal to *PS* only when the blood flow is sufficiently high. For tissues where the vascular contribution to signal enhancement is significant, the Patlak or modified Tofts models may be more appropriate, provided again that plasma flow is high. The choice of model should also reflect the MRI protocol: if the acquisition duration is short and BBB leakage is slow then models that do not allow back-diffusion (e.g. Patlak and tissue-uptake models) may be suitable, while application of a model that does include back-diffusion (e.g. modified Tofts model) can result in increased uncertainty in the fitted parameters. Similarly, application of a model that includes flow (e.g. 2CUM and 2CXM) is counter-productive if the acquired temporal resolution is insufficient. These and other considerations have been investigated theoretically by Sourbron and Buckley (2011) and are summarised accessibly in their recent review (Sourbron and Buckley, 2013). If it is unclear which model to select a-priori, data-driven approaches can be used to determine the most suitable model (Ewing and Bagher-Ebadian, 2013), although this does not guarantee that the model assumptions are met.

2.4.3. Special considerations for assessment of subtle BBB disruption

Only a small proportion of the studies included in this literature review applied DCE-MRI to normal- or abnormal appearing brain tissues with subtle BBB abnormalities. On average, these studies used longer imaging durations and lower temporal resolutions compared with studies of highly permeable tissues such as tumours. As described above, the longer scan duration is necessary to allow for significant contrast extravasation to occur. On the one hand, lower temporal resolutions might negatively effect the accuracy of quantitative measurements (Cramer et al., 2014) and preclude the measurement of blood flow; even if blood flow is of no interest, it may be necessary to account for flow in order to accurately assess permeability.

The likely influence of blood flow may be determined using computer simulations, providing plausible tissue parameter ranges are available and relevant to the subjects and tissues being studied (Larsson et al., 2009; Sourbron et al., 2009). On the other hand, lower temporal resolutions allow for higher spatial resolution and coverage. This is especially important for the assessment of diffuse diseases with subtle BBB abnormalities; nonetheless, most of the studies included in this review only imaged a single or very few slices (e.g. Cramer et al., 2014). Limited spatial resolution and coverage not only compromises the reliability of ROI based DCE-MRI measurements, but also complicates important image processing steps such as image registration for motion compensation.

Most groups studying subtle BBB disruption have applied semi-quantitative analysis approaches, for instance comparing signal enhancement-time curves statistically modelled between patient groups (Wardlaw et al., 2008; Starr et al., 2009), calculating heuristic quantities such as the area under the curve (Topakian et al., 2010) or change in T1 (Hanyu et al., 2002; Wahlund and Bronge, 2000). These approaches have the advantage of being straightforward to implement and do not require advanced image processing, but they do not distinguish between intra- and extra-vascular contrast and are influenced by the acquisition parameters and other variables. Recently, a number of more complex, model-based approaches to quantifying subtle BBB leakage have been suggested, with applications in normal ageing (Montagne et al., 2015), vascular cognitive impairment (Taheri et al., 2011b) and in the normal-appearing tissue of patients with MS (Cramer et al., 2014) and primary brain tumours (Sourbron et al., 2009).

Compared with conventional applications, studies of subtle BBB breakdown are particularly sensitive to the choice of analysis technique and also particularly susceptible to the sources of error mentioned above, such as $T1_0$ measurement uncertainty. This may partly account for the wide variation in K^{Trans} values reported in the literature for normal-appearing brain tissue, which span three orders of magnitude (see Table 2.2). Furthermore, the small DCE-MRI changes linked to subtle BBB breakdown are more likely to be influenced by secondary processes, such as random noise, scanner drift or partial volume effect (Armitage et al., 2011). However, such issues have received very little attention in the articles included in this literature review, with very few studies applying denoising strategies (Taheri et al., 2011a,b) or correcting for scanner instability (Starr et al., 2003; Topakian et al., 2010). Additionally, normal-appearing tissues suffer from a lower contrast-to-noise ratio when compared to e.g. cancerous tissue, due to low levels of signal enhancement. While it is common to perform DCE-MRI analysis on a voxel-by-voxel basis in conventional applications (e.g. Bagher-Ebadian et al., 2012; Singh et al., 2007), analysis of subtle BBB disruption was mostly performed on a ROI level (e.g. Hanyu et al., 2002; Wardlaw et al., 2009) in order to reduce noise and facilitate model fitting. In cases where voxel-by-voxel maps of DCE-MRI parameters are shown, for instance in Israeli et al. (2011), they generally have a noisy appearance and do not indicate areas of

visually increased BBB disruption in the normal-appearing tissues. Moreover, the voxel-wise low-level BBB permeability estimates are likely to be compromised by partial volume effects, especially in acquisitions with thick slices as in Montagne et al. (2015).

2.5. Conclusion

This systematic review has highlighted the wide range of applications where DCE-MRI has been used to assess BBB integrity. We found large variations in MRI procedures and data analysis methods resulting in widely varying estimates of permeability parameters. Nevertheless, DCE-MRI has been shown to provide valuable information in a growing field of applications, ranging from the grading of primary brain tumours to the assessment of healthy-appearing tissue in MS patients or dementia. In methodological terms, DCE-MRI is a relatively mature technique, but the lack of agreed standards for image acquisition, data modelling and study reporting hinders inter-study comparison and meta-analysis. As most current data apply to tumours, more data are especially required for assessing low-level BBB abnormalities. The relative lack of studies investigating the best methods of measuring low-level BBB disruption in ageing, dementia or brain microvascular disease argue for substantially more work to assess and improve the reliability of DCE-MRI in this context.

Part II.

Analysis of dynamic contrast-enhanced magnetic resonance data in the Mild Stroke Study II

Contents

3. Dynamic contrast-enhanced magnetic resonance imaging in the Mild Stroke Study II

This chapter presents an on-site clinical study of mild stroke patients, which provided the dynamic contrast-enhanced magnetic resonance imaging (DCE-MRI) data that form the basis of this thesis. In addition to introducing the clinical cohort, study procedures and image processing (section 3.2), this chapter also aims to describe and investigate some fundamental aspects of the DCE-MRI processing and analysis (section 3.3).

3.1. Introduction

Several previous on-site clinical studies assessed subtle blood-brain barrier (BBB) integrity using DCE-MRI in Alzheimer's disease (Starr et al., 2009), type-II diabetes (Starr et al., 2003) and mild ischaemic stroke (Wardlaw et al., 2008, 2009). These studies applied semi-quantitative approaches for DCE-MRI analysis, comparing signal enhancement-time curves between patient groups. In the two studies of ischaemic stroke, DCE-MRI signal enhancement was found to be higher in lacunar than cortical stroke patients in normal-appearing white matter (NAWM) and cerebrospinal fluid (CSF) (Wardlaw et al., 2008, 2009), supporting the hypothesis that cerebral small vessel disease (SVD) may be associated with diffuse endothelial dysfunction and abnormal BBB functionality (Wardlaw et al., 2003). The Mild Stroke Study II (MSSII) aimed to confirm these findings and to investigate whether BBB dysfunction is associated with presence and progression of clinical and imaging markers of cerebral SVD. While the semi-quantitative analysis approach used in the previous studies had the advantage of being straightforward to implement and did not require advanced image processing, it suffered from limited interpretability regarding specific processes such as BBB leakage. Hence, one of the main objectives of this PhD project was to explore more complex, quantitative approaches for data analysis. Although baseline assessment including image acquisition for the MSSII was completed before this project started, the patient cohort, data collection and structural image processing procedures of the MSSII form the basis of the original work presented in this thesis. Therefore, the following sections describe the general characteristics and data collection methods of the study before focusing on DCE-MRI related aspects.

3.2. The MSSII

The MSSII was designed as a prospective observational case control study and was approved by the Lothian Ethics of Medical Research Committee (REC 09/81101/54) and the NHS Lothian Research and Development Office (2009/W/NEU/14); all patients gave written informed consent. Prof Joanna M Wardlaw designed the study, obtained funding from the Wellcome Trust (grant 088134/Z/09/A), acted as principal investigator and supervised the whole project.

3.2.1. Overview

The aim of the MSSII was to further elucidate the aetiology of lacunar stroke as a discrete manifestation of cerebral SVD, particularly with regard to the proposed role of endothelial dysfunction. While the previous on-site studies provided some evidence that the BBB may be damaged in lacunar stroke patients, it was not possible to determine whether the relationship is causative or simply an association. In addition to confirming previous findings (Wardlaw et al., 2008, 2009), the MSSII was designed to identify whether increased BBB permeability at initial presentation predates the progression of clinical and imaging SVD markers, leading to disability and cognitive decline. In order to achieve this aim, clinical features (including, for instance, blood and urine markers, stroke symptoms and vascular risk factors), MRI markers of SVD and cognitive ability were assessed at baseline and one year follow-up. An overview of the study and the performed patient assessments is shown in Figure 3.1.

3.2.2. Participants

The MSSII recruited patients who presented to the Lothian stroke service with symptoms of mild ischaemic stroke; a summary of the recruitment and progression of participants in the MSSII is shown in Figure 3.2.

Patient recruitment was performed by Dr Stephen Makin, a clinical research fellow and trainee stroke physician, and overseen by Prof Martin Dennis, a consultant stroke physician, and Prof Joanna M Wardlaw. 471 potential participants were identified from the in- and out-patient stroke services in Edinburgh in several different ways. Firstly, the research fellow reviewed the stroke and acute receiving units at the Western General Hospital (Edinburgh, UK) on a daily basis and approached suitable patients as identified through their clinical symptoms and/or diagnostic imaging. Secondly, treating clinicians were informed of the study and referred suitable patients to the research fellow. Thirdly, stroke patients were referred from the Royal Infirmary by a research nurse.

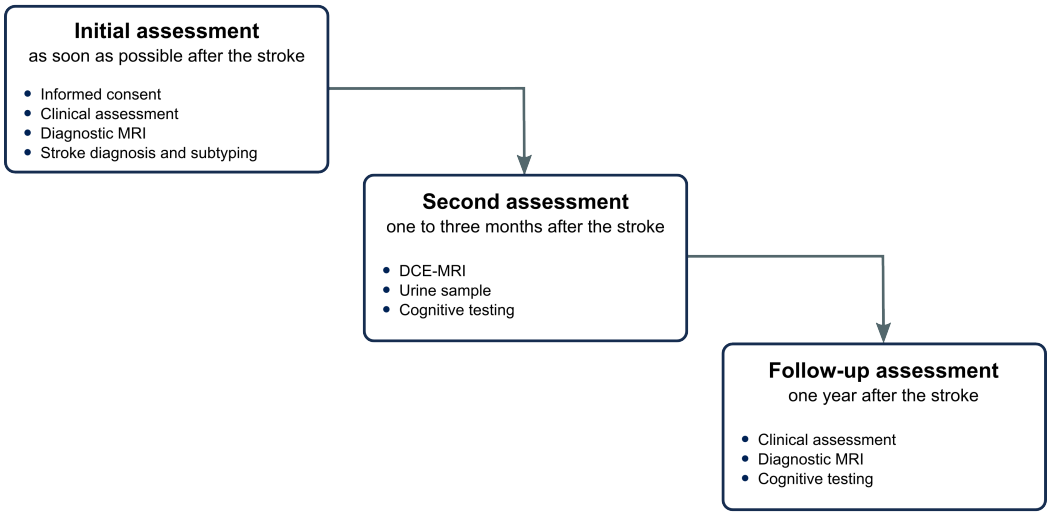

Figure 3.1.: Overview of the MSSII. Flow chart showing the patient assessments in the MSSII. Study data was collected at three different times: at presentation as soon as possible after the stroke, one to three months and one year after the index stroke.

In order to be eligible for the study, patients had to be over 18 years old and able to give consent, which excluded patients who lacked mental capacity due to e.g. cognitive impairment (defined as Mini Mental State Examination score below 24). All patients had to have a probable or definite diagnosis of lacunar or mild cortical ischaemic stroke with no other good explanation for their symptoms, which excluded patients whose initial clinical or imaging assessment showed an alternative diagnosis such as multiple sclerosis, cancer or haemorrhagic strokes. We excluded patients with transient ischaemic attacks (TIA), i.e. patients whose stroke symptoms resolved within 24 hours. Furthermore, participants had to be able to have an MRI scan, excluding patients with contraindications to MRI such as pacemakers, metal implants or claustrophobia. Patients with unstable diabetes or hypertension and major medical conditions including renal failure, which would preclude use of intravenous gadolinium contrast agents, were excluded; however, patients with stable hypertension, diabetes and other vascular risk factors were generally included. Moreover, suitable patients had to be likely to be able to return for assessments at one month and one year after the stroke. This excluded patients who were disabled by the stroke and patients with cancer or other severe, life threatening illnesses.

Overall, 264 patients were eligible and consented to enter the study from May 2010 to April 2012, including 118 patients with lacunar and 146 patients with cortical stroke. Participants were aged 66.9 ± 11.8 years on average and 42% of subjects were female. Other relevant clinical characteristics of the cohort such as SVD burden and vascular risk factors will be reported in chapters 7 and 8 of this thesis.

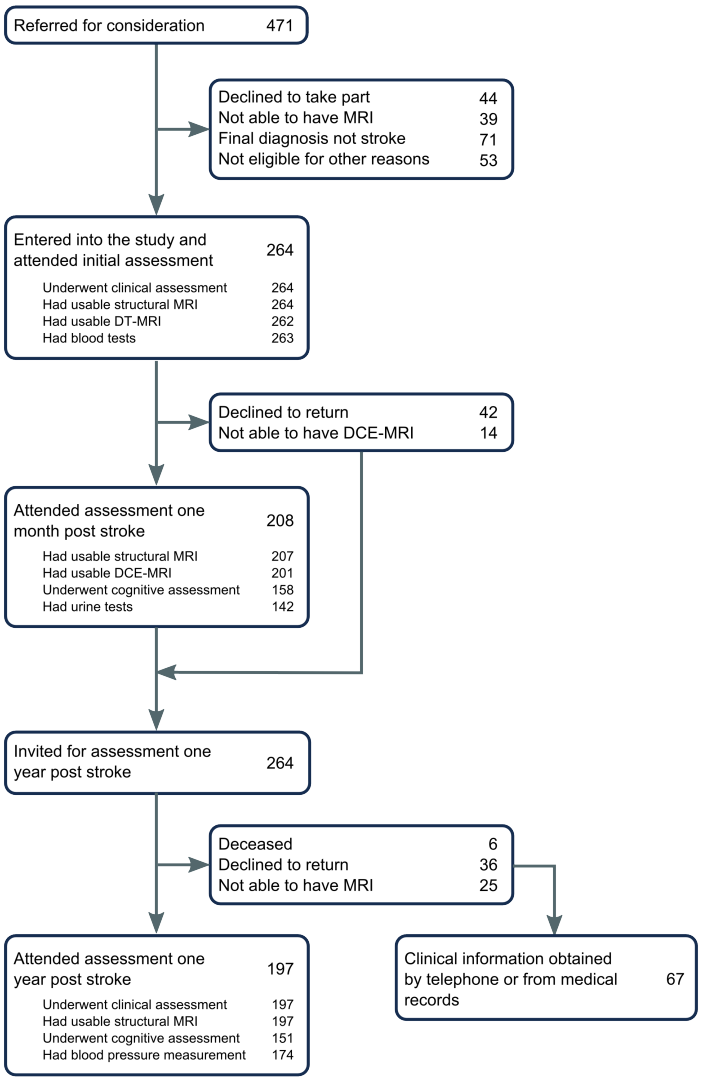

Figure 3.2.: Participant recruitment and retention in the MSSII. Flow chart showing the number of participants that were referred to the study, entered into the study and underwent the different study assessments.

3.2.3. Data collection

Patient assessments were performed at three different times: at presentation as soon as possible after the stroke, one to three months and one year after the index stroke. The following sections will describe the data that was collected at these study visits (see Figure 3.1).

Initial clinical assessment

All 264 participants underwent an initial clinical assessment as soon as possible after stroke onset (median of 6 days, interquartile range [3, 15] days). The research fellow recorded the patient's demographic details and past medical history, including previous strokes or TIA, ischaemic heart disease and peripheral vascular disease. He also recorded if there was a history or current medication of hypertension, diabetes, hyperlipidaemia, hypercholesterolaemia or atrial fibrillation. Furthermore, family history of stroke and lifestyle information were recorded, including smoking status, alcohol consumption and dietary salt intake. A detailed clinical examination was performed in order to record the details of the presenting stroke. This included the date and time of stroke onset and first assessment by the stroke service, presence and duration of symptoms such as limb weakness, sensory loss, speech disturbance, neglect and visual disturbance and the affected side if applicable. In addition, the research fellow assessed dependency using the modified Rankin score and the stroke severity on the National Institutes of Health stroke scale (NIHSS) at the time of assessment and estimated the worst NIHSS score from the patient's history. Further records comprised the patient's dominant hand, whether the stroke was treated with thrombolysis or clot retrieval, a full list of medications and the patient's blood pressure. The research fellow also recorded blood test results as provided by the NHS Lothian Biochemistry laboratory (including haematocrit, cholesterol, glucose, urea, creatinine, sodium, potassium and estimated glomerular filtration rate), the degree of carotid artery stenosis measured with doppler ultrasound and electro- and echocardiography findings (where available).

Diagnostic MRI

As part of the initial assessment, all 264 patients underwent a diagnostic MRI scan on a 1.5 T MRI scanner (Signa HDxt, General Electric, Milwaukee, WI) in the Brain Research Imaging Centre at the Western General Hospital using an 8-channel phased-array head coil. The same MRI scanner was used throughout the study and underwent regular quality assurance procedures. The imaging protocol included three-dimensional (3D) T1-weighted (T1W) inversion recovery (IR) prepared spoiled gradient echo (GRE), T2-weighted (T2W) fast spin echo (SE) with radial k-space sampling, T2*-weighted (T2*W) GRE, fluid attenuated inversion recovery (FLAIR) and diffusion tensor MRI (DT-MRI) with 30 diffusion directions (single-shot SE echo-planar imaging, diffusion weighting factor $b = 1000$ s/mm^2) and two baseline acquisitions with $b = 0$ s/mm^2. A susceptibility-weighted imaging (SWI) acquisition was performed in addition to the conventional T2*W GRE acquisition, because it had recently been shown to provide better contrast for the detection of microbleeds (Nandigam et al., 2009). The imaging

parameters for all sequences are shown in Table 3.1; the total scan time was approximately 30 min.

Diagnostic MRI assessment

All MRI scans were assessed by an experienced consultant neuroradiologist (Prof Joanna M Wardlaw), who recorded whether an acute lesion relevant to the recent stroke symptoms was present. A recent ischaemic stroke was defined as a hyperintense area on the diffusion-weighted image (with corresponding reduced signal on the apparent diffusion coefficient image) with or without increased signal on T2W or FLAIR images, in a location that corresponded to a typical vascular territory. The neuroradiologist recorded the location of the index lesion as well as the presence and location of old stroke lesions including lacunes. Old cortical or lacunar stroke lesions (infarcts) were wedge-shaped hyperintense regions on the FLAIR or T2W image, and hypointense on the T1W image including cortex and/or subcortical tissues, with or without cavitation, and with ex vacuo effect reflecting tissue loss. Periventricular and deep white matter hyperintensities (WMH) were rated from 0 (none) to 3 (severe) using the Fazekas scale for the left and right hemispheres separately and for both hemispheres combined (Fazekas et al., 1987). Moreover, WMH were scored on the Wahlund scale (Wahlund et al., 2001). The presence of enlarged perivascular spaces (EPVS) was rated on a score from 0 (none) to 4 (>40) as described in Potter et al. (2015). The rating was performed for the left and right hemispheres separately and for both hemispheres combined for each of the following locations: midbrain, hippocampus, basal ganglia and centrum semiovale. Deep and superficial cerebral atrophy were each rated in comparison to a standard age matched template (Farrell et al., 2009), using a scale from 1 (mild) to 6 (severe). The total number of microbleeds was counted on the SWI and T2*W GRE sequences in the following regions: deep white matter (WM), the basal ganglia, the grey matter (GM) and WM junction, the external/internal capsule, the thalamus and the posterior fossa. Numbers were recorded for the left and right hemispheres separately and for both hemispheres combined. Iron deposits in the basal ganglia were rated on a visual rating scale from 0 (none) to 4 (medium-high) based on comparison with four standard cases (Penke et al., 2012).

Stroke diagnosis and classification

Each patient's case was discussed at a multi-disciplinary meeting involving neurologists, stroke physicians and neuroradiologists before deciding on a final diagnosis of stroke and stroke subtype. Firstly, the final diagnosis of an ischaemic stroke was made after assessing both clinical and imaging findings. If there was a lesion that matched the clinical features, i.e. was in a relevant location of the brain and of the right apparent age to coincide with symptom

onset, the diagnosis was clearly one of stroke. If there was no relevant lesion on imaging, but a clear clinical diagnosis of ischaemic stroke and no other explanation for the symptoms, the patient was included in the study. If neither the clinical nor the imaging findings were typical of ischaemic stroke, the patient was excluded from the study.

Secondly, the acute stroke was classified as lacunar or cortical subtype. All patients were diagnosed according to clinical features using the Oxfordshire Community Stroke Project classification (Bamford et al., 1991). In addition, if there was a relevant lesion on the MRI scans, a subtype classification was made based on the imaging appearance blinded to the clinical results. Acute lacunar infarcts were required to be less than 20 mm in maximum axial diameter and in the deep WM or GM of the cerebral hemispheres or brainstem. Infarcts involving the cortex, or subcortical infarcts larger than 20 mm diameter, i.e. large striatocapsular infarcts, were likely to be of large artery atherothromboembolic origin and were classed as cortical strokes. All cases were discussed in the weekly multi-disciplinary stroke meeting; if the radiological diagnosis differed from the clinical, the imaging classification was used as the final subtype (Mead et al., 2000).

DCE-MRI and additional clinical assessments at one to three months post stroke

All participants were invited to attend a second MRI appointment at least one month and up to three months after the initial presentation. The aim of this MRI session was to assess BBB integrity using DCE-MRI, the delay being to avoid acute effects of the stroke on the local BBB. Of the 264 recruited patients, 56 did not return for the second MRI assessment because they declined the scan ($n = 42$), were too unwell ($n = 7$), lacked a venous access for contrast administration ($n = 4$) or had insufficient renal function ($n = 3$). On average, DCE-MRI was performed 38 days after the initial assessment (interquartile range [31, 54] days). The technical details of the MRI protocol are shown in Table 3.2. DCE-MRI consisted of 20 consecutive 3D T1W spoiled GRE acquisitions with a temporal resolution of 73 s and a total acquisition time of approximately 24 min. The acquisition was initiated simultaneously with an intravenous bolus injection of 0.1 mmol/kg gadoterate meglumine (Gd-DOTA, Dotarem, Guerbet, France) using a power injector. Two additional spoiled GRE acquisitions were obtained prior to contrast administration with flip angles of 2° and 12° respectively for calculation of $T1_0$. The DCE-MRI procedure was designed and tested by Dr Paul A Armitage, MRI physicist and image analyst (Armitage et al., 2011). In addition to DCE-MRI, the protocol included a pre-contrast sagittal T1W SE acquisition, a post-contrast 3D T2W fast SE acquisition and a pre- and post-contrast FLAIR acquisition. Overall, the MRI took approximately 45 min to complete. Of the 208 patients that underwent DCE-MRI, data suitable for analysis was obtained in 201 patients;

data for seven subjects were rejected due to 'tissueing' of contrast, technical faults during the scan or unacceptable data quality caused by patient movement.

Table 3.1.: Acquisition details of the diagnostic MRI sequences. '–' indicates that the parameter is not applicable for the sequence. The same protocol was used for the one year follow-up.

Sequence	Orientation	TR/TE/TI (ms) / α (°)	Field of view (cm) / matrix size	Number of slices / slice thickness/slice gap (mm)
3D T1W IR-prepared spoiled GRE	Sagittal	7.3/2.9/500 / 8	33.0×21.5 / 256×146	100 / 1.8/0.0
T2W fast SE	Axial	6000/90/– / –	24.0×24.0 / 384×384	28 / 5.0/1.0
T2*W GRE	Axial	800/15/– / 20	24.0×18.0 / 384×168	28 / 5.0/1.0
FLAIR	Axial	9000/153/2200 / –	24.0×24.0 / 384×224	28 / 5.0/1.0
SWI	Sagittal	80/50/– / 15	24.0×24.0 / 288×224	
DT-MRI	Axial	7700/82/– / –	24.0×24.0 / 128×128	38 / 5.0/1.0

Table 3.2.: Acquisition details of the MRI sequences at one to three months after presentation. '–' indicates that the parameter is not applicable for the sequence.

Sequence	Orientation	TR/TE/TI (ms) / α (°)	Field of view (cm) / matrix size	Number of slices / slice thickness/slice gap (mm)
T1W SE	Sagittal	400.0/14.0/– / –	24.0×24.0 / 256×160	5 / 5.0/0.0
FLAIR	Axial	9000.0/153.0/2200 / –	24.0×24.0 / 384×224	28 / 5.0/1.0
3D spoiled GRE	Axial	8.2/3.1/– / 2	24.0×24.0 / 256×192	42 / 4.0/0.0
3D spoiled GRE	Axial	8.2/3.1/– / 12	24.0×24.0 / 256×192	42 / 4.0/0.0
3D spoiled GRE x 20	Axial	8.2/3.1/– / 12	24.0×24.0 / 256×192	42 / 4.0/0.0
FLAIR	Axial	9000.0/153.0/2200 / –	24.0×24.0 / 384×224	28 / 5.0/1.0
3D T2W fast SE	Sagittal	3000.0/143.0/– / variable	24.0×24.0 / 320×320	128 / 1.4/0.0

All participants were asked to bring an early morning specimen of urine to their second appointment. The urine samples were analysed in the NHS Lothian Biochemistry laboratory, which provided measurements of albumin, microalbumin, creatinine, sodium and potassium levels. Moreover, the research fellow recorded a full list of medications that the patient was taking at the time and assessed the patient's cognition in order to detect mild cognitive impairment and dementia.

One year follow-up

One year after the first presentation, all participants were invited for a follow-up clinical and MRI assessment; 197 of the 264 patients returned for a follow-up appointment. If patients were unable or declined to come to the Western General Hospital for the MRI scan, the clinical assessment was performed by telephone or during home visits. If a patient could not be contacted by post or telephone, the clinical research fellow obtained as much information as possible from a relative/carer or the patient's medical records. Collected clinical data was similar to the initial assessment and included a complete medical history of the previous year (particularly for new events like recurrent stroke or myocardial infarction and new diagnoses of hypertension or diabetes), lifestyle information, a full list of medications, NIHSS score, pulse and blood pressure measurements. Moreover, patients underwent diagnostic MRI as performed at the initial assessment and cognitive testing as performed at one month post stroke. Firstly, the structural MRI scans were assessed by an experienced neuroradiologist, who recorded the same features (on the same scales) as described above and was blinded to the baseline imaging and clinical findings. Secondly, the MRI scans were compared to the baseline scans in order to assess all features for change (atrophy, WMH ratings, number of microbleeds, iron deposits and EPVS, status of the old index lesion).

3.2.4. General image processing and analysis

This section presents the computational image processing and analysis procedures that have been performed in the MSSII. Processing of the DCE-MRI data was performed by myself and will be discussed separately (see section 3.3), as it is the main focus of this thesis. All image analysis was performed blind to clinical data.

Pre-processing

All MR images were converted from DICOM to Analyze 7.5 format. Moreover, all structural and DCE-MRI images were aligned to the pre-contrast T1W spoiled GRE image (acquired

during the scan appointment one month post stroke). All registrations were performed with rigid-body transformations using FSL-FLIRT (Jenkinson et al., 2002). For participants that did not undergo MRI assessment at one month post stroke, images were instead co-registered to the T2W fast SE acquisition of the initial diagnostic MRI assessment.

Tissue segmentation and volume measurements

Information about brain tissue types and volumes were extracted semi-automatically by Dr Maria del C Valdés Hernández, an image analyst, using the in-house developed software MCMxxxVI (Valdés Hernández et al., 2010). All segmentation masks were manually checked by an independent trained image analyst (Eleni Sakka) and manually edited as necessary. The MCMxxxVI method is based on minimum variance quantisation after fusing two co-registered MRI sequences in the red-green colour space. In the quantised images, maximum and minimum thresholds of the tissue of interest were selected; the red-green colour space was used because the human eye cones are most sensitive to the frequencies in this range of the visible spectrum (Valdés Hernández et al., 2010). The software then automatically constructed the tissue segmentation mask from the quantised colour-fused volume. WMH in the brain parenchyma were extracted using the baseline FLAIR and T2*W GRE acquisitions. The resulting binary masks were manually refined using Analyze 11.0 (AnalyzeDirect, KS). WMH were identified as punctate or diffuse areas in the WM and deep/subcortical GM (DGM) of the cerebral hemispheres or in the brainstem that were 3 mm or larger in diameter and hyperintense with respect to NAWM and GM on T2W and FLAIR images (Valdés Hernández et al., 2010); some hypointensity on T1W MRI was allowed as long as not less intense than CSF. In addition, stroke lesions were manually outlined and classified as old stroke lesions or recent stroke lesions (RSL) (following the definitions used in the visual MRI assessment as described above) using the 'Region of Interest Tool' in Analyze 11.0. All stroke lesion masks were checked for accuracy by Prof Joanna M Wardlaw. NAWM masks were generated using MCMxxxVI as described in Valdés Hernández et al. (2010). DGM masks were generated automatically by a software pipeline that used FSL-SUSAN (Smith and Brady, 1997) for noise reduction, an age-relevant brain template (Farrell et al., 2009), FSL-FLIRT (Jenkinson et al., 2002) for aligning the template to each image dataset, and FSL-FIRST (Patenaude et al., 2011) for extracting the subcortical structures, followed by manual boundary correction. To minimise any residual contamination of the DGM, the mask was eroded by one voxel. Using MCMxxxVI, parts of the globus pallidus and thalamus are consistently included within the WM; consequently, the NAWM masks were corrected using the DGM masks. An example of MR images and segmentation masks is shown in Figure 3.3.

The intracranial volume (ICV) was defined as contents within the inner skull including brain tissue, CSF, veins and dura, and limited inferiorly by the tip of the odontoid peg at the foramen

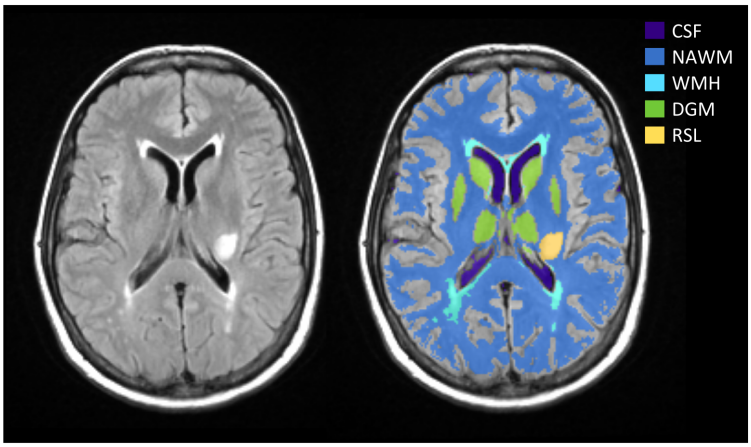

Figure 3.3.: Representative MRI data and tissue segmentation. FLAIR image (left) and tissue masks superimposed on FLAIR image. Reprinted from Heye et al. (2016a).

magnum. It was extracted from the T2*W GRE image acquired at the initial MRI assessment using the 'Object Extraction Tool' in Analyze 11.0, followed by manual editing as described in Valdés Hernández et al. (2012). Non-brain tissue (CSF, venous sinuses, choroid plexus and meninges) was extracted using MCMxxxVI and subtracted from the ICV, providing binary masks of total brain tissue. The resulting segmentation masks were used to calculate the brain tissue and WMH volumes as a percentage of ICV.

DT-MRI processing

DT-MRI images were processed by Dr Maria del C Valdés Hernández using in-house software created by Dr Paul A Armitage, which removed bulk motion and eddy current induced distortions using FSL-FLIRT (Jenkinson et al., 2002) and generated a directionally averaged diffusion weighted image, mean diffusivity (MD) and fractional anisotropy (FA) parametric images using standard methods based on multivariate linear regression. For each dataset, nonlinear registration (Modat et al., 2010) was used to align the tissue masks in the structural space (T2W) with the parametric maps in the diffusion space using the NiftyReg tool (`http://sourceforge.net/projects/niftyreg/`) applied using TractoR software (`http://www.tractor-mri.org.uk/diffusion-processing`) to obtain the transformation between the brain-extracted structural T2W image and the baseline diffusion volume. To avoid partial volume averaging with CSF due to registration inaccuracies, the CSF mask was dilated by one voxel in each direction and then subtracted from the NAWM, WMH and DGM masks in the diffusion space. Median MD and FA were extracted for NAWM and DGM in each patient; DT-MRI data for two subjects were rejected due to failure of the non-linear image registration.

3.3. Basic DCE-MRI analysis in the MSSII cohort

This section describes the basic DCE-MRI processing and analysis procedures that were performed with the MSSII data and presents resulting measurements. If not explicitly stated otherwise, all DCE-MRI related processing was performed by myself, under direct supervision of Dr Michael J Thrippleton (MRI physicist), using custom-written software programmed in MATLAB (MathWorks, Natick, MA, USA).

3.3.1. Methods

Vascular input function measurement

As discussed in section 2.4.1, measurement of the arterial input function (AIF) is a key issue in the analysis of DCE-MRI data and the optimal approach for AIF determination is still a matter of debate. In DCE-MRI of the brain, the AIF is often sampled in the superior sagittal sinus (SSS), since partial volume effects and inflow artefacts are usually reduced at that location compared with obtaining the AIF from a feeding artery (Lavini and Verhoeff, 2010). As the SSS contains venous rather than arterial blood, the AIF will be referred to by the more general term 'vascular input function' (VIF).

In order to determine the optimum approach and location for VIF measurement in the MSSII data, several different VIFs were extracted and compared in a subset of 20 patients. Firstly, VIFs were measured in the SSS, using a slice proximal to the basal ganglia structures (see Figure 3.4(a) and (b)). VIFs were obtained by (i) placing a rectangular region of interest (ROI) in the SSS on the T2W image using the 'Region of Interest Tool' in Analyze 11.0 and (ii) selecting a single voxel from the SSS on the DCE-MRI series, which provides the highest peak signal enhancement and smooth variation during the DCE-MRI time course (assessed visually using the 'Timeseries' view in FSLView). Secondly, VIFs were measured in the internal carotid artery (ICA), using a slice where the blood flow is perpendicular to the slice direction (see Figure 3.4(c)). VIFs were obtained by selecting a single voxel from the (iii) left and (iv) right ICA, following the same selection criteria as in method (ii). In order to assess reproducibility of the single-voxel selection methods, VIF extraction was repeated by Dr Michael J Thrippleton, who acted as an independent second observer and was blinded to my results, using methods (ii)-(iv). In order to obtain a noise estimate, a biexponential curve was fitted to all extracted VIFs and the sum of squared residuals (SSR) was calculated.

Based on this exploratory analysis, we chose the method that provided the most robust VIFs with high peak enhancement and a smooth decline. This method was then applied in the whole patient cohort.

The chosen VIF signal was converted into signal enhancement and contrast agent concentration as will be described below, yielding the whole-blood concentration $c_b(t)$ that was converted to blood plasma concentration using the formula $c_p = c_b/(1 - \mathrm{Hct})$. In patients where no haematocrit measurement was available in the clinical records ($n = 3$), an assumed value of $\mathrm{Hct} = 0.45$ was used.

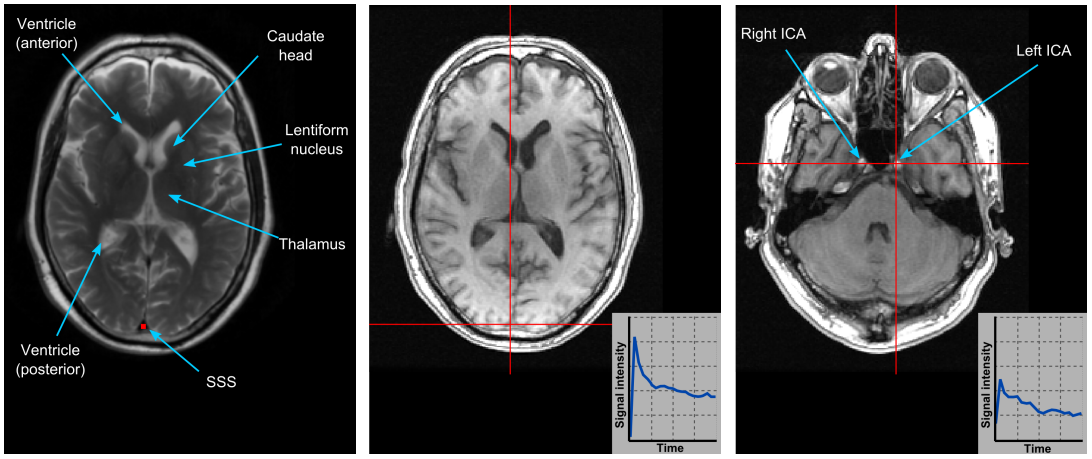

(a) ROI in SSS on T2W image (b) Single voxel in SSS on DCE-MRI (c) Single voxel in ICA on DCE-MRI

Figure 3.4.: Methods for VIF measurement. (a) For VIF measurement in the SSS a slice containing the basal ganglia structures and the lateral ventricles was used; a rectangular ROI was placed in the SSS based on the anatomical location on the T2W image, (b) a single voxel was selected from the SSS on the pre-contrast T1W spoiled GRE image (same slice as before), based on the signal intensity variation during the DCE-MRI time course; the voxel that provided the highest peak signal enhancement and a smooth decline was selected, (c) a single voxel was selected from the right and left ICA on the pre-contrast T1W spoiled GRE image, following the same criteria as the SSS voxel selection; a slice where the blood flow is perpendicular to the slice direction was chosen.

Calculation of tracer dynamics and $T1_0$

For each of the post-contrast time points t, the measured signal intensities $S(t)$ were averaged over all voxels for each tissue type. The signal enhancement $E(t)$ (representing the fractional signal increase above baseline) was then calculated as $E(t) = (S(t) - S_0)/S_0$, where S_0 is the signal intensity of the 12° pre-contrast acquisition.

$T1_0$ values were calculated based on the variable flip angle method by Brookes et al. (1999) using

$$\frac{1}{T1_0} = \frac{1}{TR} \ln\left(\frac{S_R \sin\alpha_b \cos\alpha_a - \sin\alpha_a \cos\alpha_b}{S_R \sin\alpha_b - \sin\alpha_a}\right), \tag{3.1}$$

where $S_R = S_a/S_b$, with S_a and S_b representing the signal intensities of the two pre-contrast acquisitions with flip angles $\alpha_a = 2^\circ$ and $\alpha_b = 12^\circ$.

The contrast agent concentration $C(t)$ was then estimated by numerical solution of the following equation (Armitage et al., 2005):

$$E(t) = \exp(-r_2 C(t)\mathrm{TE}) \times \left[\frac{1-\exp(-P-Q)-\cos\alpha_2\,(\exp(P)-\exp(-2P-Q))}{1-\exp(P)-\cos\alpha_2\,(\exp(P-Q)-\exp(-2P-Q))}\right]-1, \quad (3.2)$$

where $P = \mathrm{TR}/\mathrm{T1}_0$, $Q = r_1 C(t)\mathrm{TR}$ and $r_1/r_2 = 4.2/6.7$ $\mathrm{s}^{-1}\mathrm{mM}^{-1}$ (Rohrer et al., 2005). Negative concentration values were set to zero.

In addition to analysing the data based on whole-tissue averages, a subset of the DCE-MRI data ($n = 20$) was also processed on a voxel-by-voxel basis.

Calculation of semi-quantitative parameters

Semi-quantitative analysis is one of the easiest ways to characterise DCE-MRI signal enhancement curves. A semi-quantitative parameter that is frequently used in clinical brain studies is the area under the curve (AUC) (e.g. Ferl et al., 2010; Mills et al., 2009; Topakian et al., 2010; Wardlaw et al., 2008). In the MSSII data, the AUC was calculated by numerically integrating the tissue signal enhancement curves $E(t)$ from $t = 0$ (administration of contrast agent) to $t = 24$ min. In order to correct for inter-subject variability of the vascular input, the AUC was normalised to the area under the vascular signal enhancement curve $E_b(t)$, yielding the blood-normalised AUC:

$$\mathrm{AUC}_E^{bn} = \frac{\int E(t)dt}{\int E_b(t)dt}. \quad (3.3)$$

As a second semi-quantitative parameter, the late phase slope of the signal enhancement curve (slope_E) was calculated. The parameter was obtained by linear regression on the signal enhancement data between time points 4 and 20 inclusive; the first three post-contrast time points were omitted in order to exclude non-linear signal enhancement changes during the first pass of the contrast bolus. For a statistical comparison between semi-quantitative parameters in different tissue types, the Wilcoxon signed rank test was applied.

3.3.2. Results

VIF measurement

Figure 3.5 shows the vascular signal enhancement curves that were extracted from the SSS using methods (i) and (ii). Similar results were achieved with the two methods; however, selecting a single voxel from the DCE-MRI acquisition generally provided a higher peak enhancement when compared to the VIF extracted from a ROI in the T2W image. Moreover, the single-voxel VIFs were more uniform within the cohort, with a larger standard deviation seen in the ROI-based VIFs.

A comparison between single-voxel VIFs obtained from the SSS and ICA are shown in Figure 3.6. As demonstrated in Figure 3.6(a), the ICA showed significantly smaller signal enhancement when compared to the SSS. Furthermore, signal curves measured in the ICA were significantly noisier. When choosing the voxel for VIF measurement, at least one observer noted that the extracted signal curves visually appeared noisy in 12/20 patients for the left and right ICA, compared to 1/20 patients for the SSS. This visual impression was confirmed when looking at the SSR values between the extracted curves and biexponential fits (Figure 3.6(b)), which are significantly higher for the ICA. The results provided by the two independent observers were visually very similar; with the same voxel being chosen in 8/20 patients for the left ICA, 10/20 patients in the right ICA and 4/20 patients in the SSS.

Based on these results, we decided to select the VIF from a single voxel in the SSS for the whole patient cohort. The same voxel was selected in 85/201 patients (42%); where the observers chose different voxels, the VIF with the highest peak enhancement was selected for all subsequent analyses unless the signal curve was significantly noisier.

DCE-MRI measurements on a voxel-by-voxel basis

An example of DCE-MRI tracer dynamics obtained on a voxel-by-voxel basis is shown in Figure 3.7. This example is representative of the patient cohort and demonstrates that the obtained voxel-by-voxel signal enhancement curves have a low contrast-to-noise ratio (CNR). Due to the low levels of contrast uptake, the signal enhancement curves contain many negative values that resulted in physiologically unrealistic negative contrast agent concentration values. On average, the percentage of voxels that exhibit negative signal enhancement at least once over the DCE-MRI acquisition time ranged from 39% in CSF to 65% in NAWM (based on the subset of 20 patients).

Figure 3.8 presents voxel-by-voxel maps of $T1_0$ and semi-quantitative DCE-MRI parameters for the same example patient as in Figure 3.7. While the index stroke lesion is visually

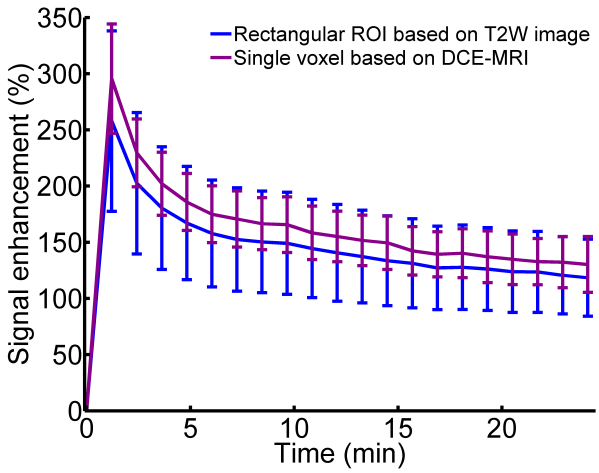

Figure 3.5.: Comparison of signal enhancement curves in the SSS obtained from different ROIs. Displayed curves are the sub-sample average ($n = 20$); error bars indicate the standard deviation. VIFs are based on (i) the average signal in a rectangular ROI placed on the T2W image (in blue), and (ii) a single voxel selected from the DCE-MRI acquisition (in purple).

enhanced in both AUC_E^{bn} and $slope_E$ maps, all other tissues have a generally noisy appearance and show signs of ring-shaped Gibbs artefacts.

DCE-MRI measurements on a tissue-average basis

When analysing the DCE-MRI data based on whole-tissue average values, the resulting tracer kinetic curves were significantly smoother (see example in Figure 3.9) and negative signal enhancement values occurred in only 0% (CSF) to 6% (WMH) of patients. Figure 3.10 shows the cohort-averaged signal intensity, signal enhancement and contrast agent concentration curves in NAWM, DGM, WMH, RSL and SSS. All tissues showed a signal enhancement of approximately 2% to 8%, with abnormal tissues (WMH and RSL) showing a steeper increase in signal over time compared with normal-appearing tissues (NAWM and DGM).

Figure 3.11 shows the relationship between the tissue-average $T1_0$ values and the distribution of voxel-by-voxel $T1_0$ values in a single patient that is representative of the subset. In all tissue types, the voxel-by-voxel $T1_0$ values showed a positively skewed distribution, with the tissue-average $T1_0$ being a close approximation of the distribution median.

Tables 3.3 and 3.4 present the cohort average $T1_0$ values and semi-quantitative DCE-MRI parameters. The late phase slope values were in line with the visual appearance of the signal enhancement curves: $slope_E$ values were significantly higher in RSL compared to all other tissues ($p < 0.001$), and also significantly higher in WMH compared to NAWM ($p < 0.001$).

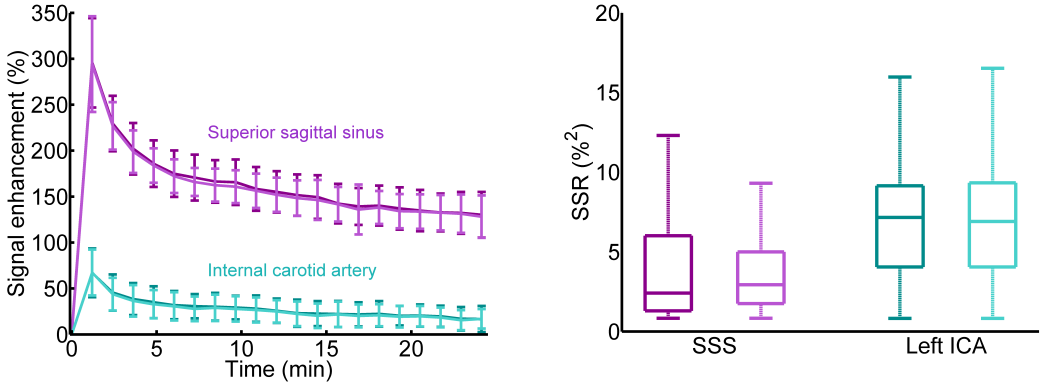

(a) Signal enhancement curves (b) Noise estimates

Figure 3.6.: Comparison of VIF measurements in the SSS and ICA.
All measurements are based on a manually selected voxel that provided the highest peak signal enhancement and smooth variation during the DCE-MRI time course. VIF extraction was performed by two independent observers; results obtained by the two observers are shown in different shades of the same colour. Voxels were selected in both the left and right ICA; however, the results were very similar and only the left ICA is shown here. (a) Cohort average signal enhancement curves ($n = 20$) obtained from the SSS (in purple) and the left ICA (in turquoise); error bars indicate the standard deviation, (b) boxplots showing the sum of squared residuals (SSR) between the extracted vascular signal enhancement curve and a fitted biexponential curve, giving an indication of the 'smoothness' of the VIF.

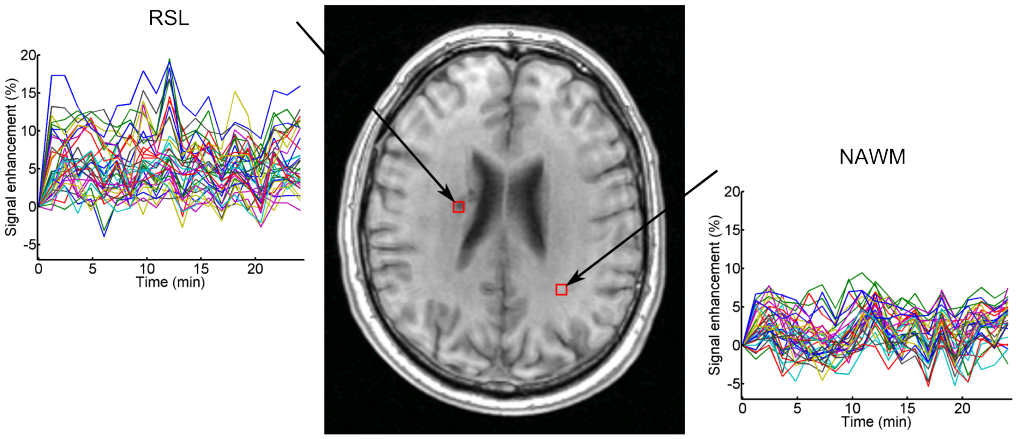

Figure 3.7.: Example of voxel-by-voxel signal enhancement curves.
Pre-contrast T1W spoiled GRE image of a single patient; voxel-by-voxel signal enhancement curves are shown for two ROIs (5×5 voxels) in NAWM (right) and a RSL (left, see Figure 3.8(a)) respectively.

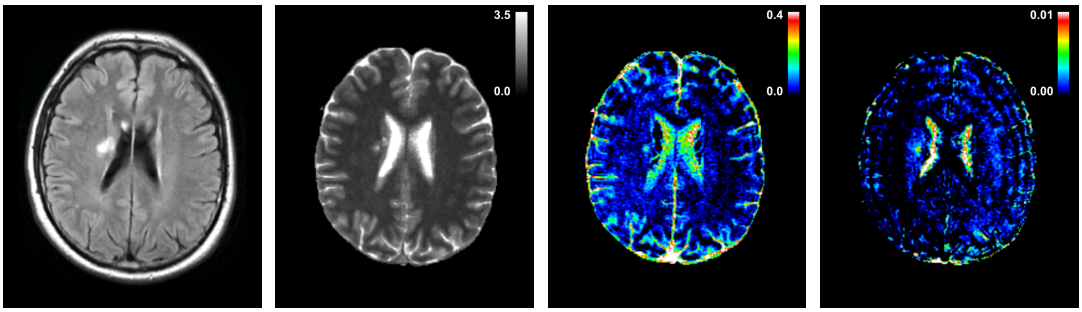

(a) FLAIR image (b) $T1_0$ (in s) (c) AUC_E^{bn} (dimensionless) (d) $slope_E$ (in %/min)

Figure 3.8.: Example of voxel-by-voxel maps of $T1_0$ and semi-quantitative DCE-MRI parameters. All images are shown for the same slice in a single patient; (a) FLAIR image, showing a RSL and WMH, (b) map of the pre-contrast longitudinal relaxation time $T1_0$ in seconds, (c) map of the blood-normalised area under the signal enhancement curve AUC_E^{bn} (dimensionless), (d) map of the late phase slope of the signal enhancement curve $slope_E$ (in %/min).

Similarly, all tissue types had significantly different AUC_E^{bn} ($p < 0.001$), with the highest values in DGM and the lowest values in NAWM.

Table 3.3.: $T1_0$ values by tissue type. Values are shown as cohort mean ± standard deviation.

Tissue type	**$T1_0$ (s)**
SSS	1.72 ± 0.25
NAWM	0.99 ± 0.13
WMH	1.10 ± 0.15
DGM	1.34 ± 0.15
RSL	1.27 ± 0.26

Table 3.4.: Semi-quantitative DCE-MRI parameters by tissue type. Values are shown as cohort median and interquartile range (data not generally normally distributed).

Tissue type	**AUC_E^{bn} (%)**	**$slope_E$ ($\cdot 10^{-2}$ %/min)**
NAWM	1.59 [1.30, 1.95]	2.59 [−0.04, 4.70]
WMH	2.30 [1.79, 2.93]	3.21 [0.18, 6.45]
DGM	3.78 [3.30, 4.51]	0.96 [−2.83, 3.84]
RSL	2.85 [1.92, 4.60]	6.49 [1.74, 12.26]

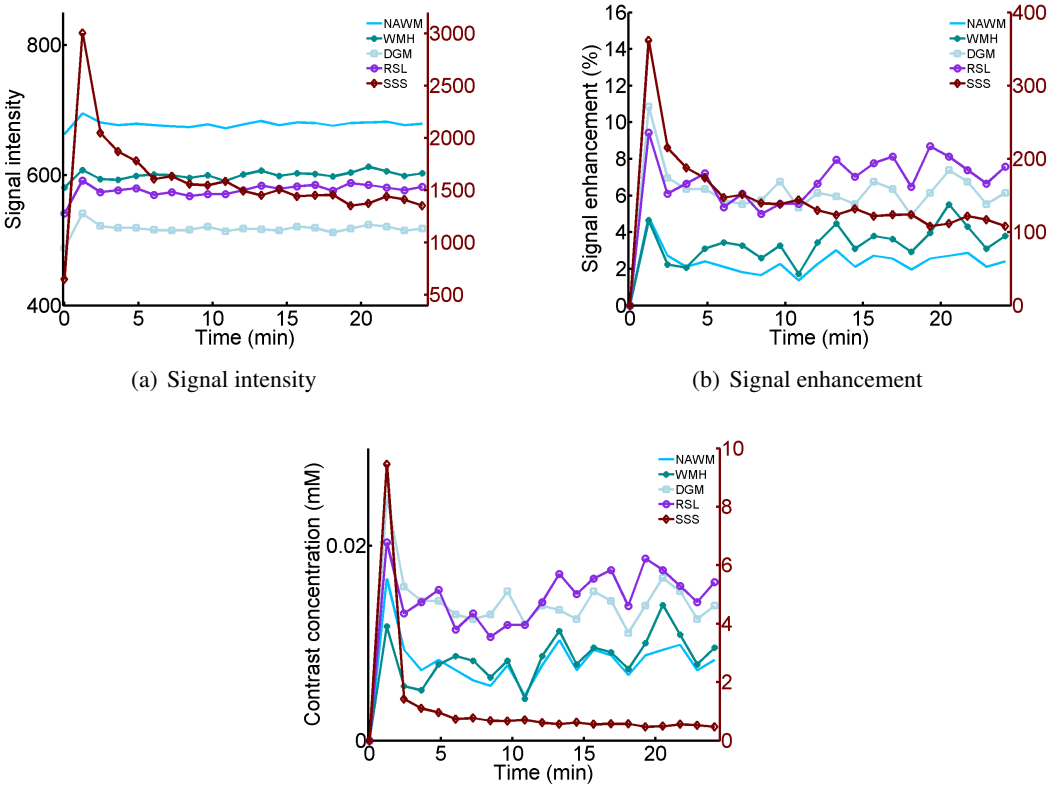

(a) Signal intensity

(b) Signal enhancement

(c) Contrast concentration

Figure 3.9.: Example of DCE-MRI tracer dynamics by tissue type.
Graphs show the (a) signal intensity, (b) signal enhancement and (c) contrast concentration curves over time for a single patient that is representative of the cohort. Values were obtained from the median signal of all voxels in each tissue type. Y-axis scales for the tissue and SSS curves are shown on the left and right respectively.

3.4. Discussion

The MSSII is a comprehensive clinical study that, in addition to a wide range of clinical information, provided DCE-MRI data for a large cohort of mild stroke patients with various degrees of cerebral SVD. The DCE-MRI protocol was designed to yield whole-brain coverage with high spatial resolution, in order to detect diffuse and subtle changes in BBB functionality. In the interest of optimising spatial resolution and coverage, the dynamic acquisitions were performed with a low temporal resolution of 73 seconds. On the downside, this precludes the measurement of blood flow and fast tracer exchange across the BBB. However, the MSSII aimed to detect low-level BBB leakage; this is a slow process and requires sufficiently long overall imaging duration rather than high temporal resolution (Barnes et al., 2015).

Different methods and locations for VIF selection were explored in the MSSII data. In order

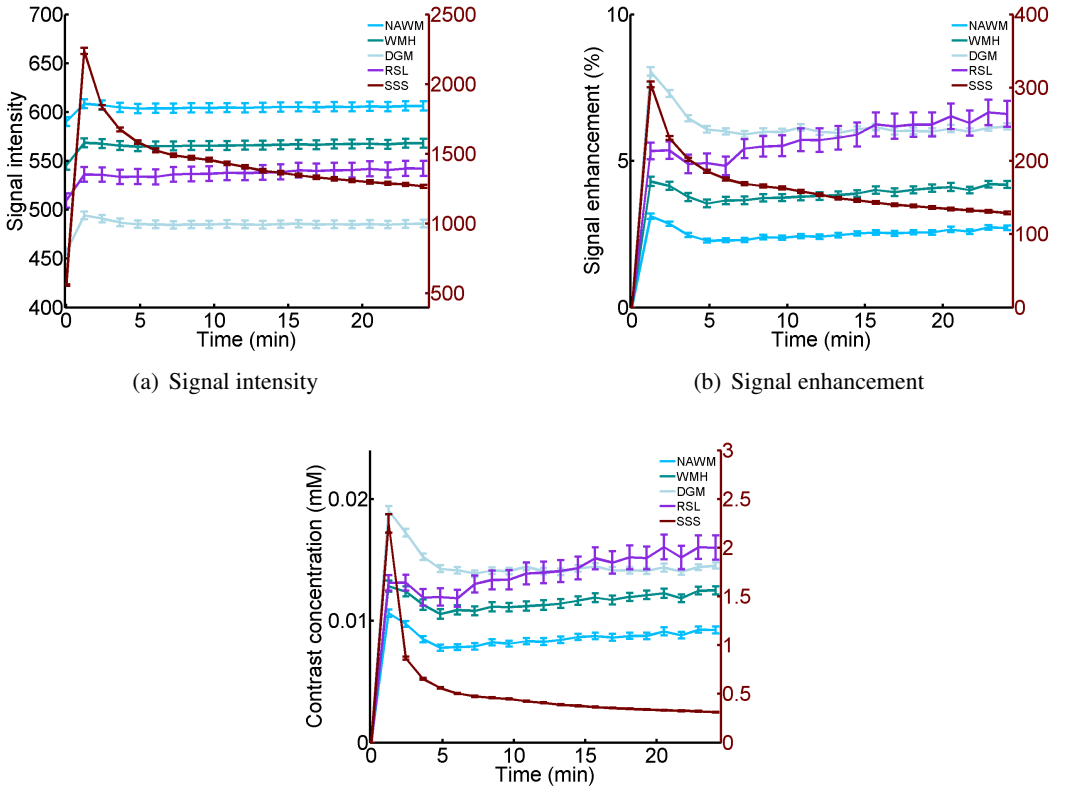

(a) Signal intensity

(b) Signal enhancement

(c) Contrast concentration

Figure 3.10.: Cohort average DCE-MRI tracer dynamics by tissue type. Graphs show the cohort average (a) signal intensity, (b) signal enhancement and (c) contrast concentration curves over time. Values were obtained from the median signal of all voxels in each tissue type and averaged over all patients ($n = 201$). Error bars indicate the mean $\pm$ standard error. Y-axis scales for the tissue and SSS curves are shown on the left and right respectively.

to obtain an accurate measurement of contrast agent inflow, the VIF should ideally be sampled in an artery close to the tissue to be analysed (Lavini and Verhoeff, 2010), e.g. in the ICA for analysis of brain tissues. However, obtaining a VIF from the ICA proved to be difficult in the MSSII cohort due to partial volume effects and low CNR. Alternatively, the VIF was measured in the SSS whose larger size allowed for a more reliable VIF measurement. Although tracer dynamics are usually described in terms of arterial blood plasma concentrations, deriving the VIF from the SSS is a widely accepted method in DCE-MRI of the brain (Lavini and Verhoeff, 2010; Yuan et al., 2013). It should be noted that previous studies deriving the VIF from the SSS use a significantly higher temporal resolution than is employed in the MSSII; however, the potential errors introduced by sampling the venous rather than arterial input are limited by the nature of this particular application. Firstly, the delay between arterial and venous responses is very short in comparison with the temporal resolution in the MSSII (Sourbron et al., 2009; Sourbron and Buckley, 2012). Secondly, the amount of extravasated contrast agent is very

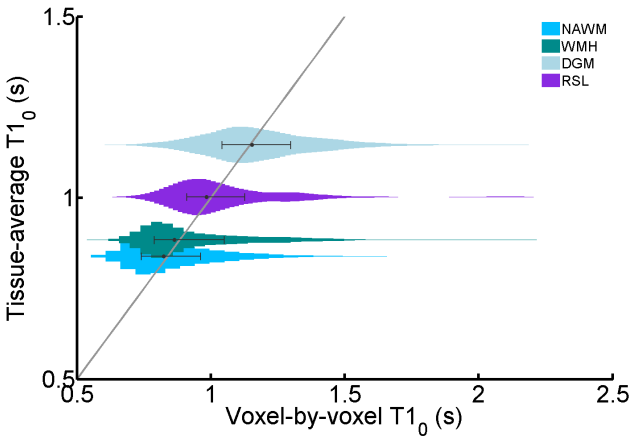

Figure 3.11.: Relationship between tissue-average and voxel-by-voxel $T1_0$ values. Graph showing the tissue-average $T1_0$ value in relationship to the distribution of voxel-by-voxel $T1_0$ values. Data are shown a single patient that is representative of the subset. For each tissue type, plots show the probability density of voxel-by-voxel $T1_0$ values, with the median and interquartile range of the distribution indicated in black. The grey line represents the line of identity.

small in normal-appearing brain tissues, so that the venous contrast agent concentration is approximately equal to the arterial inflow of contrast agent. Consequently, the SSS-derived VIF is expected to be a good approximation of the AIF.

Furthermore, we compared two different methods for ROI placement: selecting a single voxel in the SSS based on its signal enhancement during the DCE-MRI acquisition was shown to provide preferable results when compared to a ROI placed in the SSS on T2W images. This finding indicates that choosing a VIF based on structural information alone is likely to include voxels with low enhancement due to partial volume effects; thus, VIF selection should always make use of time-intensity information. A disadvantage of the method applied in this study is that it is fully manual and rather time intensive. Automatic methods for vessel detection and VIF extraction do exist, but have been reported to suffer from over-segmentation of vessels in the brain (Chen et al., 2008). Moreover, the manual selection of a single voxel is observer-dependent. Nonetheless, we achieved an acceptable inter-observer agreement of 42%; the extracted VIFs were very similar even in cases where different voxels were selected by the two observers.

A significant limitation with regards to VIF measurement is the low temporal resolution of the MSSII DCE-MRI data. In order to accurately sample the first pass of the contrast bolus, a temporal resolution of 1 s to 2 s is desirable (de Bazelaire et al., 2011; Essig et al., 2013). However, a temporal resolution of this order was not achievable in the MSSII due to the requirements for high spatial resolution and coverage. In order to overcome this problem,

several research groups have presented dual temporal resolution scanning methods with high temporal resolution during the first pass and high spatial resolution during the later phase (Jelescu et al., 2011; Leppert et al., 2014; Li et al., 2012a). Since the MSSII DCE-MRI data was collected before this project started, testing this approach was not possible within the scope of this PhD; however, a dual temporal resolution acquisition protocol may be considered for future studies. The given temporal resolution of 73 seconds does not allow for reliable sampling of the first pass of the contrast bolus and, hence, is likely to introduce errors into quantitative estimates of BBB functionality. In cases like this, the reproducibility of tracer kinetic parameters can be increased by using a generic AIF (Parker et al., 2006). However, factors such as age, heart rate, haematocrit and kidney function have been shown to cause inter-patient variability in the AIF (Port et al., 2001). Figure 3.12 compares the VIFs of three different patients in the MSSII, demonstrating that the intravascular contrast dynamics are highly variable between patients, even at later time points. Using an assumed AIF does not account for these individual variations and can, hence, also introduce systematic errors in tracer kinetic parameters (McGrath et al., 2009). In addition, we were mainly interested in the slow contrast extravasation processes that, in contrast to perfusion measurements, are less likely to be influenced by errors in first pass measurements. Consequently, the decision was made to use a patient-individual VIF despite its limitations. Another major potential source of error in VIF measurements is the blood inflow effect. This effect is caused by fresh $\left({}^{1}\mathrm{H}\right)$ spins flowing into the imaging volume, which leads to differences in longitudinal magnetisation saturation. Use of inflow-affected VIFs has been shown to cause errors of up to 80% in tracer kinetic parameters (Roberts et al., 2011). However, blood inflow effects decrease as blood travels through the imaging volume, so that VIF measurements from the SSS are likely to suffer little from inflow effects.

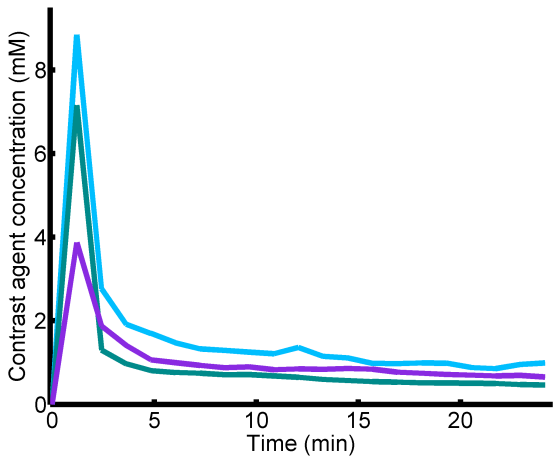

Figure 3.12.: Comparison of VIFs obtained from three different patients. Graphs showing the contrast agent concentrations over time measured in the SSS of three different patients in the MSSII cohort.

The DCE-MRI data was processed on a voxel-by-voxel basis in a small subset of the MSSII cohort ($n = 20$). The resulting signal enhancement curves over time were very noisy and, due to the low levels of enhancement, included a lot of negative values. While these negative values do not represent an immediate problem for the calculation of semi-quantitative parameters, they do result in negative contrast agent concentrations that are physiologically not applicable. Moreover, the high noise levels are expected to cause problems for tracer kinetic modelling, as they increase the instability of curve fitting algorithms, e.g. local minima. As a result of the high temporal resolution and whole-brain coverage, calculating voxel-by-voxel maps of $T1_0$ and semi-quantitative parameters was also very time consuming. Furthermore, the voxel-by-voxel AUC_E^{bn} and $slope_E$ maps are significantly affected by artefacts. In addition to motion artefacts in the phase direction, the maps most noticeably suffer from truncation artefacts in the slice direction, which manifest themselves as a series of dark rings parallel to the skull. In addition, the images are likely to be contaminated by Gibbs ringing around blood vessels with high inflow enhancement. These artefacts can cause significant differences in estimated tracer kinetic parameters, e.g. by changing the baseline signal and/or signal upslope (Di Bella et al., 2005). Although these issues could be partially addressed by applying four-dimensional post-processing algorithms (Balvay et al., 2011; Taheri and Sood, 2006), voxel-by-voxel maps of semi-quantitative and tracer kinetic parameters are unlikely to detect subtle BBB differences in normal-appearing tissues where the DCE-MRI signal enhancement is generally very low.

In the MSSII, a higher CNR was achieved by analysing the DCE-MRI data on an ROI basis. Although the ROI approach does not allow for the detection of local variations in BBB functionality, it provides a measurement of overall background BBB status, which is expected to be more powerful when looking for subtle differences between patient groups. Semi-automatic segmentation of different tissue types provided the largest possible ROIs; averaging the measured signal intensities over these large ROIs allowed for significant noise reduction before performing further calculations in the analysis pipeline. As a result, the tissue-average tracer dynamics were significantly smoother and only contained very few negative values. In order to avoid physiologically impossible values, all negative concentration values were set to zero. It should be noted that this may introduce a tissue-dependent positive bias. However, the percentage of negative data points was very small; in addition, there was no general trend in the amount of negative values with the level of enhancement (e.g. there was no significant difference between the number of negative values in NAWM and RSL). Moreover, it should be highlighted that the ROI measurements may also be contaminated by the aforementioned Gibbs artefact, potentially introducing additional positive bias.

The importance of correcting DCE-MRI signal enhancement profiles for intrinsic parameters such as $T1_0$ has been highlighted previously and comes into play when converting signal enhancement into contrast agent concentration. If $T1_0$ is not taken into account, it is impossible

to know whether differences in signal enhancement are due to a true contrast uptake difference or different tissue properties (Armitage et al., 2011). In this and many other studies, $T1_0$ was measured using the variable flip angle method (also known as 'DESPOT1', Homer and Beevers, 1985). The resulting $T1_0$ values are overestimated in comparison to values obtained using the gold standard IR method (Stikov et al., 2015). However, they correlate well with variable flip angle $T1_0$ measurements at 1.5 T in other cohorts (Muñoz Maniega et al., 2015; Zhang et al., 2013). The variable flip angle method has the advantage of yielding $T1_0$ maps with whole-brain coverage and adequate signal-to-noise ratio within an acceptable acquisition time. However, it is sensitive to flip angle variations across the brain, i.e. deviations of the actual from the operator defined flip angles caused by radio frequency (RF) field inhomogeneities, resulting in errors in $T1_0$ and other parameters (Armitage et al., 2011; Schabel and Parker, 2008). There are several potential sources for such errors. Firstly, RF non-uniformity can arise from standing wave effects caused by the dielectric properties of human tissues. This effect is worse at higher field strengths, because the RF wavelength is shorter and, thus, more frequently of the same size as the imaged structures. Moreover, field inhomogeneities can be caused by imperfections in the slab excitation profile of the RF pulse and the coil design (e.g. surface coils have poor RF uniformity compared to volume coils). Several methods have been proposed for the minimisation of RF field inhomogeneity, including special coils and tailored pulses (Roberts et al., 2011). There are also T1 measurement approaches that include estimation and/or correction for flip angle errors, such as DESPOT1-HIFI (Deoni, 2007). Unfortunately it was not possible to estimate the RF profile in this patient group; however, at 1.5 T and using a RF transmit volume coil, flip angle variations should be limited and reasonably consistent within the cohort. In future studies, especially on scanners with higher field strength, it would be prudent to correct for RF field non-uniformity. Look-Locker based methods such as TAPIR (Shah et al., 2001) also provide an alternative approach for $T1_0$ measurement, permitting faster sampling of the magnetization recovery curve than the conventional IR method. The sensitivity of these methods to flip-angle variations is reduced since the flip angle can be modelled as an unknown parameter during fitting of the IR curve.

So far, the measured signal enhancement profiles have been assessed visually and by calculating the semi-quantitative parameters AUC_E^{bn} and $slope_E$. The cohort average results give a first indication of differences in BBB function between tissue types. The higher late phase slope values in RSL and WMH are expected to be related to BBB leakage, as a linear increase in signal is likely to be caused by slow contrast extravasation. Similarly, AUC_E^{bn} is likely to be proportional to blood volume, because it represents the relative amount of contrast agent present in the tissue. Nevertheless, these semi-quantitative parameters should be interpreted with caution, because their exact relationship with physiologically relevant parameters such as blood flow and BBB permeability is unclear. In order to draw conclusions about BBB leakage, it is necessary to perform a quantitative analysis by applying tracer kinetic modelling.

3.5. Conclusion

This chapter introduced an on-site clinical study of mild stroke patients, the MSSII. This comprehensive study provides a wide range of clinical and MRI data, including DCE-MRI data with whole-brain coverage in $n = 201$ patients. In addition to presenting the study cohort and procedures, this chapter addressed several basic aspects of DCE-MRI processing and analysis. Different methods for VIF extraction were explored, with the selection of a single voxel in the SSS yielding the best results. Due to high noise levels and small overall signal enhancement, analysis of the DCE-MRI data on a voxel-by-voxel basis was found not to be suitable for the detection of subtle changes in BBB functionality. Alternatively, signal intensity, signal enhancement and contrast concentration profiles as well as $T1_0$ were calculated on a whole-tissue basis. The signal enhancement curves were characterised using the semi-quantitative measurements AUC_E^{bn} and $slope_E$. Although these parameters were shown to be significantly different between tissue types and can give an indication of BBB function, their interpretability regarding specific processes is limited. In order to obtain quantitative estimates of physiologically relevant parameters, a more complex, tracer kinetic analysis should be performed. Consequently, the next chapter aims to investigate the applicability of tracer kinetic modelling for analysis of the MSSII DCE-MRI data.

4. Tracer kinetic modelling in the Mild Stroke Study II cohort

This chapter aims to determine the tracer kinetic modelling approach most suitable for analysis of the clinical data presented in chapter 3. Besides applying a set of models to the Mild Stroke Study II (MSSII) data (section 4.2), this chapter also investigates the robustness of the modelling to its assumptions using simulations (section 4.3). Furthermore, it examines the relationship between tracer kinetic and semi-quantitative parameters both in theory and in the clinical cohort. Most contents of this chapter have been published in Heye et al. (2016a).

4.1. Introduction

As illustrated in chapters 1 and 2 of this thesis, many tracer kinetic models have been proposed for fitting dynamic contrast-enhanced magnetic resonance imaging (DCE-MRI) data, most of which have been developed and applied primarily in neuro-oncology and body imaging, where contrast uptake in tissue is typically large and rapid. However, the optimal modelling approach for research in small vessel disease (SVD) where the blood-brain barrier (BBB) remains largely intact (and extravascular contrast uptake is therefore slow) is unclear.

In their extensive review of tracer kinetic models, Sourbron and Buckley (2013) emphasised the importance of appropriate model selection. In order to find the most adequate model for a given data set, they recommended to identify a limited number of possible models using prior knowledge and then select the optimal model (i.e. the simplest model that fits the data) using a data-driven approach. Data-driven model selection has recently gained popularity in DCE-MRI, with applications in cervix carcinoma (Donaldson et al., 2010) and cerebral glioma (Artzi et al., 2015; Bagher-Ebadian et al., 2012; Ewing et al., 2006). However, a good model fit does not guarantee that the assumptions made by the model are valid and that the fitted parameters are accurate (Sourbron and Buckley, 2011). This highlights the importance of recognising the assumptions built into tracer kinetic models and assessing their likely validity for a given application, as has been discussed previously (see section 2.4). As the accuracy of tracer kinetic parameters cannot usually be assessed in clinical DCE-MRI data, several groups have used computer simulations for this purpose (Barnes et al., 2015; Larsson et al., 2009; Sourbron et al., 2009). Such simulations allow for the generation of synthetic DCE-MRI data from ‘true’ tissue parameters, which can be compared to fitted model parameters.

This work aimed to determine the tracer kinetic modelling approach most suitable for assessing subtle BBB leakage in the MSSII cohort using a data-driven approach, and to test its validity in theory using simulations. Ultimately, the purpose of this work was to obtain reliable tracer kinetic parameters for normal-appearing tissues and lesions in the MSSII cohort.

4.2. Model selection in the MSSII cohort

This section focuses on tracer kinetic analysis of the DCE-MRI data acquired within the scope of the MSSII. All analyses were performed using custom-written software programmed in MATLAB (MathWorks, Natick, MA, USA).

4.2.1. Methods

DCE-MRI data

Details of the MSSII clinical cohort and MRI procedures have been given in chapter 3; in short, DCE-MRI was performed in 208 patients with mild lacunar or cortical ischaemic stroke, and consisted of 20 consecutive three-dimensional (3D) T1-weighted (T1W) spoiled gradient echo (GRE) acquisitions (TR/TE $= 8.24/3.1$ ms, $\alpha = 12^\circ$, 24×24 cm field of view, 256×192 acquisition matrix and 42 × 4 mm slices) with a temporal resolution of 73 s and a total acquisition time of approximately 24 min. The acquisition was initiated simultaneously with an intravenous bolus injection of 0.1 mmol/kg gadoterate meglumine (Gd-DOTA, Dotarem, Guerbet, France) using a power injector. For calculation of $T1_0$, two additional 3D T1W spoiled GRE acquisitions were obtained prior to contrast administration with flip angles of 2° and 12° respectively.

Model choice and fitting

An overview of compartment models for the quantification of DCE-MRI data has been provided in section 1.2.3. Not all of the models depicted in Figure 1.11 are appropriate for analysis of the MSSII data. Firstly, the low temporal resolution does not allow for a reliable estimation of blood flow, because the first pass of the bolus is not adequately sampled; this excluded models that measure F_p such as the two-compartment exchange model (2CXM) and two-compartment uptake model (2CUM). Secondly, the assumptions made by some models clearly conflict with the nature of brain tissue with largely intact BBB. For instance, the original Tofts model is strictly valid only in situations where contrast agent in the capillaries can be neglected; however, brain tissue is highly vascular and low BBB permeability results in small amounts of

extravascular tracer so that the signal contribution from intravascular tracer is dominant and cannot be disregarded. As it was not clear which of the remaining models yields the most reliable parameter estimates and what level of model complexity is needed to accurately fit the MSSII data, a set of three nested models was fitted to the tissue concentration curves: (i) the modified Tofts model (Tofts et al., 1999), (ii) the Patlak model (Patlak et al., 1983), and (iii) the steady state model (Sourbron and Buckley, 2013). As a reminder, a schematic overview of these models and their relationship with the 2CXM is shown in Figure 4.1.

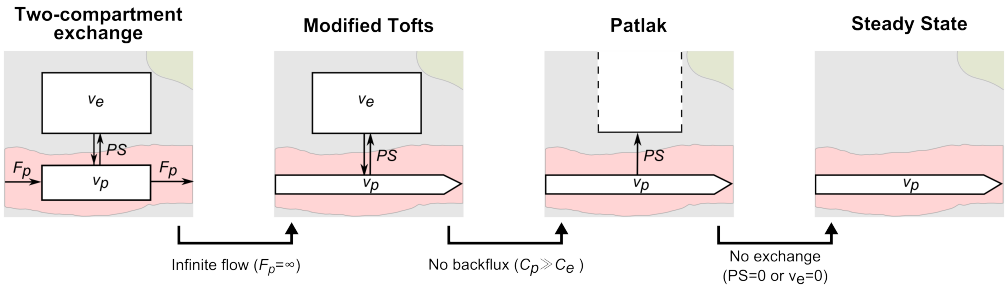

Figure 4.1.: Set of nested tracer kinetic models applied in the MSSII. Target parameters of DCE-MRI modelling are the fractional plasma volume v_p, the fractional interstitial volume v_e, the plasma flow F_p and the permeability-surface area product PS. The three models applied in the MSSII (modified Tofts, Patlak and steady state) are related to the 2CXM by a series of simplifying assumptions. Reprinted from Heye et al. (2016a).

Model fitting was performed by non-linear minimisation of the sum of squared residuals (SSR) in the following tissue types: normal-appearing white matter (NAWM), deep/subcortical grey matter (DGM), white matter hyperintensities (WMH) and recent stroke lesions (RSL), using a vascular input function (VIF) measured in the superior sagittal sinus. All parameters were restricted to positive values and $v_p + v_e$ was constrained to be less or equal to 1. In order to reduce the probability of selecting local minima (Ahearn et al., 2005), fitting was repeated 25 times with different initial values. The first three post-contrast time points of all contrast agent concentration curves were omitted from SSR calculation, since the rapid concentration changes during and immediately after the first pass are not adequately resolved by the acquisition protocol and depend more strongly on F_p, which is not included in the models (Larsson et al., 2009).

Model comparison

The competing models were ranked according to the Akaike information criterion (AIC, Akaike, 1974), which offers a data-driven criterion for the selection of the most appropriate model and has been applied in DCE-MRI by other groups (Brix et al., 2009; Ingrisch et al., 2010). The

AIC accounts for the trade-off between goodness-of-fit and model complexity, by combining the SSR associated with the model m (SSR_m) with the number of free parameters K_m:

$$\mathrm{AIC}_m = N \ln\left(\frac{\mathrm{SSR}_m}{N}\right) + 2(K_m + 1), \tag{4.1}$$

where N denotes the number of data points. For small samples, i.e. $N/K_m < 40$ as in our case, the AIC should be extended with a second-order bias correction term (Burnham, 2004), giving the small-sample version

$$\mathrm{AICc}_m = \mathrm{AIC}_m + \frac{2K_m(K_m+1)}{n - K_m - 1}. \tag{4.2}$$

The Akaike weight AW_m describes the probability that the model m is best amongst a set of M models, i.e. the model that results in the least information loss when approximating real data with the model (Luypaert et al., 2012). It is given by

$$\mathrm{AW}_m = \frac{\exp(-\Delta_m/2)}{\sum_{i=1}^{M}\exp(-\Delta_i/2)} \quad \text{with} \quad \Delta_m = \mathrm{AICc}_m - \min(\mathrm{AICc}_1, ..., \mathrm{AICc}_M). \tag{4.3}$$

4.2.2. Results

Model selection

As reported previously, DCE-MRI data suitable for analysis were obtained in 201 patients. An example of tracer kinetic model fitting in NAWM and RSL for a single patient is shown in Figure 4.2; the Patlak and modified Tofts models provided good fits to the measured signal but the steady state model was not adequate to describe the data. This observation is confirmed by analysis of the Akaike weights, which showed that the Patlak model best represents the data in most subjects for all tissue types (see Figure 4.3(a)), and was selected as the optimum model in 74% to 78% of patients for the four tissues measured (see Figure 4.3(b)).

Resulting tracer kinetic parameters

A comparison of K^{Trans} and v_p values obtained from the different tracer kinetic models is shown in Figure 4.4. For a statistical comparison between tracer kinetic parameters obtained with the different models, Wilcoxon's signed rank test was used. The modified Tofts model resulted in significantly higher K^{Trans} values in all tissue types when compared to the Patlak model ($p < 0.001$); moreover, the additional free parameter of the modified Tofts model lead to uncertainty in parameter fitting as indicated by the wider range of K^{Trans} values. Similarly, the blood volume estimates obtained from the steady state, Patlak and modified Tofts models were significantly different from each other in all tissue types ($p < 0.001$), with v_p values from

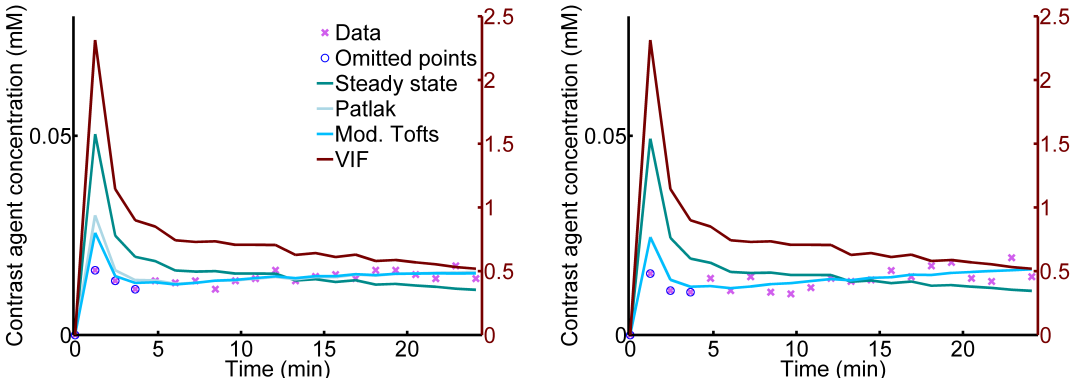

(a) NAWM (b) RSL

Figure 4.2.: Example of tracer kinetic model fitting in the MSSII data. The graphs show the concentration-time curves in (a) NAWM and (b) RSL (legend as in (a)) of a single patient. Note that the first three data points were omitted for model fitting for reasons explained in the text. Partly reprinted from Heye et al. (2016a).

the steady state model being the highest and v_p values from the modified Tofts model being the lowest. The cohort-average parameters obtained with the Patlak model are summarised in Table 4.1 and will be discussed in detail in chapter 7.

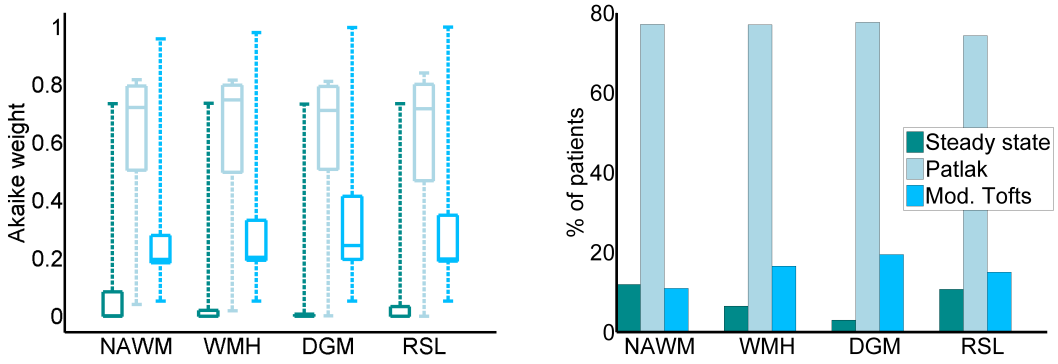

(a) Akaike weights for each model and tissue type (b) Optimum model according to Akaike weights

Figure 4.3.: Model selection according to Akaike weights. (a) Comparison of Akaike weights between the steady state, Patlak and modified Tofts models in all tissue types (the results for the three models are colour-coded as shown in (b)), (b) bar graph showing the percentage of patients in which a particular model was selected as the optimum model according to Akaike weights. Partly reprinted from Heye et al. (2016a).

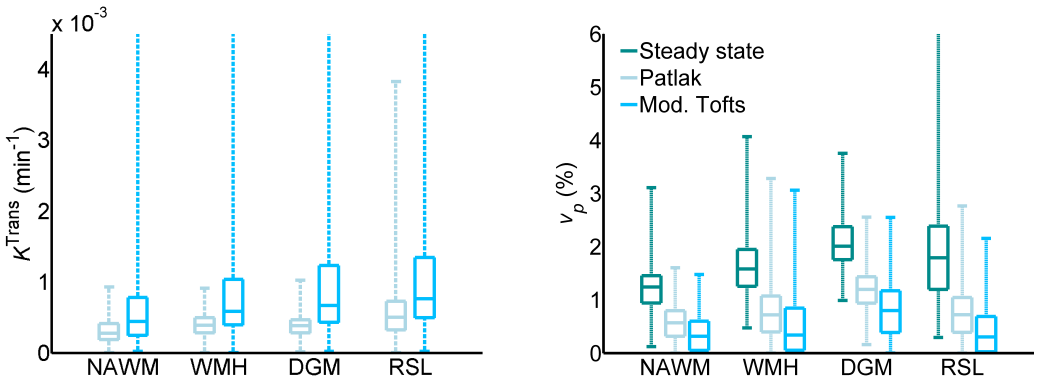

(a) K^{Trans} values (b) v_p values

Figure 4.4.: Comparison of K^{Trans} and v_p values obtained from three different tracer kinetic models. (a) K^{Trans} values obtained from the Patlak and modified Tofts models in the different tissue types (legend as in (b)), (b) v_p values obtained from the steady state, Patlak and modified Tofts models in the different tissue types.

Table 4.1.: Patlak parameters by tissue type. Values are shown as cohort median and interquartile range (data not generally normally distributed) for the four different tissue types.

Tissue type	K^{Trans} ($\cdot 10^{-4}$ min^{-1})	v_p ($\cdot 10^{-2}$)
NAWM	2.75 [1.85, 4.12]	0.57 [0.32, 0.80]
WMH	3.91 [2.80, 4.94]	0.72 [0.40, 1.07]
DGM	3.85 [2.83, 4.68]	1.20 [0.94, 1.43]
RSL	5.02 [3.24, 7.25]	0.72 [0.39, 1.05]

Relationship between Patlak and semi-quantitative parameters

The Pearson correlation coefficient was used in order to investigate the relationship between the semi-quantitative parameters (AUC_E^{bn} and slope_E) and the Patlak parameters (K^{Trans} and v_p) in the MSSII cohort. The corresponding graphs are shown in Figure 4.5. There was a strong positive correlation between slope_E and K^{Trans}, with Pearson's correlation coefficient R ranging from 0.63 in WMH to 0.82 in RSL ($p < 0.001$). Moreover, slope_E was significantly negatively correlated with v_p in all tissues but RSL ($-0.72 < R < -0.59$, $p < 0.001$). AUC_E^{bn} correlated strongly with both K^{Trans} ($0.39 < R < 0.87$, $p < 0.001$) and v_p ($0.44 < R < -0.70$, $p < 0.001$) in all tissue types.

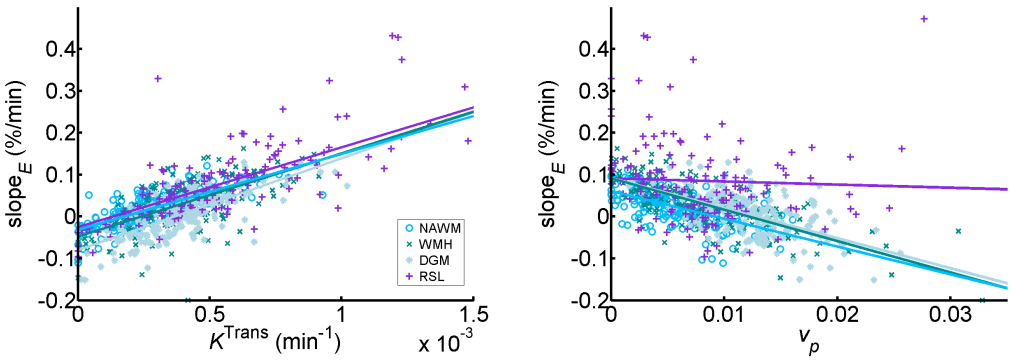

(a) Relationship between slope$_E$ and the Patlak parameters K^{Trans} (left) and v_p (right)

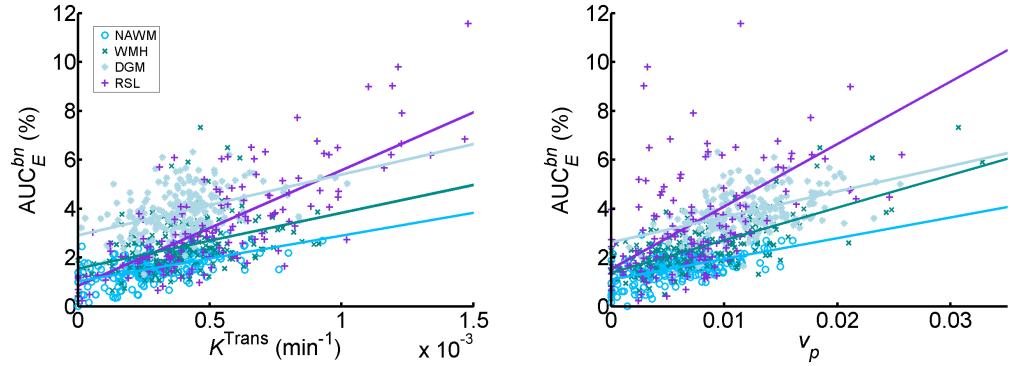

(b) Relationship between AUC$_E^{bn}$ and the Patlak parameters K^{Trans} (left) and v_p (right)

Figure 4.5.: Relationship between semi-quantitative and Patlak parameters in the MSSII patient cohort. Scatter plots showing the relationship between the semi-quantitative parameters (a) slope$_E$ and (b) AUC$_E^{bn}$ and the Patlak parameters K^{Trans} and v_p. Each data point represents the values measured in a single patient of the MSSII cohort and is colour-coded by tissue type; lines of best fit were calculated using the linear least square method and are shown for each tissue type separately.

4.3. Assessment of model validity using computer simulations

The in vivo experiments presented in the previous section showed that the Patlak model produces good fits to the DCE-MRI data from the MSSII cohort. However, this does not guarantee that the assumptions made by the Patlak model (infinite blood flow, no back-diffusion) are valid and that the fitted parameters are accurate (Sourbron and Buckley, 2011). Consequently, numerical simulations were performed in order to systematically investigate the validity of the Patlak model. As before, all simulations were implemented in MATLAB (MathWorks, Natick, MA, USA).

4.3.1. Methods

Generation of a high-resolution VIF

First, a high-resolution ($\Delta t = 0.1$ s) VIF was generated using a modified version of the function introduced by Parker et al. (2006), which consists of two Gaussians plus an exponential term modulated by a sigmoid function. This function is based on acquisitions with a high-temporal resolution and an overall acquisition time of approximately 6 min and, hence, provides an accurate representation of the first pass of the bolus. For longer acquisitions times however, it has been shown that VIFs typically exhibit a biexponential decay (Weinmann et al., 1984), which is consistent with the VIFs measured in the MSSII cohort. Consequently, in order to generate a simulated VIF with realistic first pass behaviour that also matched the MSSII data at longer times post-injection, the original function by Parker et al. (2006) was extended by an additional exponential term resulting in the following function:

$$c_b(t) = \left(\sum_{n=1}^{2} \frac{A_n}{\sigma_n \sqrt{2\pi}} \exp\left(-\frac{(t-T_n)^2}{2\sigma_n^2} \right) + \frac{\sum_{n=1}^{2} \alpha_n \exp(-\beta_n t)}{1+\exp(-s(t-\tau))} \right). \tag{4.4}$$

For the Gaussian functions and sigmoid modulation, which describe the first and second pass of the VIF, the parameters given by Parker et al. (2006) were used (A_n, σ_n, T_n, s, τ). The parameters α_n and β_n were obtained by fitting equation 4.4 to the population-average VIF from the MSSII data. Figure 4.6 shows the resulting function and the population-average VIF from the MSSII data. Finally, the whole-blood VIF was converted to blood plasma concentration using the formula $c_p = c_b/(1-\mathrm{Hct})$, with $\mathrm{Hct} = 0.45$.

Simulation of DCE-MRI measurements

Simulated tissue concentration curves were generated by convolving this VIF with the impulse response function of the 2CXM (Sourbron and Buckley, 2013). PS and v_p values were chosen to represent the range of values obtained in normal-appearing tissue, WMH and stroke lesions; v_e was chosen to be 0.2 (Syková and Nicholson, 2008) and F_p values between 10 ml/100g/min and 50 ml/100g/min were selected to represent typical values for NAWM, WMH and DGM (Brickman et al., 2009). Random noise was added to the curves to give a contrast-to-noise ratio (CNR) of 8, similar to the one observed in NAWM and DGM in the MSSII cohort; the CNR was defined as the peak contrast agent concentration divided by a noise estimate, which was calculated as the standard deviation of the difference between the measured concentration curve and the Patlak model fit ($\mathrm{CNR} = \max[C(t)]/\mathrm{std}[C(t) - C_{\mathrm{Patlak}}(t)]$). The VIF and tissue concentration curves were then down-sampled to the experimental temporal resolution ($\Delta t =$ 73 s) and these were fitted to the Patlak model as described above. As for the clinical data, the

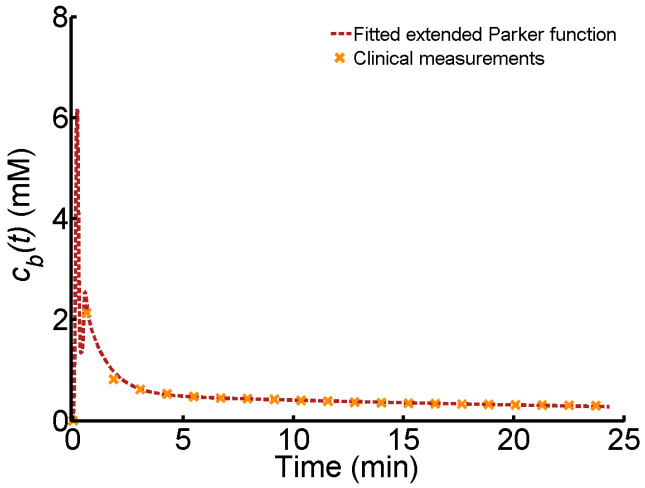

Figure 4.6.: High temporal resolution VIF generated for the simulation study. The VIF was generated based on the generic function introduced by Parker et al. (2006), yielding realistic first pass behaviour. In order to match the MSSII data at longer times post-injection, the function was extended by an additional exponential term. Shown is the whole-blood VIF, which was converted to blood plasma concentration using the formula $c_p = c_b/(1-\mathrm{Hct})$, with $\mathrm{Hct} = 0.45$.

first three post-contrast data points were neglected for calculating the SSR during model fitting. Moreover, the semi-quantitative parameters AUC_E^{bn} and slope_E were calculated as described in section 3.3.1. The simulations were repeated 1000 times for every set of parameters to quantify the influence of noise. All simulations were based on a tissue T1 of 992 ms, corresponding to typical NAWM values measured in the MSSII patient cohort.

4.3.2. Results

Accuracy of tracer kinetic parameters

The results of simulations performed to determine the validity of the Patlak model are shown in Figure 4.7. These compare the fitted Patlak parameters with the 'true' parameters used to generate synthetic signal-time curves using the 2CXM model when neglecting the first three post-contrast data points during model fitting (as in the clinical data). Both K^{Trans} and v_p were accurately estimated when PS is low, despite the very low temporal resolution and the simplifying assumptions of the Patlak model. At higher PS values, K^{Trans} was underestimated and v_p slightly overestimated as a result of back-diffusion, which is neglected in the Patlak model. The model was robust to differences in blood flow, with low flow only resulting in a slightly greater underestimation of K^{Trans}. For comparison, Figure 4.8 shows the simulation results when considering all post-contrast data points during model fitting. Due to the low

temporal resolution, the accuracy of both K^{Trans} and v_p was highly dependent on the blood flow. In particular, low F_p values lead to significant overestimation of PS for high v_p.

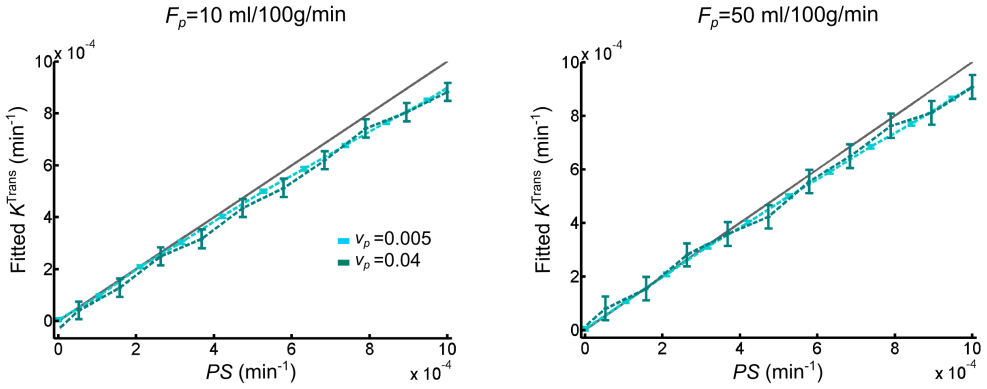

(a) Relationship between permeability surface area product PS and fitted Patlak K^{Trans}

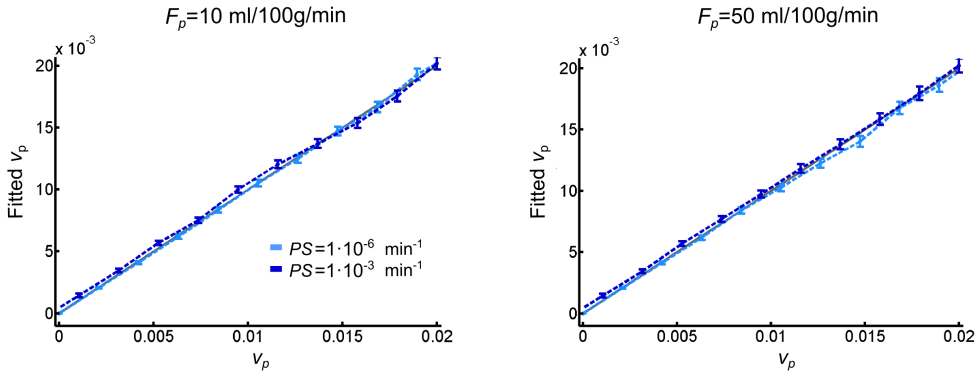

(b) Relationship between blood plasma volume v_p and fitted Patlak v_p

Figure 4.7.: Simulated accuracy of Patlak parameters. Relationship of (a) permeability surface area product PS and (b) blood plasma volume v_p values, with corresponding fitted Patlak parameters. Results are shown for two different F_p, PS and v_p values. For all simulations, v_e was set to 0.2. Error bars indicate the mean $\pm$ 1.96 standard deviations; the grey line represents the identity line. The first three post-contrast data points were omitted for model fitting. Reprinted from Heye et al. (2016a).

Theoretical relationship between semi-quantitative and tracer kinetic parameters

Figure 4.9 shows the theoretical relationship between PS and v_p, and the semi-quantitative parameters AUC_E^{bn} and slope_E in the simulated data. AUC_E^{bn} correlated strongly with v_p, but was also influenced by PS. Similarly, the enhancement slope correlated with PS, but was not

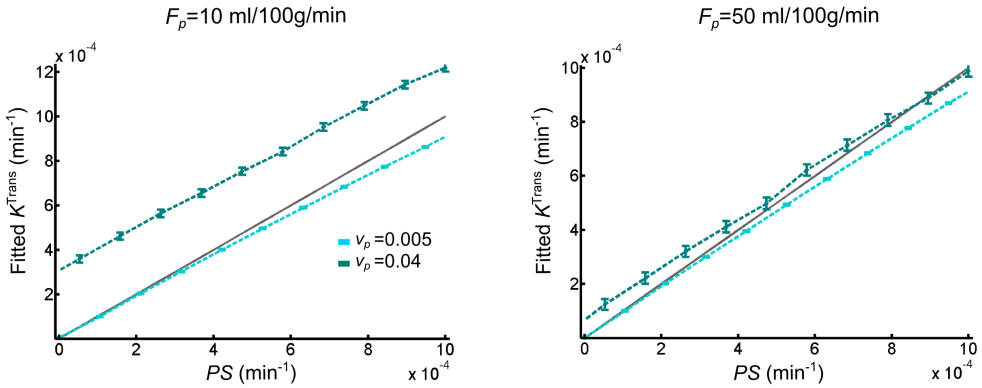

(a) Relationship between permeability surface area product PS and fitted Patlak K^{Trans}

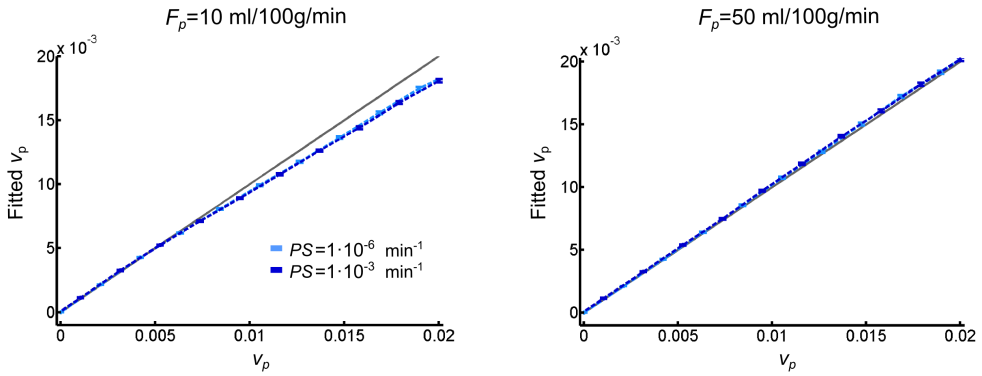

(b) Relationship between blood plasma volume v_p and fitted Patlak v_p

Figure 4.8.: Simulated accuracy of Patlak parameters considering all post-contrast data points. Relationship of (a) permeability surface area product PS and (b) blood plasma volume v_p values, with corresponding fitted Patlak parameters. Results are shown for two different F_p, PS and v_p values. For all simulations, v_e was set to 0.2. Error bars indicate the mean $\pm$ 1.96 standard deviations; the grey line represents the identity line. All post-contrast data points were used for model fitting.

independent of v_p. Moreover, the degree of correlation varied with $T1_0$ and is, thus, tissue-dependent.

4.4. Discussion

The clinical DCE-MRI data from the MSSII cohort was analysed using a set of three nested tracer kinetic models. The three models produced significantly different parameter estimates,

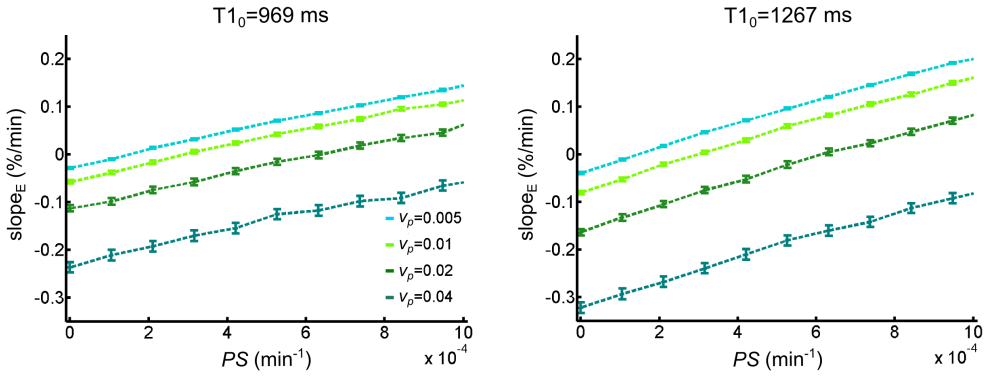

(a) Relationship between slope$_E$ and PS for different v_p and T1$_0$ values

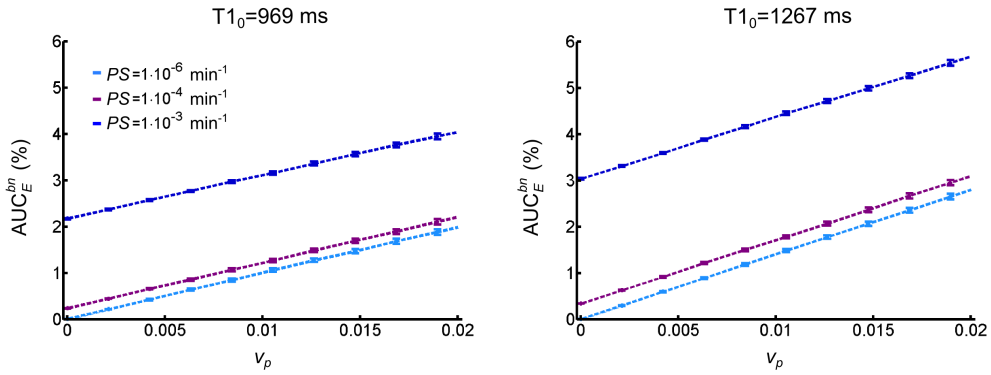

(b) Relationship between AUC$_E^{bn}$ and v_p for different PS and T1$_0$ values

Figure 4.9.: Simulated relationship between semi-quantitative parameters and tissue properties. (a) Relationship between slope$_E$ and PS for different v_p values; results are shown for two different T1$_0$ values, which correspond to typical values measured in the MSSII cohort in NAWM (left) and RSL (right), (b) Relationship between AUC$_E^{bn}$ and v_p for different PS and T1$_0$ values. All results are shown for $F_p = 10$ ml/100g/min and $v_e = 0.2$; error bars indicate the mean $\pm$ 1.96 standard deviations. Reprinted from Heye et al. (2016a).

highlighting the influence of model choice on clinical results and the importance of investigating the model fit and validity. A model comparison using the AIC revealed the Patlak model to be the most appropriate of the three models for quantification of subtle BBB disruption in this cohort. The steady-state model does not adequately fit the data; while both the Patlak and modified Tofts models fit the data similarly well, the simpler Patlak model does so using fewer free parameters and is therefore selected. The additional complexity of the modified Tofts model results in over-fitting in the low-permeability situation, consistent with a previous report regarding the behaviour of Tofts parameters in a smaller study of healthy volunteers and multiple sclerosis (MS) patients (Cramer et al., 2014). Data-driven model selection has

recently gained popularity in DCE-MRI and is often applied on a patient-individual voxel-by-voxel basis (Bagher-Ebadian et al., 2012; Ewing et al., 2006; Donaldson et al., 2010). However, it has been shown that this approach can increase bias and/or uncertainty of parameter estimates (Luypaert et al., 2012). This work aimed to overcome this limitation by identifying the model that is most suitable for the vast majority of tissues and patients and applying this model to the whole patient cohort, rather than selecting a different model based on the AIC for every individual region of interest (ROI). This avoids errors in model selection due to uncertainty in Akaike weights, which is particularly likely to occur in data with a low signal to noise ratio, and ensures that all data is analysed with the model that has been identified as generally the most adequate for the data. A detailed analysis of the tracer kinetic parameters obtained from the MSSII data and their relationship with clinical measurements will be presented in chapter 7.

The DCE-MRI data in this study has been analysed at the level of ROIs rather than voxels. As discussed in detail in chapter 3, this approach was selected due to the low CNR in single voxels and due to the influence of artefacts (e.g. Gibbs ringing and motion). Figure 4.10 shows voxel-wise maps of Patlak parameters obtained in two different MSSII subjects; these maps demonstrate that artefacts, while typically at the level of only a few percent, have a similar magnitude to the small contrast-induced signal changes, and therefore have a disproportionate influence on voxel-wise tracer kinetic parameters. Averaging over a large ROI reduces the influence of noise and artefact, enabling more robust measurement of background BBB status, especially in normal-appearing tissue where signal changes are small. However, a limitation of this approach is that it does not allow the detection of local variation in BBB function.

Numerical simulations were performed in order to investigate the validity of the Patlak model. The simulations confirmed that the Patlak model yields reliable estimates of K^{Trans} and v_p when PS is low. By omitting data that is acquired during the first pass of the contrast bolus, accurate parameter values can be obtained independent of cerebral blood flow. It should be noted that omitting the first three data point removes a significant amount of information from the curves, which may introduce bias. However, the simulations indicate that this potential bias is negligible; in fact, considering the first three time points in the simulations led to significant overestimation of K^{Trans} at low flow values. In the MSSII data, considering the first three data points led to worse fits to data at later stages in the acquisition, which carry the information about slow extravasation processes that this work is mainly interested in. The simulations also demonstrated that accurate parameter values can be obtained despite the use of a temporal resolution much lower than is typically employed in DCE-MRI. A consequence of this finding is that DCE-MRI protocols for investigating diffuse subtle BBB pathology may benefit from prioritising spatial resolution, whole-brain coverage and CNR over sampling rate. However, a disadvantage of low temporal resolution acquisition is that blood flow cannot be determined in addition to v_p and PS; where knowledge of F_p is required and temporal resolution is adequate,

the 2CUM model may be substituted for the Patlak model in low-permeability tissue (Sourbron et al., 2009; Ingrisch et al., 2012). It should also be higlighted that numerical simulations as performed in the present work are likely to depend on the choice of VIF.

The findings presented in this chapter are consistent with recent investigations by Cramer and Larsson (2014) and Barnes et al. (2015). Similar to this work, both studies investigated the accuracy of tracer kinetic parameters using computer simulations, showing that the Patlak model yields reliable estimates of low BBB permeability. However, the investigations by Cramer and Larsson (2014) and Barnes et al. (2015) include limited clinical data, with both studies being based on small samples of young, healthy volunteers and/or MS patients. In contrast, the MSSII data allowed for investigating the validity of quantitative BBB permeability estimates in a large clinical cohort of patients with SVD. Moreover, the DCE-MRI acquisitions performed by both groups employ higher temporal resolutions at overall lower acquisition times, resulting in limited spatial resolution and much less coverage than in the MSSII. Although the recent findings by Cramer and Larsson (2014) and Barnes et al. (2015) provide some guidance on acquisition parameters and postprocessing methodology for the assessment of subtle BBB leakage, it would have been unclear without the present work whether their recommendations apply in the MSSII data with a different pathology, higher spatial resolution and coverage but lower temporal resolution.

In the MSSII cohort, a comparison of semi-quantitative and Patlak parameters showed that both AUC_E^{bn} and slope_E correlate with K^{Trans} as well as v_p, with the strength of correlation varying between tissue types. This was confirmed in the simulated data, showing that the semi-quantitative measurements are highly dependent on several tissue properties, such as PS, v_p and $\mathrm{T1}_0$. These findings are in line with a previous study by Walker-Samuel et al. (2006), who demonstrated that the area under the curve (AUC) has an non-traceable relationship with all three parameters of the modified Tofts model. In contrast to the present work, the study by Walker-Samuel et al. (2006) was based on simulated data only, which had a much higher temporal resolution of 5 s. Furthermore, the focus was on the initial AUC, which comprises the first pass only and is commonly used to assess treatment effects in oncology drug trials. The work presented in this chapter confirmed that, in contrast to the fitted tracer kinetic parameters, semi-quantitative parameters reflect a combination of underlying tissue properties, hindering their interpretability regarding specific processes.

Nevertheless, it should be noted again that tracer kinetic analysis also has several limitations. Firstly, all tracer kinetic models necessarily make assumptions regarding tissue structure and the transport of blood plasma and contrast agent, which may not reflect true physiology. For instance, all tracer kinetic models considered in this work are based on the 2CXM, i.e. both the blood plasma and the interstitium are modelled as well-mixed compartments. Alternatively, the tissues could be modelled as plug-flow systems (see section 1.2.3), with both models

representing a simplification of reality while realistic tissues are likely to be a mixture of these extremes (Sourbron and Buckley, 2013). Furthermore, as the low temporal resolution of the MSSII acquisition protocol does not permit estimation of blood flow, the present work focused on three models that assume the tissue to be highly perfused (i.e. $F_p = \infty$). Although this is not the case in real tissues, it remains a good approximation when the blood flow is sufficient to equalise the arterial and capillary concentrations (requiring $PS \ll F_p$) (Sourbron and Buckley, 2011), with the simulations confirming the validity of this approximation; the choice of models should also be seen in relation to temporal resolution, which in this case is much longer than the transit time of the tissue blood compartment. Secondly, it should also be emphasised that while PS (or K^{Trans}) is commonly used as a marker of BBB permeability, it is equally influenced by the capillary surface area, which will depend on the anatomy and pathology of micro vessels. Future studies should try to determine vessel density and size so as to include realistic estimates of capillary endothelial surface area in the permeability calculations. Thirdly, the fitting of tracer kinetic models is computationally complicated, with most research groups using their own hand-written software. Consequently, the resulting values are most likely influenced by details of the implementation, for instance the curve fitting algorithm and the number of starting points (Ahearn et al., 2005). Moreover, as discussed previously, DCE-MRI studies are limited by additional sources of error such as uncertainty in $T1_0$, VIF and tissue relaxivity. These factors have been described in detail elsewhere (e.g. Armitage et al., 2011; Cheng, 2008; Roberts, 1997; Schabel and Parker, 2008) and will not be analysed further in this work. Lastly, the small signal enhancements linked to subtle BBB breakdown are likely to be susceptible to influences by secondary processes such as scanner drift; however, as highlighted in section 2.4.3, such issues have received very little attention in the DCE-MRI literature.

4.5. Conclusion

This chapter aimed to determine the tracer kinetic modelling approach most suitable for assessing subtle BBB disruption in the large MSSII patient cohort and to assess its validity using simulations. Using a data-driven approach, the Patlak model was shown to be an appropriate method for measuring low-level K^{Trans}. The simulation study demonstrated that the Patlak model yields accurate parameter estimates and is reasonably robust to the assumptions of high blood flow and negligible back-diffusion. Although the temporal resolution is very low compared to conventional DCE-MRI applications, it is adequate for the measurement of slow, subtle leakage and has the benefit of allowing high spatial resolution and coverage. These results justify the emerging popularity of the Patlak model in the study of disorders involving subtle BBB disruption and of healthy-appearing tissue (Cramer et al., 2014; Montagne et al., 2015; Taheri et al., 2011b). Semi-quantitative parameters were shown to correlate with both

K^{Trans} and v_p, thus reflecting a combination of underlying tissue properties. In contrast, tracer kinetic parameters provided accurate measures of PS and v_p that were near-independent of each other, and should hence be preferred over semi-quantitative parameters. Due to the subtle nature of BBB leakage in cerebral SVD, the tracer kinetic parameters obtained in this work are particularly susceptible to sources of error. Hence, the next chapter aims to investigate whether scanner instability occurs during the DCE-MRI acquisition and what effect it may have on tracer kinetic parameters.

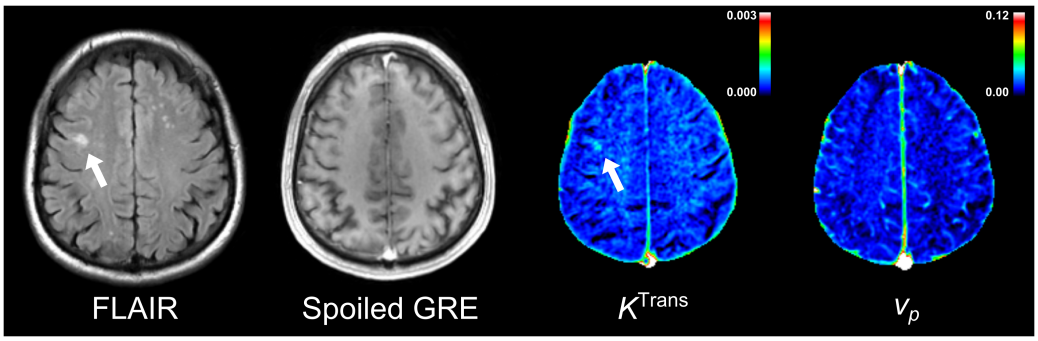

(a) Patient 1

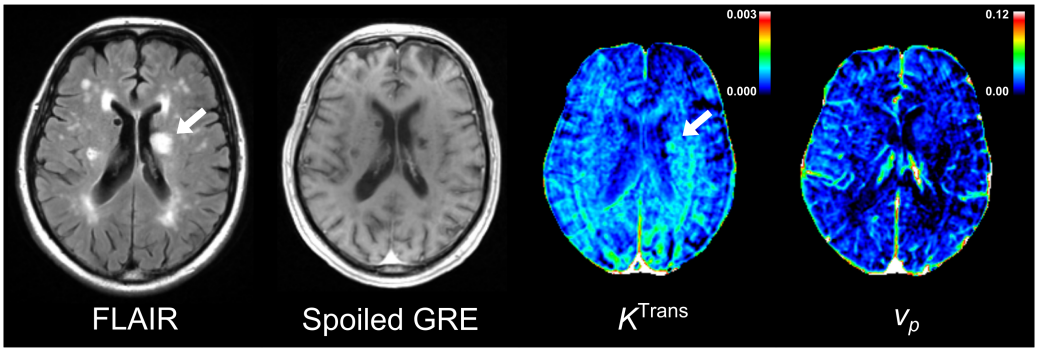

(b) Patient 2

Figure 4.10.: Example of voxel-by-voxel maps of Patlak parameters. Fluid attenuated inversion recovery (FLAIR) images, spoiled GRE images, K^{Trans} (in min^{-1}) maps and v_p maps are shown for two different patients. Both patients exhibit a RSL, which is visible in the FLAIR image (indicated by white arrow). A corresponding area of increased BBB disruption can be seen in the K^{Trans} maps. While the tracer kinetic parameter maps for patient 1 are acceptable, those of patient 2 are strongly influenced by low-level motion artefact, even though it is barely visible in the raw spoiled GRE images. Such artefacts restrict the utility of voxel-wise analysis.

Part III.

Pitfalls in the quantification of subtle blood-brain barrier leakage

Contents

5. Signal drift and its influence on tracer kinetic parameters

The purpose of this chapter is to investigate signal drift unrelated to contrast effects during the dynamic contrast-enhanced magnetic resonance imaging (DCE-MRI) acquisition and to consider its influence on tracer kinetic parameters. Drift measurements were performed in a group of healthy volunteers (section 5.2), and its effect on quantitative parameters was modelled using computer simulations (section 5.3). Most contents of this chapter have been published in Heye et al. (2016a).

5.1. Introduction

The work presented in the previous chapter provided quantitative estimates of blood-brain barrier (BBB) disruption for the Mild Stroke Study II (MSSII) patient cohort. The Patlak model was shown to produce good fits to the data and to yield accurate parameter values despite the simplifying assumptions of the model and the low temporal resolution. The resulting cohort-average K^{Trans} values range from approximately $3 \cdot 10^{-4}$ min^{-1} to $6 \cdot 10^{-4}$ min^{-1} (in normal-appearing white matter (NAWM) and recent stroke lesions (RSL) respectively), which is three to four orders of magnitude smaller than values reported for more conventional applications such as brain tumours (see Table 2.2). As discussed previously, this subtle nature of BBB leakage in cerebral small vessel disease makes the tracer kinetic parameters particularly susceptible to sources of error, which are less likely to be problematic in typical DCE-MRI applications with larger, more rapid contrast uptake. With the DCE-MRI acquisition time being particularly long in the MSSII and the observed signal enhancements ranging from only 2% to 8%, one of the main concerns when analysing the data was the influence of signal drift.

Signal drift measurements are rarely reported in the DCE-MRI literature (see section 2.3.4), an exception being Cramer et al. (2014) and Armitage et al. (2011) who reported a drift of 1% to 3% over 15 min at 3 T but did not investigate its likely effect on the results. The causes of MRI signal drift are not well-understood, but may not only be introduced by instrumental instability but also by subtle biological changes (Lowe and Russell, 1999). This becomes evident when looking at the mathematical expression of signal intensity; for a spoiled gradient echo (GRE) experiment with flip angle α and short echo time TE, the signal intensity is given by the regular

Ernst equation (Haase, 1990):

$$S = \mathrm{M}_0 \frac{(1-\exp(-\mathrm{TR}/\mathrm{T1}))\sin(\alpha)}{1-\cos(\alpha)\exp(-\mathrm{TR}/\mathrm{T1})}, \tag{5.1}$$

where M_0 is the equilibrium magnetisation. Consequently, a change in signal intensity over time can not only be caused by instability of instrumental parameters (e.g. flip angle, $\mathbf{B}_0$ field), but also biological changes that cause variations in T1.

This chapter presents contrast-free 'sham' experiments in healthy volunteers, which were performed in order to assess whether instrumental drift and/or physiological changes occur during the DCE-MRI acquisition as performed in the MSSII. Furthermore, this chapter investigates how these factors may influence tracer kinetic parameters using the simulation framework introduced in the previous chapter.

5.2. Healthy volunteer study

In order to assess whether signal drift occurs during the DCE-MRI acquisition as performed in the MSSII cohort, contrast-free 'sham' experiments were performed in healthy volunteers. The MRI study described in the following sections was approved by the local ACCORD Healthy Volunteer Research Ethics Committee (REC 14/HV/0001). Dr Michael J Thrippleton and Dr Andreas Glatz assisted with the design and testing of the MRI protocol; Prof Joanna M Wardlaw acted as principal investigator and assessed all MRI scans for clinical reporting.

5.2.1. Methods

Participants

Brain MRI scans were performed in a total of 15 participants, which were recruited through University of Edinburgh mailing lists between January 2013 and April 2015. Volunteers with no significant history of neurological or cardiovascular disease were considered as healthy and eligible to enter the study. All participants gave written informed consent.

MRI

MRI scanning was performed in the Brain Research Imaging Centre at the Western General Hospital using the same 1.5 T MRI scanner as the MSSII (Signa HDxt, General Electric, Milwaukee, WI) and the same 8-channel phased-array head coil. In order to assess signal changes

unrelated to the contrast agent, all 15 participants underwent the same DCE-MRI protocol as applied in the MSSII cohort but without administration of contrast agent (20 consecutive three-dimensional (3D) T1-weighted (T1W) spoiled GRE acquisitions with TR/TE $= 8.24/3.1$ ms, $\alpha = 12^\circ$, 24×24 cm field of view (FoV), 256×192 acquisition matrix, 42 × 4 mm slices, temporal resolution of 73 s and a total acquisition time of approximately 24 min).

In order to assess whether biological changes occur during the DCE-MRI acquisition, T1 was measured before and after the dynamic sequence using two different methods. Firstly, T1 was measured using the variable flip angle method as performed in the MSSII cohort (consisting of two additional 3D T1W spoiled GRE acquisitions with flip angles of 2° and 12° respectively). In addition, T1 was measured using the gold standard inversion recovery (IR) method (Larsson et al., 1988) in eight volunteers. For this purpose, two-dimensional (2D) IR spin echo (SE) echo-planar imaging (EPI) acquisitions were performed with multiple inversion delays (TR/TE $= 10000/25.4$ ms, 24×24 cm FoV, 256×192 acquisition matrix, 1 x 4 mm slice, TI $= [100, 340, 580, 820, 1060, 1300, 2000, 3000]$ ms). The 2D acquisitions were set up to match a single slice of the 3D T1W spoiled GRE acquisition, which contained the basal ganglia structures and the lateral ventricles.

Image processing and analysis

All images were converted from DICOM to NIfTI format. Moreover, all 3D images were aligned to the first 12° T1W spoiled GRE image with rigid-body transformations using FSL-FLIRT (Jenkinson et al., 2002); 2D rigid-body registration was used to align the IR SE EPI acquisitions to the corresponding slice in the 3D T1W spoiled GRE image. Multiple small regions of interest (ROIS) were manually placed in NAWM and deep/subcortical grey matter (DGM), using a simplified version of a standard template (Wardlaw et al., 2008). An example of ROI placement is shown in Figure 5.1. For each tissue, median signal intensities were calculated over all ROIs and converted to signal enhancement curves as described previously (see section 3.3.1). Signal drift was calculated as the change in signal intensity per minute acquisition time and is given as a percentage of the time-averaged signal.

T1 values were calculated for two different time points (before and after DCE-MRI acquisition) and the two different methods (variable flip angle and IR with variable inversion delay). Equation 3.1 was used to calculate T1 from the pair of 2° and 12° 3D T1W spoiled GRE acquisitions. As regards the IR method, T1 was calculated by fitting the following equation to the measured signal intensities S:

$$S = |A + B\exp(-\mathrm{TI}/\mathrm{T1})|. \tag{5.2}$$

All values are reported as cohort mean ± standard deviation.

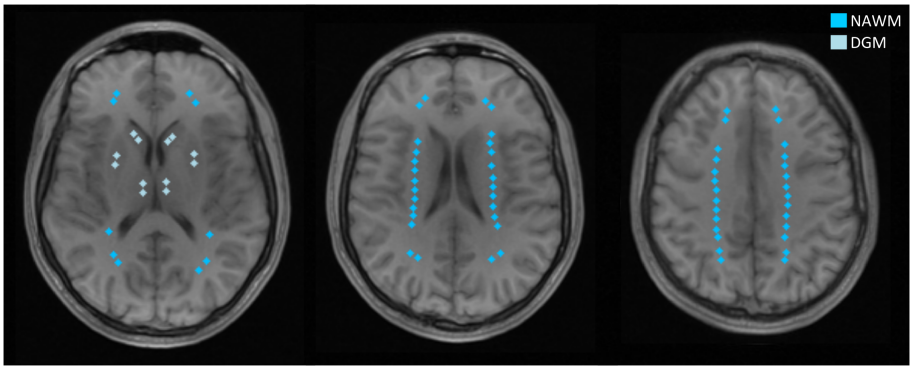

Figure 5.1.: Example of ROI placement in the healthy volunteer MRI data. Shown are three different slices of the first 12° 3D T1W spoiled GRE image. Several small rectangular ROIs were placed in DGM and NAWM.

5.2.2. Results

'Sham' DCE-MRI data was obtained in 15 healthy volunteers with a mean age of 31.4 ± 7.4 years. Figure 5.2 shows the corresponding average signal enhancement curves in NAWM and DGM. Although no contrast agent was given, the data show an approximately linear increase in signal intensity of 0.06 ± 0.03 %/min in NAWM and 0.10 ± 0.06 %/min in DGM.

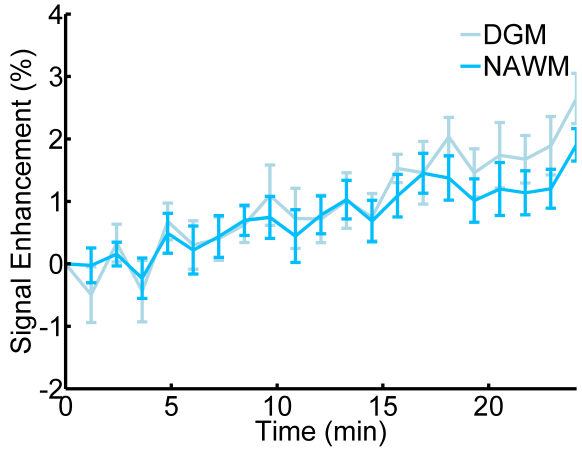

Figure 5.2.: Contrast-free DCE-MRI measurements in healthy volunteers. Shown are the cohort-average signal enhancement curves ($n = 15$) NAWM and DGM, showing a drift in signal intensity; error bars indicate the mean ± standard error. Reprinted from Heye et al. (2016a).

T1 measurements using the variable flip angle method were performed in $n = 14$ volunteers; the resulting T1 values are given in Table 5.1. As in the MSSII cohort, these values were overestimated in comparison to literature values measured with the IR method. After having performed MRI scanning in seven participants, it became evident that there is a decrease in T1 over the period of the DCE-MRI acquisition in both NAWM ($\Delta T1 = -0.9 \pm 4.4$ %) and DGM ($\Delta T1 = -1.6 \pm 4.6$ %). However, it was unclear whether these differences reflect true biological changes or are due to compromised measurement accuracy of the variable flip angle method. Consequently, T1 measurements using the gold standard IR method were added to the MRI protocol for the remaining eight volunteers; IR acquisitions of one participant were subsequently discarded due to significant movement artefacts. The resulting T1 values were in line with previous literature (Vymazal et al., 1999) and showed a similar decrease in T1 (see Table 5.1). However, a paired-sample t-test indicated that the measured change in T1 was not statistically significant (using either method).

Figure 5.3 investigates whether this non-significant change in T1 could cause the observed signal drift. It shows the estimated change in signal intensity as a function of change in T1, which was calculated using equation 5.1. Baseline T1 values were chosen as 680 ms in NAWM and 903 ms in DGM, corresponding to the cohort-average IR SE EPI measurements. According to these investigations, the measured decrease in T1 (-0.9% in NAWM and -1.2% in DGM) accounts for approximately 38% of the measured signal drift (0.06 %/min in NAWM and 0.10 %/min in DGM). The remaining signal drift is likely to be caused by instrumental instability (e.g. $\mathbf{B}_0$ and flip angle instability); patient motion may also contribute to signal drift.

Table 5.1.: T1 measurements in healthy volunteers. T1 values were obtained at two different time points: before ($T1_{pre}$) and after ($T1_{post}$) the DCE-MRI acquisition. Moreover, two different methods were used for the measurement of T1: the variable flip angle method based on a pair of 3D T1W spoiled GRE acquisitions with different flip angles and the IR method based on multiple 2D IR SE EPI acquisitions with variable TI. All values are given as cohort mean $\pm$ standard deviation; paired-sample t-tests indicate that the measured change in T1 is not statistically significant.

Tissue type	Measurement method	$T1_{pre}$ (ms)	$T1_{post}$ (ms)	$\Delta T1$ (%)	p
NAWM	variable flip angle	794 ± 29	787 ± 39	-0.9 ± 4.4	0.20
	IR with variable TI	680 ± 25	674 ± 19	-0.9 ± 2.1	0.19
DGM	variable flip angle	1209 ± 54	1188 ± 46	-1.6 ± 4.6	0.46
	IR with variable TI	903 ± 35	892 ± 32	-1.2 ± 1.1	0.27

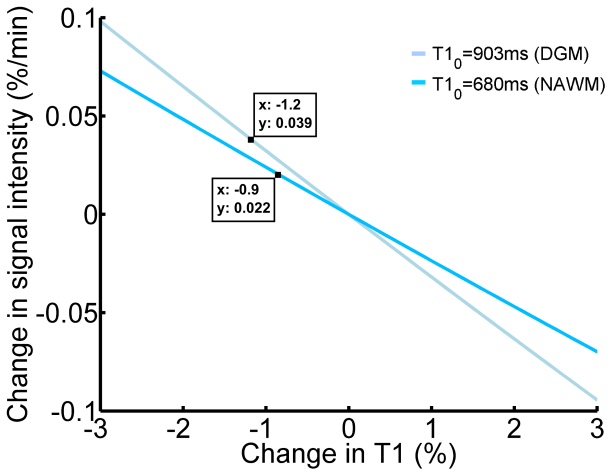

Figure 5.3.: Relationship between change in T1 and change in signal intensity. Change in signal intensity as a function of change in T1, estimated using the regular Ernst equation (equation 5.1). The relationship is shown for two different baseline T1 values, corresponding to the cohort-average IR SE EPI measurements in NAWM and DGM. Boxes indicate the T1 change measured in the healthy volunteer cohort and the corresponding change in signal intensity.

5.3. Computer simulations

The effect of scanner drift on tracer kinetic parameters was investigated using computer simulations, which are based on the simulation framework introduced in the previous chapter.

5.3.1. Methods

A detailed description of the simulation methods has been given in section 4.3.1. In short, simulated tissue concentration curves were generated by convolving a synthetic high temporal resolution VIF with the impulse response function of the two-compartment exchange model, using a range of typical K^{Trans}, v_p and F_p values for normal-appearing tissues. In addition to random noise, a signal drift of 0.08 %/min (similar to that observed in the healthy volunteers) was added to both the tissue curve and the vascular input function (VIF). The VIF and tissue concentration curves were then down-sampled to the experimental temporal resolution ($\Delta t =$ 73 s) and these were fitted to the Patlak model. In order to investigate whether the effect of drift on the tracer kinetic parameters is T1-dependent, the simulations were repeated for several T1 values representing typical values measured in the MSSII cohort.

5.3.2. Results

Figure 5.4 compares the fitted Patlak parameters with the 'true' parameters when adding a signal drift of 0.08 %/min. The plots show that the signal drift leads to systematic overestimation of K^{Trans} and underestimation of v_p with respect to expected values. However, K^{Trans} and v_p remained approximately linear functions of the specified values, largely independent of plasma flow and of one another.

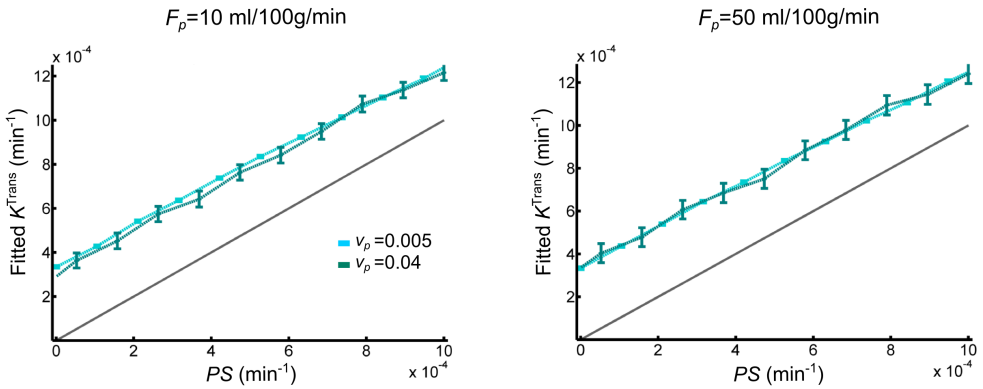

(a) Relationship between permeability surface area product PS and fitted Patlak K^{Trans}

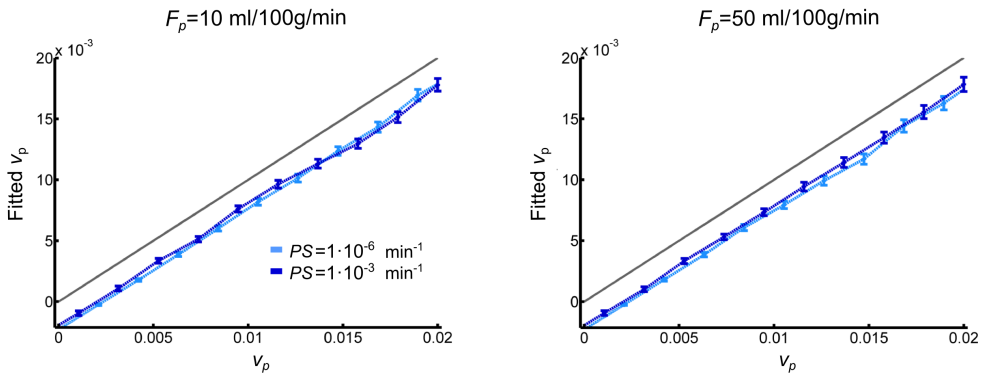

(b) Relationship between blood plasma volume v_p and fitted Patlak v_p

Figure 5.4.: Simulated accuracy of Patlak parameters including a 0.08 %/min signal drift. Relationship of (a) permeability surface area product PS and (b) blood plasma volume v_p values, with corresponding fitted Patlak parameters. Results are shown for two different F_p, PS and v_p values. For all simulations, v_e was set to 0.2 and a signal drift of 0.08 %/min was added to the curves before model fitting. Error bars indicate the mean $\pm$ 1.96 standard deviations; the grey line represents the identity line. The first three post-contrast data points were omitted for model fitting. Reprinted from Heye et al. (2016a).

Figure 5.5 shows the magnitude of the systematic error introduced by signal drift for different T1 values, which correspond to the cohort-average values measured in the MSSII cohort for NAWM, white matter hyperintensities (WMH), DGM and RSL. Across these tissue types, the maximum error ranged from approximately $2.2 \cdot 10^{-4}$ min^{-1} to $3.2 \cdot 10^{-4}$ min^{-1} for K^{Trans} and $-2.4 \cdot 10^{-3}$ to $-1.6 \cdot 10^{-3}$ for v_p, with bigger errors occurring for smaller T1 values.

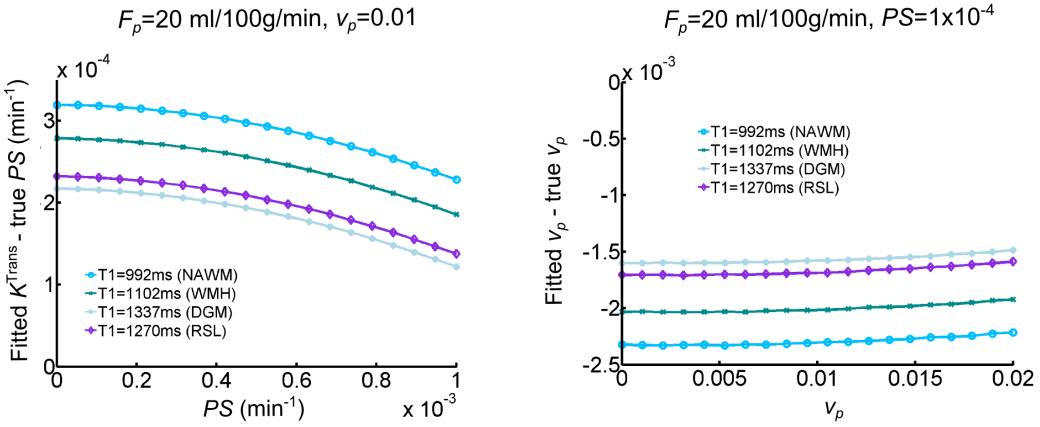

(a) Error in K^{Trans}

(b) Error in v_p

Figure 5.5.: T1-dependency of the systematic error introduced by signal drift. Plots showing the error between the fitted Patlak parameters and the corresponding 'true' values of (a) permeability surface area product PS and (b) blood plasma volume v_p. Results are shown for different T1 values, which correspond to the cohort-average values measured in the MSSII cohort for NAWM, WMH, DGM and RSL. For all simulations, v_e was set to 0.2 and a signal drift of 0.08 %/min was added to the curves before model fitting. Error bars are omitted for clarity.

5.4. Discussion

Contrast-free DCE-MRI acquisitions (otherwise identical to the ones performed in the MSSII cohort) were carried out in a group of young, healthy volunteers. Although the subjects did not receive contrast, there was a linear signal increase of approximately 0.08 %/min. These measurements are comparable to the ones reported by Cramer et al. (2014) for DCE-MRI at 3 T, who found a signal drift of 1% to 3% over 15 min. The drift observed in this study was also within the range of values obtained in a multi-centre survey of functional MRI quality assurance parameters, which concluded that 'stable scanners generally average around 1.0% [signal drift over 6.7 min] or less' (Friedman and Glover, 2006). The influence of signal drift in functional MRI is much less severe than here, since it typically has a lower frequency than

the task-related signal change, is suppressed using a high-pass filter and the scans are shorter. In DCE-MRI on the other hand, it is harder to distinguish between drift and contrast enhancement as both occur on similar time scales in the tissues considered here.

Signal drift is rarely reported in the DCE-MRI literature and the causes of signal drift unrelated to contrast agent are not well understood. In order to investigate whether signal drift may be influenced by subtle biological changes as suggested by Lowe and Russell (1999), T1 was measured before and after the DCE-MRI acquisition. Using two different methods (variable flip angle method as performed in the MSSII cohort and the gold standard IR method), a non-significant decrease in T1 was found over the acquisition time of approximately 24 min. According to the present investigations, this small T1 change may explain approximately 38% of the observed signal drift. This confirms that biological changes may be a contributing factor to signal drift, which is also consistent with a previous report of tissue-dependent drift (Armitage et al., 2011). However, there are multiple other possible sources of drift (e.g. flip angle instability, $\mathbf{B}_0$ instability, motion), whose contributions remain unknown. The present study is limited by its small sample size, which makes it difficult to draw clear conclusions about the significance of changes in T1.

In typical DCE-MRI applications with larger, more rapid signal enhancements over shorter acquisition times, the observed level of signal instability is unlikely to be problematic. Even in studies of subtle BBB leakage, the effects of scanner drift have previously been considered negligible (Cramer et al., 2014). However, the computer simulations presented in this chapter showed that the drift is predicted to cause a substantial overestimation of K^{Trans} and underestimation of v_p in the low-permeability regime. These findings are consistent with recently published investigations by Barnes et al. (2015), who added signal drifts between -10% and 10% to their computer simulations. The systematic error introduced by signal drift could account for some of the apparent leakage reported in the literature for normal-appearing tissues. Furthermore, the magnitude of drift (and hence the bias it introduces) is likely to differ between studies, which may partly account for the wide range of K^{Trans} values reported in the literature for normal-appearing brain tissues. The error introduced by signal drift is also $\mathrm{T1}_0$ dependent, which further complicates the interpretation of low-level tracer kinetic parameters because it may introduce apparent differences between tissue types. For instance, this T1 dependency may partly account for the finding in the MSSII cohort of higher v_p in WMH compared to NAWM. As a result, attempts to quantify low levels of permeability should be interpreted with caution, unless information regarding scanner drift and its likely effect on the values are available.

Barnes et al. (2015) state that the systematic error introduced by signal drift can essentially be eliminated by correcting for a previously measured level of drift. However, in practice, corrections for signal drift are limited by several factors. Firstly, a correction based on drift

measurements in a single phantom may not be sufficient if the magnitude of drift is tissue-dependent. Secondly, phantoms (particularly simple water or oil based phantoms as used by Starr et al., 2003) are often subject to temperature changes at long acquisition times, which cause changes in T1 and, hence, may lead to unreliable drift measurements. Thirdly, the magnitude of drift is likely to vary between subjects (and tissues) and may depend on factors such as age or overall health status. Consequently, drift measurements obtained in young healthy volunteers may not be adequate for the correction of DCE-MRI data obtained in elderly, diseased patients (as for instance performed by Topakian et al., 2010). Finally, the drift itself is small with regard to the often compromised signal-to-noise ratio in DCE-MRI acquisitions, which raises the question of how reliable drift estimates are (Armitage et al., 2011). It is also worth noting that DCE-MRI methods consisting of repeated T1 measurements (e.g. Taheri et al., 2011b) should largely self-compensate for signal drifts of instrumental origin and, depending on the pulse sequence used, changes in the radio frequency field strength but not for changes in $T1_0$.

5.5. Conclusion

This chapter aimed to investigate signal drift unrelated to contrast effects and its influence on tracer kinetic parameters. Drift measurements were performed in a group of healthy volunteers, showing linear signal increase of approximately 0.08 %/min. Computer simulations suggested that this drift introduces a systematic error when estimating low-level tracer kinetic parameters. Despite the confounding influence of drift, the simulations indicate that K^{Trans} and v_p estimates remain approximately linear independent functions of the extravasation rate and plasma volume respectively. They provide a valuable if relative indication of BBB integrity and blood plasma volume for applications in well-designed studies with appropriate control groups and statistical correction for confounds; such quantities remain easier to interpret than semi-quantitative measurements. Nevertheless, it is important to optimise study MRI protocols for measurement of low-level permeability and interpret quantitative results with caution.

6. Tracer kinetic modelling in an external patient cohort – lessons for inter-study comparability and study design

The work presented in this chapter is the result of a collaboration with the Diagnostic Imaging Unit at the Università Campus Bio-Medico in Rome, Italy, which I visited within the scope of a 'Postdoctoral and Early Career Researcher Exchange' award from the Scottish Funding Council organised by the SINAPSE (Scottish Imaging Network – A Platform for Scientific Excellence) Collaboration. During this visit, the local researchers kindly shared a dynamic contrast-enhanced magnetic resonance imaging (DCE-MRI) dataset of patients with common, non-specific neurological complaints with me; this chapter aims to analyse these data and to compare the results to the findings in the Mild Stroke Study II (MSSII) cohort.

6.1. Introduction

The systematic literature review presented in chapter 2 has highlighted the large variations in DCE-MRI procedures and data analysis methods, resulting in widely varying estimates of quantitative parameters. Some of this variability is inevitably due to the heterogeneity of studied pathologies and study objectives. However, even studies with similar populations and target tissues have reported significantly different parameter estimates (see Table A.3). One reason for this inconsistency is the limited comparability between estimates obtained using different tracer kinetic models; this has been demonstrated in the MSSII cohort, where the three tracer kinetic models resulted in significantly different K^{Trans} and v_p values despite being based on the same acquisition protocol and participants (see chapter 4). While same-model comparisons are more likely to be valid, there is also a wide range of other factors that influence tracer kinetic parameters. As discussed previously, two of the most influential aspects are accurate measurements of patient-individual T1 and vascular input functions (VIF) (Cheng, 2008; Just et al., 2011; Parker et al., 1996; Roberts, 1997; Schabel and Parker, 2008). Moreover, details of the acquisition protocol (including overall acquisition time, temporal and spatial resolution) impose limitations on data analysis methods and influence tracer kinetic parameters (Cramer et al., 2014; Fluckiger et al., 2012; Heisen et al., 2010; Kershaw and Cheng, 2010). Further factors that can influence DCE-MRI measurements are the scanner field strength (Pineda et al., 2015), contrast agent type and dose (Chwang et al., 2014) and region of interest (ROI) selection (Braunagel et al., 2015).

Compared with conventional applications, studies of tissues with largely intact blood-brain barrier (BBB) are particularly sensitive to the above-mentioned sources of variability. The availability of an external data set provided the opportunity to investigate the inter-study comparability of DCE-MRI methods for the measurement of subtle BBB disruption. The work presented in this chapter focuses on the secondary analysis of DCE-MRI data that targets the same tissue types as the MSSII data, but was acquired using a very different MRI protocol. The purpose of this work was to identify the tracer kinetic modelling approach most suitable for these data and to compare the results to the findings in the MSSII cohort.

6.2. Study description

This section describes the external study data, courtesy of the research team at the Università Campus Bio-Medico in Rome, Italy. Study design, participant recruitment and data collection were performed in the Diagnostic Imaging Unit, led by Prof Bruno Beomonte Zobel. The research team consisted of Dr Yuri Errante, Dr Carlo A Mallio, Dr Laura Scarciolla, Dr Luciano Carideo and Dr Carlo C Quattrocchi, who kindly permitted me to perform a secondary analysis of their DCE-MRI data and to include it in this thesis. Throughout this work, the study will be referred to as the CBMS (Campus Bio-Medico Study).

6.2.1. Participants

The data made available included 31 adult subjects who underwent MRI scanning in the Diagnostic Imaging Unit at the Campus Bio-Medico in Rome, Italy. All subjects had presented to their general practitioner with non-specific neurological symptoms such as mild headaches or subjective memory complaints, but showed no severe or focal neurological deficits. In order to exclude an underlying neurological disorder, they were referred for a head MRI examination. Patients that showed abnormalities of non-vascular origin (e.g. tumours, $n = 2$) were excluded from this analysis. Furthermore, four participants were excluded due to incomplete data ($n = 3$) or 'tissueing' of contrast agent ($n = 1$). The remaining 25 participants (10 men and 15 women, average age of 64.7 ± 15.6 years) displayed a wide range of white matter hyperintensity (WMH) burden, with white matter disease being mild in 15/25 patients and moderate to severe in 10/25 patients.

6.2.2. MRI procedures

MRI scanning was performed on a 1.5 T scanner (Magnetom Avanto, Siemens Healthcare, Erlangen, Germany) in the Diagnostic Imaging Unit at the Università Campus Bio-Medico

in Rome. DCE-MRI was performed using the time-resolved imaging with stochastic trajectories (TWIST) technique. TWIST consists of three-dimensional T1-weighted gradient echo acquisitions with partial k-space undersampling, i.e. the center of k-space (region A) is sampled more frequently than the periphery of k-space (region B) in order to reduce the acquisition time (Lim et al., 2008; Vogt et al., 2007). This method has previously been used in DCE-MRI of breast cancer (Fusco et al., 2012), astrocytoma (Jia et al., 2013) and uterine fibroids (Davenport et al., 2013). The degree of TWIST undersampling is described by two parameters: $\%A$ and $\%B$. $\%A$ determines the proportion of the central region A; for this study $\%A$ was chosen as 0.3, i.e. 30% of k-space is fully sampled each time. $\%B$ specifies the relative sampling density of region B and was chosen as 0.25; thus, 25% of k-space points in region B are sampled each time (i.e. four acquisitions are needed to completely fill region B of the k-space). Other acquisition parameters were the following: flip angle $\alpha = 12^\circ$, TR/TE $= 4.2/1.6$ ms; resulting in-plane matrix size of 128×128 with a pixel size of 2.03×2.03 mm; 64, 72 or 80 slices with a thickness of 2 mm were acquired to achieve whole-brain coverage. DCE-MRI consisted of 30 consecutive acquisitions; depending on the number of slices, the temporal resolution was 6.3 s, 7.0 s or 8.2 s respectively ($n = 18/6/1$), leading to an overall acquisition time of 3.15 min, 3.50 min or 4.10 min. It should be noted that this is approximately the temporal range that was discarded in the MSSII data. 0.1 mmol/kg of contrast agent (gadodiamide, Gd-DTPA-BMA, Omniscan, General Electric Healthcare, Amersham, UK) were administered at the beginning of the second acquisition as an intravenous bolus at a constant flow rate of 3 ml/s, followed by 20 ml saline flush. Three additional TWIST acquisitions were obtained prior to contrast administration with flip angles of 5° and 15° respectively for calculation of $T1_0$. The imaging protocol also included conventional diagnostic sequences; these varied between patients depending on their symptoms at presentation but always included an axial fluid attenuated inversion recovery (FLAIR) acquisition with TR/TE/TI $= 11460/102/2360$ ms, 320×280 acquisition matrix, pixel size 0.94×0.94 mm, 37 slices with slice thickness of 3 mm and a 0.9 mm slice gap.

6.3. Methods

This section describes the secondary analysis of the CBMS data described above. All image processing and analyses described in this section were performed by myself.

6.3.1. Image processing

All MR images were converted from DICOM to NIfTI format. Moreover, the FLAIR image and all TWIST images were aligned to the first TWIST image with rigid-body transformations using FSL-FLIRT (Jenkinson et al., 2002). As in the MSSII cohort (see section 3.3), obtaining

an arterial input function (AIF) from the internal carotid artery proved to be difficult due to partial volume and inflow effects. Instead, a VIF was extracted from a single voxel in the superior sagittal sinus (SSS) that provided the highest peak signal enhancement and smooth variation during the DCE-MRI time course (assessed visually using the 'Timeseries' view in FSLView). Multiple small ROIs were manually placed in WMH using the FLAIR image; normal-appearing white matter (NAWM) and deep/subcortical grey matter (DGM) ROIs were placed in the first 12° TWIST image using the same template as in chapter 5, but avoiding WMH visible in the FLAIR image. An example of ROI placement is shown in Figure 6.1; this approach was chosen because tissue segmentation using the MCMxxxVI method was not feasible in the CBMS data, which did not include all the necessary structural images.

For each time point, the median signal intensity was calculated over all ROIs for the same tissue and converted to signal enhancement as described previously (see section 3.3.1). $T1_0$ values were calculated based on the 5° and 15° TWIST acquisitions using equation 3.1. The contrast agent concentration was then estimated using equation 3.2 with $r_1/r_2 = 4.6/6.9$ $s^{-1}mM^{-1}$ (Rohrer et al., 2005). Negative concentration values were set to zero.

6.3.2. Tracer kinetic modelling

Quantitative analysis of the measured contrast agent concentration curves was approached in the same manner as described in chapter 4, starting with the identification of suitable tracer kinetic models. Firstly, the assumptions made by some models do not apply to brain tissues with largely intact BBB. Furthermore, although the temporal resolution of 6.3 s to 8.3 s is significantly higher than in the MSSII cohort, it is not sufficient to reliably estimate flow (de Bazelaire et al., 2011; Essig et al., 2013). Blood flow measurements rely on an accurately and rapidly sampled AIF; in addition to suffering from a low temporal resolution, the VIF could only be extracted from the SSS and, thus, is delayed and dispersed relative to the arterial input. These two constraints are similar to the situation in the MSSII cohort, and limit the range of suitable models to the same set of three nested models (steady state, Patlak and modified Tofts models). All three models were fitted to the measured contrast agent concentration curves as described in section 4.2. As before, the competing models were ranked according to the Akaike information criterion (AIC), a data-driven approach that accounts for the trade-off between goodness-of-fit and model complexity.

6.3.3. Computer simulations

As discussed previously, a good model fit does not guarantee that the assumptions made by the model are valid with respect to the specific acquisition protocol and that the fitted parameters

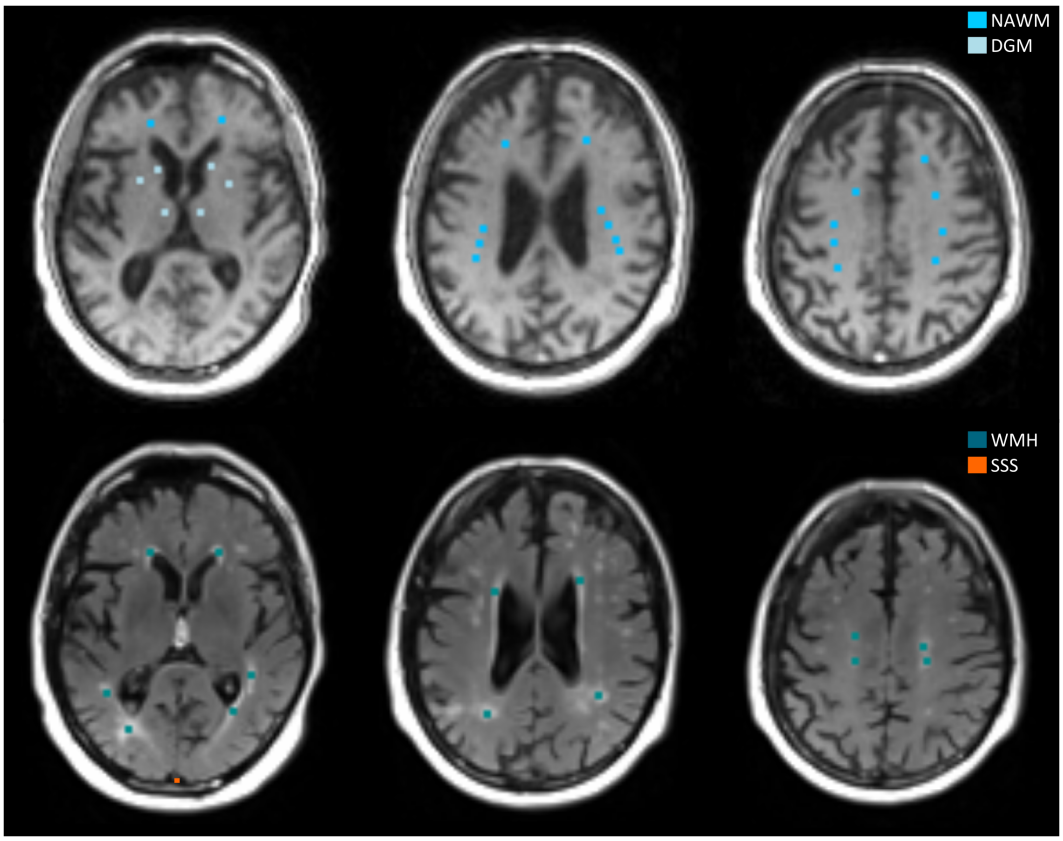

Figure 6.1.: Example of ROI placement in the CBMS cohort. Images show three different slices of the first 12° TWIST image (top row) and the corresponding slices of the FLAIR image (bottom row). Several small rectangular ROIs were placed in NAWM, DGM and WMH. The VIF was extracted from a single voxel in the SSS.

are accurate. Consequently, numerical simulations were performed in order to theoretically investigate the validity of potentially suitable models (as identified through the data-driven model selection described above). All simulations were based on the framework described in section 4.3 and implemented in MATLAB (MathWorks, Natick, MA, USA). First, a high-resolution ($\Delta t = 0.1$ s) VIF was generated by fitting the generic function introduced by Parker et al. (2006) to the population-average VIF measured in the CBMS DCE-MRI data with an overall acquisition time of 3.25 min. As before, the whole-blood VIF was converted to blood plasma concentration using the formula $c_p = c_b/(1 - \mathrm{Hct})$, with $\mathrm{Hct} = 0.45$. Simulated tissue concentration curves were generated by convolving this VIF with the impulse response function of the two-compartment exchange model (2CXM) (Sourbron and Buckley, 2013). PS and v_p values were chosen to represent the range of values obtained in normal-appearing tissue and WMH; v_e was chosen to be 0.2 (Syková and Nicholson, 2008) and F_p values between 10 ml/100g/min and 50 ml/100g/min were selected to represent typical values for NAWM, WMH and DGM (Brickman et al., 2009). The VIF and tissue concentration curves were then

down-sampled to the experimental temporal resolution ($\Delta t = 6.5$ s). The models were fitted to the down-sampled curves by non-linear minimisation of the sum of squared residuals; finally, the fitted parameters were compared with the 'true' parameters used to generate the synthetic data. In order to investigate the influence of signal drift, the simulations were repeated after adding a signal drift of 0.08 %/min to both the tissue curve and the VIF.

6.4. Results

6.4.1. Tissue characteristics

Table 6.1 presents the cohort average $T1_0$ values, which are broadly similar to the $T1_0$ values obtained in the MSSII cohort. An example of DCE-MRI tracer dynamics by tissue type is shown in Figure 6.2. Signal enhancements in NAWM, WMH and DGM ranged from approximately 3% to 20%, with DGM showing the highest enhancement levels, followed by WMH and NAWM. The tissue curves found in the CBMS cohort resembled the dynamics measured in the MSSII cohort (see Figure 3.10), with contrast agent concentrations in NAWM, WMH and DGM ranging between 0.01 mM and 0.03 mM. In contrast, the peak concentration of the VIF was significantly lower in the CBMS cohort compared to the MSSII cohort. This difference may be due to partial volume effects as a result of the larger voxel size; this is also consistent with the large spread seen in blood $T1_0$ values.

Table 6.1.: $T1_0$ values by tissue type (CBMS cohort). $T1_0$ values obtained in the MSSII cohort are shown for comparison; all values are given as cohort mean $\pm$ standard deviation.

Tissue type	$T1_0$ (s)	
	CBMS cohort	MSSII cohort
SSS	1.67 ± 0.77	1.72 ± 0.25
NAWM	0.96 ± 0.08	0.99 ± 0.13
WMH	1.28 ± 0.28	1.10 ± 0.15
DGM	1.57 ± 0.19	1.27 ± 0.26

6.4.2. Model comparison

An example of tracer kinetic model fitting in a single patient is shown in Figure 6.3. Generally, the three different models provided very similar fits in NAWM and DGM, indicating that the one-parameter steady state model sufficiently describes the data. On the other hand, contrast agent concentrations in WMH stayed slightly higher during the later stage of the acquisition,

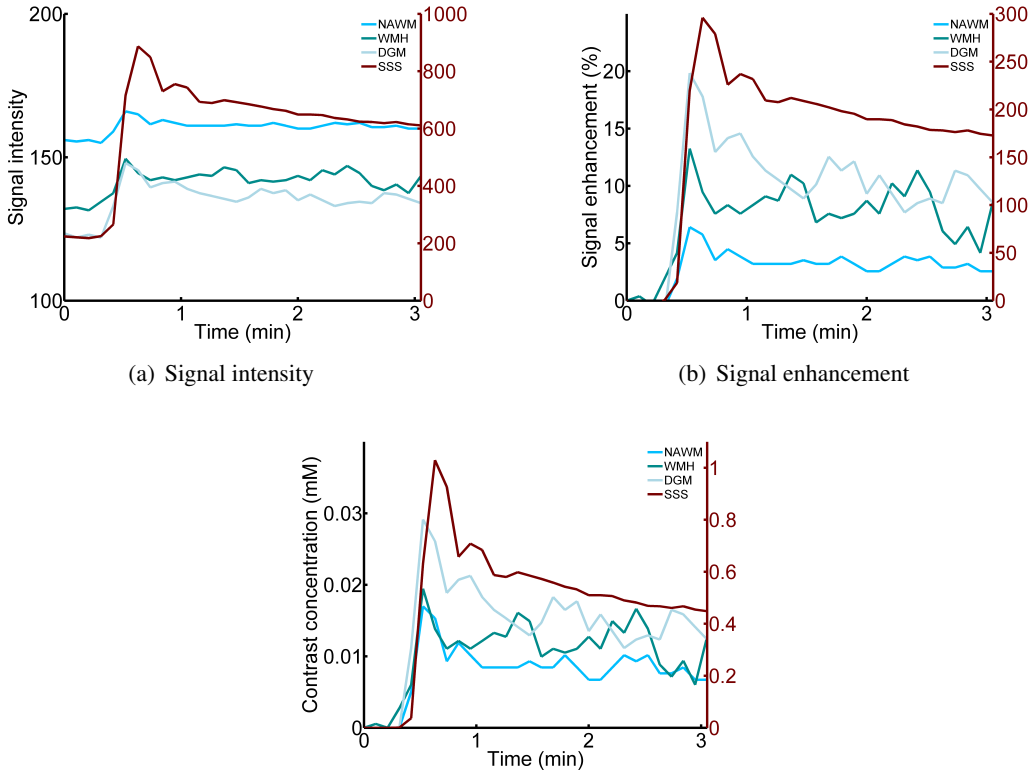

(a) Signal intensity

(b) Signal enhancement

(c) Contrast concentration

Figure 6.2.: Example of DCE-MRI tracer dynamics by tissue type (CBMS cohort). Graphs show the (a) signal intensity, (b) signal enhancement and (c) contrast concentration curves over time for a single patient that is representative of the cohort. Values were obtained from the median signal of all voxels in each tissue type. Y-axis scales for the tissue and SSS curves are shown on the left and right respectively.

which could not be captured by the steady state model. This finding suggests that there is non-negligible BBB leakage in WMH and, thus, a more complex model may be required to accurately fit the data. These observations were confirmed by analysis of the Akaike weights (see Figure 6.4). In NAWM and DGM, the steady state model was chosen as the most appropriate model in the vast majority of patients. However, model choice was less clear-cut in WMH, where the steady state model was sufficient to describe the measured tracer kinetics in 45% of patients, but the Patlak model was preferred in 36% of patients. In all tissues, the modified Tofts model was in general the least suitable choice of the three models; thus, it was disregarded in all subsequent analyses.

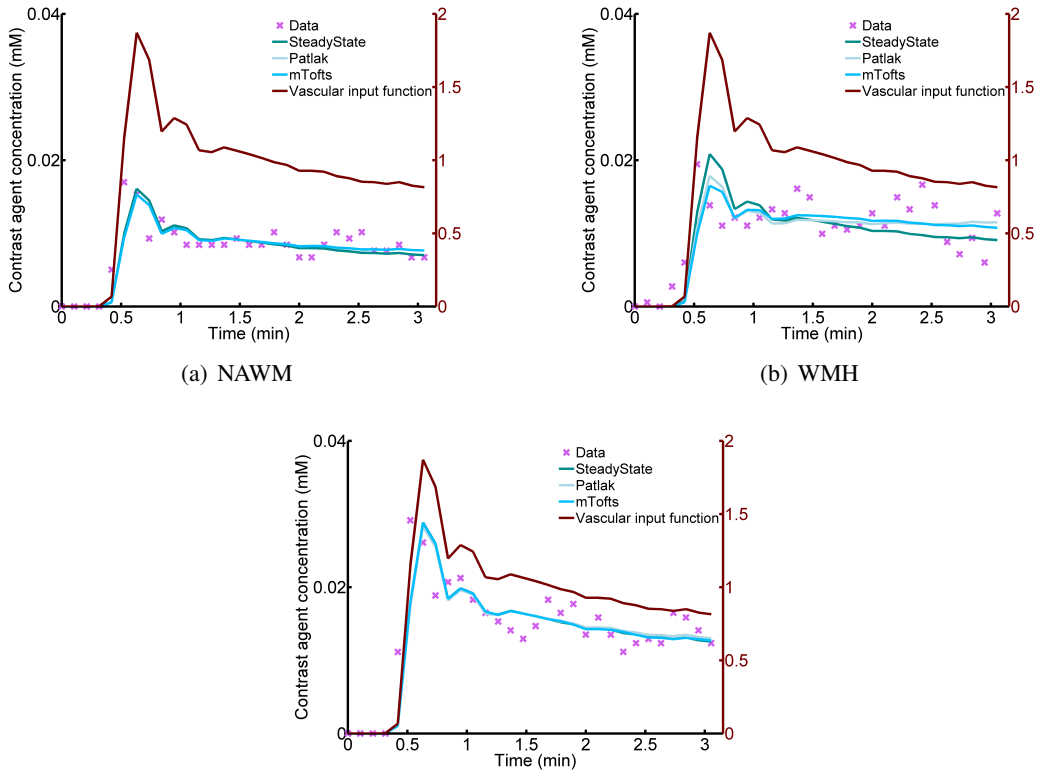

(a) NAWM

(b) WMH

(c) DGM

Figure 6.3.: Example of tracer kinetic model fitting (CBMS cohort). The graphs show the measured contrast agent concentrations and the corresponding model fits in (a) NAWM, (b) WMH and (c) DGM of a single patient.

6.4.3. Tracer kinetic parameters

A comparison of tracer kinetic parameters obtained with the Patlak and steady state models is provided in Table 6.2. The v_p estimates obtained using the Patlak model were significantly lower compared to the steady state model ($p < 0.001$ using Wilcoxon's signed rank test). In comparison with the MSSII cohort, the v_p values obtained in the CBMS cohort are of the same order of magnitude but approximately twice as high. The Patlak K^{Trans} estimates in WMH are approximately three times higher in the CBMS cohort than in the MSSII cohort. Since the data-driven model selection did not reveal an obviously dominant model in WMH, the validity of both the steady state and Patlak models were investigated using computer simulations before deciding on the best approach for obtaining quantitative parameters.

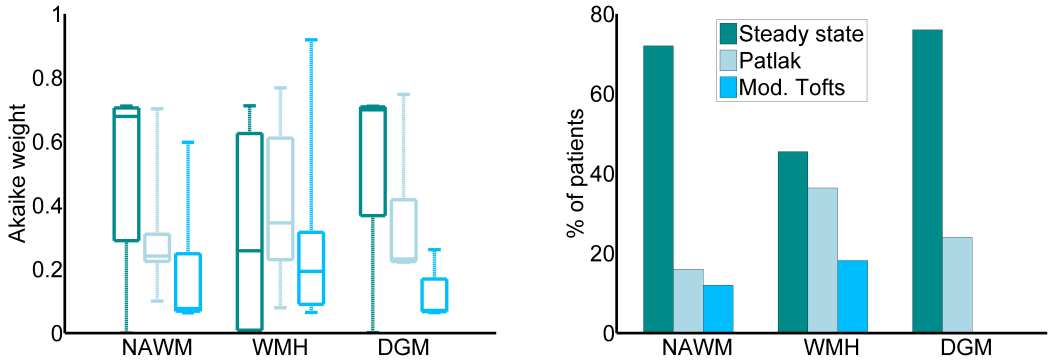

(a) Akaike weights for each model and tissue type

(b) Optimum model according to Akaike weights

Figure 6.4.: Model selection according to Akaike weights (CBMS cohort). (a) Comparison of Akaike weights between the steady state, Patlak and modified Tofts models in all tissue types (the results for the three models are colour-coded as shown in (b)) (b) bar graph showing the percentage of patients in which a particular model was selected as the optimum model according to Akaike weights.

Table 6.2.: Tracer kinetic parameters by tissue type (CBMS cohort). Values are shown as cohort median and interquartile range (data not generally normally distributed) for each tissue type. Values obtained in the MSSII cohort are shown for comparison.

	NAWM	WMH	DGM
Steady state model			
v_p ($\cdot\ 10^{-2}$)	1.26 [0.95, 1.97]	1.27 [0.95, 2.38]	2.12 [1.50, 2.98]
Patlak model			
v_p ($\cdot\ 10^{-2}$)	1.20 [0.90, 1.72]	1.12 [0.75, 1.92]	1.96 [1.37, 2.98]
K^{Trans} ($\cdot\ 10^{-4}$ min^{-1})	2.45 [0.02, 4.80]	12.09 [4.42, 18.40]	2.08 [0.00, 9.70]
MSSII cohort (Patlak model)			
v_p ($\cdot\ 10^{-2}$)	0.57 [0.32, 0.80]	0.72 [0.40, 1.07]	1.20 [0.94, 1.43]
K^{Trans} ($\cdot\ 10^{-4}$ min^{-1})	2.75 [1.85, 4.12]	3.91 [2.80, 4.94]	3.85 [2.83, 4.68]

6.4.4. Model validity

Figure 6.5 shows the synthetic VIF that was used in all computer simulations; the parameters of the fitted generic function introduced by Parker et al. (2006) were as follows: $A_1 = 0.62$ mmol·min, $A_2 = 0.12$ mmol·min, $\sigma_1 = 0.33$ min, $\sigma_2 = 0.10$ min, $T_1 = 0.95$ min, $T_2 = 0.68$ min, $\alpha = 0.78$ mmol, $\beta = 0.13$ min^{-1}, $s = 7.45$ min^{-1}, $\tau = 1.35$ min.

The results of simulations performed to determine the validity of the steady state model are shown in Figure 6.6, which compares the fitted v_p (steady state model) with the 'true' v_p used to generate synthetic signal-time curves (2CXM model). For low PS and high F_p, v_p was

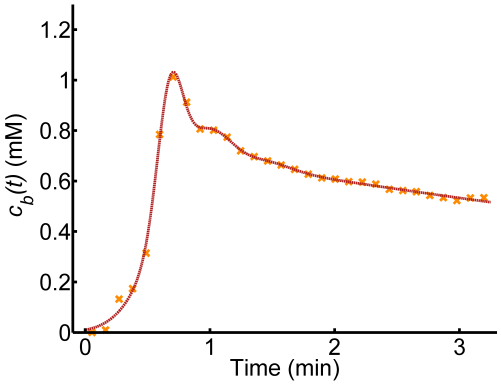

Figure 6.5.: High temporal resolution VIF generated for the simulation study (CBMS). The VIF was generated by the generic function introduced by Parker et al. (2006) to the population-average VIF measured in the CBMS DCE-MRI data. Shown is the whole-blood VIF, which was converted to blood plasma concentration using the formula $c_p = c_b/(1-\mathrm{Hct})$, with $\mathrm{Hct} = 0.45$.

accurately estimated; however, the assumption of negligible exchange across the BBB results in a systematic overestimation of v_p for high PS. Moreover, the assumption of infinite blood flow leads to underestimation of v_p at low flow values (as found in, for instance, WMH). Figure 6.7 shows the accuracy of tracer kinetic parameters obtained with the Patlak model. The model performance was highly sensitive to differences in blood flow, with low flow resulting in significant underestimation of v_p and overestimation of K^{Trans}. This is consistent with the in vivo finding of lower v_p estimates obtained using the Patlak model compared to the steady state model (see Table 6.2). In contrast to the simulations performed for the MSSII data, K^{Trans} and v_p were not largely independent of one another. Due to the short overall acquisition time, the addition of signal drift did not lead to further significant errors in estimated parameters (data not shown as there was no visible difference to Figures 6.6 and 6.7).

6.5. Discussion

DCE-MRI analysis was performed in an external patient cohort, which shared some imaging findings with the MSSII cohort. Although the target tissues were the same in both cohorts (NAWM, DGM and WMH), the acquisition protocols and methods were vastly different, particularly with regard to temporal resolution and overall acquisition time. Consequently, the data analysis methods applied in the MSSII were not directly transferable. A previous analysis of the CBMS data set was performed by the research team at the Campus Bio-Medico using the original Tofts model (Errante et al., 2013), since this was the default method in the manufacturer's commercial software tool (Tissue 4D, Siemens Healthcare, Erlangen, Germany). However,

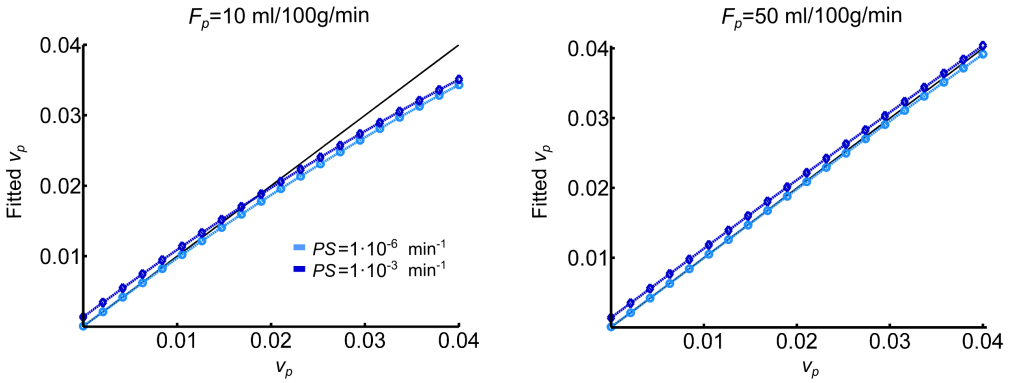

Figure 6.6.: Simulated accuracy of steady state model v_p (CBMS). Relationship between 2CXM blood plasma volume v_p values and corresponding fitted steady state model v_p. Results are shown for two different F_p, PS and v_p values. For all simulations, v_e was set to 0.2. The grey line represents the identity line.

this method disregards the signal contribution from intravascular tracer, which is dominant in normal-appearing brain tissues, and hence is not appropriate in this setting (Sourbron and Buckley, 2011). Data-driven model comparison revealed that the one-parameter steady state model was sufficient to describe the tracer dynamics in NAWM and DGM, indicating that there is no significant BBB leakage in normal-appearing tissues during the acquisition time of approximately 3 min to 4 min. This finding is consistent with a model selection study by Bagher-Ebadian et al. (2012) in glioblastoma patients, which used a similar DCE-MRI protocol with regard to temporal resolution and overall acquisition time. In WMH, there was no clear preference for one model; while the steady state model provided an adequate fit in 45% of patients, there was a trend towards an advantage of the Patlak model. This suggests that there may be increased BBB leakage in WMH compared to normal-appearing tissues; however, the short overall acquisition time is most likely not sufficient to capture slow contrast extravasation and, thus, does not allow for reliable quantification of subtle BBB leakage. Several other studies with longer measurement durations have indeed reported non-zero K^{Trans} values in normal-appearing tissues (Cramer and Larsson, 2014; Montagne et al., 2015) and WMH (Taheri et al., 2011a); nonetheless, it should be noted that some of this apparent leakage may be accounted for by the confounding effect of scanner drift (see chapter 5).

Since there was no obviously dominant model in WMH, applying a single model to the whole patient cohort may bias parameter estimates. Alternatively, the steady state or Patlak model could be chosen based on the AIC for every individual patient and tissue. However, as discussed previously, providing a good fit does not guarantee that the model assumptions are valid and that the fitted parameters are accurate. Consequently, numerical simulations were performed in order to investigate the validity of the steady state and Patlak models with regard to the

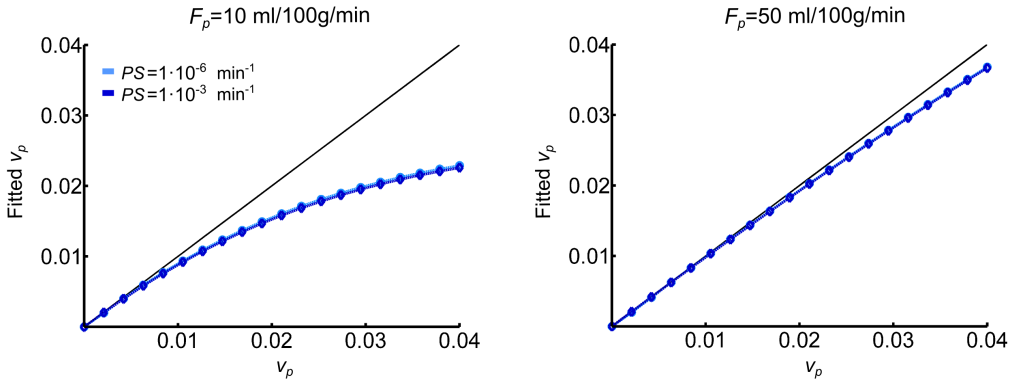

(a) Relationship between blood plasma volume v_p and fitted Patlak v_p

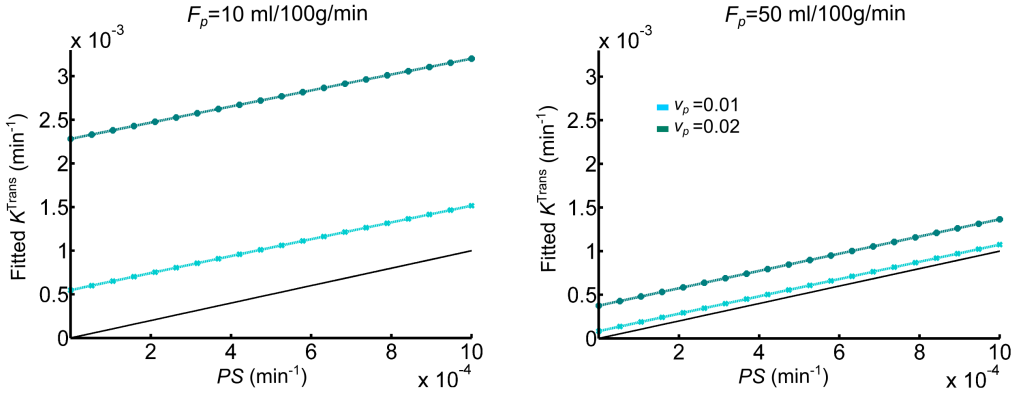

(b) Relationship between permeability surface area product PS and fitted Patlak K^{Trans}

Figure 6.7.: Simulated accuracy of Patlak parameters (CBMS). Relationship of (a) blood plasma volume v_p and (b) permeability surface area product PS values, with corresponding fitted Patlak parameters. Results are shown for two different F_p, PS and v_p values. For all simulations, v_e was set to 0.2. The grey line represents the identity line.

acquisition protocol in the CBMS. For both models, the assumption of infinite flow led to errors in estimated parameters at low flow values. The Patlak model was particularly sensitive to differences in blood flow, with low flow resulting in significant underestimation of v_p and overestimation of K^{Trans}. WMH are well-known to have reduced blood flow (Brickman et al., 2009; Marstrand et al., 2002); consequently, the Patlak model is unlikely to provide reliable estimates of either v_p or PS in WMH in this dataset. The computer simulations also confirmed that the steady state model overestimates v_p when PS is high, which may lead to inaccurate v_p values in WMH if there is indeed non-negligible leakage across the BBB. Nevertheless, the magnitude of this error is limited by the subtle nature of any potential BBB leakage likely in WMH and small compared to the flow-induced errors in Patlak parameters. In the MSSII, the

confounding effect of blood flow was minimised by excluding data acquired during the first pass of the contrast bolus. Due to the short overall acquisition time in the CBMS cohort, a similar approach would disregard the majority of the acquired data and, hence, was not considered appropriate. Consequently, we conclude that the steady state model, although limited, is the most suitable model for analysis of the DCE-MRI data in the CBMS cohort. As a result, the only quantitative parameter that could be obtained with reasonable accuracy in the CBMS cohort is the blood plasma volume v_p.

The tracer kinetic analyses performed in this chapter are likely to suffer from errors in VIF estimation. Firstly, it was not possible to obtain an AIF from a feeding vessel due to partial volume and inflow effects. The VIF extracted from the SSS is subject to bolus delay and dispersion (Sourbron and Buckley, 2013). While the differences between arterial and venous responses were negligible in the MSSII due to the very low temporal resolution, they were captured with the higher temporal resolution in the CBMS and can introduce significant errors in tracer kinetic modelling (Calamante, 2005). Secondly, there was a very large spread of $T1_0$ values obtained in the SSS. This uncertainty in $T1_0$ leads to bias in contrast agent concentrations (Schabel and Parker, 2008), which, in turn, affect tracer kinetic modelling results. Thirdly, the extracted VIFs showed very slow enhancement with unusually low peaks, suggesting that the contrast was injected by hand and at a slow rate; unfortunately, this could not be confirmed with the research team at the Università Campus Bio-Medico in Rome. Another possible explanation for the unusual VIF shape could be a confounding effect of the partial k-space undersampling employed in the TWIST sequence (see further discussion below). Since all subsequent analyses were dependent on the measured VIF, this may have introduced significant errors in tracer kinetic parameters and simulation results. In cases like this, where it is not possible to obtain reliable AIF measurements, the reproducibility of tracer kinetic parameters can be increased by using a generic AIF (Parker et al., 2006). However, factors such as age, heart rate, haematocrit and kidney function have been shown to cause inter-patient variability in the AIF (Port et al., 2001). Using an assumed AIF does not account for these individual variations and can, hence, also introduce systematic errors (that might be correlated with variables of interest) in tracer kinetic parameters (McGrath et al., 2009).

The TWIST sequence that was used to acquire the DCE-MRI data in the CBMS cohort was initially proposed for MR angiography. High temporal resolution is achieved by partial k-space undersampling: while the k-space centre is fully sampled at each time frame, the periphery is only partially sampled and missing points are shared with the previous or subsequent images to allow for reconstruction with full k-space data. Similar sequences have recently been introduced by all major MRI manufacturers, including General Electric's TRICKS (time resolved imaging of contrast kinetics) and Philips' 4D-TRAK (4D-time resolved MR angiography with keyhole). Since then, these methods have been increasingly applied in DCE-MRI because

they offer significantly improved temporal resolution. However, it is unclear how the unique method of k-space undersampling influences the measured signal dynamics. Although it has been shown that measurements from TRICKS/TWIST DCE-MRI acquisitions closely match those from full-k-space-sampling acquisitions in the human breast (Tudorica et al., 2012) and in the rabbit aorta (Kershaw and Cheng, 2011), the effects of k-space undersampling on the assessment of brain tissues have not yet been evaluated.

The difficulty in obtaining reliable quantitative parameters in the CBMS cohort highlights the importance of well thought-out study design. Both the temporal resolution and the total duration of the scan need to be carefully optimised with regard to the nature of the tissue being investigated and the target parameters. In order to quantify blood flow, a temporal resolution in the order of 1 s to 2 s is required (de Bazelaire et al., 2011; Essig et al., 2013). For accurate measurement of the BBB leakage, the scan duration needs to be long enough for significant contrast extravasation to occur; hence, target tissues with largely intact BBB (e.g. normal-appearing tissues) require longer scanning times than highly permeable tissues (e.g. tumours). Unfortunately, neither of these two requirements was fulfilled in the CBMS data, which consists of whole-brain MRI acquisitions with an overall scan duration of approximately 3 min to 4 min. The temporal resolution of 6.3 s to 8.2 s is too slow to reliably estimate flow (de Bazelaire et al., 2011; Essig et al., 2013), but fast enough to make quantitative measurements highly dependent on blood flow. In order to avoid such potential pitfalls of study design, numerical simulations should be performed prior to a study using the planned acquisition parameters. As discussed previously, whole-brain coverage is desirable when assessing diffuse diseases such as cerebral small vessel disease (SVD). However, decreasing the spatial coverage could have allowed for a higher temporal resolution and enabled blood flow measurements. Alternatively, increasing the overall acquisition time would have facilitated the quantification of BBB leakage. In this case, the temporal resolution can be relaxed further in order to improve spatial resolution and minimise partial volume effects.

The availability of an external data set promised an opportunity to investigate inter-study comparability of DCE-MRI measurements in cerebral SVD. The MSSII and CBMS cohorts displayed broadly similar tracer dynamics in NAWM, DGM and WMH. The small discrepancies may be caused by the different types of contrast agent used in the two studies (Chwang et al., 2014). Furthermore, differences may be accounted for by differences in ROI placement (Braunagel et al., 2015). DCE-MRI analysis in the MSSII cohort was based on whole-tissue segmentation masks; unfortunately, it was not possible to apply the same segmentation method in the CBMS cohort, because the necessary structural sequences were not available for all patients. The only tracer kinetic parameter that could be obtained in both the CBMS and MSSII cohorts is the blood plasma volume v_p. The estimates obtained in the CBMS cohort were approximately twice as high as in the MSSII cohort; due to the number of dissimilarities

between the CBMS and MSSII, it is hard to pinpoint the origin of these differences. Firstly, the v_p values were obtained with different models as a result of the particular limitations imposed by temporal resolution and overall acquisition time. Comparisons of tracer kinetic models within both cohorts showed that v_p estimates obtained using the Patlak model were significantly lower compared to the steady state model, which may partly explain higher v_p estimates in the CBMS cohort. Secondly, the work presented in chapter 5 showed that the long DCE-MRI acquisitions in the MSSII were most likely influenced by signal drift, which causes a systematic underestimation of v_p. Thirdly, the lower spatial resolution in the CBMS data led to uncertainty in VIF estimation; higher v_p estimates in the CBMS cohort may partly be accounted for by the lower apparent VIF concentrations. Lastly, differences in measured blood volumes may be due to true variations between the patient cohorts. Although the patient groups were of similar age and both exhibited a range of cerebral SVD features, the MSSII exclusively recruited patients who had had a minor stroke. In contrast, participants of the CBMS presented with a wide range of mild, non-specific neurological symptoms. In order to systematically investigate the influence of a particular factor on tracer kinetic parameters, as many details of the study protocol as possible should be kept the same. However, as demonstrated in this chapter and in the literature review (chapter 2), this is seldom the case in independent studies; consequently, a lack of inter-study comparability is a major problem in DCE-MRI.

6.6. Conclusion

The work presented in this chapter focused on the secondary analysis of DCE-MRI data acquired at the Università Campus Bio-Medico in Rome, Italy. The purpose of this chapter was to identify the tracer kinetic modelling approach most suitable for the particular acquisition protocol in the CBMS (which was vastly different to the protocol employed in the MSSII) and to compare the results to the findings in the MSSII cohort. Due to the nature of the acquisition protocol it proved difficult to obtain reliable quantitative parameters in this cohort. For instance, the scan duration of approximately 3 min to 4 min was not long enough to reliably capture subtle BBB leakage. Moreover, the temporal resolution of approximately 6.5 s was not sufficient to quantify blood flow; unaccounted differences in blood flow were shown to introduce significant errors in estimated tracer kinetic parameters, particularly the permeability-surface area product *PS*. Consequently, the only quantitative parameter that could be obtained with reasonable accuracy in the CBMS cohort is the blood plasma volume v_p using the steady state model. The findings of this chapter highlight the importance of carefully planned study design and of understanding the limitations of quantitative DCE-MRI measurements. Since the application of DCE-MRI to pathologies associated with subtle BBB disruption is a relatively new research area, there has been limited investigation of or guidance on appropriate meth-

odology. As a result, acquisition parameters, postprocessing and analysis approaches differ widely between studies. This leads to significant differences in tracer kinetic parameters: here, v_p estimates obtained in the CBMS cohort were approximately twice as high as in the MSSII cohort. The increasing research in this field (including work arising from this thesis (Heye et al., 2016a) and related investigations by e.g. Cramer and Larsson (2014) and Montagne et al. (2015)) will help to facilitate optimal study design and improve inter-study comparability in the future.

Part IV.

Quantitative magnetic resonance imaging markers in cerebral small vessel disease: associations with clinical and imaging variables in the Mild Stroke Study II cohort

Contents

7. Blood-brain barrier permeability and blood volume in cerebral small vessel disease

The purpose of this chapter is to analyse the dynamic contrast-enhanced MRI (DCE-MRI) parameters measured in the Mild Stroke Study II (MSSII) cohort and to investigate whether they are linked to small vessel disease (SVD) burden and progression. In particular, this chapter presents the MSSII cohort characteristics and compares the Patlak parameters obtained in chapter 4 between different tissue types (section 7.3.1), examines the associations of K^{Trans} and v_p with patient characteristics (section 7.3.2) and SVD imaging markers (section 7.3.3). Furthermore, this chapter investigates whether measurements of blood-brain barrier (BBB) leakage and blood volume predict disease progression over one year (section 7.3.4). Some contents of this chapter have been published in Heye et al. (2016a).

7.1. Introduction

Cerebral SVD is responsible for about a fifth of all strokes worldwide and about a quarter of ischaemic strokes (Sudlow and Warlow, 1997). Despite this large burden of cerebral SVD, the underlying pathological processes are still largely unknown (see section 1.1.3). Disruption of the BBB can explain many of the imaging and pathological observations related to SVD and, hence, may play an initiating role in the development of SVD (Wardlaw et al., 2003). BBB leakage has previously been shown to increase subtly with advancing age (Farrall and Wardlaw, 2009), mild cognitive impairment (Montagne et al., 2015), vascular dementia (Taheri et al., 2011b), lacunar stroke (Topakian et al., 2010; Wardlaw et al., 2009) and increasing amount of white matter hyperintensities (WMH) (Wardlaw, 2010). Most groups studying subtle BBB disruption have used semi-quantitative approaches for the analysis of DCE-MRI data (see chapter 2). These approaches provide a simple measurement of contrast uptake, but are difficult to interpret regarding physiologically relevant properties (e.g. BBB permeability, blood flow, blood volume).

As detailed in chapters 3 and 4 of this thesis, quantitative DCE-MRI measurements of BBB permeability and blood volume were obtained in the MSSII cohort of patients exhibiting a spectrum of SVD severity. This work aimed to investigate the association between these

parameters and SVD imaging features at baseline and one year follow-up and, thus, shed light on the role of BBB disruption in cerebral SVD.

7.2. Methods

7.2.1. Participants

The details of patient recruitment, inclusion and exclusion criteria have been given in section 3.2.2. In short, 264 adult patients with mild, i.e. anticipated to be non-disabling, lacunar or cortical ischaemic stroke were recruited from the local stroke services. This chapter focuses on the role of BBB disruption in cerebral SVD; consequently, all analyses in this chapter are based on the subset of the MSSII cohort that successfully underwent DCE-MRI between one and three months after the index stroke.

7.2.2. Data collection and analysis

The following sections will provide a brief summary of the data collection procedures in the MSSII that are relevant for this chapter; please refer to section 3.2.3 for detailed information.

Clinical assessments

All participants underwent an initial clinical assessment as soon as possible after stroke onset by a qualified stroke physician. The clinical research fellow (Dr Stephen Makin) collected demographic details, clinical data, life style information and medical history, including atrial fibrillation, ischaemic heart disease and peripheral vascular disease. Hypertension was defined as blood pressure of 140/90 mmHg or greater on presentation or a previous diagnosis. Smokers were defined as currently smoking or having given up within the previous 12 months and non-smokers as having never smoked or having given up more than 12 months previously. Diabetes was defined as a previous or new diagnosis at presentation following the World Health Organisation criteria for diagnosis of diabetes. Hypercholesterolaemia was defined as a total cholesterol level (measured from blood samples taken during clinic) above the recommended level of 5 mmol/L or a previous diagnosis.

One year after the first presentation, all participants were invited for a follow-up clinical and MRI assessment. If patients were unable or declined to return for the MRI scan, the clinical research fellow obtained as much clinical information as possible by phone, from the patient's medical records, a relative or carer. Collected clinical data were similar to those obtained at the

initial assessment and included a complete medical history of the previous year, in particular whether the patient had suffered from a recurrent neurovascular event (i.e. a transient ischaemic attack (TIA) or a further stroke).

Diagnostic MRI and SVD imaging markers

As part of the initial assessment, all 264 patients underwent a diagnostic MRI scan on the same 1.5 T MRI scanner. The protocol included three-dimensional (3D) T1-weighted (T1W) inversion recovery prepared spoiled gradient echo (GRE), T2-weighted fast spin echo, T2*-weighted GRE, fluid attenuated inversion recovery, susceptibility-weighted imaging and diffusion tensor MRI acquisitions. All MRI scans were assessed by an experienced neuroradiologist (Prof Joanna M Wardlaw), who was blinded to the clinical findings and recorded the presence and location of an index stroke lesion and old stroke lesions, including lacunes. WMH burden was rated from 0 (none) to 3 (severe) using the Fazekas scale; for this analysis, the Fazekas scores for periventricular and deep white matter (WM) were summed, resulting in total score ranging from 0 to 6. The presence of enlarged perivascular spaces (EPVS) was rated on a score from 0 (none) to 4 (>40) for the midbrain, hippocampus, basal ganglia and centrum semiovale; a combined EPVS score was calculated by adding up the scores for the subregions, yielding a score ranging from 0 to 16. Deep and superficial cerebral atrophy were each rated on a scale from 1 (mild) to 6 (severe) in comparison to a standard age matched template (Farrell et al., 2009); for this analysis, the scores were added up to a total atrophy score, ranging from 2 to 12. Total numbers of microbleeds were obtained by adding up the numbers counted in each subregion (deep WM, basal ganglia, grey matter (GM) and WM junction, external/internal capsule, thalamus and posterior fossa) and both hemispheres of the brain. The acute stroke was classified as lacunar or cortical subtype by a panel of stroke experts using the clinical syndrome and MRI finding of a relevant small subcortical or cortical infarct. In case of discrepancies between the clinical and imaging appearance, the imaging subtype was used.

The diagnostic MRI was repeated at approximately one year after the first assessment using the same 1.5 T MRI scanner. As before, the structural MRI scans were assessed by Prof Joanna M Wardlaw, who recorded the same features (on the same scales) as described above and was blinded to the baseline imaging and clinical findings. For statistical analysis, the degree of disease progression over one year was summed in an ordinal 'SVD progression score' that ranges from 0 to 5. One point on this scale was awarded for each of the following compared to baseline: (i) recurrent neurovascular event (i.e. TIA, further stroke or new stroke lesion on imaging), (ii) worsening of Fazekas score, (iii) worsening of brain atrophy score, (iv) worsening of EPVS score and (v) increased number of microbleeds. This approach was chosen because it allows for analysing the combined progression of the various SVD features as one disorder; a

similar method has been used previously to measure the total MRI load of cerebral SVD (Staals et al., 2014).

Tissue segmentation and volume measurements

The brain tissues and volumes were extracted semi-automatically by Dr Maria del C Valdés Hernández. As described in section 3.2.4, segmentation masks were generated for the intracranial volume (ICV) and the following tissue types (see Figure 3.3): cerebrospinal fluid (CSF), normal-appearing WM (NAWM), WMH, deep/subcortical GM (DGM) and recent stroke lesions (RSL). The resulting segmentation masks were used to calculate the brain tissue volume as a percentage of ICV (%BTV) and WMH volume as a percentage of ICV (%WMHV). All image analysis was performed blind to clinical data.

DCE-MRI measurements

Participants returned approximately one to three months after presentation for DCE-MRI, which consisted of 20 consecutive 3D T1W spoiled GRE acquisitions with a temporal resolution of 73 s and a total acquisition time of approximately 24 min. For calculation of $T1_0$, two additional 3D spoiled GRE acquisitions were obtained prior to contrast administration with flip angles of 2° and 12° respectively.

DCE-MRI were processed by myself on a region of interest (ROI) basis as described in section 3.3. Firstly, average $T1_0$ values and contrast agent concentration curves were calculated for each tissue type. Secondly, the Patlak model was fitted to the curves (see chapter 4), yielding the parameters K^{Trans} and v_p that provide quantitative measurements of BBB leakage and blood plasma volume, respectively.

7.2.3. Statistical analyses

Differences in K^{Trans} and v_p values between tissue types were investigated using Wilcoxon's signed rank test, since the data were not generally normally distributed. For each tissue type, the relationship between Patlak parameters and age was investigated using Pearson's correlation coefficient. Furthermore, both K^{Trans} and v_p were tested for differences between stroke subtypes and sexes using Wilcoxon's rank sum test.

Associations between the Patlak parameters and SVD imaging markers were investigated using a three-step approach. Firstly, simple linear regression analysis was performed for K^{Trans} and v_p in each tissue type as the dependent variable and one of the following SVD features as

explanatory variable: WMH burden, atrophy, number of microbleeds, number of lacunes, EPVS score. Secondly, predictors of K^{Trans} and v_p were investigated using multiple linear regression models with all SVD imaging markers as predictors and correction for age, stroke subtype and gender. Thirdly, multiple linear regression analysis was performed in order to investigate whether the found significant relationships also survive correction for vascular risk factors (hypertension, hypercholesterolaemia, diabetes, smoking) and $T1_0$, which is known to influence tracer kinetic parameters (Armitage et al., 2011).

Ordinal logistic regression was used to investigate predictors of disease progression over one year. The following variables at baseline were used as predictors of the SVD progression score: K^{Trans} and v_p in each tissue type, age, stroke type, %WMHV, %BTV and vascular risk factors (hypertension, hypercholesterolaemia, diabetes, smoking).

All regressions were assessed by examination of the differences between the data and model predictions, and collinearity by variance inflation factors. All statistical analyses were performed by myself in Matlab (MathWorks, Inc., MA, USA).

7.3. Results

7.3.1. Baseline cohort characteristics

Of the 264 patients recruited, 56 did not undergo DCE-MRI because they were too unwell or declined to have the scan. Of the 208 patients that underwent DCE-MRI, data suitable for analysis was obtained in 201 (data for seven subjects were rejected due to 'tissueing' of contrast, technical faults during the scan or unacceptable data quality caused by patient movement). The baseline characteristics of this sub-cohort, including SVD imaging markers and DCE-MRI parameters, are detailed in Table 7.1. For all following linear regression analyses, the WMH and brain tissue volumes %WMHV and %BTV were used as quantitative measurements of WMH and atrophy burden because they provide continuous variables; qualitative and quantitative measurements were highly correlated (see Figure 7.1).

A comparison of Patlak parameters between tissue types is shown in Figure 7.2; all differences between tissue types were significant ($p < 0.001$) except for K^{Trans} in WMH and DGM and v_p in WMH and RSL. In particular, K^{Trans} and v_p were significantly higher in WMH compared to NAWM; K^{Trans} was significantly higher in RSL compared to all other tissues. Exemplary contrast agent concentration curves and the corresponding Patlak fits for patients at different ends of the disease spectrum are presented in Figure 7.3.

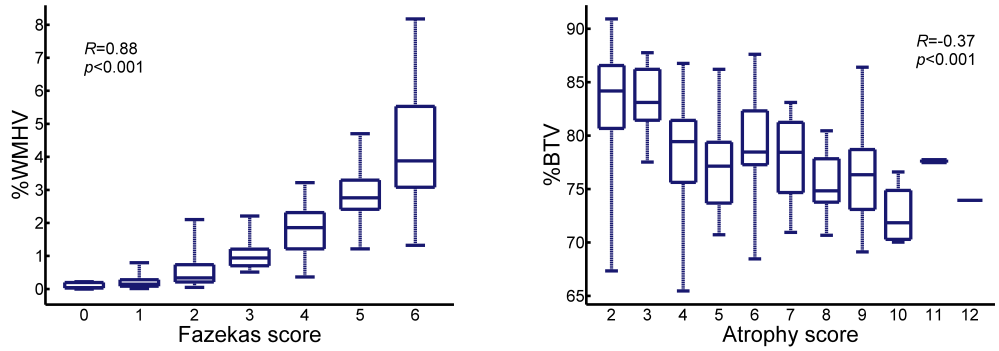

(a) WMH burden (b) Atrophy

Figure 7.1.: Relationship between visual rating scores and volume measurements. Graphs showing the relationship between (a) Fazekas score and percentage WMH volume (%WMHV) and (b) atrophy score and percentage brain tissue volume (%BTV). The degree of correlation was investigated using Spearman's R; the correlation coefficient and p-value are indicated for each relationship.

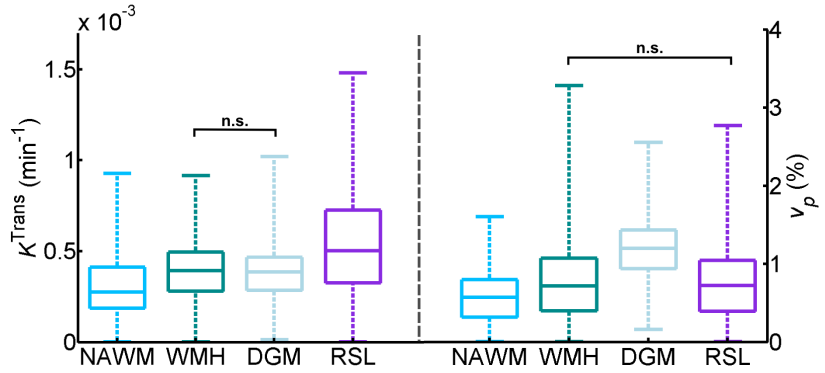

Figure 7.2.: Comparison of fitted Patlak parameters between tissue types. Boxplots showing the distribution of K^{Trans} (left) and v_p (right) in the different tissue types. Brackets with 'n.s.' indicate non-significant differences with $p > 0.50$; all other differences between tissue types are significant with $p < 0.001$ (brackets omitted for clarity). Reprinted from Heye et al. (2016a).

7.3.2. Associations with age, gender and stroke type

Figure 7.4 shows the relationship between the Patlak parameters and age. Both K^{Trans} and v_p decreased with age in NAWM, WMH and DGM; the association remained statistically significant after correction for stroke subtype, gender and SVD imaging markers in all three tissues for K^{Trans} and in WMH for v_p (see Table 7.2).

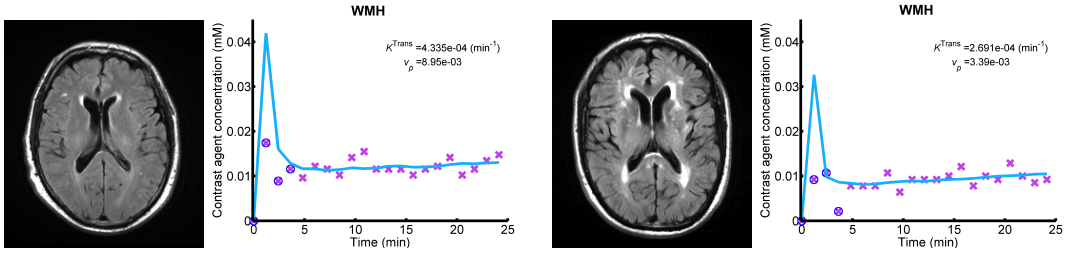

(a) Patient with low WMH burden

(b) Patient with high WMH burden

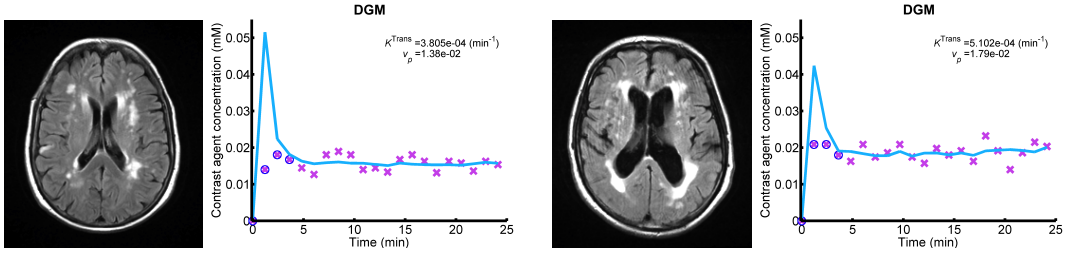

(c) Patient with low amount of atrophy

(d) Patient with high amount of atrophy

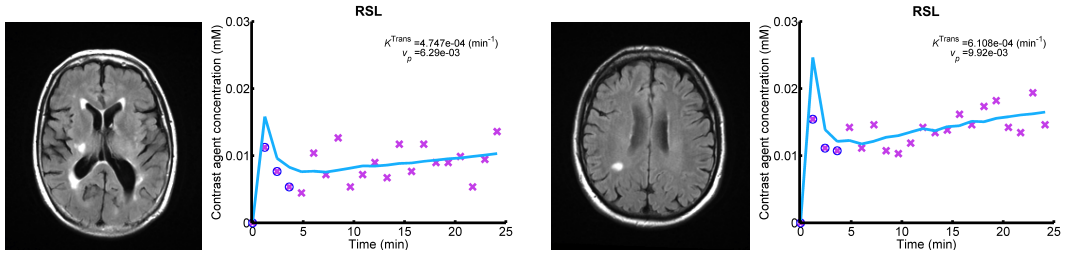

(e) Patient with lacunar stroke

(f) Patient with cortical stroke

Figure 7.3.: Examples of contrast dynamics in patients at different ends of the SVD spectrum and different tissue types. Subfigures (a) to (f) are showing exemplary data for six different patients of the MSSII cohort. A single axial slice of the FLAIR image is shown on the left; the graphs on the right display the contrast agent concentration over time in a particular tissue type and the corresponding Patlak fit.

Table 7.3 provides a comparison of Patlak parameters between lacunar and cortical stroke patients, who share similar risk factors and medication histories but were previously found to differ in BBB functionality (Wardlaw et al., 2009). K^{Trans} was significantly higher in recent cortical compared to lacunar stroke lesions ($p = 0.02$); this association survived correction for age, gender and SVD imaging markers (see Table 7.2). An additional simple linear regression analysis showed that K^{Trans} in RSL is significantly positively associated with the infarct size ($\beta = 1.0 \cdot 10^{-8}$ min^{-1}mm^{-3}; $p < 0.001$), which is likely to account for the difference between stroke subtypes. No other tissues showed significant differences between lacunar and cortical stroke patients. A comparison of Patlak parameters between genders is provided in Table 7.4. In all tissue types, K^{Trans} and v_p were higher in men compared to women; there was no significant difference in age between men and women ($p = 0.71$).

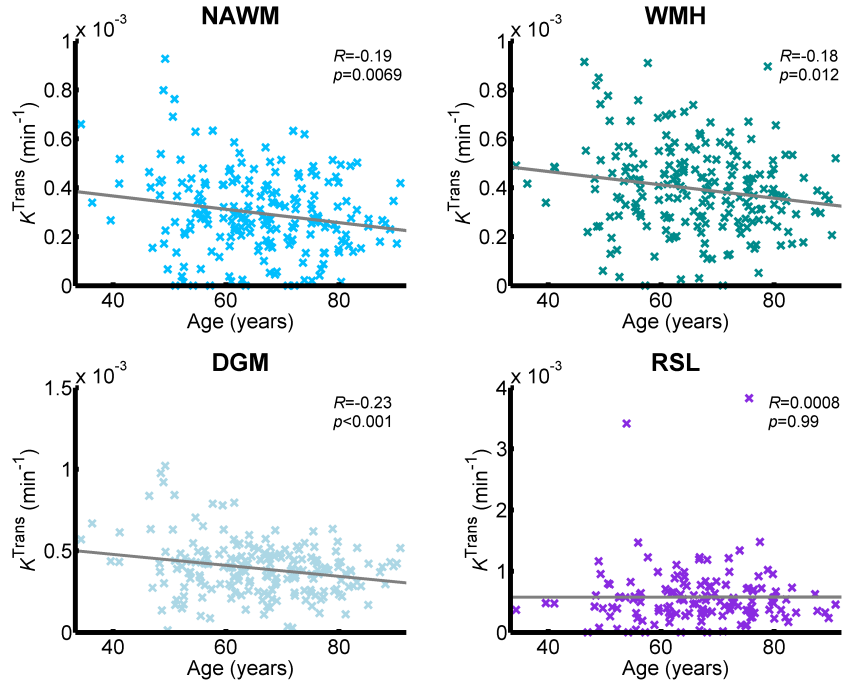

(a) Relationship between K^{Trans} and age

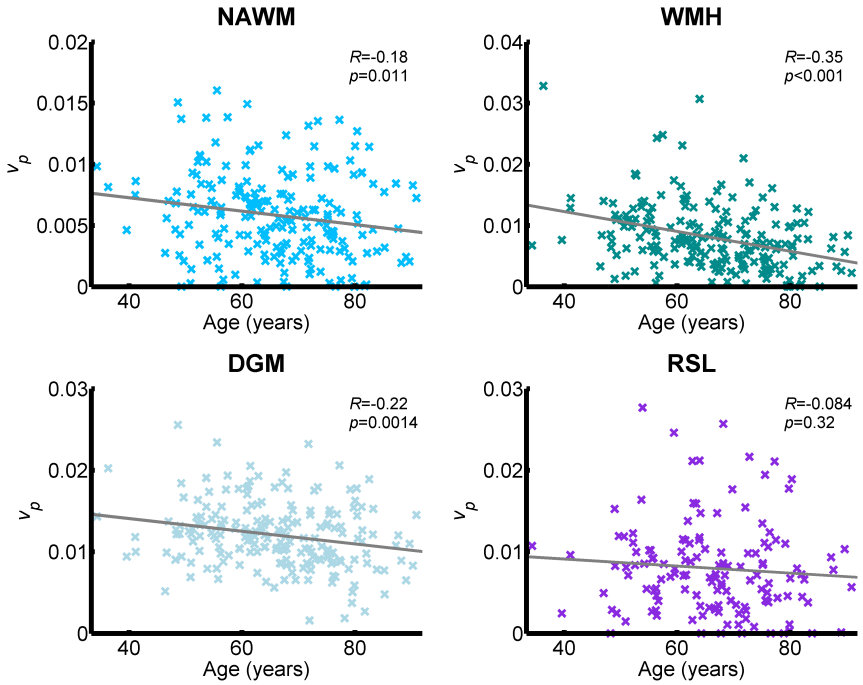

(b) Relationship between v_p and age

Figure 7.4.: Relationship between Patlak parameters and age. Graphs showing (a) K^{Trans} and (b) v_p as a function of age in the different tissue types. Grey lines are the least squares linear regression fit; Pearson's correlation coefficient R and p-value are indicated for each tissue type.

Table 7.1.: Baseline characteristics of the MSSII cohort (DCE-MRI subset). Descriptive statistics for demographic, clinical and imaging variables including DCE-MRI parameters in the different tissue types. Values for continuous imaging variables and ordinal scores are given as cohort median and interquartile range, because they were not generally normally distributed; age is given as cohort mean and standard deviation. Please note that these values apply to the subset of patients that had usable DCE-MRI data ($n = 201$); descriptive statistics for the whole MSSII cohort are given in Table 8.1.

Parameter	Value
Demographic variables	
Age (years)	66.0 ± 11.5
Gender (% female)	39.3
Clinical variables	
Stroke subtype (% lacunar)	46
Hypertension (%)	56
Smoker (%)	36
Diabetes (%)	12
SVD imaging markers	
Combined Fazekas score	3 [2, 5]
Combined Atrophy score	4 [2, 6]
Microbleeds present (%)	16.4
Lacunes present (%)	26.4
Combined EPVS score	5 [4, 6]
Imaging variables	
Structural MRI	
WMH volume (%)	0.91 [0.31, 2.36]
Brain tissue volume (%)	80.45 [77.03, 84.18]
Stroke lesion volume ($\cdot 10^3$ mm^3)	1.82 [0.88, 6.78]
DCE-MRI	
K^{Trans} ($\cdot 10^{-4}$ min^{-1})	
NAWM	2.75 [1.85, 4.12]
WMH	3.91 [2.80, 4.94]
DGM	3.85 [2.83, 4.68]
RSL	5.02 [3.24, 7.25]
v_p ($\cdot 10^{-2}$)	
NAWM	0.57 [0.32, 0.80]
WMH	0.72 [0.40, 1.07]
DGM	1.20 [0.94, 1.43]
RSL	0.72 [0.39, 1.05]

7.3.3. Associations with SVD imaging features

The results of all simple linear regression analyses between SVD features at baseline and Patlak parameters are provided in Table 7.5. Most significant associations between DCE-MRI

Table 7.2.: Multiple linear regression analyses of DCE-MRI parameters and SVD imaging markers at baseline. Separate models were fitted for K^{Trans} and v_p in each tissue type as dependent variable and age, stroke type, gender, WMH volume %WMHV, brain tissue volume %BTV, number of microbleeds, number of lacunes and EPVS score as explanatory variables. Results are given as β coefficient, 95% confidence interval (CI) and p-value.

Tissue	Predictor	K^{Trans} ($\cdot 10^{-5}$ min^{-1})		v_p ($\cdot 10^{-4}$)	
		β (95% CI)	p	β (95% CI)	p
NAWM	Age (years)	−0.33 (−0.63, −0.03)	**0.031**	−0.4 (−1.0, 0.25)	0.23
	Gender[a]	−4.5 (−9.3, 0.36)	0.069	−2.4 (−13, 7.9)	0.65
	Stroke subtype[b]	−3.5 (−8.1, 1.2)	0.15	6.0 (−4.0, 16)	0.24
	%WMHV (%)	0.54 (−1.2, 2.3)	0.55	2.3 (−1.5, 6.1)	0.23
	%BTV (%)	0.045 (−0.57, 0.66)	0.89	0.97 (−0.36, 2.3)	0.15
	EPVS score	0.63 (−0.50, 1.8)	0.27	−0.38 (−2.8, 2.0)	0.76
	Microbleeds	−0.11 (−0.55, 0.34)	0.64	0.6 (−0.36, 1.6)	0.22
	Lacunes	−1.3 (−3.6, 1.1)	0.29	−0.98 (−6.0, 4.0)	0.70
WMH	Age (years)	−0.43 (−0.75,−0.097)	**0.011**	−1.2 (−2.1, −0.24)	**0.014**
	Gender[a]	−4.5 (−9.7, 0.79)	0.095	−9.8 (−25, 5.0)	0.19
	Stroke subtype[b]	−0.021 (−5.1, 5.1)	0.99	6.4 (−8.0, 21)	0.38
	%WMHV (%)	0.88 (−1.1, 2.8)	0.37	−7.3 (−13, −1.8)	**0.0090**
	%BTV (%)	−0.26 (−0.93, 0.42)	0.45	−0.024 (−1.9, 1.9)	0.98
	EPVS score	0.16 (−1.1, 1.4)	0.79	−0.7 (−4.2, 2.8)	0.69
	Microbleeds	−0.0065 (−0.49, 0.48)	0.98	0.75 (−0.63, 2.1)	0.28
	Lacunes	−1.5 (−4.1, 1.0)	0.24	−1.8 (−9.0, 5.4)	0.62
DGM	Age (years)	−0.67 (−0.96, −0.37)	**<0.001**	−0.61 (−1.3, 0.12)	0.099
	Gender[a]	−2.9 (−7.6, 1.9)	0.23	−3.3 (−15, 8.3)	0.57
	Stroke subtype[b]	−2.7 (−7.3, 1.9)	0.25	6.3 (−5.0, 18)	0.27
	%WMHV (%)	1.4 (−0.4, 3.1)	0.13	1.3 (−3.0, 5.6)	0.55
	%BTV (%)	−0.70 (−1.3, −0.089)	**0.025**	0.57 (−0.92, 2.1)	0.45
	EPVS score	0.18 (−0.92, 1.3)	0.74	−1.9 (−4.6,0.82)	0.17
	Microbleeds	−0.10 (−0.54, 0.34)	0.64	0.7 (−0.38, 1.8)	0.20
	Lacunes	−0.93 (−3.2, 1.4)	0.43	1.2 (−4.5, 6.9)	0.67
RSL	Age (years)	−0.59 (−1.6, 0.47)	0.27	−0.5 (−1.7, 0.75)	0.43
	Gender[a]	−7.9 (−26, 9.9)	0.38	−4.6 (−26, 16)	0.67
	Stroke subtype[b]	−23 (−39, −5.7)	**0.0093**	−11 (−31, 8.7)	0.26
	%WMHV (%)	−2.1 (−8.4, 4.1)	0.50	−2.7 (−10, 4.7)	0.47
	%BTV (%)	−1.9 (−4.1, 0.28)	0.088	−0.14 (−2.7, 2.4)	0.91
	EPVS score	1.3 (−2.8, 5.4)	0.53	−0.6 (−5.4, 4.2)	0.80
	Microbleeds	−0.12 (−1.7, 1.4)	0.87	1.2 (−0.57, 3.0)	0.18
	Lacunes	−1.1 (−8.5, 6.3)	0.77	−4.6 (−13, 4.1)	0.29

[a]Male=0, female=1, [b]cortical=0, lacunar=1

parameters and SVD features were found for v_p in WMH, which was significantly negatively correlated with WMH volume, cerebral atrophy and EPVS score (see Figure 7.5). After correction for age, stroke type, gender and all other imaging features (see Table 7.2), only the association with %WMHV remained statistically significant ($\beta = -7.3 \cdot 10^{-4}$; $p = 0.0090$). This relationship also survived correction for vascular risk factors and $T1_0$ (see Table 7.6).

Table 7.3.: Comparison of Patlak parameters between lacunar and cortical stroke patients. Summary of group-average K^{Trans} and v_p for lacunar versus cortical stroke patients in the different tissue types. Given values are the cohort median and interquartile range; Wilcoxon's rank-sum test was used to test for differences between groups.

Tissue	K^{Trans} ($\cdot 10^{-4}$ min^{-1})			v_p ($\cdot 10^{-2}$)		
	Lacunar	Cortical	p	Lacunar	Cortical	p
NAWM	2.73 [1.93, 3.86]	2.77 [1.80, 4.21]	0.36	0.58 [0.37, 0.79]	0.54 [0.25, 0.80]	0.24
WMH	3.95 [2.82, 4.87]	3.81 [2.77, 4.96]	0.90	0.73 [0.45, 1.07]	0.70 [0.37, 1.08]	0.47
DGM	3.85 [2.81, 4.53]	3.87 [2.88, 4.75]	0.61	1.21 [0.98, 1.45]	1.17 [0.90, 1.39]	0.27
RSL	4.51 [3.13, 6.14]	5.71 [3.56, 8.35]	**0.02**	0.71 [0.28, 1.00]	0.73 [0.48, 1.13]	0.14

Table 7.4.: Comparison of Patlak parameters between male and female patients. Summary of group-average K^{Trans} and v_p for men versus women in the different tissue types. Given values are the cohort median and interquartile range; Wilcoxon's rank-sum test was used to test for differences between groups.

Tissue	K^{Trans} ($\cdot 10^{-4}$ min^{-1})			v_p ($\cdot 10^{-2}$)		
	Male	Female	p	Male	Female	p
NAWM	2.99 [2.17, 4.22]	2.59 [1.60, 3.67]	0.05	0.58 [0.29, 0.76]	0.56 [0.34, 0.80]	0.87
WMH	4.07 [2.95, 4.99]	3.69 [2.42, 4.94]	0.14	0.78 [0.48, 1.10]	0.67 [0.34, 1.00]	0.07
DGM	4.06 [3.07, 4.82]	3.62 [2.42, 4.39]	**0.03**	1.20 [0.94, 1.45]	1.19 [0.94, 1.39]	0.66
RSL	5.25 [3.15, 7.61]	4.54 [3.54, 6.68]	0.44	0.73 [0.46, 1.03]	0.67 [0.28, 1.06]	0.31

Using simple linear regression, none of the SVD imaging markers was a significant predictor of K^{Trans}. However, in the multivariate model, K^{Trans} in DGM was negatively associated with brain tissue volume ($\beta = -0.70 \cdot 10^{-5}$ min^{-1}/%; $p = 0.025$). This relationship was also significant in the multivariate linear regression model with additional correction for vascular risk factors and $T1_0$ (see Table 7.7).

7.3.4. Disease progression at one year follow-up

180 of the 201 patients returned for a follow-up MRI assessment approximately one year after the initial stroke. 32 of these patients (17.8%) had a recurrent neurovascular event between baseline and one year follow-up. 10 patients (5.6%) showed an increase in Fazekas score, while brain atrophy progressed in 27 subjects (15.0%) and EPVS in 29 subjects (16.1%). 17 participants (9.4%) had more microbleeds at follow-up than at baseline. 32 patients (17.8%) showed disease progression in more than one of these features, i.e. SVD progression score > 1 (see Figure 7.6).

Table 7.8 provides the results of the ordinal logistic regression analyses of disease progression at one year follow-up. The strongest predictor of SVD progression was the WMH burden

Table 7.5.: Simple linear regression analyses of DCE-MRI parameters and SVD imaging markers at baseline. Separate models models were fitted for K^{Trans} and v_p in each tissue type as dependent variable and one of the following SVD imaging features as explanatory variable: WMH volume %WMHV, brain tissue volume %BTV, number of microbleeds, number of lacunes, EPVS score. Results are given as β coefficient, 95% CI and p-value.

Predictor	Tissue	K^{Trans} ($\cdot 10^{-5}$ min^{-1})		v_p ($\cdot 10^{-4}$)	
		β (95% CI)	p	β (95% CI)	p
%WMHV (%)	NAWM	−0.49 (−1.9, 0.91)	0.49	0.29 (−2.7, 3.3)	0.85
	WMH	−0.33 (−1.8, 1.2)	0.67	−11 (−15, −6.6)	**<0.001**
	DGM	−0.13 (−1.5, 1.3)	0.85	−1.6 (−4.9, 1.8)	0.37
	RSL	−1.9 (−6.8, 3.1)	0.46	−3.7 (−9.4, 2.0)	0.20
%BTV (%)	NAWM	0.41 (−0.025, 0.84)	0.064	1.2 (0.32, 2.1)	**0.0083**
	WMH	0.24 (−0.23, 0.71)	0.31	2.4 (1.0, 3.8)	**<0.001**
	DGM	0.15 (−0.29, 0.58)	0.51	1.4 (0.34, 2.4)	**0.0096**
	RSL	−1.0 (−2.6, 0.57)	0.21	0.63 (−1.2, 2.5)	0.50
Microbleeds	NAWM	−0.13 (−0.55, 0.29)	0.54	0.51 (−0.39, 1.4)	0.27
	WMH	−0.023 (−0.48, 0.43)	0.92	−0.44 (−1.8, 0.93)	0.53
	DGM	−0.091 (−0.51, 0.33)	0.67	0.39 (−0.63, 1.4)	0.45
	RSL	−0.089 (−1.5, 1.3)	0.90	0.56 (−1.0, 2.2)	0.49
Lacunes	NAWM	−0.41 (−2.5, 1.7)	0.70	1.1 (−3.4, 5.6)	0.64
	WMH	−0.37 (−2.6, 1.9)	0.75	−2.0 (−8.8, 4.9)	0.57
	DGM	0.14 (−2.0, 2.3)	0.90	2.2 (−2.9, 7.3)	0.40
	RSL	−2.0 (−8.5, 4.5)	0.55	−5.2 (−13, 2.3)	0.17
EPVS score	NAWM	0.19 (−0.78, 1.2)	0.70	−0.044 (−2.1, 2.0)	0.97
	WMH	−0.051 (−1.1, 1.0)	0.92	−3.8 (−7.0, −0.65)	**0.018**
	DGM	0.027 (−0.95, 1.0)	0.96	−1.5 (−3.9, 0.81)	0.20
	RSL	−0.21 (−3.7, 3.3)	0.91	−2.0 (−6.1, 2.1)	0.34

(see Figure 7.7(a)). The odds ratio for %WMHV at baseline was 1.5 ($p < 0.002$), i.e. the odds of disease progression increased by approximately 50% per point increase in WMH volume. Moreover, v_p in NAWM and DGM was a significant positive predictor of SVD progression score, with high v_p increasing the risk of disease progression (odds ratios of 2.8 per absolute percent increase in NAWM v_p and 2.3 per absolute percent increase in DGM v_p; $p = 0.029/0.044$; see Figure 7.7(b)).

7.4. Discussion

The K^{Trans} estimates obtained with the Patlak model were greater in WMH than in NAWM. This is consistent with some pathology studies (e.g. Tomimoto et al., 1996; Wharton et al., 2015; Young et al., 2008) and other DCE-MRI studies that reported increased BBB disruption in areas of WMH compared to NAWM (Hanyu et al., 2002; Taheri et al., 2011b; Topakian

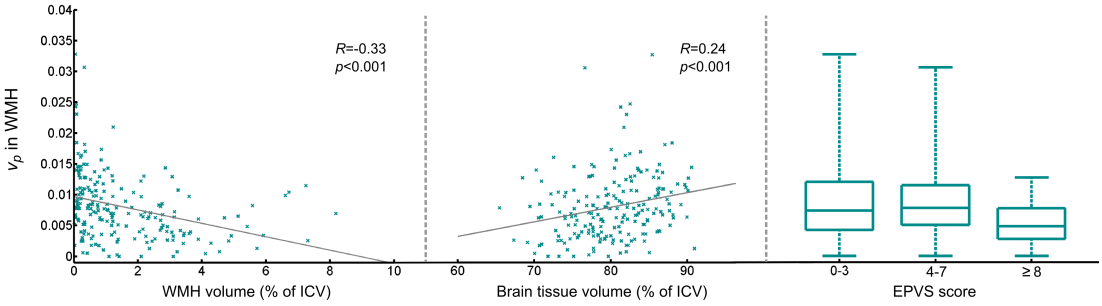

Figure 7.5.: Relationship between v_p in WMH and WMH volume, brain tissue volume and EPVS score at baseline. Only the association between v_p and WMH volume (Pearson's $R = -0.33$, $p < 0.001$) survived correction for age, sex, stroke type and all other SVD imaging features (see Table 7.2).

Table 7.6.: Multiple linear regression analysis of v_p in WMH and WMH volume at baseline. WMH v_p was regressed against WMH volume %WMHV, corrected for age, stroke subtype, gender, vascular risk factors and $T1_0$. Results are given as β coefficient, 95% CI and p-value.

Predictor	**v_p in WMH ($\cdot 10^{-4}$)**	
	β (95% CI)	p
%WMHV (%)	−9.2 (−14, −4.4)	**<0.001**
Age (years)	−1.4 (−2.2, −0.7)	**<0.001**
Gender[a]	−7.9 (−22, 6.2)	0.27
Stroke subtype[b]	6.1 (−7.5, 20)	0.38
Hypertension	−12 (−26, 2.6)	0.11
Hypercholesterolaemia	−7.3 (−22, 7.0)	0.31
Diabetes	6.3 (−15, 27)	0.55
Smoking[c]	−1.1 (−16, 14)	0.89
$T1_0$	97 (45, 150)	**<0.001**

[a]Male=0, female=1, [b]cortical=0, lacunar=1, [c]currently smoking or had given up within the previous 12 months

et al., 2010). In contrast, a recent study by Huisa et al. (2015) found increased BBB disruption in NAWM surrounding the WMH rather than in the WMH themselves, while others failed to detect any BBB leakage in or around WMH (Wahlund and Bronge, 2000); however, both of these studies were based on very small patient cohorts ($n = 22$ and $n = 10$ respectively). The highest K^{Trans} values were found in the RSL, comparable to findings of Thornhill et al. (2010) in acute-phase stroke lesions and known tissue changes from many pathology examinations. Moreover, K^{Trans} was found to be significantly higher in recent cortical compared to lacunar stroke lesions; this finding is likely to be accounted for by the greater severity and greater lesion size of cortical strokes. We did not find increased BBB disruption in normal-appearing tissues of lacunar compared to cortical stroke patients. This contradicts previous findings of elevated

Table 7.7.: Multiple linear regression analysis of K^{Trans} in DGM and brain tissue volume at baseline. DGM K^{Trans} was regressed against brain tissue volume %BTV, corrected for age, stroke subtype, gender, vascular risk factors and $T1_0$. Results are given as β coefficient, 95% CI and p-value.

Predictor	K^{Trans} in DGM ($\cdot 10^{-5}$ min^{-1})	
	β (95% CI)	p
%BTV (%)	−0.62 (−1.2,0.0046)	0.052
Age (years)	−0.57 (−0.88, −0.26)	**<0.001**
Gender[a]	−1.7 (−6.5, 3.0)	0.48
Stroke subtype[b]	−3.2 (−7.7, 1.4)	0.17
Hypertension	−0.91 (−5.7, 3.8)	0.71
Hypercholesterolaemia	−2.0 (−6.8, 2.8)	0.41
Diabetes	2.7 (−4.3, 9.7)	0.45
Smoking[c]	2.5 (−2.5, 7.6)	0.32
$T1_0$	6.8 (−12, 25)	0.47

[a]Male=0, female=1, [b]cortical=0, lacunar=1, [c]currently smoking or had given up within the previous 12 months

BBB permeability in NAWM and CSF of lacunar patients (Wardlaw et al., 2009); however, this earlier study, amongst other differences, used different image processing methods and did not calculate quantitative DCE-MRI parameters.

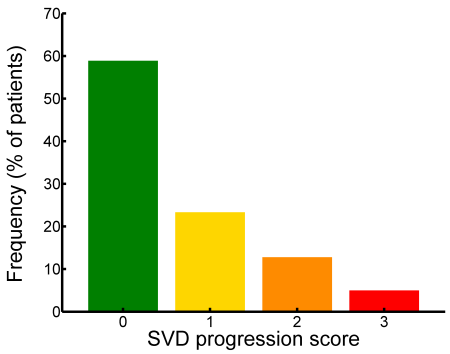

Figure 7.6.: Disease progression at one year follow-up. Bar graph showing the frequency of SVD progression scores. The degree of disease progression was measured using a combined score, with points being given for a recurrent neurovascular event, increased number of microbleeds, worsening of Fazekas score, brain atrophy score and EPVS score. Consequently, patients with a score of 0 did not show any visible disease progression; patients with a score > 1 showed disease progression in more than one of these features.

K^{Trans} was greater in DGM than in NAWM, which may partly reflect the higher vessel density and vascular surface area of GM (Schlageter et al., 1999), consistent with the higher measured

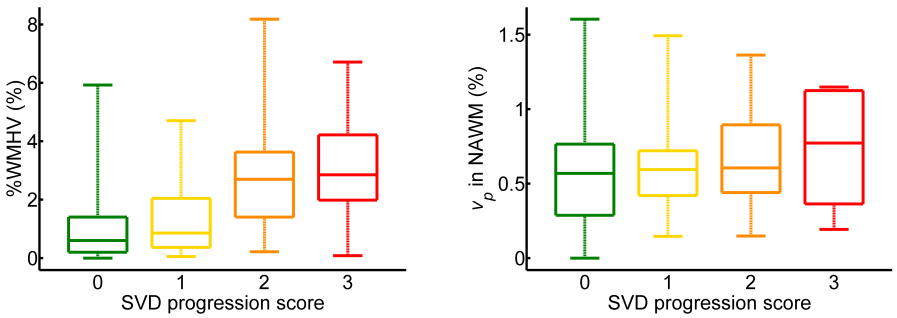

(a) %WMHV (b) v_p in NAWM

Figure 7.7.: Predictors of disease progression at one year follow-up. Relationship between SVD progression score and (a) relative WMH volume %WMHV and (b) blood plasma volume v_p in NAWM at baseline. Both relationships were statistically significant after correction for age, sex, stroke type, brain tissue volume and vascular risk factors (see Table 7.8).

blood plasma volume and known higher blood flow in DGM structures (Brickman et al., 2009). K^{Trans} in DGM was also found to increase with brain atrophy after correction for age and vascular risk factors. A similar association has been found in a study on Alzheimer's disease, where the CSF:plasma albumin ratio was positively correlated with the severity of medial temporal lobe atrophy (Matsumoto et al., 2007). While several perfusion studies have shown that reduced cerebral blood flow is linked to brain atrophy (Alosco et al., 2013; Kitagawa et al., 1985; Zonneveld et al., 2015), information about the relationship between BBB permeability and brain atrophy is scarce. It should be noted that the finding of increased K^{Trans} with low brain volume may be influenced by collinearity in the statistical analysis as the brain tissue volume decreases with age, which was also a predictor in the model. However, the relevant variance inflation factors did not exceed a value of 2.3, which was well below recommended cut-off points of between 5 and 10 (Stine, 1995).

Age was negatively associated with both K^{Trans} and v_p in normal-appearing tissues and WMH. A reduction in cerebral blood volume with age is consistent with literature reports (Marchal et al., 1992; Shaul et al., 2014). However, the finding of decreasing K^{Trans} with age contradicts previous reports. For instance, a comprehensive literature review and meta-analysis (Farrall and Wardlaw, 2009) found that BBB permeability increases subtly with age (mostly based on studies using CSF:plasma albumin ratio). This is consistent with pathological studies, which have shown that the function and structure of the BBB deteriorate during ageing (De Reuck, 2012; Elahy et al., 2015; Marques et al., 2013; Popescu et al., 2009). However, using CSF:plasma albumin ratio as a measure of BBB permeability has its own shortcomings (Chen, 2011) and there is very little information on the association between BBB permeability and age from DCE-MRI studies. Su et al. (1998) showed a non-significant increase in BBB

permeability with normal ageing in a small study of normal-appearing canine brain tissue, while a small study by Montagne et al. (2015) found a significant increase of BBB permeability with age in the hippocampus of non-demented older subjects, but not in other GM structures or WM. A possible explanation for the apparent decrease of K^{Trans} with age in our study is that the K^{Trans} measurements (commonly used as a marker of BBB permeability) are equally influenced by capillary surface area and/or volume, which are assumed not to change with age or other features in the models. A reduction in capillary density has been reported to occur with ageing (Brown and Thore, 2011) and is also consistent with our finding of reduction in cerebral blood volume with age. It is therefore desirable to obtain estimates of vessel density/size in future studies so as to include them in the permeability calculations. Moreover, it should be noted that the measurements may also be influenced by cerebral blood flow, which is well-known to decrease with age (Aanerud et al., 2012; Leenders et al., 1990; Martin et al., 1991; Stoquart-ElSankari et al., 2007). However, the numerical simulations presented in chapter 4 suggested that the Patlak parameters are robust to differences in blood flow, making a confounding effect unlikely.

WMH were found to have greater v_p than NAWM. This may seem surprising, since WMH are often regarded as 'ischaemic' lesions and might therefore be expected to have reduced plasma volume. However, very few studies have measured cerebral blood volume and blood flow in WMH themselves, as opposed to general measurements in patients with WMH, and the results are conflicting. While some studies using dynamic susceptibility MRI (DSC-MRI) have reported reduced blood volume in WMH compared to NAWM, e.g. Sachdev et al. (2004, $n = 55$), a positron emission tomography study by Yamauchi et al. (1990, $n = 7$) found increased blood volume in WMH compared to NAWM. Marstrand et al. (2002, $n = 21$) found no significant difference in blood volume in WMH compared to NAWM; this is also consistent with our findings in the external SVD patient cohort (see chapter 6, $n = 25$). A recent 7 T MRI study found reduced blood volume in deep WMH, but unchanged blood volume in periventricular WMH (Anderson et al., 2014, $n = 23$). Although DCE-MRI is a more quantitative marker of microvascular properties than DSC-MRI, previous studies applying DCE-MRI in SVD have not reported v_p values for WMH. A possible explanation for the higher WMH blood volume found in this study is that a few WMH are found in tissue that was originally DGM, especially in the head of the caudate nucleus, where baseline blood volume is likely to be higher than in WM. However, the volume of hyperintensities in DGM is small compared to the overall WMH volume and, hence, unlikely to account for the measured differences. Another explanation for increased plasma volume in WMH arises from cerebrovascular autoregulation mechanisms. In the early stages of ischaemia, the human brain counteracts a reduction in blood flow with vasodilation (Kulik et al., 2008; Kunz and Iadecola, 2009). Thus, elevated blood volume measurements may be due to dilated blood vessels and indicate early stages of tissue damage. This is also consistent with our finding that raised blood volume measurements in NAWM and

DGM increase the risk of visible disease progression over one year. However, it should be noted that all patients included in this study presented with a stroke; consequently, their brains have most likely been exposed to ischaemic processes for several years and autoregulatory function may already be impaired (Powers, 1991). Plasma volume in WMH was also found to decrease with increasing WMH volume, possibly representing advancing tissue damage as the disease burden increases and there is less tissue to supply. The exact role of cerebral blood volume and BBB breakdown in WMH remains to be defined; future studies should assess BBB permeability, cerebral blood flow and blood volume in WMH as well as normal tissues so as to resolve this issue.

WMH volume at baseline was found to be a strong predictor of disease progression at one year follow-up. This confirms findings of a number of other studies, which reported a significant relationship between WMH burden at baseline and WMH progression (Sachdev et al., 2007; Schmidt et al., 2003; van Dijk et al., 2008) as well as cognitive decline (Benedictus et al., 2015; Debette et al., 2007). Several other factors have previously been implicated in the progression of cerebral SVD, including age (Taylor et al., 2003), hypertension (Verhaaren et al., 2013) and diabetes (Taylor et al., 2003). In the analysis presented in this chapter, none of these risk factors were significant predictors of SVD progression; this may be due to the follow-up time of one year, which is short compared to other longitudinal studies. An additional grant from Chest Heart and Stroke Scotland is currently funding clinical and cognitive follow-up at three years post stroke; these data will allow future research to investigate predictors of long-term disease progression and cognitive decline. Unfortunately, there was no DCE-MRI assessment at follow-up, which could have enabled the investigation into the progression of subtle BBB disruption and/or the reproducibility of quantitative estimates. This was not included in the original grant in order to decrease the imaging time at follow-up; this limited the burden for the patient and, thus, increased the likelihood of the patient returning. It should also be noted that the analysis performed here only captures the progression of WMH. However, a reduction in WMH burden was seen in several patients, which is consistent with a recent report of regressing WMH in ischaemic stroke patients (Cho et al., 2015). A more complex analysis that considers this apparent 'shrinkage' of WMH and investigates its clinical relevance will be performed in future work.

The statistical analyses presented in this chapter did not include Bonferroni correction for multiple comparisons. This decision was made because Bonferroni adjustment has been criticised for being overly conservative and increasing the likelihood of type II errors (Perneger, 1998). Nevertheless, it should be noted that the significance of reported results may be overestimated due to multiple comparisons. Moreover, as discussed previously, the analyses presented in this chapter are limited by the choice of large-tissue ROIs, which do not allow for an investigation of local variation in DCE-MRI parameters. However, in comparison to recent work (Huisa

et al., 2015; Montagne et al., 2015), this study provides whole-brain coverage in a large, well phenotyped patient sample. Semi-quantitative analysis of spatially-relevant subregions (e.g. NAWM surrounding WMH, similar to the work presented in Muñoz Maniega et al., 2015) is currently being performed by other researchers in the group; a similar approach using quantitative DCE-MRI measurements will be considered in future work.

7.5. Conclusion

The purpose of this chapter was to analyse the DCE-MRI parameters measured in the MSSII cohort with regard to differences between tissue types and associations with general clinical characteristics, SVD imaging markers and disease progression. K^{Trans} was found to be higher in WMH than in NAWM, consistent with previous suggestions of increased BBB disruption in WM pathology. However, there was no evidence that normal-appearing tissue K^{Trans} is higher in lacunar versus cortical stroke patients, linked to high SVD burden at baseline (in particular, the amount of WMH, EPVS, microbleeds and lacunes) or predicts disease progression at one year follow-up. Both K^{Trans} and v_p appeared to decrease with advancing age; while the reduction in cerebral blood volume with age is consistent the literature, the finding of decreasing K^{Trans} with age contradicts previous reports and may be governed by changes in capillary shape, size and/or density rather than true change in subtle BBB permeability, i.e. overall leakage may decrease due to falling surface area, outweighing an increase (if any) in permeability. Plasma volume was higher in WMH compared to NAWM; this finding may be explained by vasodilation in response to the expected reduced blood flow in presumed ischaemic tissue. Moreover, raised blood volume measurements in NAWM and DGM were found to increase the risk of disease progression over one year, suggesting that elevated blood volume measurements may indicate early stages of tissue damage due to SVD. The strongest predictor of disease progression at one year follow-up was the WMH volume at baseline, which is consistent with literature reports and supports the potential use of WMH volume as an outcome measure in preventive trials. In order to further clarify the role of BBB disruption and other microvascular properties in SVD aetiology and progression, future studies should include longitudinal observations and assess capillary anatomy to complement DCE-MRI measurements.

Table 7.8.: Ordinal logistic regression analyses of disease progression at one year follow-up. The degree of disease progression was measured using a combined score, with points being given for a recurrent neurovascular event, increased number of microbleeds, worsening of Fazekas score, brain atrophy score and EPVS score. Separate models models were fitted for K^{Trans} and v_p in each tissue type and age, stroke subtype, WMH volume %WMHV, brain tissue volume %BTV and $T1_0$ at baseline as predictors of SVD progression score. The model was also corrected for vascular risk factors (hypertension, diabetes, smoking and hypercholesterolaemia); however, these factors were statistically insignificant and are omitted from this table for brevity. Results are given as odds ratio, 95% CI and p-value; the odds ratios express the relative odds of a high SVD progression score per point increase in the predictor variable.

Tissue	Predictor	SVD progression score	
		Odds ratio (95% CI)	p
NAWM	K^{Trans} ($\cdot 10^4$ min^{-1})	0.96 (0.78, 1.2)	0.71
	v_p ($\cdot 10^2$)	2.9 (1.1, 7.4)	**0.029**
	Age (years)	1.0 (0.98, 1.1)	0.27
	Gender[a]	0.92 (0.47, 1.8)	0.8
	Stroke subtype[b]	1.7 (0.91, 3.1)	0.099
	%WMHV (%)	1.5 (1.2, 1.9)	**<0.001**
	%BTV (%)	0.93 (0.85, 1.0)	0.1
	$T1_0$ (s)	0.18 (0.0068, 4.7)	0.3
WMH	K^{Trans} ($\cdot 10^4$ min^{-1})	1.0 (0.87, 1.2)	0.7
	v_p ($\cdot 10^2$)	1.5 (0.74, 3.0)	0.27
	Age (years)	1.0 (0.98, 1.1)	0.36
	Gender[a]	0.98 (0.5, 1.9)	0.94
	Stroke subtype[b]	1.7 (0.92, 3.2)	0.089
	%WMHV (%)	1.5 (1.2, 1.9)	**<0.001**
	%BTV (%)	0.94 (0.86, 1.0)	0.15
	$T1_0$ (s)	0.78 (0.059, 10)	0.85
DGM	K^{Trans} ($\cdot 10^4$ min^{-1})	0.95 (0.77, 1.2)	0.6
	v_p ($\cdot 10^2$)	2.3 (1.0, 5.2)	**0.044**
	Age (years)	1.0 (0.98, 1.1)	0.31
	Gender[a]	0.89 (0.45, 1.8)	0.74
	Stroke subtype[b]	1.7 (0.92, 3.2)	0.088
	%WMHV (%)	1.5 (1.2, 1.9)	**<0.001**
	%BTV (%)	0.92 (0.84, 1.0)	0.087
	$T1_0$ (s)	0.21 (0.016, 2.9)	0.25
RSL	K^{Trans} ($\cdot 10^4$ min^{-1})	0.95 (0.87, 1.0)	0.24
	v_p ($\cdot 10^2$)	1.3 (0.66, 2.6)	0.44
	Age (years)	0.99 (0.94, 1.0)	0.57
	Gender[a]	0.79 (0.35, 1.8)	0.56
	Stroke subtype[b]	1.7 (0.78, 3.5)	0.19
	%WMHV (%)	1.5 (1.2, 2.0)	**0.0019**
	%BTV (%)	0.92 (0.84, 1.0)	0.12
	$T1_0$ (s)	2.5 (0.50, 12)	0.27

[a]Male=0, female=1, [b]cortical=0, lacunar=1

8. Blood pressure and sodium: association with magnetic resonance imaging markers in cerebral small vessel disease

The previous work described in this thesis was embedded into the Mild Stroke Study II (MSSII), which is a comprehensive clinical study looking at several aspects of cerebral small vessel disease (SVD). As such, this project benefited from the various assessments other than dynamic contrast-enhanced magnetic resonance imaging (DCE-MRI; e.g. blood markers, cognitive testing and diffusion tensor MRI (DT-MRI)). The work presented in this chapter was performed within the wider scope of the MSSII and aimed to investigate the association between MRI findings and blood pressure, dietary salt intake and plasma sodium concentration. The contents of this chapter are the result of joint work with Dr Michael J Thrippleton, which has been published in Heye and Thrippleton et al. (2016b). The author and Dr Michael J Thrippleton contributed equally to the statistical analyses presented in this chapter. The author also provided the DCE-MRI measurements used in this work; clinical parameters, volume measurements and DT-MRI parameters were provided by other members of the research team. These contributions by others will be clearly indicated throughout the text.

8.1. Introduction

As discussed in section 1.1.3 of this thesis, the pathogenesis of cerebral SVD is poorly understood. However, hypertension and other vascular risk factors have been identified. Previous work revealed associations between blood pressure and white matter hyperintensity (WMH) burden and between blood pressure and pre-visible white matter damage assessed by DT-MRI (Aribisala et al., 2014; Maclullich et al., 2009). The influence of dietary salt intake on stroke incidence and mortality is well-known (Li et al., 2012b) but may be only partly mediated by its effect on blood pressure (Strazzullo et al., 2009). Plasma sodium concentration is assumed to be tightly regulated but there is some evidence to suggest that even small variations can affect physical and mental health in the elderly population (Decaux, 2006; Schrier, 2010). The role of dietary and plasma sodium in cerebral SVD is unclear.

This work aimed to investigate the association between blood pressure, dietary salt intake and plasma sodium concentration with MRI findings in the MSSII cohort of patients exhibiting a spectrum of SVD severity. In particular, this work assessed associations with WMH volume,

brain tissue volume, DT-MRI measures of tissue integrity and DCE-MRI measurements of blood-brain barrier (BBB) leakage and cerebral blood volume.

8.2. Methods

8.2.1. Participants

The details of patient recruitment, inclusion and exclusion criteria have been given in section 3.2.2. In short, 264 adult patients with non-disabling lacunar or mild cortical ischaemic stroke were recruited from the local stroke services.

8.2.2. Data collection

This section will provide a brief summary of the data collection procedures in the MSSII that are relevant for this chapter; please refer to section 3.2.3 for detailed information.

On presentation, the research fellow Dr Stephen Makin collected clinical data, medical and life style history. Hypertension was defined as blood pressure of 140/90 mmHg or greater on presentation or a previous diagnosis. Smokers were defined as currently smoking or having given up within the previous 12 months and non-smokers as having never smoked or having given up more than 12 months previously. Pulse pressure (PP) and mean arterial pressure (MAP) were calculated from the systolic and diastolic blood pressures (SBP and DBP) as SBP - DBP and 1/3 SBP + 2/3 DBP, respectively. Salt intake was assessed by asking participants to describe their addition of salt to food during cooking and at the dining table using the following salt intake score: 1 = always, 2 = often, 3 = occasionally, 4 = rarely, and 5 = never; the mean of the two scores was subtracted from 6 to give an ordinal categorical variable in the range of 1 (minimum use of salt) to 5 (maximum use of salt) for use in statistical analyses. Plasma sodium concentration was measured from blood samples taken during clinic assessment.

As part of the initial assessment, all 264 patients underwent a diagnostic MRI scan on a 1.5 T MRI scanner. The protocol included three-dimensional (3D) T1-weighted (T1W) inversion recovery prepared spoiled gradient echo (GRE), T2-weighted fast spin echo, T2*-weighted GRE, fluid attenuated inversion recovery, susceptibility-weighted imaging and DT-MRI acquisitions. Participants returned approximately one to three months after presentation for DCE-MRI, which consisted of 20 consecutive 3D T1W spoiled GRE acquisitions with a temporal resolution of 73 s and a total acquisition time of approximately 24 min.

8.2.3. Image processing and analysis

Information about brain tissue types and volumes were extracted semi-automatically by Dr Maria del C Valdés Hernández. As described in section 3.2.4, segmentation masks were generated for the intracranial volume (ICV) and the following tissue types (see Figure 3.3): cerebrospinal fluid, normal-appearing white matter (NAWM), WMH, deep/subcortical grey matter (DGM) and recent stroke lesions. The resulting segmentation masks were used to calculate the brain tissue volume as a percentage of ICV (%BTV) and WMH volume as a percentage of ICV (%WMHV).

DT-MRI data were processed by Dr Maria del C Valdés Hernández to generate mean diffusivity (MD) and fractional anisotropy (FA) parametric images, using in-house software created by Dr Paul A Armitage (please refer to section 3.2.4 for detailed information). In each patient, median MD and FA were extracted for NAWM and DGM.

DCE-MRI were processed as described in section 3.3. Our previously published analysis (Heye and Thrippleton et al. 2016b) focused on a semi-quantitative area under the curve (AUC) parameter, because the tracer kinetic modelling work presented in chapter 4 was still ongoing. Since then, the analysis was repeated using the Patlak parameters K^{Trans} and v_p, which provide quantitative measurements of BBB leakage and blood volume.

8.2.4. Statistical analysis

Descriptive statistics in the text are given as mean $\pm$ standard deviation. Regressions were assessed by examination of the differences between the data and model predictions, and collinearity by variance inflation factors. All statistical analyses were performed by myself using Matlab (MathWorks, Inc., MA, USA) and by Dr Michael J Thrippleton using SPSS version 19 (IBM Corp., NY, USA), with support from Dr Francesca Chappell. Predictors of %WMHV and %BTV were investigated using multiple linear regression models with correction for age, smoking status, stroke subtype and additional factors given in the text and tables. Residuals for the %WMHV model were not approximately normally distributed; to correct for this, the transformed outcome variable $\ln(0.005 + \%\mathrm{WMHV})$ was regressed instead. DGM MD (units 10^{-6} mm^{2}s^{-1}) was also transformed to $\ln(-700 + \mathrm{MD})$ for this reason.

8.3. Results

8.3.1. Cohort characteristics

A total of 264 subjects were recruited into the study with a mean age of 66.9 ± 11.8 years and a ratio of 45:55 for diagnosis of lacunar-to-cortical stroke; 39% of patients were smokers and 72% had hypertension. An overview of cohort-average demographic, clinical, and imaging variables is provided in Table 8.1.

8.3.2. Associations with WMH and brain tissue volume

PP ($\beta = 0.0092$ mmHg^{-1}; $p = 0.036$) and a diagnosis of hypertension ($\beta = 0.46$; $p = 0.0093$) were significant predictors of increased WMH volume as a percentage of ICV with correction for age, stroke subtype and smoking status (see Table 8.2 and Figure 8.1). Repetition of the analysis with replacement of PP and MAP with diastolic and systolic blood pressure showed that systolic but not diastolic blood pressure was positively associated with transformed %WMHV ($\beta = 0.0079$ mmHg^{-1}; $p = 0.040$). Salt intake score was also positively associated with WMH volume ($\beta = 0.14$; $p = 0.021$; see Figure 8.1); further analyses using the separate scores for cooking and table salt usage were consistent with this finding ($\beta = -0.11/-0.067$; $p = 0.020/0.18$ for cooking/table salt; note that the coefficient sign change is expected, since the combined score was inverted). Regression analysis of brain tissue volume with the same covariates revealed a positive association between plasma sodium concentration and %BTV corresponding to an absolute increase in brain tissue volume of 2% ICV per 10 mmol/l sodium ($p = 0.019$). Age was the most significant factor in the analyses of both %WMHV and %BTV ($p < 0.0001$).

8.3.3. Associations with DT-MRI

DT-MRI data were obtained in 262 subjects (DT-MRI data for two subjects were rejected due to failure of the non-linear image registration). The influence of blood pressure, added salt intake and plasma sodium concentration on these variables was modelled with correction for smoking, stroke subtype and age, as well as normalised WMH volume to account for SVD severity (see Table 8.3). Plasma sodium concentration was negatively associated with MD in NAWM ($\beta = -1.2 \cdot 10^{-6}$ mm^{2}s^{-1}mmol^{-1}l; $p = 0.011$) and FA in DGM ($\beta = -0.9 \cdot 10^{-3}$ mmol^{-1}l; $p = 0.021$). Salt intake score was negatively associated with FA in DGM ($\beta = -3.4 \cdot 10^{-3}$; $p = 0.0012$); additional analyses using the separate scores for salt usage during cooking and at the table were consistent with this finding ($\beta = 2.0/2.5$; $p = 0.016/0.0052$ for cooking/table

Table 8.1.: Baseline characteristics of the MSSII cohort. Descriptive statistics for demographic, clinical and imaging variables including DT-MRI and DCE-MRI parameters in NAWM and DGM. Values for continuous demographic and clinical variables are given as cohort mean and standard deviation; values for imaging variables are given as cohort median and interquartile range, because they were not generally normally distributed.

Parameter	n	Value
Demographic variables		
Age (years)	264	66.9 ± 11.8
Gender (% female)	264	42
Clinical variables		
Stroke subtype (% lacunar)	264	45
Hypertension (%)	264	72
Smoker[a] (%)	262	39
Diabetes (%)	264	11
PP (mmHg)	264	63.1 ± 20.1
MAP (mmHg)	264	102.6 ± 15.2
Salt intake score	250	2.7 ± 1.3
Plasma sodium concentration (mmol/l)	260	139.2 ± 3.3
Imaging variables		
Structural MRI		
WMH volume (%)	264	0.89 [0.31, 2.39]
Brain tissue volume (%)	264	70.68 [67.31, 73.99]
DT-MRI		
MD ($\cdot 10^{-4}$ mm^2/s)		
NAWM	262	7.87 [7.64, 8.10]
DGM	262	7.89 [7.63, 8.28]
FA ($\cdot 10^{-1}$)		
NAWM	262	2.56 [2.42, 2.69]
DGM	262	2.32 [2.20, 2.47]
DCE-MRI		
K^{Trans} ($\cdot 10^{-4}$ min^{-1})		
NAWM	201	2.75 [1.85, 4.12]
DGM	201	3.85 [2.83, 4.68]
v_p ($\cdot 10^{-2}$)		
NAWM	201	0.57 [0.32, 0.80]
DGM	201	1.20 [0.94, 1.43]

[a]Currently smoking or had given up within the previous 12 months

salt). In NAWM, there were corresponding trends for reduced FA with increasing salt score ($\beta = -1.3 \cdot 10^{-3}$; $p = 0.19$) and lower plasma sodium ($\beta = 0.62 \cdot 10^{-3}$ mmol^{-1}l; $p = 0.090$) but these were not significant at the two-tailed 5% type 1 error level.

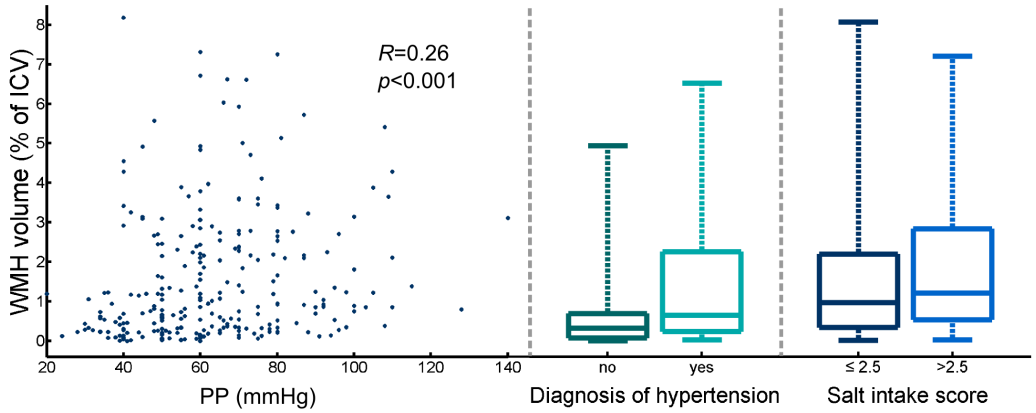

Figure 8.1.: Relationship between WMH volume and PP, diagnosis of hypertension and salt intake score. The association between WMH volume and PP (Spearman's $R = 0.26$, $p < 0.001$) survived correction for age and all other factors listed in Table 8.2. Reprinted from Heye and Thrippleton et al. (2016b).

Table 8.2.: Multiple linear regression analysis of %WMHV and %BTV. Separate models models were fitted with %WMHV and %BTV, respectively, as the dependent variable and PP, MAP, hypertension, salt intake score, plasma sodium, smoking, stroke subtype and age as explanatory variables. Results are given as β coefficient, 95% confidence interval (CI) and p-value.

Predictor	**ln(0.005+%WMHV)**		**%BTV**	
	β (95% CI)	p	β (95% CI)	p
PP (mmHg)	0.0092 (0.00059, 0.018)	**0.036**	−0.022 (−0.054, 0.011)	0.20
MAP (mmHg)	−0.0037 (−0.015, 0.0073)	0.51	0.013 (−0.029, 0.055)	0.55
Hypertension	0.46 (0.11, 0.81)	**0.0093**	−0.68 (−2.0, 0.65)	0.31
Salt intake score	0.14 (0.021, 0.25)	**0.021**	0.26 (−0.19, 0.70)	0.26
Sodium (mmol/l)	−0.029 (−0.072, 0.014)	0.18	0.20 (0.033, 0.36)	**0.019**
Smoking	0.31 (−0.0033, 0.63)	0.052	−1.2 (−2.4, 0.039)	0.058
Stroke subtype[a]	0.27 (−0.023, 0.57)	0.07	−0.40 (−1.5, 0.73)	0.49
Age (years)	0.053 (0.039, 0.067)	**<0.001**	−0.25 (−0.30, −0.20)	**<0.001**

[a]Cortical=0, lacunar=1

8.3.4. Associations with DCE-MRI

Of the 264 patients recruited, DCE-MRI data suitable for analysis was obtained in 201 patients. DCE-MRI parameters K^{Trans} and v_p were modelled using the same covariates as for DT-MRI data (see Table 8.4). Plasma sodium concentration was positively associated with v_p in NAWM ($\beta = 2.1 \cdot 10^{-4}\text{mmol}^{-1}\text{l}$; $p = 0.0043$) and hypertension was a significant negative predictor ($\beta = -1.3 \cdot 10^{-3}$; $p = 0.032$). Age was negatively associated with v_p in both NAWM and DGM ($p = 0.015/0.0054$); age was also the only significant predictor of K^{Trans} in both NAWM and DGM (negative association, $p < 0.001$).

Table 8.3.: Multiple linear regression analysis of DT-MRI measurements. Separate models models were fitted with MD and FA in NAWM and DGM as the dependent variable and PP, MAP, hypertension, salt intake score, plasma sodium, smoking, stroke subtype, age and %WMHV as explanatory variables. Please note that DGM MD was transformed to $\ln(-700 + \text{MD})$ to correct for not approximately normally distributed residuals. Results are given as β coefficient, 95% CI and p-value.

Tissue	Predictor	MD ($\cdot 10^{-6}$ mm^{2}s^{-1})		FA ($\cdot 10^{-3}$)	
		β (95% CI)	p	β (95% CI)	p
NAWM	PP (mmHg)	0.16 (−0.021, 0.34)	0.083	−0.030 (−0.17, 0.11)	0.68
	MAP (mmHg)	−0.14 (−0.38, 0.090)	0.23	−0.041 (−0.22, 0.14)	0.66
	Hypertension	0.64 (−6.7, 8.0)	0.86	−2.1 (−7.9, 3.7)	0.48
	Salt intake score	0.54 (−1.9, 3.0)	0.66	−1.3 (−3.2, 0.63)	0.19
	Sodium (mmol/l)	−1.2 (−2.1, −0.28)	**0.011**	0.62 (−0.096, 1.3)	0.09
	Smoking[a]	3.8 (−2.9, 10.)	0.27	−1.5 (−6.8, 3.7)	0.57
	Stroke subtype[b]	0.60 (−5.7, 6.9)	0.85	−0.047 (−5.0, 4.9)	0.98
	Age (years)	1.2 (0.89, 1.5)	**<0.001**	−0.53 (−0.77, −0.28)	**<0.001**
	%WMHV (%)	4.9 (2.8, 7.0)	**<0.001**	−4.5 (−6.1, −2.9)	**<0.001**
DGM	PP (mmHg)	0.00079 (−0.0018, 0.0033)	0.54	0.056 (−0.095, 0.21)	0.47
	MAP (mmHg)	0.0020 (−0.0013, 0.0052)	0.24	−0.094 (−0.29, 0.10)	0.34
	Hypertension	0.046 (−0.058, 0.15)	0.39	−3.7 (−9.8, 2.4)	0.23
	Salt intake score	0.013 (−0.022, 0.048)	0.46	−3.4 (−5.5, −1.4)	**0.0012**
	Sodium (mmol/l)	−0.0027 (−0.015, 0.010)	0.68	−0.90 (−1.7, −0.14)	**0.021**
	Smoking[a]	0.016 (−0.078, 0.11)	0.74	2.0 (−3.6, 7.6)	0.48
	Stroke subtype[b]	0.096 (0.0079, 0.18)	**0.033**	−9.8 (−15, −4.5)	**<0.001**
	Age (years)	0.014 (0.0095, 0.018)	**<0.001**	0.088 (−0.18, 0.35)	0.51
	%WMHV (%)	0.15 (0.12, 0.18)	**<0.001**	−2.3 (−4.0, −0.56)	**0.0097**

[a]Currently smoking or had given up within the previous 12 months, [b]cortical=0, lacunar=1

8.4. Discussion

The finding that arterial blood pressure is associated with increased WMH volume is broadly consistent with the results of previous studies (Aribisala et al., 2014; Maclullich et al., 2009; Liu et al., 2012; Shrestha et al., 2009; Verhaaren et al., 2013; Waldstein et al., 2012) and with the hypothesis that sustained pressure elevation and pressure fluctuations in the small cerebral vessels result in microvascular damage (O'Rourke and Safar, 2005). The independent association with clinical diagnosis of hypertension, additional to that of PP, likely reflects the historical effect of blood pressure elevation on vasculature and end organs in addition to that at the time of the study. Others have shown that WMH volume is also predicted by increased large artery stiffness, which may be one cause of increased pressure fluctuations in the small cerebral vessels (Brisset et al., 2013; Poels et al., 2012).

A novel finding of this study is that routinely adding more salt to food, which likely increases overall dietary salt intake in addition to the amounts of salt already present in food, is associated with greater WMH volume. There was also a highly significant negative association between

Table 8.4.: Multiple linear regression analysis of DCE-MRI measurements. Separate models models were fitted with K^{Trans} and v_p in NAWM and DGM as the dependent variable and PP, MAP, hypertension, salt intake score, plasma sodium, smoking, stroke subtype, age and %WMHV as explanatory variables. Results are given as β coefficient, 95% CI and p-value.

Tissue	Predictor	K^{Trans} ($\cdot 10^{-5}$ min^{-1})		v_p ($\cdot 10^{-4}$)	
		β (95% CI)	p	β (95% CI)	p
NAWM	PP (mmHg)	0.035 (−0.10, 0.17)	0.60	−0.035 (−0.31, 0.24)	0.80
	MAP (mmHg)	−0.049 (−0.23, 0.13)	0.58	0.037 (−0.33, 0.40)	0.84
	Hypertension	4.3 (−1.4, 10.0)	0.14	−13 (−26, −1.2)	**0.032**
	Salt intake score	−0.14 (−2.0, 1.7)	0.88	0.11 (−3.7, 4.0)	0.95
	Sodium (mmol/l)	0.084 (−0.61, 0.77)	0.81	2.1 (0.66, 3.5)	**0.0043**
	Smoking[a]	−2.6 (−7.8, 2.6)	0.33	−9.3 (−20, 1.4)	0.090
	Stroke subtype[b]	−4.2 (−9.0, 0.45)	0.076	5.5 (−4.1, 15)	0.26
	Age (years)	−0.46 (−0.71, −0.20)	**<0.001**	−0.66 (−1.2, −0.13)	**0.015**
	%WMHV (%)	0.66 (−0.92, 2.3)	0.41	3.2 (−0.071, 6.4)	0.055
DGM	PP (mmHg)	0.098 (−0.034, 0.23)	0.14	−0.081 (−0.39, 0.23)	0.61
	MAP (mmHg)	−0.031 (−0.20, 0.14)	0.72	−0.048 (−0.46, 0.36)	0.82
	Hypertension	2.8 (−2.9, 8.4)	0.33	−11 (−24, 2.4)	0.11
	Salt intake score	0.70 (−1.1, 2.6)	0.45	−0.13 (−4.5, 4.3)	0.95
	Sodium (mmol/l)	−0.43 (−1.1, 0.25)	0.22	1.1 (−0.50, 2.7)	0.17
	Smoking[a]	2.2 (−2.9, 7.4)	0.39	−10 (−22, 2.1)	0.11
	Stroke subtype[b]	−3.4 (−8.0, 1.3)	0.15	5.2 (−5.8, 16)	0.35
	Age (years)	−0.52 (−0.77, −0.26)	**<0.001**	−0.86 (−1.5, −0.26)	**0.0054**
	%WMHV (%)	1.0 (−0.53, 2.6)	0.196	2.1 (−1.6, 5.8)	0.26

[a]Currently smoking or had given up within the previous 12 months, [b]cortical=0, lacunar=1

the salt intake score and FA in normal-appearing DGM, suggestive of 'previsible' reduced tissue integrity (Aribisala et al., 2014). The interactions between salt intake, blood pressure and cerebrovascular disease are not fully understood: it is widely accepted that sodium intake increases blood pressure (Mente et al., 2014) and that hypertension leads to cardiovascular disease including stroke (He et al., 2013; O'Donnell et al., 2014) and there is indirect evidence to support the beneficial effects of reducing the salt intake on the incidence of cardiovascular disease (O'Donnell et al., 2014; Cappuccio and Ji, 2012). Furthermore, epidemiological studies indicate that salt intake is associated with increased risk of stroke and cardiovascular disease independently of blood pressure (Aburto et al., 2013; Gardener et al., 2012; Strazzullo et al., 2009). The findings presented here, which are corrected for blood pressure (both PP and MAP), hypertension and age (as much as one can), suggest this might also be the case in cerebral SVD. Studies in the literature addressing the role of sodium in SVD are lacking and the pathophysiological mechanism of any harm is unclear. A possible direct effect of salt on the endothelium, in addition to any effect via elevated blood pressure, might account for the increased stroke risk due to salt beyond that accounted for by hypertension alone: for example, salt-sensitive (versus salt-resistant) hypertension is associated with peripheral endothelial dysfunction (Bragulat et al., 2001) which, if also present in the brain, might account for the dynamic cerebral and systemic endothelial dysfunction seen in several studies of SVD

(Stevenson et al., 2010) and the increased level of WMH seen here. However, although the linear model used here fitted the data well, the significance of salt intake score as an independent predictor of WMH could also be influenced by complex non-linear interactions between salt intake, blood pressure and vascular disease, which become steeper with advancing age, in hypertensives and high salt intake (O'Donnell et al., 2014).

In contrast to dietary sodium consumption, plasma sodium concentration did not predict WMH volume but was associated with brain tissue volume, corresponding to an increase of 2% of ICV per 10 mmol/l sodium. Lower plasma sodium was also associated with increased MD in NAWM and increased FA in DGM. The explanations for these associations are unknown and should be explored in future studies. Changes in brain volume may occur following acute changes in osmolality, but are thought to be temporary and rapidly reversed following changes in solute balance (Verbalis, 2010). Furthermore, none of the participants in this study were either hypernatraemic (defined as [Na]$>$146 mmol/l) or severely hyponatraemic ([Na]$<$125 mmol/l), though 13% were mild to moderately hyponatraemic (125$\leq$[Na]$\leq$135 mmol/l). These findings may reflect transient changes related to hydration state, diet, time of day or other factors. Most patients were managed as outpatients, not being ill enough to require hospital admission, and were mobile, cognitively competent outpatients with no clinical evidence of dehydration. However, plasma sodium was also associated with blood plasma volume measured with DCE-MRI one month later, corresponding to a relative increase in v_p in NAWM of 36% per 10 mmol/l sodium. This finding suggests that part of the association with brain volume may be accounted for by differences in blood volume; it is also consistent with our previous analysis based on the AUC as a semi-quantitative measurement of contrast uptake (Heye and Thrippleton et al., 2016b). It should be noted that most significant correlations with salt intake and blood pressure were found for volume measurements rather than DCE-MRI parameters, indicating that DCE-MRI may be of limited clinical use for this application.

All analyses presented in this work were corrected for whether subjects were smokers. In line with the previous literature, smokers had both greater WMH volume (Staals et al., 2014) and lower brain volume (Swan and Lessov-Schlaggar, 2007) corresponding to a total brain volume difference of approximately 1% of ICV.

The results concerning added dietary salt are limited by the qualitative and self-reported nature of these data. The index, based on a simple questionnaire, was designed for use in a clinical setting and did not attempt to assess total salt intake, an acknowledged complex task due to problems with accurate recall, and by the highly variable amounts of salt present in food or added by manufacturers during processing. However, the index used here may better reflect salt appetite and long-term exposure to salt. There is no gold-standard way to assess the salt intake of these patients retrospectively, and even the validity of a 24 hours urine collection, which is not practical in this cohort, has been questioned (Titze et al., 2013). More complex

questionnaires given by a dietician can provide a measure of intake but also depend on self-report and would not have been appropriate with this cohort of patients. A disadvantage of both detailed dietary questionnaires and biochemical tests is that they provide a snapshot of salt consumption, which may not reflect long-term exposure and habits, particularly during recovery from a stroke where intake may have been influenced by the recent stroke and lifestyle advice. Future work might focus on a more quantitative assessment of salt intake in patients presenting with mild stroke. Despite these reservations, the index used here correlated well with WMH volume and the trend was preserved when assessed using our two separate salt scores.

A second limitation is that the blood tests, while quantitative, measured plasma sodium concentration at a single point in time contemporaneous with measurement of WMH volume, brain tissue volume, FA and MD but not K^{Trans} and v_p. As plasma sodium concentration shows strong individuality, it is unlikely to vary much unless the patient is over or under hydrated (Zhang et al., 2014). The plasma sodium concentration can also be influenced by kidney function, glucose level and medication (13.3% of patients had reduced kidney function (estimated glomerular filtration rate $<$60 ml/min/1.73 m^2) and 19.3% of patients took the diuretic medications Bendrofluimethiazide or Furosemide). However, correcting for these potential confounds made little difference to the results. It should also be noted that the DT-MRI measurements used in this work were obtained using a single diffusion weighting factor b, i.e. assuming a simple monoexponential relationship between MRI signal and b value. However, it is recognised that this assumption does not fully account for tissue behaviour, so that the diffusion coefficient is sensitive to capillary perfusion (Koh et al., 2011). A more sophisticated approach using multiple b values can correct for intravoxel incoherent motion (Le Bihan et al., 1986) and should be considered in future work. Finally, it should be highlighted that the age range of participants in this study was wide (34 years to 96 years) and findings may be confounded by age-related effects not fully eliminated by the model; it is therefore desirable to replicate the findings in a larger study or in a sample with narrower age range.

8.5. Conclusion

This chapter aimed to investigate the association between blood pressure, dietary salt intake and plasma sodium concentration with MRI findings in the MSSII cohort. This work was performed within the wider scope of the MSSII; in addition to DCE-MRI parameters, it also looked at tissue volumes obtained from structural MRI and DT-MRI measurements. Using multiple linear regression analyses, we showed that arterial blood pressure and diagnosis of hypertension predict WMH volume in patients with mild stroke. Added dietary salt intake was also independently associated with WMH. Plasma sodium concentration, while not associated

with WMH volume, was a significant predictor of brain tissue volume and of blood volume in NAWM. These results are consistent with previous findings that raised blood pressure is associated with WMH burden and raise the possibility of an independent role for dietary salt in the development of cerebral SVD.

Part V.

Conclusions and Perspectives

Contents

9. Discussion and conclusion

It has been suggested that subtle breakdown of the blood-brain barrier (BBB) plays a role in the pathophysiology of cerebral small vessel disease (SVD). Dynamic contrast-enhanced magnetic resonance imaging (DCE-MRI) is widely used for assessing BBB permeability and other microvascular properties in brain tumours and body tissues, where contrast agent uptake is typically large and rapid. However, in diseases where leakage is subtle, the magnitude and rate of enhancement caused by contrast extravasation are extremely low. Consequently, the optimal approach for quantifying BBB integrity in this situation and the reliability of resulting measurements is unclear. The main purpose of this thesis was to assess and improve the reliability of quantitative assessment of subtle BBB disruption, in order to illuminate its potential role in cerebral SVD. After summarising the main findings (section 9.1), this final chapter outlines the contributions that this work has made towards achieving these goals (section 9.2). Moreover, this chapter highlights limitations of the work presented in this thesis and suggests avenues for future research (section 9.3).

9.1. Summary of findings

Part I of this thesis provided an overview of cerebral SVD and DCE-MRI methods. After introducing the fundamental concepts that the work in this thesis is based on (chapter 1), a systematic literature review of DCE-MRI methods in the brain was presented (chapter 2). The review revealed 95 studies that assessed BBB disruption in 18 different pathologies; these studies showed considerable heterogeneity with regard to image acquisition and analysis methods. With the majority of studies investigating tumours, the review identified a relative lack of studies investigating the best methods of measuring low-level BBB disruption in ageing, dementia or cerebral microvascular disease.

Part II of this thesis focused on the analysis of DCE-MRI data acquired within the scope of an on-site clinical study of mild stroke patients, the Mild Stroke Study II (MSSII). The DCE-MRI data acquired in the MSSII consisted of whole-brain acquisitions (with a temporal resolution of 73 s and an overall acquisition time of approximately 24 min) in 201 patients. In addition to presenting the study cohort and procedures, chapter 3 addressed several basic aspects of DCE-MRI processing and analysis. Patient-individual vascular input functions were extracted from a single voxel in the superior sagittal sinus. Due to low contrast-to-noise ratio (CNR) and small overall signal enhancement, analysis of the DCE-MRI data on a voxel-by-voxel basis was found not to be suitable for the detection of subtle changes in BBB functionality.

Therefore, signal intensity, signal enhancement and contrast concentration profiles as well as $T1_0$ were calculated on a whole-tissue basis for normal-appearing white matter (NAWM), white matter hyperintensities (WMH), deep/subcortical grey matter (DGM) and recent stroke lesions. The signal enhancement curves were characterised using the semi-quantitative measurements AUC_E^{bn} and $slope_E$. Chapter 4 investigated which of several tracer kinetic modelling approaches was most suitable for assessing subtle BBB disruption in the MSSII patient cohort. A data-driven model comparison using the Akaike information criterion suggested that the Patlak model is an appropriate method for measuring v_p and low-level K^{Trans}. Numerical simulations were performed in order to investigate the validity of the Patlak model. The simulations confirmed that the Patlak model yields reliable estimates of K^{Trans} and v_p when PS is low. By omitting data that is acquired during the first pass of the contrast bolus, accurate parameter values could be obtained independently of cerebral blood flow and despite the use of a temporal resolution much lower than is typically employed in DCE-MRI. Semi-quantitative parameters were shown to correlate with both K^{Trans} and v_p and to be highly dependent on blood flow and $T1_0$, thus reflecting a combination of underlying tissue properties.

Part III of this thesis investigated two potential pitfalls in the quantification of subtle BBB disruption. Firstly, chapter 5 investigated signal drift unrelated to contrast effects and its influence on tracer kinetic parameters; this was of particular concern due to the long overall acquisition time of the MSSII data. Drift measurements were performed in a group of healthy volunteers ($n = 15$), showing a linear signal increase of approximately 0.08 %/min. Computer simulations showed that this drift introduces a systematic error when estimating low-level tracer kinetic parameters. Despite the confounding influence of drift, the simulations indicate that K^{Trans} and v_p estimates remain approximately linear independent functions of the extravasation rate and plasma volume respectively. Secondly, chapter 6 addressed issues concerning inter-study comparability and study design, which arose from the retrospective analysis of DCE-MRI data acquired in an external study, the Campus Bio-Medico Study (CBMS; $n = 25$). Due to the nature of the acquisition protocol it proved difficult to obtain reliable quantitative parameters in this cohort. For instance, the scan duration of approximately 3 min to 4 min was not long enough to reliably capture subtle BBB leakage. Moreover, the temporal resolution of approximately 6.5 s was not sufficient to quantify blood flow. Unaccounted differences in blood flow were shown to introduce significant errors in estimated tracer kinetic parameters, particularly the permeability-surface area product PS. Consequently, the only quantitative parameter that could be obtained with reasonable accuracy in the CBMS cohort is the blood plasma volume v_p using the steady state model. The lack of agreed standards for DCE-MRI assessment of subtle BBB disruption and the effect of unknown drift lead to significant differences in tracer kinetic parameters: here, v_p estimates obtained in the CBMS cohort were approximately twice as high as in the MSSII cohort, which is unlikely as the patient populations were similar in many respects.

Lastly, part IV of this thesis examined the relationship between MRI parameters and clinical measurements in the MSSII cohort. Chapter 7 investigated the tracer kinetic parameters obtained in part II with regard to differences between tissue types and associations with clinical characteristics, SVD imaging markers and disease progression. K^{Trans} was found to be higher in WMH than in NAWM, indicating that the BBB is impaired in white matter pathology. However, there was no evidence that BBB permeability in normal-appearing tissues is linked to higher SVD burden or predicts disease progression. Both K^{Trans} and v_p appeared to decrease with advancing age; the finding of decreasing K^{Trans} with age is inconsistent with other literature reports and may be governed by differences in capillary shape, size and/or density rather than indicating change in BBB permeability. Plasma volume was higher in WMH compared to NAWM; this finding may be explained by vasodilation in response to the expected reduced blood flow in presumed ischaemic tissue. Plasma volume in WMH was also found to decrease with increasing WMH volume, possibly representing advancing tissue damage as the disease burden increases and there is less tissue to supply. Moreover, raised blood volume measurements in NAWM and DGM were found to increase the risk of disease progression over one year, suggesting that elevated blood volume measurements may indicate early stages of tissue damage due to SVD. The strongest predictor of disease progression at one year follow-up was the WMH volume at baseline. The work presented in chapter 8 investigated the association of MRI findings with blood pressure, dietary salt intake and plasma sodium concentration. This work was performed within the wider scope of the MSSII; in addition to DCE-MRI parameters, it also looked at tissue volumes obtained from structural MRI and diffusion tensor MRI (DT-MRI) measurements. Using multiple linear regression analyses, it was shown that arterial pulse pressure and diagnosis of hypertension are positive predictors of WMH volume. Added dietary salt intake was also independently associated with WMH volume. Plasma sodium concentration, while not associated with WMH volume, was a significant predictor of brain tissue volume and of blood volume v_p in NAWM.

9.2. Strengths and contributions

9.2.1. Contributions to DCE-MRI methodology for the assessment of subtle BBB disruption

In the past, DCE-MRI has been mainly applied in body tissues without BBB and in diseases with large abnormalities in BBB functionality. Consequently, previous reviews of DCE-MRI methods (Barnes et al., 2012; Bergamino et al., 2014; Jain, 2013; Türkbey et al., 2010) and attempts to standardise methodology (DCE MRI Technical Committee, 2012; Leach et al., 2012) have mainly focused on specific applications such as oncology. As far as the author is

aware, the comprehensive literature review performed within the scope of this project (Heye et al., 2014) provided the first systematic overview of DCE-MRI methods in the brain that covers a wide range of applications including ageing, microvascular disease and dementia.

When this project began, there was very little information available relating to the methodology for measuring low-level BBB disruption. As regards data analysis methods, most groups studying subtle BBB disruption have applied semi-quantitative analysis approaches (e.g. Hanyu et al., 2002; Wardlaw et al., 2008; Starr et al., 2009; Topakian et al., 2010; Wahlund and Bronge, 2000; Wardlaw et al., 2008). The few studies that have used model-based approaches to quantifying subtle BBB leakage (e.g. Israeli et al., 2011; Taheri et al., 2011b) did not explicitly justify their methodology or investigate its validity. Data-driven model selection and simulation studies have recently gained popularity in DCE-MRI, with most studies focussing on oncology applications (e.g. Bagher-Ebadian et al., 2012; Ewing et al., 2006; Larsson et al., 2009; Sourbron et al., 2009). A similar approach in the MSSII cohort showed that the Patlak model is an appropriate method for measuring v_p and low-level K^{Trans}. While this finding only strictly applies to the particular acquisition protocol used in the MSSII, it is consistent with recent investigations by Cramer and Larsson (2014) and Barnes et al. (2015). The contemporaneous work presented in this thesis sets itself apart from these studies by investigating a much larger clinical cohort and exploring in depth potential technical influences and biological confounds. Moreover, the MSSII employs a temporal resolution that is significantly lower than typically used in DCE-MRI. To the best of the author's knowledge, it has not been shown previously that accurate quantitative parameters can be obtained despite a very low temporal resolution. Ultimately, the model selection work presented in this thesis (in combination with similar work by e.g. Cramer and Larsson, 2014) increases confidence in applying tracer kinetic models in disorders with subtle BBB disruption and justifies the emerging popularity of the Patlak model in this situation. However, this work also serves to highlight that low-level tracer kinetic parameters should be interpreted with caution; for instance, K^{Trans} is often interpreted as BBB permeability although it is equally influenced by the capillary surface area, which may dominate measurements if BBB permeability is subtle (see section 9.3).

A novel finding of the work presented in this thesis is that low-level tracer kinetic parameter measurements are subject to substantial systematic errors introduced by signal drift. Signal drift measurements are rarely reported in the DCE-MRI literature and the effect of signal drift has previously been considered negligible (Cramer et al., 2014). This work highlights the importance of measuring drift during DCE-MRI studies in order to assess its magnitude and likely effects on quantitative parameters. Since this work was undertaken, another study has examined the effect of signal drift on tracer kinetic parameters using computer simulations (Barnes et al., 2015); however, these investigations were not accompanied by in vivo measurements. Despite the confounding influence of drift, tracer kinetic parameters provided (in this case) independent

indications of BBB integrity and blood plasma volume; while the work presented in this thesis sounds a note of caution regarding the absolute values of tracer kinetic parameters, it has also shown that such quantities remain easier to interpret than semi-quantitative measurements.

This thesis has also highlighted the importance of study design and has given some general guidance on protocol design for investigating diffuse, subtle BBB pathology. For instance, the finding in the MSSII that accurate estimates of BBB permeability can be obtained despite a very low sampling rate, means that temporal resolution can be reduced for the benefit of spatial resolution, whole-brain coverage and CNR. Moreover, the difficulty in obtaining reliable measurements of BBB permeability in the CBMS cohort highlighted the importance of a sufficiently long acquisition time. Numerical simulations have been shown to be a useful tool for assessing the validity of tracer kinetic models with regard to a particular acquisition protocol and should be performed before a study protocol is finalised. While it is impossible to prescribe a universal 'recipe' for future studies, this thesis provides researchers interested in applying DCE-MRI to the measurement of subtle BBB abnormalities with a number of important aspects to consider.

9.2.2. Contributions to understanding the pathophysiology of cerebral SVD

Previous on-site clinical studies suggested that cerebral SVD may be associated with abnormal BBB functionality, which could explain many of the imaging and pathological observations related to SVD (Wardlaw et al., 2003). The MSSII aimed to confirm these findings and to investigate whether BBB dysfunction is associated with the presence and progression of clinical and imaging markers of cerebral SVD. To the best of the author's knowledge, this is the first study that provides quantitative measurements of BBB leakage and blood volume in a large cohort of patients with cerebral SVD. Related studies either only calculate semi-quantitative DCE-MRI parameters (e.g. Wardlaw et al., 2008; Topakian et al., 2010) or are based on significantly smaller sample sizes (e.g. Huisa et al., 2015; Montagne et al., 2015; Taheri et al., 2011a). Moreover, an important advantage of the MSSII compared to other studies is that it provides DCE-MRI data with whole-brain coverage; this not only better captures the diffuse nature of the disease, but also facilitates pre-processing steps such as image registration, which is important in order to compensate for motion and to allow overlay of tissue masks derived from structural images. In addition, most studies in the field focus on WMH as the most prominent manifestation of cerebral SVD, but do not cover the whole disease spectrum (e.g. Hanyu et al., 2002; Huisa et al., 2015; Wahlund and Bronge, 2000). In contrast, all patients in the MSSII underwent detailed radiological MRI assessment, which quantified several aspects of SVD in addition to WMH, e.g. including lacunes and microbleeds.

The work presented in this thesis could not fully clarify the role of BBB leakage and other microvascular properties in cerebral SVD. On the one hand, the findings of this study are consistent with increased BBB leakage occurring in WMH, as previously suggested by some pathology and imaging studies (Tomimoto et al., 1996; Wharton et al., 2015; Young et al., 2008; Hanyu et al., 2002; Taheri et al., 2011b; Topakian et al., 2010). On the other hand, there was no evidence that normal-appearing tissue K^{Trans} increases with SVD burden or predicts disease progression. While this finding does not support the hypothesis that endothelial failure plays an initiating role in the development of SVD, it should be noted that the K^{Trans} measurements are likely to be governed by capillary structure rather than BBB permeability; this limitation will be discussed in detail below. In contrast, experimental work on a relevant rat model, which has proceeded in parallel with the human MRI work presented here, has confirmed earlier findings of weak endothelial tight junctions creating a weak BBB that predisposes to tissue damage and development of SVD (Bailey et al., 2011, 2014). Raised blood volume measurements in normal-appearing tissues were shown to increase the risk of visible disease progression over one year, which is a novel finding. Previous studies applying DCE-MRI in SVD have either not investigated or not reported cerebral blood volume, although it is closely linked to other microvascular properties such as blood flow. The work presented in this thesis has provided some mechanistic insight into the role of blood volume in cerebral SVD and raises the possibility that elevated blood volume measurements may be used as an early indicator of impending tissue damage due to SVD. Nevertheless, it should be noted that elevated blood volume measurements were a significantly weaker predictor of disease progression when compared to WMH volume at baseline. Since DCE-MRI parameters are also significantly more difficult to obtain and less reliable, DCE-MRI is currently not the most appropriate technique for predicting SVD disease progression in clinical practice.

This project benefited from the comprehensive design of the MSSII. The availability of various clinical and imaging data in addition to DCE-MRI (e.g. blood markers and DT-MRI) allowed for a range of analyses. Consequently, this thesis presented several findings that go beyond investigating the role of the BBB. For instance, this work has confirmed previous findings that WMH burden is linked to raised blood pressure and that disease progression in cerebral SVD patients is strongly predicted by WMH burden at baseline. Furthermore, the finding that increased dietary salt intake is associated with greater WMH volume raises the possibility of an independent role for dietary salt in the development of cerebral SVD, consistent with findings for other cardiovascular diseases (see Heye and Thrippleton et al. 2016b). Overall, the exact pathological processes that cause cerebral SVD are still largely unknown; nevertheless, the work presented in this thesis adds to the knowledge in the field and has yielded novel findings that can be validated or contradicted in future studies.

9.3. Limitations and future directions

A significant limitation of this work is that the MSSII data had been collected before this project started, so that it was not possible to make changes to the image acquisition. There are a number of potential improvements to the imaging strategy, which should be considered in future research. The DCE-MRI data that formed the basis of this PhD project were acquired on a 1.5 T MRI scanner using a three-dimensional T1-weighted spoiled gradient echo (GRE) sequence. While spoiled GRE methods allow for large spatial coverage and high spatial resolution, they have two main disadvantages. Firstly, they are known to be sensitive to flip angle inaccuracy and radio frequency (RF) field inhomogeneity (Subashi et al., 2014; Tofts, 2010), particularly at high field strengths (Cheng and Wright, 2006). Indeed, measurements in healthy volunteers using the same protocol and scanner as in the MSSII showed that significant signal drift occurs during the acquisition period. This change in signal intensity over time is most likely caused by instability of instrumental parameters (e.g. flip angle, $\mathbf{B}_0$ field), but true variations in T1 may also contribute to signal drift; this aspect should be investigated using larger sample sizes. Future studies could reduce the sensitivity to instrumental instability by employing DCE-MRI methods that consist of repeated T1 measurements (e.g. Shah et al., 2001), which can self-compensate for changes in the RF field strength and flip angle and for signal drift. Nevertheless, scanners with stable and homogeneous magnetic fields are important in order to improve measurements of subtle BBB abnormalities in the future. Secondly, spoiled GRE methods often suffer from a low signal-to-noise ratio (SNR); in the MSSII, a low SNR was found to hinder voxel-by-voxel analysis. Technical developments in hardware and acquisition methods are likely to improve the quality of DCE-MRI data and facilitate the measurement of subtle BBB abnormalities in the future. For instance, newer scanners with higher field strengths not only provide a substantially higher SNR, but also have faster gradients that allow for shorter repetition times. Consequently, future studies should be performed on a newer scanner with a higher field strength. In addition, a large number of recent studies focus on the development of efficient imaging techniques, which significantly shorten acquisition times without compromising spatial resolution (e.g. Jung et al., 2009; Tsao et al., 2003). Strategies for improving both temporal and spatial resolution often employ partial k-space acquisition techniques, including keyhole imaging (van Vaals et al., 1993), view-sharing (such as the TWIST sequence employed in chapter 6) or compressed sensing (e.g. Han et al., 2012). For further acceleration of DCE-MRI acquisitions, these approaches have recently been combined with parallel imaging (Rosenkrantz et al., 2015; Yoon et al., 2014). However, it has not yet been explored in detail how these unique methods of k-space undersampling influence the measured signal dynamics. Moreover, most methods that significantly shorten acquisition times inevitably degrade the SNR; in contrast to traditional DCE-MRI applications, this trade-off is most likely not sensible for the measurement of subtle BBB leakage, where image quality

is more important than temporal resolution.

As discussed throughout this thesis, DCE-MRI studies are limited by several assumptions and sources of error. While the presented work directly investigated some of these aspects (e.g. validity of model assumptions, influence of signal drift), others received relatively little attention because they have been explored in detail elsewhere (e.g. arterial input function and $T1_0$ measurement). The importance of correcting DCE-MRI signal enhancement profiles for intrinsic parameters such as $T1_0$ and r_1 has been highlighted previously. In this study, the DCE-MRI analysis relied on assumed in vitro values for contrast agent relaxivities. Since relaxivity measurements are known to vary significantly between tissue samples and different disease stages (Armitage et al., 2011), this represents a significant weakness and potential source of error. However, reliable estimation of r_1 is challenging so that relaxivity properties of in vivo brain tissues remain largely unknown. Moreover, $T1_0$ was measured using the variable flip angle method, which is known to be sensitive to RF field inhomogeneities across the brain (Schabel and Parker, 2008). In future studies, it would be prudent to employ methods that estimate the RF field and can correct for flip angle errors, such as DESPOT1-HIFI (Deoni, 2007). An additional source of error that was not investigated in this thesis is the water exchange effect. The tracer kinetic models used in this study assume that the water exchange between the vascular, EES and intracellular compartments is in the fast-exchange limit, i.e. that the tissue relaxes with a single T1. While the water exchange between the intracellular and extravascular extracellular space most likely has a negligible effect on DCE-MRI (Bains et al., 2010), Larsson et al. (2001) found a significant effect of transendothelial water exchange on DCE-MRI derived parameters in the brain. Particularly in brain tissues with a largely intact BBB, as investigated here, the assumption of fast water exchange is likely to introduce systematic errors. Although several models that account for water exchange have been developed (e.g. Carreira et al., 2009; Li et al., 2005), these typically include a large number of free parameters that could not have been fitted reliably in the MSSII data. The influence of water exchange effects on low-level DCE-MRI measurements should be investigated in future studies.

A confounding factor that has been identified here and should be investigated in future work is the effect of noise and artefacts on low-level tracer kinetic parameters. Due to the small magnitude of contrast-induced signal changes in normal-appearing tissues, low-level motion artefacts and Gibbs ringing were found to have a disproportionate effect on voxel-wise maps of tracer kinetic parameters (see Figure 4.10), possibly because of the high enhancements in vascular, permeable tissues ghosting into the brain tissue. The influence of noise and artefacts was reduced by averaging over large regions of interest; however, voxel-wise analysis is desirable in order to detect local variations in BBB function. Several image processing techniques have been suggested for denoising (Gal et al., 2008; Taheri and Sood, 2006) of DCE-MRI data as well as compensation of motion effects (Hamy et al., 2014; Melbourne

et al., 2011), partial volume effects (Taheri and Sood, 2007) and Gibbs ringing (Di Bella et al., 2005). It would be interesting to apply these methods in the MSSII data and explore whether they can improve the quality of voxel-wise tracer kinetic analysis.

The main aim of the MSSII was to investigate whether cerebral SVD is linked to BBB permeability. However, the DCE-MRI parameter K^{Trans} (or PS) is equally influenced by the capillary surface area. Microvascular architecture is known to vary with age and disease state (Bailey et al., 2012; Brown and Thore, 2011) and, thus, is likely to have a significant effect on the obtained K^{Trans} measurements. In the MSSII cohort, falling capillary density could explain the apparent reduction in K^{Trans} with advancing age, which is at variance with virtually all other human and experimental model data on the ageing brain. In order to obtain estimates of BBB permeability (rather than BBB leakage), future studies should try to determine vessel density and size. Traditionally, this type of information is obtained by pathologists; however, problems caused by cerebral SVD are rarely fatal so that pathological studies are not usually accomplishable in this situation. Recently, a number of MRI techniques have emerged for in vivo measurement of microvessel density and size (Troprès et al., 2015). While most of these methods have been applied and validated in pre-clinical studies, Xu et al. (2011, 2012) recently showed that vessel size imaging is feasible in acute stroke patients and can be combined with perfusion imaging. Since most microvascular properties (structural and functional) are interrelated, such combined approaches may help future studies to obtain several complementary parameters in a clinically acceptable imaging time and to investigate the bigger picture of microvascular changes in cerebral SVD. However, it should be noted that quantitative vessel size imaging is (just like quantitative analysis of DCE-MRI) based on several simplifying assumptions (Kiselev et al., 2005) and requires special acquisition sequences. Therefore, it is not yet well established and its potential for human in vivo applications remains to be explored.

While the work presented in this thesis has demonstrated that it is possible to obtain quantitative estimates of subtle BBB leakage using DCE-MRI, uncertainty over the physiological meaning of these parameters remains. There is a concern that DCE-MRI parameters, particularly when trying to measure subtle effects, are more dependent on the various sources of error than on the physiological properties of interest. In order to fully clarify whether DCE-MRI can provide valid measurements of subtle BBB leakage, comparison studies with 'true' measures of microvascular properties are urgently needed. However, obtaining ground truth measurements for comparison is often difficult in practice. For instance, other in vivo estimates of BBB disruption (e.g. the commonly used CSF:plasma albumin ratio) also suffer from limited interpretability (Chen, 2011). As mentioned previously, investigations into the pathophysiology of cerebral SVD are currently being performed in a relevant rat model (Bailey et al., 2014); while histopathological studies are difficult to implement in humans, animal models may enable a

validation of low-level DCE-MRI measurements as performed previously in other pathologies (e.g. Ferrier et al., 2007; Knight et al., 2005). Furthermore, the validity of DCE-MRI measurements could be explored theoretically using computational fluid dynamics and phantom measurements. Phantom- and model-based evaluation methods have recently been developed for dynamic contrast-enhanced computed tomography (Driscoll et al., 2011; Hariharan et al., 2013; Peladeau-Pigeon and Coolens, 2013) and could potentially be adapted for DCE-MRI measurements of subtle BBB leakage.

Finally, BBB disruption is only one of several competing theories that seek to explain the causes of cerebral SVD (Wardlaw et al., 2013b). Following the MSSII, two on-site clinical studies have been established to investigate other (possibly related) processes that may play a role in the pathophysiology of cerebral SVD. For instance, vessel wall thickening was seen in early pathological studies (Bailey et al., 2012; Gouw et al., 2011); this has lead to the suggestion that the arterioles might also be stiffer and therefore less able to vasodilate to increase blood supply when necessary. In order to test this hypothesis, 60 patients with lacunar or cortical mild stroke are undergoing BOLD (Blood Oxygen Level Dependent) MRI, which combined with a CO_2 respiratory challenge enables the measurement of cerebrovascular reactivity in vivo (Rostrup et al., 1994). Furthermore, there is some evidence to suggest that inflammatory processes are involved in the development of cerebral SVD (Bailey et al., 2012; Gouw et al., 2011; Fazekas et al., 1993). Novel MRI techniques can image the uptake of ultrasmall superparamagnetic iron oxide particles (USPIOs) into inflammatory cells and, thus, detect areas of inflammation (Dousset et al., 2006). An on-site pilot project currently investigates whether this method allows for detection of inflammation in cerebral SVD. It is hoped that, in combination with the work presented here, these investigations will ultimately provide a better understanding of the pathogenesis of cerebral SVD, which is required to develop effective treatments that can prevent severe outcomes such as strokes and dementia.

9.4. Final summary

The work described in this thesis has demonstrated that it is possible to estimate subtle BBB disruption using DCE-MRI, provided that the measurement and data analysis strategies are carefully optimised. However, absolute values of tracer kinetic parameters should be interpreted with caution, particularly when making comparisons between studies, and sources of error and their influence should be estimated where possible. The exact role of BBB breakdown and other microvascular changes in SVD pathology remain to be defined; however, the work presented in this thesis contributes further insights and, together with technical advances, will help to facilitate optimal study design in the future.

Bibliography

Aanerud, J., Borghammer, P., Chakravarty, M. M., Vang, K., Rodell, A. B., Jónsdottir, K. Y., Mø ller, A., Ashkanian, M., Vafaee, M. S., Iversen, P., Johannsen, P., and Gjedde, A. (2012). Brain energy metabolism and blood flow differences in healthy aging. *Journal of Cerebral Blood Flow and Metabolism*, 32(7):1177–87.

Abbott, N. J. and Friedman, A. (2012). Overview and introduction: the blood-brain barrier in health and disease. *Epilepsia*, 53 Suppl 6:1–6.

Abe, T., Mizobuchi, Y., Nakajima, K., Otomi, Y., Irahara, S., Obama, Y., Majigsuren, M., Khashbat, D., Kageji, T., Nagahiro, S., and Harada, M. (2015). Diagnosis of brain tumors using dynamic contrast-enhanced perfusion imaging with a short acquisition time. *SpringerPlus*, 4:88.

Abo-Ramadan, U., Durukan, A., Pitkonen, M., Marinkovic, I., Tatlisumak, E., Pedrono, E., Soinne, L., Strbian, D., and Tatlisumak, T. (2009). Post-ischemic leakiness of the blood-brain barrier: a quantitative and systematic assessment by Patlak plots. *Experimental Neurology*, 219(1):328–33.

Aburto, N. J., Ziolkovska, A., Hooper, L., Elliott, P., Cappuccio, F. P., and Meerpohl, J. J. (2013). Effect of lower sodium intake on health: systematic review and meta-analyses. *BMJ (Clinical Research Ed.)*, 346:f1326.

Ahearn, T. S., Staff, R. T., Redpath, T. W., and Semple, S. I. K. (2005). The use of the Levenberg-Marquardt curve-fitting algorithm in pharmacokinetic modelling of DCE-MRI data. *Physics in Medicine and Biology*, 50(9):N85–92.

Ahn, S. S., Shin, N.-Y., Chang, J. H., Kim, S. H., Kim, E. H., Kim, D. W., and Lee, S.-K. (2014). Prediction of methylguanine methyltransferase promoter methylation in glioblastoma using dynamic contrast-enhanced magnetic resonance and diffusion tensor imaging. *Journal of Neurosurgery*, 121(2):367–73.

Akaike, H. (1974). A new look at the statistical model identification. *IEEE Transactions on Automatic Control*, 19(6):716–723.

Aksoy, D., Bammer, R., Mlynash, M., Venkatasubramanian, C., Eyngorn, I., Snider, R. W., Gupta, S. N., Narayana, R., Fischbein, N., and Wijman, C. A. C. (2013). Magnetic resonance imaging profile of blood-brain barrier injury in patients with acute intracerebral hemorrhage. *Journal of the American Heart Association*, 2(3):e000161.

Ali, M. M., Janic, B., Babajani-Feremi, A., Varma, N. R. S., Iskander, A. S. M., Anagli, J., and Arbab, A. S. (2010). Changes in vascular permeability and expression of different angiogenic factors following anti-angiogenic treatment in rat glioma. *PloS one*, 5(1):e8727.

Almeida-Freitas, D. B., Pinho, M. C., Otaduy, M. C. G., Braga, H. F., Meira-Freitas, D., and Da Costa Leite, C. (2014). Assessment of irradiated brain metastases using dynamic contrast-enhanced magnetic resonance imaging. *Neuroradiology*, 56(6):437–443.

Alosco, M. L., Gunstad, J., Jerskey, B. A., Xu, X., Clark, U. S., Hassenstab, J., Cote, D. M., Walsh, E. G., Labbe, D. R., Hoge, R., Cohen, R. A., and Sweet, L. H. (2013). The adverse effects of reduced cerebral perfusion on cognition and brain structure in older adults with cardiovascular disease. *Brain and Behavior*, 3(6):626–36.

Anderson, V. C., Obayashi, J. T., Kaye, J. A., Quinn, J. F., Berryhill, P., Riccelli, L. P., Peterson, D., and Rooney, W. D. (2014). Longitudinal relaxographic imaging of white matter hyperintensities in the elderly. *Fluids and Barriers of the CNS*, 11:24.

Aribisala, B. S., Morris, Z., Eadie, E., Thomas, A., Gow, A., Valdés Hernández, M. D. C., Royle, N. A., Bastin, M. E., Starr, J., Deary, I. J., and Wardlaw, J. M. (2014). Blood pressure, internal carotid artery flow parameters, and age-related white matter hyperintensities. *Hypertension*, 63(5):1011–1018.

Aribisala, B. S., Valdés Hernández, M. D. C., Royle, N. A., Morris, Z., Muñoz Maniega, S., Bastin, M. E., Deary, I. J., and Wardlaw, J. M. (2013). Brain atrophy associations with white matter lesions in the ageing brain: the Lothian Birth Cohort 1936. *European Radiology*, 23(4):1084–92.

Armitage, P. A., Behrenbruch, C., Brady, M., and Moore, N. (2005). Extracting and visualizing physiological parameters using dynamic contrast-enhanced magnetic resonance imaging of the breast. *Medical Image Analysis*, 9(4):315–29.

Armitage, P. A., Farrall, A. J., Carpenter, T. K., Doubal, F. N., and Wardlaw, J. M. (2011). Use of dynamic contrast-enhanced MRI to measure subtle blood-brain barrier abnormalities. *Magnetic Resonance Imaging*, 29(3):305–14.

Artzi, M., Liberman, G., Nadav, G., Vitinshtein, F., Blumenthal, D. T., Bokstein, F., Aizenstein, O., and Bashat, D. B. (2015). Human cerebral blood volume measurements using dynamic contrast enhancement in comparison to dynamic susceptibility contrast MRI. *Neuroradiology*, 57(7):671–8.

Aryal, M. P., Nagaraja, T. N., Keenan, K. A., Bagher-Ebadian, H., Panda, S., Brown, S. L., Cabral, G., Fenstermacher, J. D., and Ewing, J. R. (2014). Dynamic contrast enhanced

MRI parameters and tumor cellularity in a rat model of cerebral glioma at 7 T. *Magnetic Resonance in Medicine*, 71(6):2206–14.

Awasthi, R., Pandey, C. M., Sahoo, P., Behari, S., Kumar, V., Kumar, S., Misra, S., Husain, N., Soni, P., Rathore, R. K. S., and Gupta, R. K. (2012). Dynamic contrast-enhanced magnetic resonance imaging-derived kep as a potential biomarker of matrix metalloproteinase 9 expression in patients with glioblastoma multiforme: a pilot study. *Journal of Computer Assisted Tomography*, 36(1):125–30.

Baezner, H., Blahak, C., Poggesi, A., Pantoni, L., Inzitari, D., Chabriat, H., Erkinjuntti, T., Fazekas, F., Ferro, J. M., Langhorne, P., O'Brien, J., Scheltens, P., Visser, M. C., Wahlund, L. O., Waldemar, G., Wallin, A., and Hennerici, M. G. (2008). Association of gait and balance disorders with age-related white matter changes: the LADIS study. *Neurology*, 70(12):935–42.

Bagher-Ebadian, H., Jain, R., Nejad-Davarani, S. P., Mikkelsen, T., Lu, M., Jiang, Q., Scarpace, L., Arbab, A. S., Narang, J., Soltanian-Zadeh, H., Paudyal, R., and Ewing, J. R. (2012). Model selection for DCE-T1 studies in glioblastoma. *Magnetic Resonance in Medicine*, 68(1):241–51.

Bailey, E. L., McBride, M. W., Beattie, W., McClure, J. D., Graham, D., Dominiczak, A. F., Sudlow, C. L. M., Smith, C., and Wardlaw, J. M. (2014). Differential gene expression in multiple neurological, inflammatory and connective tissue pathways in a spontaneous model of human small vessel stroke. *Neuropathology and Applied Neurobiology*, 40(7):855–72.

Bailey, E. L., McCulloch, J., Sudlow, C., and Wardlaw, J. M. (2009). Potential animal models of lacunar stroke: a systematic review. *Stroke*, 40(6):e451–8.

Bailey, E. L., Smith, C., Sudlow, C. L. M., and Wardlaw, J. M. (2012). Pathology of lacunar ischemic stroke in humans – a systematic review. *Brain Pathology*, 22(5):583–91.

Bailey, E. L., Wardlaw, J. M., Graham, D., Dominiczak, A. F., Sudlow, C. L. M., and Smith, C. (2011). Cerebral small vessel endothelial structural changes predate hypertension in stroke-prone spontaneously hypertensive rats: a blinded, controlled immunohistochemical study of 5- to 21-week-old rats. *Neuropathology and Applied Neurobiology*, 37(7):711–26.

Bains, L. J., McGrath, D. M., Naish, J. H., Cheung, S., Watson, Y., Taylor, M. B., Logue, J. P., Parker, G. J. M., Waterton, J. C., and Buckley, D. L. (2010). Tracer kinetic analysis of dynamic contrast-enhanced MRI and CT bladder cancer data: A preliminary comparison to assess the magnitude of water exchange effects. *Magnetic Resonance in Medicine*, 64(2):595–603.

Balvay, D., Kachenoura, N., Espinoza, S., Thomassin-naggara, I., Fournier, L. S., and Clement, O. (2011). Signal-to-Noise Ratio improvement in dynamic contrast-enhanced CT and MR imaging with automated principal component analysis filtering. *Radiology*, 258(2):435–445.

Bamford, J., Sandercock, P., Dennis, M., Burn, J., and Warlow, C. (1991). Classification and natural history of clinically identifiable subtypes of cerebral infarction. *Lancet*, 337(8756):1521–6.

Barber, T. W., Brockway, J. A., and Higgins, L. S. (1970). The density of tissues in and about the head. *Acta Neurologica Scandinavica*, 46(1):85–92.

Barnes, S. L., Whisenant, J. G., Loveless, M. E., and Yankeelov, T. E. (2012). Practical dynamic contrast enhanced MRI in small animal models of cancer: data acquisition, data analysis, and interpretation. *Pharmaceutics*, 4(3):442–78.

Barnes, S. R., Ng, T. S. C., Montagne, A., Law, M., Zlokovic, B. V., and Jacobs, R. E. (2015). Optimal acquisition and modeling parameters for accurate assessment of low Ktrans blood-brain barrier permeability using dynamic contrast-enhanced MRI. *Magnetic Resonance in Medicine [epub ahead of print]*.

Benedictus, M. R., van Harten, A. C., Leeuwis, A. E., Koene, T., Scheltens, P., Barkhof, F., Prins, N. D., and van der Flier, W. M. (2015). White matter hyperintensities relate to clinical progression in subjective cognitive decline. *Stroke*, 46(9):2661–4.

Benisty, S., Gouw, A. A., Porcher, R., Madureira, S., Hernandez, K., Poggesi, A., van der Flier, W. M., Van Straaten, E. C. W., Verdelho, A., Ferro, J., Pantoni, L., Inzitari, D., Barkhof, F., Fazekas, F., and Chabriat, H. (2009). Location of lacunar infarcts correlates with cognition in a sample of non-disabled subjects with age-related white-matter changes: the LADIS study. *Journal of Neurology, Neurosurgery and Psychiatry*, 80(5):478–83.

Bergamino, M., Barletta, L., Castellan, L., Mancardi, G., and Roccatagliata, L. (2015). Dynamic contrast-enhanced MRI in the study of brain tumors. Comparison between the extended Tofts-Kety model and a Phenomenological Universalities (PUN) algorithm. *Journal of Digital Imaging*, 28(6):748–54.

Bergamino, M., Bonzano, L., Levrero, F., Mancardi, G. L., and Roccatagliata, L. (2014). A review of technical aspects of T1-weighted dynamic contrast-enhanced magnetic resonance imaging (DCE-MRI) in human brain tumors. *Physica Medica*, 30(6):1–9.

Bergamino, M., Saitta, L., Barletta, L., Bonzano, L., Mancardi, G. L., Castellan, L., Ravetti, J. L., and Roccatagliata, L. (2013). Measurement of blood-brain barrier permeability with t1-weighted dynamic contrast-enhanced MRI in brain tumors: a comparative study with two different algorithms. *ISRN Neuroscience*, 2013:905279.

Bloch, F. (1946). Nuclear induction. *Physical Review*, 70(7-8):460–474.

Bokura, H., Kobayashi, S., and Yamaguchi, S. (1998). Distinguishing silent lacunar infarction from enlarged Virchow-Robin spaces: a magnetic resonance imaging and pathological study. *Journal of Neurology*, 245(2):116–22.

Bragulat, E., de la Sierra, A., Antonio, M. T., and Coca, A. (2001). Endothelial dysfunction in salt-sensitive essential hypertension. *Hypertension*, 37(2 Pt 2):444–8.

Brandt, C. T., Simonsen, H., Liptrot, M., Sø gaard, L. V., Lundgren, J. D., Ostergaard, C., Frimodt-Mø ller, N., and Rowland, I. J. (2008). In vivo study of experimental pneumococcal meningitis using magnetic resonance imaging. *BMC Medical Imaging*, 8:1.

Braunagel, M., Radler, E., Ingrisch, M., Staehler, M., Schmid-Tannwald, C., Rist, C., Nikolaou, K., Reiser, M. F., and Notohamiprodjo, M. (2015). Dynamic contrast-enhanced magnetic resonance imaging measurements in renal cell carcinoma: effect of region of interest size and positioning on interobserver and intraobserver variability. *Investigative Radiology*, 50(1):57–66.

Breteler, M. M., van Amerongen, N. M., van Swieten, J. C., Claus, J. J., Grobbee, D. E., van Gijn, J., Hofman, A., and van Harskamp, F. (1994). Cognitive correlates of ventricular enlargement and cerebral white matter lesions on magnetic resonance imaging. The Rotterdam Study. *Stroke*, 25(6):1109–15.

Brickman, A. M., Zahra, A., Muraskin, J., Steffener, J., Holland, C. M., Habeck, C., Borogovac, A., Ramos, M. A., Brown, T. R., Asllani, I., and Stern, Y. (2009). Reduction in cerebral blood flow in areas appearing as white matter hyperintensities on magnetic resonance imaging. *Psychiatry Research: Neuroimaging*, 172(2):117–120.

Brisset, M., Boutouyrie, P., Pico, F., Zhu, Y., Zureik, M., Schilling, S., Dufouil, C., Mazoyer, B., Laurent, S., Tzourio, C., and Debette, S. (2013). Large-vessel correlates of cerebral small-vessel disease. *Neurology*, 80(7):662–669.

Brix, G., Semmler, W., Port, R., Schad, L. R., Layer, G., and Lorenz, W. J. (1991). Pharmacokinetic parameters in CNS Gd-DTPA enhanced MR imaging. *Journal of Computer Assisted Tomography*, 15(4):621–8.

Brix, G., Zwick, S., Kiessling, F., and Griebel, J. (2009). Pharmacokinetic analysis of tissue microcirculation using nested models: multimodel inference and parameter identifiability. *Medical Physics*, 36(7):2923–33.

Brookes, J. A., Redpath, T. W., Gilbert, F. J., Murray, A. D., and Staff, R. T. (1999). Accuracy of T1 measurement in dynamic contrast-enhanced breast MRI using two- and three-dimensional variable flip angle fast low-angle shot. *Journal of Magnetic Resonance Imaging*, 9(2):163–71.

Brown, W. R., Moody, D. M., Thore, C. R., and Challa, V. R. (2000). Apoptosis in leukoaraiosis. *American Journal of Neuroradiology*, 21(1):79–82.

Brown, W. R. and Thore, C. R. (2011). Review: cerebral microvascular pathology in ageing and neurodegeneration. *Neuropathology and Applied Neurobiology*, 37(1):56–74.

Budde, M. D., Gold, E., Jordan, E. K., and Frank, J. A. (2012). Differential microstructure and physiology of brain and bone metastases in a rat breast cancer model by diffusion and dynamic contrast enhanced MRI. *Clinical & Experimental Metastasis*, 29(1):51–62.

Burnham, K. P. (2004). Multimodel inference: understanding AIC and BIC in model selection. *Sociological Methods & Research*, 33(2):261–304.

Calamante, F. (2005). Bolus dispersion issues related to the quantification of perfusion MRI data. *Journal of Magnetic Resonance Imaging*, 22(6):718–22.

Calamante, F. (2013). Arterial input function in perfusion MRI: a comprehensive review. *Progress in Nuclear Magnetic Resonance Spectroscopy*, 74:1–32.

Cao, Y., Tsien, C. I., Sundgren, P. C., Nagesh, V., Normolle, D., Buchtel, H., Junck, L., and Lawrence, T. S. (2009). Dynamic contrast-enhanced magnetic resonance imaging as a biomarker for prediction of radiation-induced neurocognitive dysfunction. *Clinical Cancer Research*, 15(5):1747–54.

Cappuccio, F. P. and Ji, C. (2012). Less salt and less risk of stroke: further support to action. *Stroke*, 43(5):1195–1196.

Carreira, G. C., Gemeinhardt, O., Beyersdorff, D., Schnorr, J., Taupitz, M., and Lüdemann, L. (2009). Effects of water exchange on MRI-based determination of relative blood volume using an inversion-prepared gradient echo sequence and a blood pool contrast medium. *Magnetic Resonance Imaging*, 27(3):360–9.

Cha, S., Yang, L., Johnson, G., Lai, A., Chen, M.-H., Tihan, T., Wendland, M., and Dillon, W. P. (2006). Comparison of microvascular permeability measurements, K(trans), determined with conventional steady-state T1-weighted and first-pass T2*-weighted MR imaging methods in gliomas and meningiomas. *American Journal of Neuroradiology*, 27(2):409–17.

Chassidim, Y., Veksler, R., Lublinsky, S., Pell, G. S., Friedman, A., and Shelef, I. (2013). Quantitative imaging assessment of blood-brain barrier permeability in humans. *Fluids and Barriers of the CNS*, 10(1):9.

Chen, J., Yao, J., and Thomasson, D. (2008). Automatic determination of arterial input function for dynamic contrast enhanced MRI in tumor assessment. *Medical Image Computing and Computer-assisted Intervention*, 11(Pt 1):594–601.

Chen, R.-L. (2011). Is it appropriate to use albumin CSF/plasma ratio to assess blood brain barrier permeability? *Neurobiology of Aging*, 32(7):1338–9.

Cheng, H.-L. M. (2008). Investigation and optimization of parameter accuracy in dynamic contrast-enhanced MRI. *Journal of Magnetic Resonance Imaging*, 28(3):736–43.

Cheng, H.-L. M. and Wright, G. A. (2006). Rapid high-resolution T(1) mapping by variable flip angles: accurate and precise measurements in the presence of radiofrequency field inhomogeneity. *Magnetic Resonance in Medicine*, 55(3):566–74.

Cho, A.-H., Kim, H.-R., Kim, W., and Yang, D. W. (2015). White matter hyperintensity in ischemic stroke patients: it may regress over time. *Journal of Stroke*, 17(1):60–6.

Choi, H. S., Kim, A. H., Ahn, S. S., Shin, N. Y., Kim, J., and Lee, S. K. (2013). Glioma grading capability: Comparisons among parameters from dynamic contrast-enhanced MRI and ADC value on DWI. *Korean Journal of Radiology*, 14(3):487–492.

Chu, J.-P., Mak, H. K.-F., Yau, K. K.-W., Zhang, L., Tsang, J., Chan, Q., and Ka-Kit Leung, G. (2012). Pilot study on evaluation of any correlation between MR perfusion (Ktrans) and diffusion (apparent diffusion coefficient) parameters in brain tumors at 3 Tesla. *Cancer Imaging*, 12(1):1–6.

Chwang, W. B., Jain, R., Bagher-Ebadian, H., Nejad-Davarani, S. P., Iskander, a. S. M., Vanslooten, A., Schultz, L., Arbab, A. S., and Ewing, J. R. (2014). Measurement of rat brain tumor kinetics using an intravascular MR contrast agent and DCE-MRI nested model selection. *Journal of Magnetic Resonance Imaging*, 1229:1223–1229.

Cordonnier, C., Al-Shahi Salman, R., and Wardlaw, J. (2007). Spontaneous brain microbleeds: systematic review, subgroup analyses and standards for study design and reporting. *Brain*, 130(8):1988–2003.

Cramer, S. P. and Larsson, H. B. W. (2014). Accurate determination of blood-brain barrier permeability using dynamic contrast-enhanced T1-weighted MRI: a simulation and in vivo study on healthy subjects and multiple sclerosis patients. *Journal of Cerebral Blood Flow and Metabolism*, 34(10):1655–65.

Cramer, S. P., Simonsen, H., Frederiksen, J. L., Rostrup, E., and Larsson, H. B. W. (2014). Abnormal blood-brain barrier permeability in normal appearing white matter in multiple sclerosis investigated by MRI. *NeuroImage Clinical*, 4:182–9.

Davenport, M. S., Heye, T., Dale, B. M., Horvath, J. J., Breault, S. R., Feuerlein, S., Bashir, M. R., Boll, D. T., and Merkle, E. M. (2013). Inter- and intra-rater reproducibility of quantitative dynamic contrast enhanced MRI using TWIST perfusion data in a uterine fibroid model. *Journal of Magnetic Resonance Imaging*, 38(2):329–35.

DCE MRI Technical Committee (2012). DCE MRI quantification profile, Quantitative Imaging Biomarkers Alliance. Version 1.0. Reviewed draft.

de Bazelaire, C., Calmon, R., Thomassin, I., Brunon, C., Hamy, A.-S., Fournier, L., Balvay, D., Espié, M., Siauve, N., Clément, O., de Kerviler, E., and Cuénod, C.-A. (2011). Accuracy of perfusion MRI with high spatial but low temporal resolution to assess invasive breast cancer response to neoadjuvant chemotherapy: a retrospective study. *BMC Cancer*, 11:361.

de Groot, J. C., de Leeuw, F. E., Oudkerk, M., van Gijn, J., Hofman, A., Jolles, J., and Breteler, M. M. (2000). Cerebral white matter lesions and cognitive function: the Rotterdam Scan Study. *Annals of Neurology*, 47(2):145–51.

de Leeuw, F.-E., de Groot, J., Achten, E., Oudkerk, M., Ramos, L., Heijboer, R., Hofman, A., Jolles, J., van Gijn, J., and Breteler, M. (2001). Prevalence of cerebral white matter lesions in elderly people: a population based magnetic resonance imaging study. The Rotterdam Scan Study. *Journal of Neurology, Neurosurgery and Psychiatry*, 70(1):9–14.

de Leeuw, F.-E., Korf, E., Barkhof, F., and Scheltens, P. (2006). White matter lesions are associated with progression of medial temporal lobe atrophy in Alzheimer disease. *Stroke*, 37(9):2248–52.

De Reuck, J. L. (2012). Histopathological stainings and definitions of vascular disruptions in the elderly brain. *Experimental Gerontology*, 47(11):834–837.

Debette, S., Bombois, S., Bruandet, A., Delbeuck, X., Lepoittevin, S., Delmaire, C., Leys, D., and Pasquier, F. (2007). Subcortical hyperintensities are associated with cognitive decline in patients with mild cognitive impairment. *Stroke*, 38(11):2924–30.

Debette, S. and Markus, H. S. (2010). The clinical importance of white matter hyperintensities on brain magnetic resonance imaging: systematic review and meta-analysis. *BMJ*, 341:c3666.

Decaux, G. (2006). Is asymptomatic hyponatremia really asymptomatic? *The American Journal of Medicine*, 119(7):S79–S82.

Deoni, S. C. L. (2007). High-resolution T1 mapping of the brain at 3T with driven equilibrium single pulse observation of T1 with high-speed incorporation of RF field inhomogeneities (DESPOT1-HIFI). *Journal of Magnetic Resonance Imaging*, 26(4):1106–11.

Di Bella, E. V. R., Parker, D. L., and Sinusas, A. J. (2005). On the dark rim artifact in dynamic contrast-enhanced MRI myocardial perfusion studies. *Magnetic Resonance in Medicine*, 54(5):1295–9.

Dichgans, M. and Zietemann, V. (2012). Prevention of vascular cognitive impairment. *Stroke*, 43(11):3137–46.

Donaldson, S. B., West, C. M. L., Davidson, S. E., Carrington, B. M., Hutchison, G., Jones, A. P., Sourbron, S. P., and Buckley, D. L. (2010). A comparison of tracer kinetic models for T1-weighted dynamic contrast-enhanced MRI: application in carcinoma of the cervix. *Magnetic Resonance in Medicine*, 63(3):691–700.

Doubal, F. N., Dennis, M. S., and Wardlaw, J. M. (2011). Characteristics of patients with minor ischaemic strokes and negative MRI: a cross-sectional study. *Journal of Neurology, Neurosurgery, and Psychiatry*, 82(5):540–2.

Doubal, F. N., MacLullich, A. M. J., Ferguson, K. J., Dennis, M. S., and Wardlaw, J. M. (2010). Enlarged perivascular spaces on MRI are a feature of cerebral small vessel disease. *Stroke*, 41(3):450–4.

Dousset, V., Brochet, B., Deloire, M. S. A., Lagoarde, L., Barroso, B., Caille, J.-M., and Petry, K. G. (2006). MR imaging of relapsing multiple sclerosis patients using ultra-small-particle iron oxide and compared with gadolinium. *American Journal of Neuroradiology*, 27(5):1000–5.

Driscoll, B., Keller, H., and Coolens, C. (2011). Development of a dynamic flow imaging phantom for dynamic contrast-enhanced CT. *Medical Physics*, 38(8):4866–80.

Dufouil, C., de Kersaint-Gilly, A., Besançon, V., Levy, C., Auffray, E., Brunnereau, L., Alpérovitch, A., and Tzourio, C. (2001). Longitudinal study of blood pressure and white matter hyperintensities: the EVA MRI Cohort. *Neurology*, 56(7):921–6.

Durukan, A., Marinkovic, I., Strbian, D., Pitkonen, M., Pedrono, E., Soinne, L., Abo-Ramadan, U., and Tatlisumak, T. (2009). Post-ischemic blood-brain barrier leakage in rats: one-week follow-up by MRI. *Brain Research*, 1280:158–65.

Elahy, M., Jackaman, C., Mamo, J. C., Lam, V., Dhaliwal, S. S., Giles, C., Nelson, D., and Takechi, R. (2015). Blood-brain barrier dysfunction developed during normal aging is

associated with inflammation and loss of tight junctions but not with leukocyte recruitment. *Immunity & Ageing*, 12:2.

Engelhorn, T., Schwarz, M. a., Hess, A., Budinsky, L., Pitann, P., Eyüpoglu, I., and Doerfler, A. (2013). Definition of Ktrans and FA thresholds for better assessment of experimental glioma using high-field MRI: a feasibility study. *Clinical Neuroradiology*, 24(4):337–345.

Enzinger, C., Smith, S., Fazekas, F., Drevin, G., Ropele, S., Nichols, T., Behrens, T., Schmidt, R., and Matthews, P. M. (2006). Lesion probability maps of white matter hyperintensities in elderly individuals: results of the Austrian stroke prevention study. *Journal of Neurology*, 253(8):1064–70.

Errante, Y., Mallio, C. A., Scarciolla, L., Carideo, L., Beomonte Zobel, B., and Quattrocchi, C. C. (2013). DCE-MRI of white matter hyperintensities and normal-appearing white matter: voxel-based analysis of quantitative pharmacokinetic parameters. In *Proceedings of the European Society for Magnetic Resonance in Medicine and Biology*, page 130.

Essig, M., Shiroishi, M. S., Nguyen, T. B., Saake, M., Provenzale, J. M., Enterline, D., Anzalone, N., Dörfler, A., Rovira, A., Wintermark, M., and Law, M. (2013). Perfusion MRI: the five most frequently asked technical questions. *American Journal of Roentgenology*, 200(1):24–34.

Ewing, J. R. and Bagher-Ebadian, H. (2013). Model selection in measures of vascular parameters using dynamic contrast-enhanced MRI: experimental and clinical applications. *NMR in Biomedicine*, 26(8):1028–41.

Ewing, J. R., Brown, S. L., Lu, M., Panda, S., Ding, G., Knight, R. a., Cao, Y., Jiang, Q., Nagaraja, T. N., Churchman, J. L., and Fenstermacher, J. D. (2006). Model selection in magnetic resonance imaging measurements of vascular permeability: Gadomer in a 9L model of rat cerebral tumor. *Journal of Cerebral Blood Flow and Metabolism*, 26(3):310–320.

Ewing, J. R., Knight, R. A., Nagaraja, T. N., Yee, J. S., Nagesh, V., Whitton, P. A., Li, L., and Fenstermacher, J. D. (2003). Patlak plots of Gd-DTPA MRI data yield blood-brain transfer constants concordant with those of 14C-sucrose in areas of blood-brain opening. *Magnetic Resonance in Medicine*, 50(2):283–92.

Farjam, R., Tsien, C. I., Lawrence, T. S., and Cao, Y. (2014). DCE-MRI defined subvolumes of a brain metastatic lesion by principle component analysis and fuzzy-c-means clustering for response assessment of radiation therapy. *Medical Physics*, 41(1):011708.

Farrall, A. J. and Wardlaw, J. M. (2009). Blood-brain barrier: ageing and microvascular disease – systematic review and meta-analysis. *Neurobiology of Aging*, 30(3):337–52.

Farrell, C., Chappell, F., Armitage, P. A., Keston, P., Maclullich, A., Shenkin, S., and Wardlaw, J. M. (2009). Development and initial testing of normal reference MR images for the brain at ages 65-70 and 75-80 years. *European Radiology*, 19(1):177–83.

Fazekas, F., Chawluk, J. B., Alavi, A., Hurtig, H. I., and Zimmerman, R. A. (1987). MR signal abnormalities at 1.5 T in Alzheimer's dementia and normal aging. *American Journal of Roentgenology*, 149(2):351–6.

Fazekas, F., Kleinert, R., Offenbacher, H., Schmidt, R., Kleinert, G., Payer, F., Radner, H., and Lechner, H. (1993). Pathologic correlates of incidental MRI white matter signal hyperintensities. *Neurology*, 43(9):1683–9.

Feigin, V. L., Lawes, C. M. M., Bennett, D. A., and Anderson, C. S. (2003). Stroke epidemiology: a review of population-based studies of incidence, prevalence, and case-fatality in the late 20th century. *The Lancet Neurology*, 2(1):43–53.

Ferl, G. Z., Xu, L., Friesenhahn, M., Bernstein, L. J., Barboriak, D. P., and Port, R. E. (2010). An automated method for nonparametric kinetic analysis of clinical DCE-MRI data: application to glioblastoma treated with bevacizumab. *Magnetic Resonance in Medicine*, 63(5):1366–75.

Ferrier, M. C., Sarin, H., Fung, S. H., Schatlo, B., Pluta, R. M., Gupta, S. N., Choyke, P. L., Oldfield, E. H., Thomasson, D., and Butman, J. A. (2007). Validation of dynamic contrast-enhanced magnetic resonance imaging-derived vascular permeability measurements using quantitative autoradiography in the RG2 rat brain tumor model. *Neoplasia*, 9(7):546–55.

Fisher, C. M. (1968). The arterial lesions underlying lacunes. *Acta Neuropathologica*, 12(1):1–15.

Fisher, C. M. (1979). Capsular infarcts: the underlying vascular lesions. *Archives of Neurology*, 36(2):65–73.

Fisher, C. M. (1982). Lacunar strokes and infarcts: a review. *Neurology*, 32(8):871–6.

Fisher, C. M. (1991). Lacunar infarcts – a review. *Cerebrovascular Diseases*, 1(6):311–320.

Fisher, C. M. (1998). Lacunes: small, deep cerebral infarcts. 1965. *Neurology*, 50(4):841–53.

Fluckiger, J. U., Schabel, M. C., and Dibella, E. V. R. (2012). The effect of temporal sampling on quantitative pharmacokinetic and three-time-point analysis of breast DCE-MRI. *Magnetic Resonance Imaging*, 30(7):934–43.

Fox, N. C. and Schott, J. M. (2004). Imaging cerebral atrophy: normal ageing to Alzheimer's disease. *The Lancet*, 363(9406):392–4.

Franke, C. L., van Swieten, J. C., and van Gijn, J. (1991). Residual lesions on computed tomography after intracerebral hemorrhage. *Stroke*, 22(12):1530–3.

Friedman, L. and Glover, G. H. (2006). Report on a multicenter fMRI quality assurance protocol. *Journal of Magnetic Resonance Imaging*, 23(6):827–39.

Fusco, R., Sansone, M., Maffei, S., Raiano, N., and Petrillo, A. (2012). Dynamic contrast-enhanced MRI in breast cancer: a comparison between distributed and compartmental tracer kinetic models. *Journal of Biomedical Graphics and Computing*, 2(2):23.

Gaitán, M. I., Shea, C. D., Evangelou, I. E., Stone, R. D., Fenton, K. M., Bielekova, B., Massacesi, L., and Reich, D. S. (2011). Evolution of the blood-brain barrier in newly forming multiple sclerosis lesions. *Annals of Neurology*, 70(1):22–9.

Gal, Y., Mehnert, A., Bradley, A., McMahon, K., Kennedy, D., and Crozier, S. (2008). A new denoising method for dynamic contrast-enhanced MRI. In *Annual International Conference of the IEEE Engineering in Medicine and Biology Society*, pages 847–50.

Garde, E., Mortensen, E. L., Krabbe, K., Rostrup, E., and Larsson, H. B. (2000). Relation between age-related decline in intelligence and cerebral white-matter hyperintensities in healthy octogenarians: a longitudinal study. *The Lancet*, 356(9230):628–34.

Gardener, H., Rundek, T., Wright, C. B., Elkind, M. S. V., and Sacco, R. L. (2012). Dietary sodium and risk of stroke in the Northern Manhattan study. *Stroke*, 43(5):1200–5.

Gattringer, T., Eppinger, S., Pinter, D., Pirpamer, L., Berghold, A., Wünsch, G., Ropele, S., Wardlaw, J. M., Enzinger, C., and Fazekas, F. (2015). Morphological MRI characteristics of recent small subcortical infarcts. *International Journal of Stroke*, 10(7):1037–43.

Gorelick, P. B., Scuteri, A., Black, S. E., Decarli, C., Greenberg, S. M., Iadecola, C., Launer, L. J., Laurent, S., Lopez, O. L., Nyenhuis, D., Petersen, R. C., Schneider, J. a., Tzourio, C., Arnett, D. K., Bennett, D. a., Chui, H. C., Higashida, R. T., Lindquist, R., Nilsson, P. M., Roman, G. C., Sellke, F. W., and Seshadri, S. (2011). Vascular contributions to cognitive impairment and dementia: a statement for healthcare professionals from the american heart association/american stroke association. *Stroke*, 42(9):2672–713.

Gouw, A. A., Seewann, A., van der Flier, W. M., Barkhof, F., Rozemuller, A. M., Scheltens, P., and Geurts, J. J. G. (2011). Heterogeneity of small vessel disease: a systematic review of MRI and histopathology correlations. *Journal of Neurology, Neurosurgery, and Psychiatry*, 82(2):126–35.

Gouw, A. A., van der Flier, W. M., Fazekas, F., van Straaten, E. C. W., Pantoni, L., Poggesi, A., Inzitari, D., Erkinjuntti, T., Wahlund, L. O., Waldemar, G., Schmidt, R., Scheltens, P., and Barkhof, F. (2008). Progression of white matter hyperintensities and incidence of new lacunes over a 3-year period: the Leukoaraiosis and Disability study. *Stroke*, 39(5):1414–20.

Groeschel, S., Chong, W. K., Surtees, R., and Hanefeld, F. (2006). Virchow-Robin spaces on magnetic resonance images: normative data, their dilatation, and a review of the literature. *Neuroradiology*, 48(10):745–54.

Gupta, R. K., Awasthi, R., Rathore, R. K. S., Verma, A., Sahoo, P., Paliwal, V. K., Prasad, K. N., Pandey, C. M., and Narayana, P. A. (2012). Understanding epileptogenesis in calcified neurocysticercosis with perfusion MRI. *Neurology*, 78(9):618–25.

Haase, A. (1990). Snapshot FLASH MRI. Applications to T1, T2, and chemical-shift imaging. *Magnetic Resonance in Medicine*, 13(1):77–89.

Hamy, V., Dikaios, N., Punwani, S., Melbourne, A., Latifoltojar, A., Makanyanga, J., Chouhan, M., Helbren, E., Menys, A., Taylor, S., and Atkinson, D. (2014). Respiratory motion correction in dynamic MRI using robust data decomposition registration - application to DCE-MRI. *Medical Image Analysis*, 18(2):301–13.

Han, S., Paulsen, J. L., Zhu, G., Song, Y., Chun, S., Cho, G., Ackerstaff, E., Koutcher, J. A., and Cho, H. (2012). Temporal/spatial resolution improvement of in vivo DCE-MRI with compressed sensing-optimized FLASH. *Magnetic Resonance Imaging*, 30(6):741–52.

Hanyu, H., Asano, T., Tanaka, Y., Iwamoto, T., Takasaki, M., and Abe, K. (2002). Increased blood-brain barrier permeability in white matter lesions of Binswanger's disease evaluated by contrast-enhanced MRI. *Dementia and Geriatric Cognitive Disorders*, 14(1):1–6.

Hariharan, P., Freed, M., and Myers, M. R. (2013). Use of computational fluid dynamics in the design of dynamic contrast enhanced imaging phantoms. *Physics in Medicine and Biology*, 58(18):6369–91.

Haris, M., Gupta, R. K., Singh, A., Husain, N., Husain, M., Pandey, C. M., Srivastava, C., Behari, S., and Rathore, R. K. S. (2008a). Differentiation of infective from neoplastic brain lesions by dynamic contrast-enhanced MRI. *Neuroradiology*, 50(6):531–40.

Haris, M., Husain, N., Singh, A., Awasthi, R., Singh Rathore, R. K., Husain, M., and Gupta, R. K. (2008b). Dynamic contrast-enhanced (DCE) derived transfer coefficient (ktrans) is a surrogate marker of matrix metalloproteinase 9 (MMP-9) expression in brain tuberculomas. *Journal of Magnetic Resonance Imaging*, 28(3):588–97.

Haris, M., Husain, N., Singh, A., Husain, M., Srivastava, S., Srivastava, C., Behari, S., Rathore, R. K. S., Saksena, S., and Gupta, R. K. (2008c). Dynamic contrast-enhanced derived cerebral blood volume correlates better with leak correction than with no correction for vascular endothelial growth factor, microvascular density, and grading of astrocytoma. *Journal of Computer Assisted Tomography*, 32(6):955–65.

Harrer, J. U., Parker, G. J. M., Haroon, H. A., Buckley, D. L., Embelton, K., Roberts, C., Balériaux, D., and Jackson, A. (2004). Comparative study of methods for determining vascular permeability and blood volume in human gliomas. *Journal of Magnetic Resonance Imaging*, 20(5):748–57.

He, F. J., Li, J., and Macgregor, G. A. (2013). Effect of longer term modest salt reduction on blood pressure: Cochrane systematic review and meta-analysis of randomised trials. *BMJ (Clinical Research Ed.)*, 346:f1325.

Heisen, M., Fan, X., Buurman, J., van Riel, N. A. W., Karczmar, G. S., and ter Haar Romeny, B. M. (2010). The influence of temporal resolution in determining pharmacokinetic parameters from DCE-MRI data. *Magnetic Resonance in Medicine*, 63(3):811–6.

Heye, A. K., Culling, R. D., Valdés Hernández, M. D. C., Thrippleton, M. J., and Wardlaw, J. M. (2014). Assessment of blood-brain barrier disruption using dynamic contrast-enhanced MRI. A systematic review. *NeuroImage Clinical*, 6:262–274.

Heye, A. K., Thrippleton, M. J., Armitage, P. A., Valdés Hernández, M. D. C., Makin, S. D., Glatz, A., Sakka, E., and Wardlaw, J. M. (2016a). Tracer kinetic modelling for DCE-MRI quantification of subtle blood-brain barrier permeability. *NeuroImage*, 125:446–455.

Heye, A. K., Thrippleton, M. J., Chappell, F. M., Valdés Hernández, M. D. C., Armitage, P. A., Makin, S. D., Muñoz Maniega, S., Sakka, E., Flatman, P. W., Dennis, M. S., and Wardlaw, J. M. (2016b). Blood pressure and sodium: association with MRI markers in cerebral small vessel disease. *Journal of Cerebral Blood Flow and Metabolism*, 36(1):264–274.

Hoff, B. A., Bhojani, M. S., Rudge, J., Chenevert, T. L., Meyer, C. R., Galbán, S., Johnson, T. D., Leopold, J. S., Rehemtulla, A., Ross, B. D., and Galbán, C. J. (2012). DCE and DW-MRI monitoring of vascular disruption following VEGF-Trap treatment of a rat glioma model. *NMR in Biomedicine*, 25(7):935–42.

Homer, J. and Beevers, M. S. (1985). Driven-equilibrium single-pulse observation of T1 relaxation. A reevaluation of a rapid "new" method for determining NMR spin-lattice relaxation times. *Journal of Magnetic Resonance (1969)*, 63(2):287–297.

Hormuth, D. a., Skinner, J. T., Does, M. D., and Yankeelov, T. E. (2014). A comparison of individual and population-derived vascular input functions for quantitative DCE-MRI in rats. *Magnetic Resonance Imaging*, 32(4):397–401.

Huisa, B. N., Caprihan, A., Thompson, J., Prestopnik, J., Qualls, C. R., and Rosenberg, G. A. (2015). Long-term blood-brain barrier permeability changes in Binswanger disease. *Stroke*, 46(9):2413–8.

Iannotti, F., Fieschi, C., Alfano, B., Picozzi, P., Mansi, L., Pozzilli, C., Punzo, A., Del Vecchio, G., Lenzi, G. L., and Salvatore, M. (1987). Simplified, noninvasive PET measurement of blood-brain barrier permeability. *Journal of Computer Assisted Tomography*, 11(3):390–7.

Ingrisch, M., Sourbron, S., Morhard, D., Ertl-Wagner, B., Kümpfel, T., Hohlfeld, R., Reiser, M., and Glaser, C. (2012). Quantification of perfusion and permeability in multiple sclerosis: dynamic contrast-enhanced MRI in 3D at 3T. *Investigative Radiology*, 47(4):252–8.

Ingrisch, M., Sourbron, S., Reiser, M., and Peller, M. (2010). Model selection in dynamic contrast enhanced MRI: The Akaike Information Criterion. In *World Congress on Medical Physics and Biomedical Engineering, IFMBE Proceedings Volume 25/4*, pages 356–358.

Israeli, D., Tanne, D., Daniels, D., Last, D., Shneor, R., Guez, D., Landau, E., Roth, Y., Ocherashvilli, A., Bakon, M., Hoffman, C., Weinberg, A., Volk, T., and Mardor, Y. (2011). The application of MRI for depiction of subtle blood brain barrier disruption in stroke. *International Journal of Biological Sciences*, 7(1):1–8.

Jackson, C. and Sudlow, C. (2005). Comparing risks of death and recurrent vascular events between lacunar and non-lacunar infarction. *Brain*, 128(11):2507–17.

Jagust, W. J., Zheng, L., Harvey, D. J., Mack, W. J., Vinters, H. V., Weiner, M. W., Ellis, W. G., Zarow, C., Mungas, D., Reed, B. R., Kramer, J. H., Schuff, N., DeCarli, C., and Chui, H. C. (2008). Neuropathological basis of magnetic resonance images in aging and dementia. *Annals of Neurology*, 63(1):72–80.

Jain, R. (2013). Measurements of tumor vascular leakiness using DCE in brain tumors: clinical applications. *NMR in Biomedicine*, 26(8):1042–9.

Jeerakathil, T., Wolf, P. A., Beiser, A., Massaro, J., Seshadri, S., D'Agostino, R. B., and DeCarli, C. (2004). Stroke risk profile predicts white matter hyperintensity volume: the Framingham Study. *Stroke*, 35(8):1857–61.

Jelescu, I. O., Leppert, I. R., Narayanan, S., Araújo, D., Arnold, D. L., and Pike, G. B. (2011). Dual-temporal resolution dynamic contrast-enhanced MRI protocol for blood-brain barrier

permeability measurement in enhancing multiple sclerosis lesions. *Journal of Magnetic Resonance Imaging*, 33(6):1291–300.

Jenkinson, M., Bannister, P., Brady, M., and Smith, S. (2002). Improved optimization for the robust and accurate linear registration and motion correction of brain images. *NeuroImage*, 17(2):825–41.

Jia, Z.-Z., Geng, D.-Y., Liu, Y., Chen, X.-R., and Zhang, J. (2013). Microvascular permeability of brain astrocytoma with contrast-enhanced magnetic resonance imaging: correlation analysis with histopathologic grade. *Chinese Medical Journal*, 126(10):1953–6.

Jung, H., Sung, K., Nayak, K. S., Kim, E. Y., and Ye, J. C. (2009). k-t FOCUSS: a general compressed sensing framework for high resolution dynamic MRI. *Magnetic Resonance in Medicine*, 61(1):103–16.

Just, N., Koh, D.-M., D'Arcy, J., Collins, D. J., and Leach, M. O. (2011). Assessment of the effect of haematocrit-dependent arterial input functions on the accuracy of pharmacokinetic parameters in dynamic contrast-enhanced MRI. *NMR in Biomedicine*, 24(7):902–15.

Kalaria, R. N. (2002). Small vessel disease and Alzheimer's dementia: pathological considerations. *Cerebrovascular Diseases*, 13(Suppl. 2):48–52.

Kang, D.-W., Han, M.-K., Kim, H.-J., Yun, S.-C., Jeon, S.-B., Bae, H.-J., Kwon, S. U., and Kim, J. S. (2012). New ischemic lesions coexisting with acute intracerebral hemorrhage. *Neurology*, 79(9):848–55.

Kassner, A., Roberts, T., Taylor, K., Silver, F., and Mikulis, D. (2005). Prediction of hemorrhage in acute ischemic stroke using permeability MR imaging. *American Journal of Neuroradiology*, 26(9):2213–7.

Kassner, A., Roberts, T. P. L., Moran, B., Silver, F. L., and Mikulis, D. J. (2009). Recombinant tissue plasminogen activator increases blood-brain barrier disruption in acute ischemic stroke: an MR imaging permeability study. *American Journal of Neuroradiology*, 30(10):1864–9.

Kermode, A. G., Tofts, P. S., Thompson, A. J., MacManus, D. G., Rudge, P., Kendall, B. E., Kingsley, D. P., Moseley, I. F., du Boulay, E. P., and McDonald, W. I. (1990). Heterogeneity of blood-brain barrier changes in multiple sclerosis: an MRI study with gadolinium-DTPA enhancement. *Neurology*, 40(2):229–35.

Kershaw, L. E. and Cheng, H.-L. M. (2010). Temporal resolution and SNR requirements for accurate DCE-MRI data analysis using the AATH model. *Magnetic Resonance in Medicine*, 64(6):1772–80.

Kershaw, L. E. and Cheng, H.-L. M. (2011). A general dual-bolus approach for quantitative DCE-MRI. *Magnetic Resonance Imaging*, 29(2):160–6.

Kiselev, V. G., Strecker, R., Ziyeh, S., Speck, O., and Hennig, J. (2005). Vessel size imaging in humans. *Magnetic Resonance in Medicine*, 53(3):553–63.

Kitagawa, Y., Meyer, J. S., Tanahashi, N., Rogers, R. L., Tachibana, H., Kandula, P., Dowell, R. E., and Mortel, K. F. (1985). Cerebral blood flow and brain atrophy correlated by xenon contrast CT scanning. *Computerized Radiology*, 9(6):331–40.

Kleppestø, M., Larsson, C., Groote, I., Salo, R., Vardal, J., Courivaud, F., and Bjø rnerud, A. (2014). T 2 *-correction in dynamic contrast-enhanced MRI from double-echo acquisitions. *Journal of Magnetic Resonance Imaging*, 39(5):1314–1319.

Knight, R. A., Nagaraja, T. N., Ewing, J. R., Nagesh, V., Whitton, P. A., Bershad, E., Fagan, S. C., and Fenstermacher, J. D. (2005). Quantitation and localization of blood-to-brain influx by magnetic resonance imaging and quantitative autoradiography in a model of transient focal ischemia. *Magnetic Resonance in Medicine*, 54(4):813–21.

Knudsen, K. A., Rosand, J., Karluk, D., and Greenberg, S. M. (2001). Clinical diagnosis of cerebral amyloid angiopathy: validation of the Boston criteria. *Neurology*, 56(4):537–9.

Koh, T. S., Bisdas, S., Koh, D. M., and Thng, C. H. (2011). Fundamentals of tracer kinetics for dynamic contrast-enhanced MRI. *Journal of Magnetic Resonance Imaging*, 34(6):1262–76.

Krueck, W. G., Schmiedl, U. P., Maravilla, K. R., Spence, A. M., Starr, F. L., and Kenney, J. (1994). MR assessment of radiation-induced blood-brain barrier permeability changes in rat glioma model. *American Journal of Neuroradiology*, 15(4):625–32.

Kulik, T., Kusano, Y., Aronhime, S., Sandler, A. L., and Winn, H. R. (2008). Regulation of cerebral vasculature in normal and ischemic brain. *Neuropharmacology*, 55(3):281–8.

Kunz, A. and Iadecola, C. (2009). Cerebral vascular dysregulation in the ischemic brain. *Handbook of Cinical Neurology*, 92:283–305.

Kwee, R. M. and Kwee, T. C. (2007). Virchow-Robin spaces at MR imaging. *Radiographics*, 27(4):1071–86.

Lammie, G. A., Brannan, F., and Wardlaw, J. M. (1998). Incomplete lacunar infarction (Type Ib lacunes). *Acta Neuropathologica*, 96(2):163–71.

Larsen, V. A., Simonsen, H. J., Law, I., Larsson, H. B. W., and Hansen, A. E. (2013). Evaluation of dynamic contrast-enhanced T1-weighted perfusion MRI in the differentiation of tumor recurrence from radiation necrosis. *Neuroradiology*, 55(3):361–9.

Larsson, C., Kleppestø, M., Grothe, I., Vardal, J., and Bjø rnerud, A. (2014). T1 in high-grade glioma and the influence of different measurement strategies on parameter estimations in DCE-MRI. *Journal of Magnetic Resonance Imaging*, 42(1):97–104.

Larsson, C., Kleppestø, M., Rasmussen, I., Salo, R., Vardal, J., Brandal, P., and Bjø rnerud, A. (2013). Sampling requirements in DCE-MRI based analysis of high grade gliomas: simulations and clinical results. *Journal of Magnetic Resonance Imaging*, 37(4):818–29.

Larsson, H. B., Frederiksen, J., Kjaer, L., Henriksen, O., and Olesen, J. (1988). In vivo determination of T1 and T2 in the brain of patients with severe but stable multiple sclerosis. *Magnetic Resonance in Medicine*, 7(1):43–55.

Larsson, H. B., Rosenbaum, S., and Fritz-Hansen, T. (2001). Quantification of the effect of water exchange in dynamic contrast MRI perfusion measurements in the brain and heart. *Magnetic Resonance in Medicine*, 46(2):272–81.

Larsson, H. B., Stubgaard, M., Frederiksen, J. L., Jensen, M., Henriksen, O., and Paulson, O. B. (1990). Quantitation of blood-brain barrier defect by magnetic resonance imaging and gadolinium-DTPA in patients with multiple sclerosis and brain tumors. *Magnetic Resonance in Medicine*, 16(1):117–31.

Larsson, H. B. W., Courivaud, F., Rostrup, E., and Hansen, A. E. (2009). Measurement of brain perfusion, blood volume, and blood-brain barrier permeability, using dynamic contrast-enhanced T(1)-weighted MRI at 3 tesla. *Magnetic Resonance in Medicine*, 62(5):1270–81.

Lassen, N. A. and Perl, W. (1979). *Tracer kinetic methods in medical physiology*. Raven Press, New York.

Lauterbur, P. C. (1973). Image formation by induced local interactions: examples employing nuclear magnetic resonance. *Nature*, 242(5394):190–191.

Lavini, C. and Verhoeff, J. J. C. (2010). Reproducibility of the gadolinium concentration measurements and of the fitting parameters of the vascular input function in the superior sagittal sinus in a patient population. *Magnetic Resonance Imaging*, 28(10):1420–1430.

Le Bihan, D., Breton, E., Lallemand, D., Grenier, P., Cabanis, E., and Laval-Jeantet, M. (1986). MR imaging of intravoxel incoherent motions: application to diffusion and perfusion in neurologic disorders. *Radiology*, 161(2):401–7.

Leach, M. O., Morgan, B., Tofts, P. S., Buckley, D. L., Huang, W., Horsfield, M. A., Chenevert, T. L., Collins, D. J., Jackson, A., Lomas, D., Whitcher, B., Clarke, L., Plummer, R., Judson, I., Jones, R., Alonzi, R., Brunner, T., Koh, D. M., Murphy, P., Waterton, J. C., Parker, G., Graves, M. J., Scheenen, T. W. J., Redpath, T. W., Orton, M., Karczmar, G., Huisman, H.,

Barentsz, J., and Padhani, A. (2012). Imaging vascular function for early stage clinical trials using dynamic contrast-enhanced magnetic resonance imaging. *European Radiology*, 22(7):1451–64.

Lee, J., Cárdenas-Rodríguez, J., Pagel, M. D., Platt, S., Kent, M., and Zhao, Q. (2014). Comparison of analytical and numerical analysis of the reference region model for DCE-MRI. *Magnetic Resonance Imaging*, 32(7):845–853.

Leenders, K. L., Perani, D., Lammertsma, A. A., Heather, J. D., Buckingham, P., Healy, M. J., Gibbs, J. M., Wise, R. J., Hatazawa, J., and Herold, S. (1990). Cerebral blood flow, blood volume and oxygen utilization. Normal values and effect of age. *Brain*, 113(1):27–47.

Leppert, I. R., Narayanan, S., Araújo, D., Giacomini, P. S., Lapierre, Y., Arnold, D. L., and Pike, G. B. (2014). Interpreting therapeutic effect in multiple sclerosis via MRI contrast enhancing lesions: now you see them, now you don't. *Journal of Neurology*, 261(4):809–816.

Li, K.-L., Buonaccorsi, G., Thompson, G., Cain, J. R., Watkins, A., Russell, D., Qureshi, S., Evans, D. G., Lloyd, S. K., Zhu, X., and Jackson, A. (2012a). An improved coverage and spatial resolution – using dual injection dynamic contrast-enhanced (ICE-DICE) MRI: a novel dynamic contrast-enhanced technique for cerebral tumors. *Magnetic Resonance in Medicine*, 68(2):452–62.

Li, K. L., Zhu, X. P., Waterton, J., and Jackson, A. (2000). Improved 3D quantitative mapping of blood volume and endothelial permeability in brain tumors. *Journal of Magnetic Resonance Imaging*, 12(2):347–57.

Li, W., Long, J. A., Watts, L. T., Jiang, Z., Shen, Q., Li, Y., and Duong, T. Q. (2014). A quantitative MRI method for imaging blood-brain barrier leakage in experimental traumatic brain injury. *PLoS one*, 9(12):e114173.

Li, X., Rooney, W. D., and Springer, C. S. (2005). A unified magnetic resonance imaging pharmacokinetic theory: intravascular and extracellular contrast reagents. *Magnetic Resonance in Medicine*, 54(6):1351–9.

Li, X., Rooney, W. D., Várallyay, C. G., Gahramanov, S., Muldoon, L. L., Goodman, J. A., Tagge, I. J., Selzer, A. H., Pike, M. M., Neuwelt, E. A., and Springer, C. S. (2010). Dynamic-contrast-enhanced-MRI with extravasating contrast reagent: rat cerebral glioma blood volume determination. *Journal of Magnetic Resonance*, 206(2):190–9.

Li, X.-Y., Cai, X.-L., Bian, P.-D., and Hu, L.-R. (2012b). High salt intake and stroke: meta-analysis of the epidemiologic evidence. *CNS Neuroscience & Therapeutics*, 18(8):691–701.

Lim, R. P., Shapiro, M., Wang, E. Y., Law, M., Babb, J. S., Rueff, L. E., Jacob, J. S., Kim, S., Carson, R. H., Mulholland, T. P., Laub, G., and Hecht, E. M. (2008). 3D time-resolved MR angiography (MRA) of the carotid arteries with time-resolved imaging with stochastic trajectories: comparison with 3D contrast-enhanced Bolus-Chase MRA and 3D time-of-flight MRA. *American Journal of Neuroradiology*, 29(10):1847–54.

Liu, W., Liu, R., Sun, W., Peng, Q., Zhang, W., Xu, E., Cheng, Y., Ding, M., Li, Y., Hong, Z., Wu, J., Zeng, J., Yao, C., and Huang, Y. (2012). Different impacts of blood pressure variability on the progression of cerebral microbleeds and white matter lesions. *Stroke*, 43(11):2916–22.

Lobo, A., Launer, L. J., Fratiglioni, L., Andersen, K., Di Carlo, A., Breteler, M. M., Copeland, J. R., Dartigues, J. F., Jagger, C., Martinez-Lage, J., Soininen, H., and Hofman, A. (2000). Prevalence of dementia and major subtypes in Europe: A collaborative study of population-based cohorts. Neurologic Diseases in the Elderly Research Group. *Neurology*, 54(11 Suppl 5):S4–9.

Loeb, C., Gandolfo, C., Croce, R., and Conti, M. (1992). Dementia associated with lacunar infarction. *Stroke*, 23(9):1225–9.

Longstreth, W., Manolio, T. A., Arnold, A., Burke, G. L., Bryan, N., Jungreis, C. A., Enright, P. L., O'Leary, D., and Fried, L. (1996). Clinical correlates of white matter findings on cranial magnetic resonance imaging of 3301 elderly people: the Cardiovascular Health Study. *Stroke*, 27(8):1274–1282.

Look, D. C. and Locker, D. R. (1970). Time Saving in Measurement of NMR and EPR Relaxation Times. *Review of Scientific Instruments*, 41(2):250.

Lowe, M. J. and Russell, D. P. (1999). Treatment of baseline drifts in fMRI time series analysis. *Journal of Computer Assisted Tomography*, 23(3):463–73.

Lüdemann, L., Hamm, B., and Zimmer, C. (2000). Pharmacokinetic analysis of glioma compartments with dynamic Gd-DTPA-enhanced magnetic resonance imaging. *Magnetic Resonance Imaging*, 18(10):1201–14.

Lüdemann, L., Warmuth, C., Plotkin, M., Förschler, A., Gutberlet, M., Wust, P., and Amthauer, H. (2009). Brain tumor perfusion: comparison of dynamic contrast enhanced magnetic resonance imaging using T1, T2, and T2* contrast, pulsed arterial spin labeling, and H2(15)O positron emission tomography. *European Journal of Radiology*, 70(3):465–74.

Lüdemann, L., Wurm, R., and Zimmer, C. (2002). Pharmacokinetic modeling of Gd-DTPA extravasation in brain tumors. *Investigative Radiology*, 37(10):562–70.

Lummel, N., Wollenweber, F. A., Demaerel, P., Bochmann, K., Malik, R., Opherk, C., and Linn, J. (2015). Clinical spectrum, underlying etiologies and radiological characteristics of cortical superficial siderosis. *Journal of Neurology*, 262(6):1455–62.

Luypaert, R., Ingrisch, M., Sourbron, S., and de Mey, J. (2012). The Akaike information criterion in DCE-MRI: does it improve the haemodynamic parameter estimates? *Physics in Medicine and Biology*, 57(11):3609–28.

Maclullich, A. M. J., Ferguson, K. J., Reid, L. M., Deary, I. J., Starr, J. M., Seckl, J. R., Bastin, M. E., and Wardlaw, J. M. (2009). Higher systolic blood pressure is associated with increased water diffusivity in normal-appearing white matter. *Stroke*, 40(12):3869–71.

Maclullich, A. M. J., Wardlaw, J. M., Ferguson, K. J., Starr, J. M., Seckl, J. R., and Deary, I. J. (2004). Enlarged perivascular spaces are associated with cognitive function in healthy elderly men. *Journal of Neurology, Neurosurgery and Psychiatry*, 75(11):1519–23.

Mäntylä, R., Aronen, H. J., Salonen, O., Korpelainen, M., Peltonen, T., Standertskjöld-Nordenstam, C., and Erkinjuntti, T. (1999). The prevalence and distribution of white-matter changes on different MRI pulse sequences in a post-stroke cohort. *Neuroradiology*, 41(9):657–65.

Manuchehri, A. M., Sathyapalan, T., Lowry, M., Turnbull, L. W., Rowland-Hill, C., and Atkin, S. L. (2007). Effect of dopamine agonists on prolactinomas and normal pituitary assessed by dynamic contrast enhanced magnetic resonance imaging (DCE-MRI). *Pituitary*, 10(3):261–6.

Marchal, G., Rioux, P., Petit-Taboué, M.-C., Sette, G., Travère, J.-M., Poec, C. L., Courtheoux, P., Derlon, J.-M., and Baron, J.-C. (1992). Regional cerebral oxygen consumption, blood flow, and blood volume in healthy human aging. *Archives of Neurology*, 49(10):1013–1020.

Markus, H. S. (2008). Genes, endothelial function and cerebral small vessel disease in man. *Experimental Physiology*, 93(1):121–7.

Marques, F., Sousa, J. a. C., Sousa, N., and Palha, J. A. (2013). Blood-brain-barriers in aging and in Alzheimer's disease. *Molecular Neurodegeneration*, 8(1):38.

Marstrand, J. R., Garde, E., Rostrup, E., Ring, P., Rosenbaum, S., Mortensen, E. L., and Larsson, H. B. W. (2002). Cerebral perfusion and cerebrovascular reactivity are reduced in white matter hyperintensities. *Stroke*, 33(4):972–6.

Martin, A. J., Friston, K. J., Colebatch, J. G., and Frackowiak, R. S. (1991). Decreases in regional cerebral blood flow with normal aging. *Journal of Cerebral Blood Flow and Metabolism*, 11(4):684–9.

Martinez-Ramirez, S., Pontes-Neto, O. M., Dumas, A. P., Auriel, E., Halpin, A., Quimby, M., Gurol, M. E., Greenberg, S. M., and Viswanathan, A. (2013). Topography of dilated perivascular spaces in subjects from a memory clinic cohort. *Neurology*, 80(17):1551–6.

Matsumoto, Y., Yanase, D., Noguchi-Shinohara, M., Ono, K., Yoshita, M., and Yamada, M. (2007). Blood-brain barrier permeability correlates with medial temporal lobe atrophy but not with amyloid-beta protein transport across the blood-brain barrier in Alzheimer's disease. *Dementia and Geriatric Cognitive Disorders*, 23(4):241–5.

McDonald, R. J., McDonald, J. S., Kallmes, D. F., Jentoft, M. E., Murray, D. L., Thielen, K. R., Williamson, E. E., and Eckel, L. J. (2015). Intracranial gadolinium deposition after contrast-enhanced MR imaging. *Radiology*, 275(3):772–82.

McGrath, D. M., Bradley, D. P., Tessier, J. L., Lacey, T., Taylor, C. J., and Parker, G. J. M. (2009). Comparison of model-based arterial input functions for dynamic contrast-enhanced MRI in tumor bearing rats. *Magnetic Resonance in Medicine*, 61(5):1173–84.

McRobbie, D. W., Moore, E. A., Graves, M. J., and Prince, M. R. (2006). *MRI from picture to proton*. Cambridge University Press, Cambridge.

Mead, G. E., Lewis, S. C., Wardlaw, J. M., Dennis, M. S., and Warlow, C. P. (2000). How well does the Oxfordshire community stroke project classification predict the site and size of the infarct on brain imaging? *Journal of Neurology, Neurosurgery, and Psychiatry*, 68(5):558–62.

Melbourne, A., Hipwell, J., Modat, M., Mertzanidou, T., Huisman, H., Ourselin, S., and Hawkes, D. J. (2011). The effect of motion correction on pharmacokinetic parameter estimation in dynamic-contrast-enhanced MRI. *Physics in Medicine and Biology*, 56(24):7693–708.

Mente, A., O'Donnell, M. J., Rangarajan, S., McQueen, M. J., Poirier, P., Wielgosz, A., Morrison, H., Li, W., Wang, X., Di, C., Mony, P., Devanath, A., Rosengren, A., Oguz, A., Zatonska, K., Yusufali, A. H., Lopez-Jaramillo, P., Avezum, A., Ismail, N., Lanas, F., Puoane, T., Diaz, R., Kelishadi, R., Iqbal, R., Yusuf, R., Chifamba, J., Khatib, R., Teo, K., and Yusuf, S. (2014). Association of urinary sodium and potassium excretion with blood pressure. *The New England Journal of Medicine*, 371(7):601–11.

Mills, S. J., Soh, C., O'Connor, J. P. B., Rose, C. J., Buonaccorsi, G. A., Cheung, S., Zhao, S., Parker, G. J. M., and Jackson, A. (2009). Tumour enhancing fraction (EnF) in glioma: relationship to tumour grade. *European Radiology*, 19(6):1489–98.

Miyati, T., Banno, T., Mase, M., Kasai, H., Shundo, H., Imazawa, M., and Ohba, S. (1997). Dual dynamic contrast-enhanced MR imaging. *Journal of Magnetic Resonance Imaging*, 7(1):230–5.

Modat, M., Ridgway, G. R., Taylor, Z. A., Lehmann, M., Barnes, J., Hawkes, D. J., Fox, N. C., and Ourselin, S. (2010). Fast free-form deformation using graphics processing units. *Computer Methods and Programs in Biomedicine*, 98(3):278–84.

Montagne, A., Barnes, S. R., Law, M., Zlokovic, B. V., Montagne, A., Barnes, S. R., Sweeney, M. D., Halliday, M. R., Sagare, A. P., Zhao, Z., Toga, A. W., Jacobs, R. E., Liu, C. Y., Amezcua, L., Harrington, M. G., and Chui, H. C. (2015). Blood-Brain Barrier Breakdown in the Aging Human Hippocampus. *Neuron*, 85(2):296–302.

Moreau, F., Patel, S., Lauzon, M. L., McCreary, C. R., Goyal, M., Frayne, R., Demchuk, A. M., Coutts, S. B., and Smith, E. E. (2012). Cavitation after acute symptomatic lacunar stroke depends on time, location, and MRI sequence. *Stroke*, 43(7):1837–42.

Muñoz Maniega, S., Valdés Hernández, M. D. C., Clayden, J. D., Royle, N. A., Murray, C., Morris, Z., Aribisala, B. S., Gow, A. J., Starr, J. M., Bastin, M. E., Deary, I. J., and Wardlaw, J. M. (2015). White matter hyperintensities and normal-appearing white matter integrity in the aging brain. *Neurobiology of Aging*, 36(2):909–18.

Murray, C. J. and Lopez, A. D. (1997). Global mortality, disability, and the contribution of risk factors: Global Burden of Disease Study. *The Lancet*, 349(9063):1436–42.

Murray, C. J. L. and Lopez, A. D. (2013). Measuring the global burden of disease. *The New England journal of medicine*, 369(5):448–57.

Nagaraja, T. N., Aryal, M. P., Brown, S. L., Bagher-Ebadian, H., Mikkelsen, T., Yang, J. J., Panda, S., Keenan, K. a., Cabral, G., and Ewing, J. R. (2013). Cilengitide-induced temporal variations in transvascular transfer parameters of tumor vasculature in a rat glioma model: Identifying potential MRI biomarkers of acute effects. *PloS one*, 8(12):2–10.

Nagaraja, T. N., Karki, K., Ewing, J. R., Divine, G. W., Fenstermacher, J. D., Patlak, C. S., and Knight, R. A. (2010). The MRI-measured arterial input function resulting from a bolus injection of Gd-DTPA in a rat model of stroke slightly underestimates that of Gd-[14C]DTPA and marginally overestimates the blood-to-brain influx rate constant determined by Patlak plots. *Magnetic Resonance in Medicine*, 63(6):1502–9.

Nandigam, R. N. K., Viswanathan, A., Delgado, P., Skehan, M. E., Smith, E. E., Rosand, J., Greenberg, S. M., and Dickerson, B. C. (2009). MR imaging detection of cerebral microbleeds: effect of susceptibility-weighted imaging, section thickness, and field strength. *American Journal of Neuroradiology*, 30(2):338–43.

Norrving, B. (2003). Long-term prognosis after lacunar infarction. *The Lancet Neurology*, 2(4):238–45.

Noseworthy, M. D. and Bray, T. M. (2000). Zinc deficiency exacerbates loss in blood-brain barrier integrity induced by hyperoxia measured by dynamic MRI. *Proceedings of the Society for Experimental Biology and Medicine*, 223(2):175–82.

Obermeier, B., Daneman, R., and Ransohoff, R. M. (2013). Development, maintenance and disruption of the blood-brain barrier. *Nature Medicine*, 19(12):1584–96.

O'Brien, J., Ames, D., Chiu, E., Schweitzer, I., Desmond, P., and Tress, B. (1998). Severe deep white matter lesions and outcome in elderly patients with major depressive disorder: follow up study. *BMJ*, 317(7164):982–4.

O'Connor, J. P. B., Jackson, A., Parker, G. J. M., Roberts, C., and Jayson, G. C. (2012). Dynamic contrast-enhanced MRI in clinical trials of antivascular therapies. *Nature Reviews. Clinical Oncology*, 9(3):167–77.

O'Donnell, M., Mente, A., Rangarajan, S., McQueen, M. J., Wang, X., Liu, L., Yan, H., Lee, S. F., Mony, P., Devanath, A., Rosengren, A., Lopez-Jaramillo, P., Diaz, R., Avezum, A., Lanas, F., Yusoff, K., Iqbal, R., Ilow, R., Mohammadifard, N., Gulec, S., Yusufali, A. H., Kruger, L., Yusuf, R., Chifamba, J., Kabali, C., Dagenais, G., Lear, S. A., Teo, K., and Yusuf, S. (2014). Urinary sodium and potassium excretion, mortality, and cardiovascular events. *The New England Journal of Medicine*, 371(7):612–23.

O'Rourke, M. F. and Safar, M. E. (2005). Relationship between aortic stiffening and microvascular disease in brain and kidney: cause and logic of therapy. *Hypertension*, 46(1):200–4.

Pantoni, L. (2010). Cerebral small vessel disease: from pathogenesis and clinical characteristics to therapeutic challenges. *The Lancet Neurology*, 9(7):689–701.

Parker, G. J. M., Roberts, C., Macdonald, A., Buonaccorsi, G. A., Cheung, S., Buckley, D. L., Jackson, A., Watson, Y., Davies, K., and Jayson, G. C. (2006). Experimentally-derived functional form for a population-averaged high-temporal-resolution arterial input function for dynamic contrast-enhanced MRI. *Magnetic Resonance in Medicine*, 56(5):993–1000.

Parker, G. J. M., Tanner, S. F., and Leach, M. O. (1996). Pitfalls in the measurement of tissue permeability over short time-scales using multi-compartment models with a low temporal resolution blood input function. In *4th Meeting of the International Society for Magnetic Resonance in Medicine*, page 1582.

Patenaude, B., Smith, S. M., Kennedy, D. N., and Jenkinson, M. (2011). A Bayesian model of shape and appearance for subcortical brain segmentation. *NeuroImage*, 56(3):907–22.

Patlak, C. S., Blasberg, R. G., and Fenstermacher, J. D. (1983). Graphical evaluation of blood-to-brain transfer constants from multiple-time uptake data. *Journal of Cerebral Blood Flow and Metabolism*, 3(1):1–7.

Peladeau-Pigeon, M. and Coolens, C. (2013). Computational fluid dynamics modelling of perfusion measurements in dynamic contrast-enhanced computed tomography: development, validation and clinical applications. *Physics in Medicine and Biology*, 58(17):6111–31.

Penke, L., Valdés Hernandéz, M. D. C., Muñoz Maniega, S., Gow, A. J., Murray, C., Starr, J. M., Bastin, M. E., Deary, I. J., and Wardlaw, J. M. (2012). Brain iron deposits are associated with general cognitive ability and cognitive aging. *Neurobiology of Aging*, 33(3):510–517.e2.

Perneger, T. V. (1998). What's wrong with Bonferroni adjustments. *BMJ (Clinical Research Ed.)*, 316(7139):1236–8.

Pineda, F. D., Medved, M., Fan, X., Ivancevic, M. K., Abe, H., Shimauchi, A., Newstead, G. M., and Karczmar, G. S. (2015). Comparison of dynamic contrast-enhanced MRI parameters of breast lesions at 1.5 and 3.0 T: a pilot study. *The British Journal of Radiology*, 88(1049):20150021.

Poels, M. M. F., Zaccai, K., Verwoert, G. C., Vernooij, M. W., Hofman, A., van der Lugt, A., Witteman, J. C. M., Breteler, M. M. B., Mattace-Raso, F. U. S., and Ikram, M. A. (2012). Arterial stiffness and cerebral small vessel disease: the Rotterdam Scan Study. *Stroke*, 43(10):2637–42.

Poggesi, A., Pracucci, G., Chabriat, H., Erkinjuntti, T., Fazekas, F., Verdelho, A., Hennerici, M., Langhorne, P., O'Brien, J., Scheltens, P., Visser, M. C., Crisby, M., Waldemar, G., Wallin, A., Inzitari, D., and Pantoni, L. (2008). Urinary complaints in nondisabled elderly people with age-related white matter changes: the Leukoaraiosis And DISability (LADIS) Study. *Journal of the American Geriatrics Society*, 56(9):1638–43.

Popescu, B. O., Toescu, E. C., Popescu, L. M., Bajenaru, O., Muresanu, D. F., Schultzberg, M., and Bogdanovic, N. (2009). Blood-brain barrier alterations in ageing and dementia. *Journal of the Neurological Sciences*, 283(1-2):99–106.

Port, R. E., Knopp, M. V., and Brix, G. (2001). Dynamic contrast-enhanced MRI using Gd-DTPA: interindividual variability of the arterial input function and consequences for the assessment of kinetics in tumors. *Magnetic Resonance in Medicine*, 45(6):1030–8.

Potter, G. M., Chappell, F. M., Morris, Z., and Wardlaw, J. M. (2015). Cerebral perivascular spaces visible on magnetic resonance imaging: development of a qualitative rating scale and its observer reliability. *Cerebrovascular Diseases*, 39(3-4):224–31.

Potter, G. M., Doubal, F. N., Jackson, C. A., Chappell, F. M., Sudlow, C. L., Dennis, M. S., and Wardlaw, J. M. (2010). Counting cavitating lacunes underestimates the burden of lacunar infarction. *Stroke*, 41(2):267–72.

Potter, G. M., Doubal, F. N., Jackson, C. A., Chappell, F. M., Sudlow, C. L., Dennis, M. S., and Wardlaw, J. M. (2013). Enlarged perivascular spaces and cerebral small vessel disease. *International Journal of Stroke*, 10(3):376–81.

Powers, W. J. (1991). Cerebral hemodynamics in ischemic cerebrovascular disease. *Annals of Neurology*, 29(3):231–40.

Prince, M., Bryce, R., Albanese, E., Wimo, A., Ribeiro, W., and Ferri, C. P. (2013). The global prevalence of dementia: a systematic review and metaanalysis. *Alzheimer's & Dementia*, 9(1):63–75.e2.

Prins, N. D., van Straaten, E. C. W., van Dijk, E. J., Simoni, M., van Schijndel, R. A., Vrooman, H. A., Koudstaal, P. J., Scheltens, P., Breteler, M. M. B., and Barkhof, F. (2004). Measuring progression of cerebral white matter lesions on MRI: visual rating and volumetrics. *Neurology*, 62(9):1533–9.

Provenzale, J. M., York, G., Moya, M. G., Parks, L., Choma, M., Kealey, S., Cole, P., and Serajuddin, H. (2006). Correlation of relative permeability and relative cerebral blood volume in high-grade cerebral neoplasms. *American Journal of Roentgenology*, 187(4):1036–42.

Purcell, E., Torrey, H., and Pound, R. (1946). Resonance absorption by nuclear magnetic moments in a solid. *Physical Review*, 69(1-2):37–38.

Quarles, C. C., Gore, J. C., Xu, L., and Yankeelov, T. E. (2012). Comparison of dual-echo DSC-MRI- and DCE-MRI-derived contrast agent kinetic parameters. *Magnetic Resonance Imaging*, 30(7):944–53.

Roberts, C., Little, R., Watson, Y., Zhao, S., Buckley, D. L., and Parker, G. J. M. (2011). The effect of blood inflow and B(1)-field inhomogeneity on measurement of the arterial input function in axial 3D spoiled gradient echo dynamic contrast-enhanced MRI. *Magnetic Resonance in Medicine*, 65(1):108–19.

Roberts, H. C., Roberts, T. P., Brasch, R. C., and Dillon, W. P. (2000). Quantitative measurement of microvascular permeability in human brain tumors achieved using dynamic contrast-enhanced MR imaging: correlation with histologic grade. *American Journal of Neuroradiology*, 21(5):891–9.

Roberts, T. P. L. (1997). Physiologic measurements by contrast-enhanced MR imaging: Expectations and limitations. *Journal of Magnetic Resonance Imaging*, 7(1):82–90.

Rohrer, M., Bauer, H., Mintorovitch, J., Requardt, M., and Weinmann, H.-J. (2005). Comparison of magnetic properties of MRI contrast media solutions at different magnetic field strengths. *Investigative Radiology*, 40(11):715–24.

Rosenberg, G. A. (2009). Inflammation and white matter damage in vascular cognitive impairment. *Stroke*, 40(3 Suppl):S20–3.

Rosenberg, G. A. (2012). Neurological diseases in relation to the blood-brain barrier. *Journal of Cerebral Blood Flow and Metabolism*, 32(7):1139–51.

Rosenkrantz, A. B., Geppert, C., Grimm, R., Block, T. K., Glielmi, C., Feng, L., Otazo, R., Ream, J. M., Romolo, M. M., Taneja, S. S., Sodickson, D. K., and Chandarana, H. (2015). Dynamic contrast-enhanced MRI of the prostate with high spatiotemporal resolution using compressed sensing, parallel imaging, and continuous golden-angle radial sampling: preliminary experience. *Journal of Magnetic Resonance Imaging*, 41(5):1365–73.

Rost, N. S., Rahman, R. M., Biffi, A., Smith, E. E., Kanakis, A., Fitzpatrick, K., Lima, F., Worrall, B. B., Meschia, J. F., Brown, R. D., Brott, T. G., Sorensen, A. G., Greenberg, S. M., Furie, K. L., and Rosand, J. (2010). White matter hyperintensity volume is increased in small vessel stroke subtypes. *Neurology*, 75(19):1670–7.

Rostrup, E., Larsson, H. B., Toft, P. B., Garde, K., Thomsen, C., Ring, P., Sø ndergaard, L., and Henriksen, O. (1994). Functional MRI of CO2 induced increase in cerebral perfusion. *NMR in biomedicine*, 7(1-2):29–34.

Rouhl, R. P. W., van Oostenbrugge, R. J., Knottnerus, I. L. H., Staals, J. E. A., and Lodder, J. (2008). Virchow-Robin spaces relate to cerebral small vessel disease severity. *Journal of Neurology*, 255(5):692–6.

Roy, B., Awasthi, R., Bindal, A., Sahoo, P., Kumar, R., Behari, S., Ojha, B. K., Husain, N., Pandey, C. M., Rathore, R. K. S., and Gupta, R. K. (2013). Comparative evaluation of 3-dimensional pseudocontinuous arterial spin labeling with dynamic contrast-enhanced perfusion magnetic resonance imaging in grading of human glioma. *Journal of Computer Assisted Tomography*, 37(3):321–326.

Sachdev, P., Wen, W., Chen, X., and Brodaty, H. (2007). Progression of white matter hyperintensities in elderly individuals over 3 years. *Neurology*, 68(3):214–22.

Sachdev, P., Wen, W., Shnier, R., and Brodaty, H. (2004). Cerebral blood volume in T2-weighted white matter hyperintensities using exogenous contrast based perfusion MRI. *The Journal of Neuropsychiatry and Clinical Neurosciences*, 16(1):83–92.

Sahoo, P., Rathore, R. K. S., Awasthi, R., Roy, B., Verma, S., Rathore, D., Behari, S., Husain, M., Husain, N., Pandey, C. M., Mohakud, S., and Gupta, R. K. (2013). Subcompartmentalization of extracellular extravascular space (EES) into permeability and leaky space with local arterial input function (AIF) results in improved discrimination between high- and low-grade glioma using dynamic contrast-enhanced (DCE) MRI. *Journal of Magnetic Resonance Imaging*, 38(3):677–688.

Samuelsson, M., Söderfeldt, B., and Olsson, G. B. (1996). Functional outcome in patients with lacunar infarction. *Stroke*, 27(5):842–6.

Schabel, M. C. and Parker, D. L. (2008). Uncertainty and bias in contrast concentration measurements using spoiled gradient echo pulse sequences. *Physics in Medicine and Biology*, 53(9):2345–73.

Scheltens, P., Barkhof, F., Leys, D., Pruvo, J. P., Nauta, J. J., Vermersch, P., Steinling, M., and Valk, J. (1993). A semiquantative rating scale for the assessment of signal hyperintensities on magnetic resonance imaging. *Journal of the Neurological Sciences*, 114(1):7–12.

Schlageter, K. E., Molnar, P., Lapin, G. D., and Groothuis, D. R. (1999). Microvessel organization and structure in experimental brain tumors: microvessel populations with distinctive structural and functional properties. *Microvascular Research*, 58(3):312–28.

Schmidt, R., Enzinger, C., Ropele, S., Schmidt, H., and Fazekas, F. (2003). Progression of cerebral white matter lesions: 6-year results of the Austrian Stroke Prevention Study. *Lancet*, 361(9374):2046–8.

Schrier, R. W. (2010). Does 'asymptomatic hyponatremia' exist? *Nature Reviews Nephrology*, 6(4):185–185.

Shah, N. J., Zaitsev, M., Steinhoff, S., and Zilles, K. (2001). A new method for fast multislice T(1) mapping. *NeuroImage*, 14(5):1175–85.

Shames, D. M., Kuwatsuru, R., Vexler, V., Mühler, A., and Brasch, R. C. (1993). Measurement of capillary permeability to macromolecules by dynamic magnetic resonance imaging: A quantitative noninvasive technique. *Magnetic Resonance in Medicine*, 29(5):616–622.

Shaul, M. E., Hallacoglu, B., Sassaroli, A., Shukitt-Hale, B., Fantini, S., Rosenberg, I. H., and Troen, A. M. (2014). Cerebral blood volume and vasodilation are independently diminished by aging and hypertension: a near infrared spectroscopy study. *Journal of Alzheimer's Disease*, 42 Suppl 3:S189–98.

Shin, K. E., Ahn, K. J., Choi, H. S., Jung, S. L., Kim, B. S., Jeon, S. S., and Hong, Y. G. (2014). DCE and DSC MR perfusion imaging in the differentiation of recurrent tumour from treatment-related changes in patients with glioma. *Clinical Radiology*, 69(6):e264–e272.

Shinohara, R. T., Crainiceanu, C. M., Caffo, B. S., Gaitán, M. I., and Reich, D. S. (2011). Population-wide principal component-based quantification of blood-brain-barrier dynamics in multiple sclerosis. *NeuroImage*, 57(4):1430–46.

Shoamanesh, A., Kwok, C. S., and Benavente, O. (2011). Cerebral microbleeds: histopathological correlation of neuroimaging. *Cerebrovascular Diseases*, 32(6):528–34.

Shrestha, I., Takahashi, T., Nomura, E., Ohtsuki, T., Ohshita, T., Ueno, H., Kohriyama, T., and Matsumoto, M. (2009). Association between central systolic blood pressure, white matter lesions in cerebral MRI and carotid atherosclerosis. *Hypertension Research*, 32(10):869–874.

Singh, A., Haris, M., Rathore, D., Purwar, A., Sarma, M., Bayu, G., Husain, N., Rathore, R. K. S., and Gupta, R. K. (2007). Quantification of physiological and hemodynamic indices using T(1) dynamic contrast-enhanced MRI in intracranial mass lesions. *Journal of Magnetic Resonance Imaging*, 26(4):871–80.

Skinner, J. T., Yankeelov, T. E., Peterson, T. E., and Does, M. D. (2012). Comparison of dynamic contrast-enhanced MRI and quantitative SPECT in a rat glioma model. *Contrast Media & Molecular Imaging*, 7(6):494–500.

Smith, S. M. and Brady, J. M. (1997). SUSAN—A new approach to low level image processing. *International Journal of Computer Vision*, 23(1):45–78.

Song, S. K., Lee, S.-K., Lee, J. J., Lee, J. E., Choi, H. S., Sohn, Y. H., and Lee, P. H. (2011). Blood-brain barrier impairment is functionally correlated with clinical severity in patients of multiple system atrophy. *Neurobiology of Aging*, 32(12):2183–9.

Sourbron, S. (2014). A tracer-kinetic field theory for medical imaging. *IEEE Transactions on Medical Imaging*, 33(4):935–46.

Sourbron, S., Ingrisch, M., Siefert, A., Reiser, M., and Herrmann, K. (2009). Quantification of cerebral blood flow, cerebral blood volume, and blood-brain-barrier leakage with DCE-MRI. *Magnetic Resonance in Medicine*, 62(1):205–17.

Sourbron, S. P. and Buckley, D. L. (2011). On the scope and interpretation of the Tofts models for DCE-MRI. *Magnetic Resonance in Medicine*, 66(3):735–745.

Sourbron, S. P. and Buckley, D. L. (2012). Tracer kinetic modelling in MRI: estimating perfusion and capillary permeability. *Physics in Medicine and Biology*, 57(2):R1–33.

Sourbron, S. P. and Buckley, D. L. (2013). Classic models for dynamic contrast-enhanced MRI. *NMR in Biomedicine*, 26(8):1004–27.

Staals, J., Makin, S. D. J., Doubal, F. N., Dennis, M. S., and Wardlaw, J. M. (2014). Stroke subtype, vascular risk factors, and total MRI brain small-vessel disease burden. *Neurology*, 83(14):1228–34.

Starr, J. M., Farrall, A. J., Armitage, P. A., McGurn, B., and Wardlaw, J. (2009). Blood-brain barrier permeability in Alzheimer's disease: a case-control MRI study. *Psychiatry Research*, 171(3):232–41.

Starr, J. M., Wardlaw, J., Ferguson, K., MacLullich, A., Deary, I. J., and Marshall, I. (2003). Increased blood-brain barrier permeability in type II diabetes demonstrated by gadolinium magnetic resonance imaging. *Journal of Neurology, Neurosurgery, and Psychiatry*, 74(1):70–6.

Stevenson, S. F., Doubal, F. N., Shuler, K., and Wardlaw, J. M. (2010). A systematic review of dynamic cerebral and peripheral endothelial function in lacunar stroke versus controls. *Stroke*, 41(6):e434–42.

Stikov, N., Boudreau, M., Levesque, I. R., Tardif, C. L., Barral, J. K., and Pike, G. B. (2015). On the accuracy of T1 mapping: searching for common ground. *Magnetic Resonance in Medicine*, 73(2):514–22.

Stine, R. A. (1995). Graphical interpretation of variance inflation factors. *The American Statistician*, 49(1):53–56.

Stoquart-ElSankari, S., Balédent, O., Gondry-Jouet, C., Makki, M., Godefroy, O., and Meyer, M.-E. (2007). Aging effects on cerebral blood and cerebrospinal fluid flows. *Journal of Cerebral Blood Flow and Metabolism*, 27(9):1563–72.

Strazzullo, P., D'Elia, L., Kandala, N.-B., and Cappuccio, F. P. (2009). Salt intake, stroke, and cardiovascular disease: meta-analysis of prospective studies. *BMJ (Clinical Research Ed.)*, 339:b4567.

Strong, K., Mathers, C., and Bonita, R. (2007). Preventing stroke: saving lives around the world. *The Lancet Neurology*, 6(2):182–7.

Su, M. Y., Head, E., Brooks, W. M., Wang, Z., Muggenburg, B. A., Adam, G. E., Sutherland, R., Cotman, C. W., and Nalcioglu, O. (1998). Magnetic resonance imaging of anatomic and vascular characteristics in a canine model of human aging. *Neurobiology of Aging*, 19(5):479–85.

Subashi, E., Choudhury, K. R., and Johnson, G. A. (2014). An analysis of the uncertainty and bias in DCE-MRI measurements using the spoiled gradient-recalled echo pulse sequence. *Medical Physics*, 41(3):032301.

Sudlow, C. L. and Warlow, C. P. (1997). Comparable studies of the incidence of stroke and its pathological types: results from an international collaboration. International Stroke Incidence Collaboration. *Stroke*, 28(3):491–9.

Swan, G. E. and Lessov-Schlaggar, C. N. (2007). The effects of tobacco smoke and nicotine on cognition and the brain. *Neuropsychology Review*, 17(3):259–73.

Syková, E. and Nicholson, C. (2008). Diffusion in brain extracellular space. *Physiological Reviews*, 88(4):1277–340.

Taheri, S., Candelario-Jalil, E., Estrada, E. Y., and Rosenberg, G. A. (2009). Spatiotemporal correlations between blood-brain barrier permeability and apparent diffusion coefficient in a rat model of ischemic stroke. *PloS one*, 4(8):e6597.

Taheri, S., Gasparovic, C., Huisa, B. N., Adair, J. C., Edmonds, E., Prestopnik, J., Grossetete, M., Shah, N. J., Wills, J., Qualls, C., and Rosenberg, G. A. (2011a). Blood-brain barrier permeability abnormalities in vascular cognitive impairment. *Stroke*, 42(8):2158–63.

Taheri, S., Gasparovic, C., Shah, N. J., and Rosenberg, G. A. (2011b). Quantitative measurement of blood-brain barrier permeability in human using dynamic contrast-enhanced MRI with fast T1 mapping. *Magnetic Resonance in Medicine*, 65(4):1036–42.

Taheri, S. and Sood, R. (2006). Kalman filtering for reliable estimation of BBB permeability. *Magnetic Resonance Imaging*, 24(8):1039–1049.

Taheri, S. and Sood, R. (2007). Partial volume effect compensation for improved reliability of quantitative blood-brain barrier permeability. *Magnetic Resonance Imaging*, 25(5):613–25.

Taylor, W. D., MacFall, J. R., Provenzale, J. M., Payne, M. E., McQuoid, D. R., Steffens, D. C., and Krishnan, K. R. R. (2003). Serial MR imaging of volumes of hyperintense white matter lesions in elderly patients: correlation with vascular risk factors. *American Journal of Roentgenology*, 181(2):571–6.

Thompson, E. M., Guillaume, D. J., Dósa, E., Li, X., Nazemi, K. J., Gahramanov, S., Hamilton, B. E., and Neuwelt, E. A. (2012). Dual contrast perfusion MRI in a single imaging session for assessment of pediatric brain tumors. *Journal of Neuro-oncology*, 109(1):105–14.

Thornhill, R. E., Chen, S., Rammo, W., Mikulis, D. J., and Kassner, A. (2010). Contrast-enhanced MR imaging in acute ischemic stroke: T2* measures of blood-brain barrier permeability and their relationship to T1 estimates and hemorrhagic transformation. *American Journal of Neuroradiology*, 31(6):1015–22.

Titze, J., Dahlmann, A., Lerchl, K., Kopp, C., Rakova, N., Schröder, A., and Luft, F. C. (2013). Spooky sodium balance. *Kidney International*, 85(4):759–767.

Tofts, P. S., editor (2005). *Quantitative MRI of the brain: measuring changes caused by disease*. John Wiley & Sons.

Tofts, P. S. (2010). T1-weighted DCE imaging concepts: modelling, acquisition and analysis. *MAGNETOM Flash*, 3.

Tofts, P. S., Brix, G., Buckley, D. L., Evelhoch, J. L., Henderson, E., Knopp, M. V., Larsson, H. B., Lee, T. Y., Mayr, N. A., Parker, G. J., Port, R. E., Taylor, J., and Weisskoff, R. M. (1999). Estimating kinetic parameters from dynamic contrast-enhanced T(1)-weighted MRI of a diffusable tracer: standardized quantities and symbols. *Journal of Magnetic Resonance Imaging*, 10(3):223–32.

Tofts, P. S. and Kermode, A. G. (1991). Measurement of the blood-brain barrier permeability and leakage space using dynamic MR imaging. 1. Fundamental concepts. *Magnetic Resonance in Medicine*, 17(2):357–67.

Tomimoto, H., Akiguchi, I., Suenaga, T., Nishimura, M., Wakita, H., Nakamura, S., and Kimura, J. (1996). Alterations of the blood-brain barrier and glial cells in white-matter lesions in cerebrovascular and Alzheimer's disease patients. *Stroke*, 27(11):2069–74.

Topakian, R., Barrick, T. R., Howe, F. a., and Markus, H. S. (2010). Blood-brain barrier permeability is increased in normal-appearing white matter in patients with lacunar stroke and leucoaraiosis. *Journal of Neurology, Neurosurgery, and Psychiatry*, 81(2):192–7.

Troprès, I., Pannetier, N., Grand, S., Lemasson, B., Moisan, A., Péoc'h, M., Rémy, C., and Barbier, E. L. (2015). Imaging the microvessel caliber and density: principles and applications of microvascular MRI. *Magnetic Resonance in Medicine*, 73(1):325–41.

Tsao, J., Boesiger, P., and Pruessmann, K. P. (2003). k-t BLAST and k-t SENSE: dynamic MRI with high frame rate exploiting spatiotemporal correlations. *Magnetic Resonance in Medicine*, 50(5):1031–42.

Tudorica, L. A., Oh, K. Y., Roy, N., Kettler, M. D., Chen, Y., Hemmingson, S. L., Afzal, A., Grinstead, J. W., Laub, G., Li, X., and Huang, W. (2012). A feasible high spatiotemporal resolution breast DCE-MRI protocol for clinical settings. *Magnetic Resonance Imaging*, 30(9):1257–67.

Türkbey, B., Thomasson, D., Pang, Y., Bernardo, M., and Choyke, P. L. (2010). The role of dynamic contrast-enhanced MRI in cancer diagnosis and treatment. *Diagnostic and Interventional Radiology*, 16(3):186–92.

Valdés Hernández, M. D. C., Ferguson, K. J., Chappell, F. M., and Wardlaw, J. M. (2010). New multispectral MRI data fusion technique for white matter lesion segmentation: method and comparison with thresholding in FLAIR images. *European Radiology*, 20(7):1684–91.

Valdés Hernández, M. D. C., Royle, N. A., Jackson, M. R., Muñoz Maniega, S., Penke, L., Bastin, M. E., Deary, I. J., and Wardlaw, J. M. (2012). Color Fusion of Magnetic Resonance Images Improves Intracranial Volume Measurement in Studies of Aging. *Open Journal of Radiology*, 02(01):1–9.

van der Flier, W. M., van Straaten, E. C. W., Barkhof, F., Verdelho, A., Madureira, S., Pantoni, L., Inzitari, D., Erkinjuntti, T., Crisby, M., Waldemar, G., Schmidt, R., Fazekas, F., and Scheltens, P. (2005). Small vessel disease and general cognitive function in nondisabled elderly: the LADIS study. *Stroke*, 36(10):2116–20.

van Dijk, E. J., Prins, N. D., Vrooman, H. A., Hofman, A., Koudstaal, P. J., and Breteler, M. M. B. (2008). Progression of cerebral small vessel disease in relation to risk factors and cognitive consequences: Rotterdam Scan study. *Stroke*, 39(10):2712–9.

van Straaten, E. C. W., Fazekas, F., Rostrup, E., Scheltens, P., Schmidt, R., Pantoni, L., Inzitari, D., Waldemar, G., Erkinjuntti, T., Mäntylä, R., Wahlund, L.-O., and Barkhof, F. (2006). Impact of white matter hyperintensities scoring method on correlations with clinical data: the LADIS study. *Stroke*, 37(3):836–40.

van Vaals, J. J., Brummer, M. E., Dixon, W. T., Tuithof, H. H., Engels, H., Nelson, R. C., Gerety, B. M., Chezmar, J. L., and den Boer, J. A. (1993). "Keyhole" method for accelerating imaging of contrast agent uptake. *Journal of Magnetic Resonance Imaging*, 3(4):671–5.

Verbalis, J. G. (2010). Brain volume regulation in response to changes in osmolality. *Neuroscience*, 168(4):862–70.

Verhaaren, B. F. J., Vernooij, M. W., de Boer, R., Hofman, A., Niessen, W. J., van der Lugt, A., and Ikram, M. A. (2013). High blood pressure and cerebral white matter lesion progression in the general population. *Hypertension*, 61(6):1354–1359.

Vermeer, S. E., Longstreth, W. T., and Koudstaal, P. J. (2007). Silent brain infarcts: a systematic review. *The Lancet Neurology*, 6(7):611–9.

Vermeer, S. E., Prins, N. D., den Heijer, T., Hofman, A., Koudstaal, P. J., and Breteler, M. M. B. (2003). Silent brain infarcts and the risk of dementia and cognitive decline. *The New England Journal of Medicine*, 348(13):1215–22.

Vernooij, M. W., van der Lugt, A., Ikram, M. A., Wielopolski, P. A., Niessen, W. J., Hofman, A., Krestin, G. P., and Breteler, M. M. B. (2008). Prevalence and risk factors of cerebral microbleeds: the Rotterdam Scan Study. *Neurology*, 70(14):1208–14.

Vidarsson, L., Thornhill, R. E., Liu, F., Mikulis, D. J., and Kassner, A. (2009). Quantitative permeability magnetic resonance imaging in acute ischemic stroke: how long do we need to scan? *Magnetic Resonance Imaging*, 27(9):1216–22.

Vogt, F., Eggebrecht, H., and Laub, G. (2007). High spatial and temporal resolution MRA (TWIST) in acute aortic dissection. In *Proc ISMRM, Berlin*, page 92.

Vymazal, J., Righini, A., Brooks, R. A., Canesi, M., Mariani, C., Leonardi, M., and Pezzoli, G. (1999). T1 and T2 in the brain of healthy subjects, patients with Parkinson disease, and patients with multiple system atrophy: relation to iron content. *Radiology*, 211(2):489–95.

Wahlund, L. O., Barkhof, F., Fazekas, F., Bronge, L., Augustin, M., Sjögren, M., Wallin, A., Ader, H., Leys, D., Pantoni, L., Pasquier, F., Erkinjuntti, T., and Scheltens, P. (2001). A new rating scale for age-related white matter changes applicable to MRI and CT. *Stroke*, 32(6):1318–22.

Wahlund, L.-O. and Bronge, L. (2000). Contrast-enhanced MRI of white matter lesions in patients with blood-brain barrier dysfunction. *Annals of the New York Academy of Sciences*, 903:477–481.

Waldstein, S. R., Wendell, C. R., Lefkowitz, D. M., Siegel, E. L., Rosenberger, W. F., Spencer, R. J., Manukyan, Z., and Katzel, L. I. (2012). Interactive relations of blood pressure and age to subclinical cerebrovascular disease. *Journal of Hypertension*, 30(12):2352–2356.

Walker-Samuel, S., Leach, M. O., and Collins, D. J. (2006). Evaluation of response to treatment using DCE-MRI: the relationship between initial area under the gadolinium curve (IAUGC) and quantitative pharmacokinetic analysis. *Physics in Medicine and Biology*, 51(14):3593–3602.

Wang, H., Golob, E. J., and Su, M.-Y. (2006). Vascular volume and blood-brain barrier permeability measured by dynamic contrast enhanced MRI in hippocampus and cerebellum

of patients with MCI and normal controls. *Journal of Magnetic Resonance Imaging*, 24(3):695–700.

Wardlaw, J. M. (2010). Blood-brain barrier and cerebral small vessel disease. *Journal of the Neurological Sciences*, 299(1-2):66–71.

Wardlaw, J. M., Dennis, M. S., Warlow, C. P., and Sandercock, P. A. (2001). Imaging appearance of the symptomatic perforating artery in patients with lacunar infarction: occlusion or other vascular pathology? *Annals of Neurology*, 50(2):208–15.

Wardlaw, J. M., Doubal, F., Armitage, P. A., Chappell, F., Carpenter, T., Muñoz Maniega, S., Farrall, A., Sudlow, C., Dennis, M., and Dhillon, B. (2009). Lacunar stroke is associated with diffuse blood-brain barrier dysfunction. *Annals of Neurology*, 65(2):194–202.

Wardlaw, J. M., Doubal, F. N., Valdés Hernández, M. D. C., Wang, X., Chappell, F. M., Shuler, K., Armitage, P. A., Carpenter, T. C., and Dennis, M. S. (2013a). Blood-brain barrier permeability and long-term clinical and imaging outcomes in cerebral small vessel disease. *Stroke*, 44(2):525–7.

Wardlaw, J. M., Farrall, A., Armitage, P. A., Carpenter, T., Chappell, F., Doubal, F., Chowdhury, D., Cvoro, V., and Dennis, M. S. (2008). Changes in background blood-brain barrier integrity between lacunar and cortical ischemic stroke subtypes. *Stroke*, 39(4):1327–32.

Wardlaw, J. M., Sandercock, P. A. G., Dennis, M. S., and Starr, J. (2003). Is breakdown of the blood-brain barrier responsible for lacunar stroke, leukoaraiosis, and dementia? *Stroke*, 34(3):806–12.

Wardlaw, J. M., Smith, C., and Dichgans, M. (2013b). Mechanisms of sporadic cerebral small vessel disease: insights from neuroimaging. *The Lancet Neurology*, 12(5):483–97.

Wardlaw, J. M., Smith, E. E., Biessels, G. J., Cordonnier, C., Fazekas, F., Frayne, R., Lindley, R. I., O'Brien, J. T., Barkhof, F., Benavente, O. R., Black, S. E., Brayne, C., Breteler, M., Chabriat, H., DeCarli, C., de Leeuw, F. E., Doubal, F., Duering, M., Fox, N. C., Greenberg, S., Hachinski, V., Kilimann, I., Mok, V., Oostenbrugge, R. V., Pantoni, L., Speck, O., Stephan, B. C. M., Teipel, S., Viswanathan, A., Werring, D., Chen, C., Smith, C., van Buchem, M., Norrving, B., Gorelick, P. B., and Dichgans, M. (2013c). Neuroimaging standards for research into small vessel disease and its contribution to ageing and neurodegeneration. *The Lancet Neurology*, 12(8):822–838.

Warntjes, J. B. M., Leinhard, O. D., West, J., and Lundberg, P. (2008). Rapid magnetic resonance quantification on the brain: optimization for clinical usage. *Magnetic Resonance in Medicine*, 60(2):320–9.

Wei, X.-E., Wang, D., Li, M.-H., Zhang, Y.-Z., Li, Y.-H., and Li, W.-B. (2011). A useful tool for the initial assessment of blood-brain barrier permeability after traumatic brain injury in rabbits: dynamic contrast-enhanced magnetic resonance imaging. *The Journal of Trauma*, 71(6):1645–50.

Weinmann, H. J., Laniado, M., and Mützel, W. (1984). Pharmacokinetics of GdDTPA/dimeglumine after intravenous injection into healthy volunteers. *Physiological Chemistry and Physics and Medical NMR*, 16(2):167–72.

Wharton, S. B., Simpson, J. E., Brayne, C., and Ince, P. G. (2015). Age-associated white matter lesions: the MRC Cognitive Function and Ageing Study. *Brain Pathology*, 25(1):35–43.

Wilkinson, I. D., Jellineck, D. A., Levy, D., Giesel, F. L., Romanowski, C. A. J., Miller, B.-A., and Griffiths, P. D. (2006). Dexamethasone and enhancing solitary cerebral mass lesions: alterations in perfusion and blood-tumor barrier kinetics shown by magnetic resonance imaging. *Neurosurgery*, 58(4):640–6.

Wuerfel, J., Haertle, M., Waiczies, H., Tysiak, E., Bechmann, I., Wernecke, K. D., Zipp, F., and Paul, F. (2008). Perivascular spaces – MRI marker of inflammatory activity in the brain? *Brain*, 131(9):2332–40.

Xu, C., Schmidt, W. U. H., Galinovic, I., Villringer, K., Hotter, B., Ostwaldt, A.-C., Denisova, N., Kellner, E., Kiselev, V., and Fiebach, J. B. (2012). The potential of microvessel density in prediction of infarct growth: a two-month experimental study in vessel size imaging. *Cerebrovascular Diseases*, 33(4):303–9.

Xu, C., Schmidt, W. U. H., Villringer, K., Brunecker, P., Kiselev, V., Gall, P., and Fiebach, J. B. (2011). Vessel size imaging reveals pathological changes of microvessel density and size in acute ischemia. *Journal of Cerebral Blood Flow and Metabolism*, 31(8):1687–95.

Yamauchi, H., Fukuyama, H., Harada, K., Yamaguchi, S., Miyoshi, T., Doi, T., Kimura, J., Iwasaki, Y., Asato, R., and Yonekura, Y. (1990). White matter hyperintensities may correspond to areas of increased blood volume: correlative MR and PET observations. *Journal of Computer Assisted Tomography*, 14(6):905–8.

Yankeelov, T. E., Luci, J. J., Lepage, M., Li, R., Debusk, L., Lin, P. C., Price, R. R., and Gore, J. C. (2005). Quantitative pharmacokinetic analysis of DCE-MRI data without an arterial input function: a reference region model. *Magnetic Resonance Imaging*, 23(4):519–29.

Yoon, H., Park, S.-h., and Ye, J. C. (2014). Improved volumetric imaging for DCE-MRI using parallel imaging and dynamic compressed sensing. In *GlobalSIP 2014: Information Processing for Big Data*, volume 1, pages 646–649.

Young, V. G., Halliday, G. M., and Kril, J. J. (2008). Neuropathologic correlates of white matter hyperintensities. *Neurology*, 71(11):804–11.

Yuan, J., Chow, S. K. K., Zhang, Q., Yeung, D. K. W., Ahuja, A. T., and King, A. D. (2013). The use of dynamic tracer concentration in veins for quantitative DCE-MRI kinetic analysis in head and neck. *PloS one*, 8(3):e59885.

Zhang, N., Zhang, L., Qiu, B., Meng, L., Wang, X., and Hou, B. L. (2012). Correlation of volume transfer coefficient Ktrans with histopathologic grades of gliomas. *Journal of Magnetic Resonance Imaging*, 36(2):355–63.

Zhang, X., Petersen, E. T., Ghariq, E., De Vis, J. B., Webb, A. G., Teeuwisse, W. M., Hendrikse, J., and van Osch, M. J. P. (2013). In vivo blood T(1) measurements at 1.5 T, 3 T, and 7 T. *Magnetic Resonance in Medicine*, 70(4):1082–6.

Zhang, Y., Yeung, H. N., O'Donnell, M., and Carson, P. L. (1998). Determination of sample time for T1 measurement. *Journal of Magnetic Resonance Imaging*, 8(3):675–681.

Zhang, Z., Duckart, J., Slatore, C. G., Fu, Y., Petrik, A. F., Thorp, M. L., and Cohen, D. M. (2014). Individuality of the plasma sodium concentration. *American Journal of Physiology. Renal Physiology*, 306(12):F1534–43.

Zhu, X. P., Li, K. L., Kamaly-Asl, I. D., Checkley, D. R., Tessier, J. J., Waterton, J. C., and Jackson, A. (2000). Quantification of endothelial permeability, leakage space, and blood volume in brain tumors using combined T1 and T2* contrast-enhanced dynamic MR imaging. *Journal of Magnetic Resonance Imaging*, 11(6):575–85.

Zhu, Y.-C., Tzourio, C., Soumaré, A., Mazoyer, B., Dufouil, C., and Chabriat, H. (2010). Severity of dilated Virchow-Robin spaces is associated with age, blood pressure, and MRI markers of small vessel disease: a population-based study. *Stroke*, 41(11):2483–90.

Zonneveld, H. I., Loehrer, E. A., Hofman, A., Niessen, W. J., van der Lugt, A., Krestin, G. P., Ikram, M. A., and Vernooij, M. W. (2015). The bidirectional association between reduced cerebral blood flow and brain atrophy in the general population. *Journal of Cerebral Blood Flow and Metabolism*, 35(11):1882–7.

A. Additional tables for systematic literature review

This section provides additional data extracted from DCE-MRI publications that were included in the systematic literature review (Chapter 2). Table A.1 lists all included studies, their sample characteristics and main purposes. Detailed information about the imaging protocol is given in Table A.2, while Table A.3 provides a list of K^{Trans} values reported for different tissue types.

Table A.1.: List of included studies and their main characteristics. Age is given as cohort mean and standard deviation if available; otherwise the range is stated. '–' indicates that the information was not provided in the article.

Publication	Sample type	Pathology	Sample size	Age (years)	Main purpose
Abe et al. (2015)	Human	Low grade glioma	4	53.3 (35–77)	Determine the utility of DCE-MRI for the differential diagnosis of brain tumours
		High grade glioma	13	59.2 (34–84)	
		Metastasis	6	64.3 (48–77)	
		Lymphoma	3	69.0 (55–78)	
Abo-Ramadan et al. (2009)	Rat	Focal ischaemia	107	n/a	Compare quantitative post-ischaemic BBB leakiness with controls
		Healthy controls	6	n/a	
Ahn et al. (2014)	Human	Glioblastoma	43	58.0±14.5	Assess whether the MGMT methylation status can be predicted by DCE-MRI
Aksoy et al. (2013)	Human	Intracerebral haemmorrhage	25	–	Quantify BBB permeability following spontaneous intracerebral haemorrhage and investigate relationship with haematoma size and location
Ali et al. (2010)	Rat	Glioma	44	n/a	Determine the changes in tumour size, DCE-MRI parameters and VEGF2 expression in VEGF tyrosine kinase inhibitor treated glioma
Almeida-Freitas et al. (2014)	Human	Metastasis	26	56.7±12.8	Evaluate the ability of DCE-MRI to asess the effect of stereotactic radiosurgery on brain metastases and predict outcome
Armitage et al. (2011)	Human	Mild ischaemic stroke	60	67.0±12.0	Determine effect of scanner noise, drift, intrinsic tissue properties and imaging sequence parameters on DCE-MRI
		Healthy controls	6	33.0±4.0	
Artzi et al. (2015)	Human	Glioblastoma	11	38.0±18.0	Investigate the relationship between DCE-MRI and DSC-MRI measurements of cerebral blood volume
		Healthy controls	17	32.0±10.0	
Aryal et al. (2014)	Rat	Glioma	18	n/a	Test for correlations between DCE-MRI parameters and tumour cellularity
Awasthi et al. (2012)	Human	Glioblastoma	47	–	Look for association of MMP-9 expression with quantitative DCE-MRI measures
Bagher-Ebadian et al. (2012)	Human	Glioblastoma	10	23–75	Select a model for DCE-MRI assessment of the heterogeneous glioblastoma based on a voxel-by-voxel decision
Bergamino et al. (2013)	Human	Tumour	25	54.6±10.0	Assess the feasibility of measuring BBB permeability in brain tumours and compare two tracer kinetic models
Bergamino et al. (2014)	Human	Astrocytic tumours	30	58.8±8.1	Compare the modified Tofts model and an empirical PUN algorithm in brain tumours

Continued on next page

Table A.1 — *Continued from previous page*

Publication	Sample type	Pathology	Sample size	Age (years)	Main purpose
Brandt et al. (2008)	Rat	Pneumococcal meningitis	29	n/a	Compare BBB leakiness in infected animals with controls
		Healthy controls	13		
Budde et al. (2012)	Rat	Metastasis	12	n/a	Assess BBB status of brain metastases compared to healthy brain tissue
Cao et al. (2009)	Human	Tumour	10	45.0±15.5	Determine whether early assessment of BBB leakiness can predict late neurocognitive dysfunction after radiation therapy
Cha et al. (2006)	Human	Glioma	20	47.0±15.5	Compare permeability measurements determined with DCE-MRI and DSC-MRI methods
		Meningeoma	7		
Choi et al. (2013)	Human	Glioma	9	n/a	Assess ability of DCE-MRI parameters for glioma grading and compare with ADC
Chu et al. (2012)	Human	Tumour	13	54.6±17.7	Assess correlation of permeability parameters with ADC in different brain tumour types
Chwang et al. (2014)	Rat	Glioma	9	n/a	Compare DCE-MRI parameters using two different contrast agents
Cramer et al. (2014)	Human	MS	4	37.9±10.0	Investigate whether BBB permeability is disrupted in NAWM in MS patients compared to controls
		Healthy controls	24	37.1±12.0	
Cramer and Larsson (2014)	Human	MS	4	n/a	Explore the optimal conditions and model for accurate estimation of low permeability
		Optic neuritis	1	n/a	
		Healthy controls	17	33.0±10.0	
Durukan et al. (2009)	Rat	Focal ischaemia	10	n/a	Monitor the temporal pattern of post-ischaemic BBB permeability
Engelhorn et al. (2013)	Rat	Glioma	12	n/a	Define a K^{Trans} and FA threshold for tumour assessment
Ewing et al. (2003)	Rat	Focal ischaemia	–	n/a	Compare DCE-MRI derived measures with ^{14}C-sucrose levels determined by quantitative autoradiography
Farjam et al. (2014)	Human	Metastasis	20	56.4±9.5	Develop a model-free analysis technique for the assessment of response of brain metastases to radiotherapy
Ferl et al. (2010)	Human	Glioma	16	50.3 (36–63)	Develop a model-free analysis technique for the assessment of response of brain metastases to radiotherapy
Ferrier et al. (2007)	Rat	Glioma	5	n/a	Compare DCE-MRI parameters with ^{14}C-aminoisobutyric acid levels determined by quantitative autoradiography
Gaitán et al. (2011)	Human	MS	80	40.3±10.4	Investigate the BBB permeability enhancement dynamics of MS lesions
Gupta et al. (2012)	Human	Neurocysticercosis	30	7–61	Determine differences in DCE-MRI and MMP-9 levels between asymptomatic and symptomatic subjects
		Healthy controls	5	–	

Continued on next page

Table A.1 — *Continued from previous page*

Publication	Sample type	Pathology	Sample size	Age (years)	Main purpose
Hanyu et al. (2002)	Human	Binswanger's disease	17	78.0 (69–86)	Investigate whether Binswanger's disease patients have increased BBB permeability
		Ischaemic events	10	77.0 (72–83)	
		Healthy controls	14	79.0 (73–88)	
Haris et al. (2008a)	Human	Tuberculoma	13	5–42	Correlate DCE-MRI derived permeability indices with immunohistochemically obtained VEGF and MMP-9 levels
Haris et al. (2008b)	Human	Astrocytoma	64	35.0±9.5	Look for the impact of leak correction on correlation of permeability indices with microvessel density and VEGF
Haris et al. (2008c)	Human	Infective lesion	26	26.6±9.3	Assess the utility of DCE-MRI and immunohistochemically derived measures in the differentiation of infective from neoplastic brain lesions
		Low grade glioma	25	36.3±11.2	
		High grade glioma	52	47.5±11.3	
Harrer et al. (2004)	Human	High grade glioma	18	55.5±10.8	Compare three tracer kinetic analysis techniques: a conventional established technique and two novel techniques
Hoff et al. (2012)	Rat	Glioma	17	n/a	Evaluate DCE- and DWI-MRI as biomarkers for VEGF-Trap treatment response in gliomas
Hormuth et al. (2014)	Rat	Glioma	8	n/a	Determine how the tracer kinetic parameters estimated with a population VIF differ from those with individual VIF
Ingrisch et al. (2012)	Human	MS	19	35.0±12.0	Investigate the feasibility of DCE-MRI for the quantification of permeability and perfusion in MS
Jelescu et al. (2011)	Human	MS	4	37.5 (30–44)	Compare a new dual-temporal resolution DCE-MRI protocol with simulated standard protocol
Jia et al. (2013)	Human	Astrocytoma	67	64.0±12.0	Evaluate the effectiveness of permeability parameters in the grading of astrocytoma
Kassner et al. (2005)	Human	Acute ischaemic stroke	10	38–80	Investigate evidence that increased BBB leakage in acute ischaemic stroke predicts increased risk of haemorrhage
Kassner et al. (2009)	Human	Acute ischaemic stroke	36	67.7±15.2	Investigate the role of DCE-MRI in stroke patients treated with and without rtPA
Kermode et al. (1990)	Human	MS	8	31.0 (15–43)	Analyse enhancement patterns in MS lesions
Kleppestøet al. (2014)	Human	Glioma	7	69.0	Evaluate the importance of T2* effect on the AIF and resulting tracer kinetic parameters
Krueck et al. (1994)	Rat	Glioma	17	n/a	Quantify radiation-induced changes of BBB permeability

Continued on next page

Table A.1 — *Continued from previous page*

Publication	Sample type	Pathology	Sample size	Age (years)	Main purpose
Larsen et al. (2013)	Human	Glioma	19	56.7±11.9	Investigate whether DCE-MRI can be used to differentiate radiation necrosis from tumour recurrence
Larsson et al. (2013)	Human	High grade glioma	15	53.7 (32–66)	Investigate the effect of variations in temporal resolution and total measurement times on tracer kinetic parameters
Larsson et al. (2014)	Human	High grade glioma	23	–	Investigate the influence of T1 mapping on kinetic parameters in longitudinal analysis of gliomas
Larsson et al. (1990)	Human	Glioma	1	–	Develop and test a model for quantifying BBB defects
		MS	4		
Larsson et al. (2009)	Human	Grade III astrocytoma	6	46.0 (28–59)	Present and test new analytic methodology estimating perfusion and permeability parameters
		Grade IV glioblastoma	4		
		Healthy controls	5	–	
Lee et al. (2014)	Dog	Tumour	7	n/a	Compare the performance of analytical and numerical analysis of the reference region model
Leppert et al. (2014)	Human	MS	44	34.0	Investigate how different protocols influence the detection of enhancing MS lesions
Li et al. (2000)	Human	Tomour	11	–	Compare new first pass method for DCE-MRI analysis with standard models
Li et al. (2012a)	Human	Vestibular schwannoma	3	–	Present and test a new dual temporal resolution-based tracer kinetic parametric mapping method
		Healthy controls	2	68.6	
Li et al. (2014)	Rat	Traumatic injury	3	n/a	Develop an improved DCE-MRI method in traumatic brain injuries and compare results with Evans Blue staining and T2 maps
Li et al. (2010)	Rat	Glioma	7	n/a	Accurately map the tumour blood volume using a three-side equilibrium water exchange model
Lüdemann et al. (2000)	Human	Glioma	25	42.4±18.5	Develop and test new technique for DCE-MRI data analysis and apply for differentiation of glioma types
Lüdemann et al. (2002)	Human	Glioma	25		Quantify BBB permeability of different brain tumour entities
		Meningeoma	4	47.8±18.0	
		Lymphoma	2		
Lüdemann et al. (2009)	Human	High grade glioma	9		Compare DCE-MRI using T1, T2, and T2* contrast, pulsed arterial spin labeling, and $H_2^{15}O$ positron emission tomography
		Meningeoma	2	53.0 (17–78)	
		Metastasis	1		

Continued on next page

Table A.1 — *Continued from previous page*

Publication	Sample type	Pathology	Sample size	Age (years)	Main purpose
Manuchehri et al. (2007)	Human	Prolactinoma	23	15–69	Investigate if dopamine agonists change functional vascularity, leading to reduction of prolactin levels and tumour size
		Healthy controls	15	22–41	
Mills et al. (2009)	Human	Glioma	45	48.0 (18–77)	Determine whether the enhancing fractions differ between low and high grade glioma
Miyati et al. (1997)	Human	Tumour	21	–	Develop and apply a dual DCE-MRI method for estimating perfusion and permeability parameters
Montagne et al. (2015)	Human	Normal ageing	18	73.2 (55–91)	Investigate BBB breakdown in the ageing brain
		Mild cognitive impairment	21	72.0 (55–81)	
		MS	19	26–53	
		Healthy young controls	6	23–47	
Nagaraja et al. (2010)	Rat	Focal ischaemia	15	n/a	Test whether the AIF measured with Gd-DTPA DCE-MRI in the SSS approximates the AIF of ^{14}C-labeled Gd-DTPA measured in femoral artery blood
Nagaraja et al. (2013)	Rat	Glioma	31	n/a	Investigate the effect of cilengitide treatment on DCE-MRI parameters
Noseworthy and Bray (2000)	Rat	Zinc deficiency	36	n/a	Evaluate if zinc deficiency affects BBB integrity
Provenzale et al. (2006)	Human	High grade glioma	10	51.0 (32–62)	Correlate the degree of contrast enhancement on DCE-MRI and the relative cerebral blood volume values on DSC-MRI
Quarles et al. (2012)	Rat	Gliosarcoma	10	n/a	Validate a dual-echo DSC-MRI approach for the estimation of permeability parameters
		Glioblastoma	10		
Roberts et al. (2000)	Human	Glioma	22	14–79	Assess correlation of permeability and perfusion measurements with tumour histologic grade
Roy et al. (2013)	Human	Glioma	64	43.0	Compare ASL with DCE-MRI for glioma grading
Sahoo et al. (2013)	Human	Glioma	184	21–63	Introduce a modified version of the modified Tofts model with additional leakage space and local AIF for glioma grading
Shin et al. (2014)	Human	Glioma	31	54.5±11.9	Compare the utility of DSC-MRI and DCE-MRI in distinguishing treatment related changes from recurrent disease in glioma patients
Shinohara et al. (2011)	Human	MS	10	43.4±13.2	Quantify typical spatiotemporal enhancement patterns in acute MS lesions by functional principal components analysis

Continued on next page

Table A.1 — *Continued from previous page*

Publication	Sample type	Pathology	Sample size	Age (years)	Main purpose
Singh et al. (2007)	Human	Low grade glioma	5	30.4±9.4	
		High grade glioma	5	55.8±6.4	Quantify physiological and haemodynamic parameters using a new method with leakage correction
		Tuberculoma	5	23.2±12.6	
		Healthy controls	5	33.4±7.4	
Skinner et al. (2012)	Rat	Glioma	8	n/a	Compare DCE-MRI and SPECT in glioma patients
Song et al. (2011)	Human	Multiple system atrophy	16	59.0±10.3	Evaluate BBB integrity and its functional significance using the CSF:plasma albumin ratio and DCE-MRI
		Healthy controls	13	60.5±10.3	
Sourbron et al. (2009)	Human	Tumour	15	–	Develop and evaluate a new methodology to measure perfusion and permeability parameters from DCE-MRI
Starr et al. (2003)	Human	Type 2 diabetes	10	68.2 (65–70)	Identify increased BBB permeability in type II diabetes patients in comparison with healthy controls
		Healthy controls	10	67.8	
Starr et al. (2009)	Human	Alheimer's disease	15	73.7	Measure BBB permeability in Alzheimer's patients compared to healthy old subjects
		Healthy controls	15	72.7	
Su et al. (1998)	Dog	Normal ageing	15	n/a	Investigate age related neuroanatomical and cerebrovascular changes using different MRI techniques
Taheri et al. (2009)	Rat	Focal ischaemia	16	n/a	Investigate correlations between the alteration of ADC and BBB permeability in ischaemic stroke
Taheri et al. (2011a)	Human	Ischaemic vascular disease	36	65.6±2.4	
		Stroke	8	55.9±5.8	Estimate BBB permeability in both healthy subjects and patients with white matter pathology
		White matter hyperintensity	9	60.0±6.6	
		Healthy controls	17	44.0±4.0	
Taheri et al. (2011b)	Human	MS	10	64.0±15.0	Quantify BBB permeability in patients with vascular cognitive impairment compared to healthy controls
		Vascular cognitive impairment	45		
		Healthy controls	20	51.0±19.0	
Thompson et al. (2012)	Human	Tumour	7	9.3±3.7	Characterise the vascular and permeability properties of paediatric brain tumours using two contrast agents for DSC- and DCE-MRI in a single imaging session
Thornhill et al. (2010)	Human	Acute ischaemic stroke	18	68.0±17.5	Compare different permeability measures using DSC- and DCE-MRI
Topakian et al. (2010)	Human	Small vessel disease	24	67.1±8.9	Investigate BBB permeability in white matter of patients with small vessel disease compared to controls
		Healthy controls	15	65.5±6.7	

Continued on next page

Table A.1 — *Continued from previous page*

Publication	Sample type	Pathology	Sample size	Age (years)	Main purpose
Vidarsson et al. (2009)	Human	Acute ischaemic stroke	8	37–93	Examine the effects of decreasing DCE-MRI scan time on the precision of permeability estimates
Wahlund and Bronge (2000)	Human	Cognitive impairment	10	72.5±4.1	Investigate whether DCE-MRI shows enhanced BBB permeability in WMH of demented patients
Wang et al. (2006)	Human	Mild cognitive impairment	11	74.0±7.0	Measure BBB disruption in patients with mild cognitive impairment in comparison with controls
		Healthy controls	11	74.0±3.0	
Wardlaw et al. (2008)	Human	Lacunar stroke	29	67.0	Assess background BBB leakage in patients with lacunar ischaemic stroke compared with cortical stroke controls
		Mild cortical stroke	19	66.0	
Wardlaw et al. (2009)	Human	Lacunar stroke	51	64.0±12.0	Test for subtle generalised BBB leakiness in patients with lacunar stroke compared with cortical stroke controls
		Mild cortical stroke	46	69.0±10.0	
Wei et al. (2011)	Rabbit	Traumatic injury	30	n/a	Evaluate DCE-MRI in the assessment of the extent of traumatic head injuries
Wilkinson et al. (2006)	Human	Mass lesion	17	70.0 (29–94)	Assess the microhaemodynamic consequences of high-dose dexamethasone treatment in patients with space-occupying intracranial lesions
Zhang et al. (2012)	Human	Glioma	28	47.0±14.2	Investigate the suitability of DCE-MRI for the grading of glial brain tumours
Zhu et al. (2000)	Human	Acoustic schwannoma	5	55.5±13.1	Quantify permeability and perfusion in brain tumours using combined DCE- and DSC-MRI to differentiate tumour types
		Meningeoma	5		
		Astrocytoma	5		

Additional abbreviations used in this table: ADC (apparent diffusion coefficient), ASL (arterial spin labelling), MGMT (methylguanine methyltransferase), MMP (matrix metalloproteinase), rtPA (recombinant tissue plasminogen activator), SPECT (single-photon emission computed tomography), VEGF (vascular endothelial growth factor)

Table A.2.: List of reported DCE-MRI scanning methods. The table contains the MRI sequence acronyms as used in the publication. Please note that manufactures use different acronyms for the same sequence, e.g. spoiled GRE = SPGR = RF-FAST = FLASH = T1-FFE and fast spoiled GRE = FSPGR = TurboFLASH. '–' indicates that the information was not provided in the article.

Publication	Scanner type	Sequence	TR / TE (ms)	FoV (mm) / matrix size	Slice thickness (mm)	Number of slices	Contrast agent	Dose	Imaging duration (min)	Temporal resolution
Abe et al. (2015)	3 T, GE	FSPGR	4.4 / 1.0	300x210 / 128x90	8.0	16	Gd-DTPA	0.100 mmol/kg	3.31	3.3 s
Abo-Ramadan et al. (2009)	4.7 T, Bruker	IR-FLASH	2.2 / 1.4	40x40 / 128x128	2.0	1	Gd-DTPA	0.500 mmol/kg	20.00–30.00	∼60.0 s
Ahn et al. (2014)	3 T, Philips	–	6.3 / 3.1	240x240 / 192x192	3.0	–	Gd-BT-DO3A	0.100 mmol/kg	6.30	5.8 s
Aksoy et al. (2013)	1.5 T, GE	SPGR	7.8 / 3.4	220x220 / 192x256	5.0	12	Gd-DTPA	0.100 mmol/kg	9.00	14.0 s
Ali et al. (2010)	3 T, GE	SPGR	11.3 / 1.8	40x40 / 128x128	1.0	15	Albumin-Gd-DTPA	0.300 mmol/kg	20.00	∼23.5 s
Almeida-Freitas et al. (2014)	1.5 T, GE	SPGR	5.9/1.9	256x256 / 192x192	7.0	–	Gd-DTPA	0.050 mmol/kg	6.50	5.6 s
Armitage et al. (2011)	1.5 T, GE	FSPGR	8.1 / 2.2	240x240 / 256x256	4.0	–	Gd-DTPA-BMA	20.000 mmol	32.20	69.0 s
Artzi et al. (2015)	3 T, GE	SPGR	5.7 / 1.2	250x250 / 256x256	5.0	–	Gd-DOTA	0.100 mmoll/kg	6.00	6.0 s
Aryal et al. (2014)	7 T, Varian	dual-echo SPGR	60.0 / [2.0/4.0]	– / 128x64	2.0	3	Gd-DTPA	0.250 mmol/kg	10.00	4.0 s
Awasthi et al. (2012)	1.5 T, GE	SPGR	5.0 / 1.4	360x270 / 128x128	6.0	12	Gd-DTPA-BMA	0.020 mmol/kg	2.80	5.3 s
Bagher-Ebadian et al. (2012)	3 T, GE	SPGR	0.8 / 5.8	240x240 / 256x128	5.0	16	Gd-DTPA	0.100 mmol/kg	6.80	5.8 s
Bergamino et al. (2013)	1.5 T, Siemens	Turbo FLASH	6.7 / 1.0	250x300 / 320x384	5.0	20	Gd-BT-DO3A	0.100 mmol/kg	–	–
Bergamino et al. (2014)	1.5, Siemens	Turbo FLASH	6.7 / 1.0	250x300 / 320x384	5.0	20	Gd-BT-DO3A	0.100 mmol/kg	3.90	7.8 s
Brandt et al. (2008)	4.7 T, Varian	FLASH	11.0 / 4.0	40x40 / 128x128	1.0	12	Gd-DTPA	0.500 mmol/kg	–	–
Budde et al. (2012)	7 T, Bruker	GRE	600.0 / 10.0	30x30 / 128x128	0.5	15	Gd-DTPA	0.300 mmol/kg	12.00	12.0 s
Cao et al. (2009)	1.5 T, GE	GRE	1.1 / 3.4	220x220 / 256x256	6.0	22	Gd-DTPA	0.050 mmol/kg	4.56	7.2 s

Continued on next page

Table A.2 — *Continued from previous page*

Publication	Scanner type	Sequence	TR / TE (ms)	FoV (mm) / matrix size	Slice thickness (mm)	Number of slices	Contrast agent	Dose	Imaging duration (min)	Temporal resolution
Cha et al. (2006)	1.5 T, GE	SPGR	6.5 / 1.2	260x260 / 128x128	3.0	-	Gd-DTPA-BMA	0.100 mmol/kg	6.58	32.9 s
Choi et al. (2013)	3 T, Philips	–	–	240x240 / 192x192	3.0	–	Gd-BT-DO3A	0.100 mmol/kg	∼7.00	∼7.0 s
Chu et al. (2012)	3 T, Philips	T1-FFE	13.0 / 1.4	230x193 / 164x137	6.0	–	Gd-DOTA	0.100 mmol/kg	–	–
Chwang et al. (2014)	3 T, GE	SPGR	5.7 / 1.4	60x60 / 128x128	1.5	13–15	Gadofosveset	0.030 mmol/kg	15.00	11.6 s
							Gd-DTPA	0.100 mmol/kg		
Cramer et al. (2014)	3 T, Philips	SPGR	3.9 / 1.9	230x182 / 96x61	8.0	5	Gd-BT-DO3A	0.045 mmol/kg	15.70	1.3 s
Cramer and Larsson (2014)	3 T, Philips	SPGR	3.9 / 1.9	230x182 / 96x61	8.0	5	Gd-BT-DO3A	0.045 mmol/kg	15.70	1.3 s
Durukan et al. (2009)	4.7 T, Bruker	IR-FLASH	2.2 / 1.4	40x40 / 128x128	2.0	1	Gd-DTPA	0.500 mmol/kg	20.00–25.00	∼60.0 s
Engelhorn et al. (2013)	4.7 T, Bruker	FLASH	11.3 / 4.1	100x100 / 128x128	1.0	–	Gd-BT-DO3A	0.200 mmol/kg	–	–
Ewing et al. (2003)	7 T, SMIS	TOMROP	50.0 / 4.0	32x32 / 64x64	2.0	5	Gd-DTPA	0.100 mmol/kg	39.00–51.00	3.00 min
Farjam et al. (2014)	3 T, Philips	–	5.1 / 1.0	240x240 / 128x128	2.0	80	Gd-DTPA	0.100 mmol/kg	2.00	4.0 s
Ferl et al. (2010)	1.5 T, Siemens	FLASH	–	– / 256x256	5.0	16	Gd-DTPA	0.100 mmol/kg	5.00	4.8 s
Ferrier et al. (2007)	3 T, Philips	T1-FFE	8.1 / 2.3	77x77 /256x244	1.0	16	Gd-DTPA	0.250 mmol/kg	10.00	20.0 s
Gaitán et al. (2011)	1.5 and 3 T, GE	FSPGR	5.6 / 1.8	– / –	2.0	–	Gd-DTPA	0.100 mmol/kg	4.60	34.5 s
Gupta et al. (2012)	3 T, GE	SPGR	5.0 / 2.1	240x240 / 128x128	6.0	12	Gd-DTPA-BMA	0.200 mmol/kg	3.01	5.7 s
Hanyu et al. (2002)	1.5 T, Siemens	FSE	300.0 / 24.0	250x250 / 256x256	8.0	3	Gd-DTPA	0.100 mmol/kg	30.00	5.00 min
Haris et al. (2008a)	1.5 T, GE	SPGR	5.0 / 1.4	360x270 / 128x128	6.0	12	Gd-DTPA-BMA	0.200 mmol/kg	2.80	5.3 s
Haris et al. (2008b)	1.5 T, GE	SPGR	5.0 / 1.4	360x270 / 128x128	6.0	12	Gd-DTPA-BMA	0.200 mmol/kg	2.80	5.3 s

Continued on next page

Table A.2 — *Continued from previous page*

Publication	Scanner type	Sequence	TR / TE (ms)	FoV (mm) / matrix size	Slice thickness (mm)	Number of slices	Contrast agent	Dose	Imaging duration (min)	Temporal resolution
Haris et al. (2008c)	1.5 T, GE	SPGR	5.0 / 1.4	360x270 / 128x128	6.0	12	Gd-DTPA-BMA	0.200 mmol/kg	2.80	5.3 s
Harrer et al. (2004)	1.5 T, Philips	SPGR	4.2 / 1.2	250x250 / 128x128	6.0	25	Gd-DTPA	0.100 mmol/kg	6.00	6.0 s
Hoff et al. (2012)	9.4 T, Varian	GRE	85.0 / 3.2	30x30 / 128x64	1.0	13	Gd-DTPA	0.150 mmol/kg	15.00	10.9 s
Hormuth et al. (2014)	9.4T, Agilent	SPGR	10.0 / 2.1	– / 96x96	–	2	Gd-DTPA	0.050 mmol/kg	20.00	2.0 s
Ingrisch et al. (2012)	3 T, Siemens	SPGR	2.3 / 0.9	218x177 / 128x104	3.0	44	Gd-BT-DO3A	0.100 mmol/kg	7.00	2.1 s
Jelescu et al. (2011)	3 T, Siemens	FLASH	5.6 / 2.6	256x192 / 128x96	3.0	20	Gd-DTPA	0.100 mmol/kg	2.22	5.0 s (first 13 aquisitions)
							Gd-BT-DO3A			32.0 s (last 36 acquisitions)
Jia et al. (2013)	3 T, Siemens	TWIST	4.9 / 1.9	240x240 / 138x192	3.6	–	Gd-DTPA-BMA	0.100 mmol/kg	∼5.00	4.3 s
Kassner et al. (2005)	1.5 T, GE	GRE	5.9 / 1.5	240x240 / 128x128	7.0	8	Gd-DTPA-BMA	7.500 mmol	4.80	∼5.0 s
Kassner et al. (2009)	1.5 T, GE	GRE	5.9 / 1.5	240x240 / 128x128	5.0	12–14	Gd-DTPA-BMA	7.500 mmol	4.65	9.0 s
Kermode et al. (1990)	0.5 T, Picker	SE	500.0 / 40.0	– / –	–	8	Gd-DTPA	0.100–0.200 mmol/kg	151.00	∼4.00 min
		IR	1020.0 / 40.0							
Kleppestøet al. (2014)	3 T, Philips	SR dual-echo GRE	8.2 / [2.5/5.6]	228x228 / 120x120	4.0	–	Gd-BT-DO3A	0.100 mmol/kg	5.67	3.4 s
Krueck et al. (1994)	1.5 T, GE	SE	233.0 / 21.0	80x80 / 256x128	3.0	–	Gd-DTPA	0.030 mmol/kg	20.00	2.00–3.00 min
Larsen et al. (2013)	3 T, Philips	SPGR	3.9 / 1.9	230x182 / 96x61	8.0	5	Gd-DTPA	0.050 mmol/kg	3.75	1.3 s
Larsson et al. (2013)	3 T, Philips	SR GRE	8.2 /2.5	240x240 / 120x120	4.0	11	Gd-BT-DO3A	0.100 mmol/kg	5.50	3.4 s

Continued on next page

Table A.2 — *Continued from previous page*

Publication	Scanner type	Sequence	TR / TE (ms)	FoV (mm) / matrix size	Slice thickness (mm)	Number of slices	Contrast agent	Dose	Imaging duration (min)	Temporal resolution
Larsson et al. (2014)	3 T, Philips	SR GRE	8.2 /2.5	240x240 / 120x120	4.0	11	Gd-BT-DO3A	0.100 mmol/kg	5.50	3.4 s
Larsson et al. (1990)	1.5 T, Siemens	SE	500.0 / [30.0/60.0/ 90.0/120.0]	154x589 / 128x256	4.0	1	Gd-DTPA	0.100 mmol/kg	60.00	68.0 s initially, gradually increasing to ∼5.00 min
Larsson et al. (2009)	3 T, Philips	SR GRE	3.8 / 1.9	240x182 /96x61	8.0	4	Gd-DTPA	0.050 mmol/kg	3.00	1.0 s
Lee et al. (2014)	3 T, GE	Refocused GRE	34.0 / 2.8	182x182 / 192x192	3.0	5	–	–	5.93/5.07	8.7 s
Leppert et al. (2014)	3 T, Siemens	FLASH	5.6 / 2.6	192x256 / 96x128	6.0	20	Gd-BT-DO3A	0.100 mmol/kg	1.13	5.0 s
				192x256 / 192x256	6.0	40			19.35	32 s
Li et al. (2000)	1.5 T, Philips	SPGR	4.3 / 1.1	230x230 / 128x128	6.0	25	Gd-DTPA	0.100 mmol/kg	11.05–11.90	5.1 s
Li et al. (2012a)	–	Fast GRE	-	240x240 / 240x240	Prebolus: 6.42	22	Gd-DOTA	Prebolus: 0.017 mmol/kg	10.70	Prebolus: 1.0 s
					Bolus: 2.0	70		Bolus: 0.100 mmol/kg		Bolus: 10.7 s
Li et al. (2014)	7 T, Bruker	FLASH	64.0 / 2.0	22x22 / 128x128	1.0	5	Gd-DTPA-BMA	0.100 mmol/kg	12.00	8.0 s
Li et al. (2010)	11.75 T, Bruker	Fast GRE	25.0 / 1.4	55x22 / 128x64	1.0	3	Gd-DTPA-BMA	0.050 mmol/kg	–	1.6 s
Lüdemann et al. (2000)	1.5 T, Siemens	Rapid TurboFLASH	11.0 / 4.2	230x230 / 64x128	5.0	1	Gd-DTPA	0.100 mmol/kg	12.20	61.0 s
Lüdemann et al. (2002)	1.5 T, Siemens	Rapid TurboFLASH	11.0 / 4.2	230x230 / 64x128	5.0	1	Gd-DTPA	0.100 mmol/kg	12.20	61.0 s
Lüdemann et al. (2009)	1.5 T, Siemens	Rapid TurboFLASH	11.0 / 4.2	230x230 / 64x128	5.0	1	Gd-DTPA	0.100 mmol/kg	12.20	61.0 s

Continued on next page

Table A.2 — *Continued from previous page*

Publication	Scanner type	Sequence	TR / TE (ms)	FoV (mm) / matrix size	Slice thickness (mm)	Number of slices	Contrast agent	Dose	Imaging duration (min)	Temporal resolution
Manuchehri et al. (2007)	1.5 T, GE	FSPGR	9.1 / 2.1	180x180 / 256x256	4.5	1	Gd-DTPA	0.100 mmol/kg	3.00 or 4.00	2.4 s
Mills et al. (2009)	3 T, Philips	T1-FFE	3.5 / 1.1	– / 128x128	4.2	–	Gd-DTPA-BMA	0.100 mmol/kg	5.67	3.4 s
Miyati et al. (1997)	1.5 T, Philips	Dual-echo T1-FFE	60.0 / [5.8/21.7]	270x160 / 256x152	5.0	–	Gd-DTPA	0.100 mmol/kg	2.10	2.0 s
Montagne et al. (2015)	3 T, GE	SPGR	– / –	– / –	5.0	–	Gd-BOPTA	0.050 mmol/kg	16	15.4
Nagaraja et al. (2010)	7 T, Bruker	TOMROP	2000.0 / 2.2	32x32 / 128x64	2.0	5	Gd-DTPA	0.080 mmol/kg	25.00	2.50 min
Nagaraja et al. (2013)	7 T, Varian	Dual-echo GRE	60.0/[2.0/4.0]	32X32 / 128X64	2.0	3	Gd-DTPA	0.250 mmol/kg	10.00	4.0 s
Noseworthy and Bray (2000)	2 T, Sisco	SE	500.0 / 25.0	70x60 / 128x256	3.1	1	Gd-DTPA	0.100 mmol/kg	36.00	4.00 min
Provenzale et al. (2006)	1.5 T, GE	FSPGR	11.9 / 5.3	24x24 / 256x128	7.5	10	Gd-DTPA	0.100 mmol/kg	–	–
Quarles et al. (2012)	4.7 T, Varian	GRE	15.6 / 1.9	40x40 / 64x64	2.0	1	Gd-DTPA	0.200 mmol/kg	16.00	1.0 s
Roberts et al. (2000)	1.5 T, –	SPGR	8.3 / 1.5	24x24 / 256x128	3.0	28	Gd-DTPA	0.100 mmol/kg	3.03	26.0 s
Roy et al. (2013)	3 T, GE	SPGR	5.0/2.1	240x240 / 128x128	6.0	12	Gd-DTPA-BMA	–	3.00	5.7s
Sahoo et al. (2013)	1.5 T, GE	FSPGR	5.0/1.4	360x270 / 256x256	6.0	12	Gd-DTPA-BMA	0.200 mmol/kg	2.80	5.3s
	3 T, GE		5/2.1	240x240 / 128x128					3.00	5.6 s
Shin et al. (2014)	3 T, Siemens	VIBE	4.3 / 1.5	250x250 / 192x138	4.0	20	Gd-BT-DO3A	0.100 mmol/kg	1.80	5.5 s
Shinohara et al. (2011)	3 T, GE	FSPGR	5.6 / 1.8	– / –	8.0	–	Gd-DTPA	0.100 mmol/kg	58.00-155.00	35.0 s
Singh et al. (2007)	1.5 T, GE	SPGR	5.0 / 1.4	360x270 / 128x128	6.0	12	Gd-DTPA	0.2 mmol/kg	2.80	5.3 s
Skinner et al. (2012)	9.4T, Agilent	SPGR	10.0 / 2.1	– / 96x96	–	2	Gd-DTPA	0.050 mmol/kg	20.00	2.0 s
Song et al. (2011)	3 T, Philips	–	6.4 / 3.1	– / –	3.0	–	Gd-BT-DO3A	0.100 mmol/kg	∼6.00	∼7.7 s
Sourbron et al. (2009)	3 T, Siemens	Turbo-FLASH	223.0 / 1.3	240x240 / 128x128	3.5	6	Gd-DTPA	2x0.050 mmol/kg	∼7.00	1.3 s

Continued on next page

Table A.2 — *Continued from previous page*

Publication	Scanner type	Sequence	TR / TE (ms)	FoV (mm) / matrix size	Slice thickness (mm)	Number of slices	Contrast agent	Dose	Imaging duration (min)	Temporal resolution
Starr et al. (2003)	1.9 T, –	–	29.0 / 9.0	240x240 / 240x240	3.0	–	Gd-DTPA	0.200 mmol/kg	90.00	5.00–30.00 min
Starr et al. (2009)	1.5 T, GE	FSPGR	29.0 / 3.0	– / 256x256	3.0	36	Gd-DTPA	10.000 mmol	34.35	3.82 min
Su et al. (1998)	1.5 T, GE	SE	117.0 / 14.0	120x90 / 256x128	6.0	4	Gd-DTPA	0.150 mmol/kg	12.00	15.0 s
Taheri et al. (2009)	4.7 T, Bruker	IR SE EPI	8.0 / 19.4	40x40 / 64x64	2.0	2	Gd-DTPA	0.100 mmol/kg	∼46.67	∼3.33 min
Taheri et al. (2011a)	1.5 T, Siemens	TAPIR	15.0 / [2.8/5.1/7.4]	220x220 / 128x128	5.0	6	Gd-DTPA	0.025 mmol/kg	28.00	3.50 min
Taheri et al. (2011b)	1.5 T, Siemens	TAPIR	15.0 / [2.8/5.1/7.4]	220x220 / 128x128	5.0	6	Gd-DTPA	0.025 mmol/kg	28.00	3.50 min
Thompson et al. (2012)	3 T Siemens / Philips	Fast GRE	1500.0 / 20.0	240x240 / 256x256	–	16/32	Gadoteridol	0.100 mmol/kg	–	–
Thornhill et al. (2010)	1.5 T, GE	GRE	5.9 / 1.5	240x240 / 128x128	5.0	12–14	Gd-DTPA-BMA	7.500 mmol	4.65	9.0 s
Topakian et al. (2010)	1.5 T, GE	FSPGR	7.3 / 3.4	240x240 / 256x256	4.0	36	Gd-DTPA	20.000 mmol	∼3.00	∼6.7 s
Vidarsson et al. (2009)	1.5 T, GE	SPGR	5.9 / 1.5	240x240 / 256x192	7.0	–	Gd-DTPA-BMA	7.500 mmol	4.65	9.0 s
Wahlund and Bronge (2000)	1.5 T, Siemens	SE	600.0 / 14.0	173x230 / 192x256	5.0	19	Gd-DTPA-BMA	0.200 mmol/kg	25.00	5.00–10.00 min
		GE	10.0 / 4.0	191x255 / 192x256	2.8	64			20.00	10.00 min
Wang et al. (2006)	1.5 T, Philips	RF-FAST	10.0 / 3.0	220x220 / 256x256	8.0	20	Gd-DTPA-BMA	0.110 mmol/kg	6.80	25.5 s
Wardlaw et al. (2008)	1.5 T, GE	SPGR	29.0 / 3.0	240x240 / 256x256	3.0	–	Gd-DTPA-BMA	20.000 mmol	∼30.00	3.77 min
		FSPGR	8.1 / 3.0		4.0				1.2 s	
Wardlaw et al. (2009)	1.5 T, GE	FSPGR	8.1 / 3.0	240x240 / 256x256	4.0	–	Gd-DTPA-BMA	20.000 mmol	29.90	1.2 s
Wei et al. (2011)	–, Philips	THRIVE	6.8 / 3.2	100x100 / –	–	–	Gd-DTPA	0.100 mmol/kg	7.50	15.0 s
Wilkinson et al. (2006)	1.5 T, Philips	FSPGR	37.0 / 4.0	230x230 / 128x256	5.0	3	Gd-BT-DO3A	10.000 mmol	2.70	3.6 s

Continued on next page

Table A.2 — *Continued from previous page*

Publication	Scanner type	Sequence	TR / TE (ms)	FoV (mm) / matrix size	Slice thickness (mm)	Number of slices	Contrast agent	Dose	Imaging duration (min)	Temporal resolution
Zhang et al. (2012)	1.5 T, Siemens	Turbo FLASH	199.0 / 1.1	211x260 / 256x256	5.0	10	Gd-DTPA	0.100 mmol/kg	6.00	4.0 s
Zhu et al. (2000)	1.5 T, Philips	T1-FFE	4.3–7.0 / 1.1–1.6	– / 128x128	–	25	Gd-DTPA	0.100 mmol/kg	11.00–12.00	5.1–8.8 s

Additional abbreviations used in this table: GE (General Electric), SPGR (spoiled gradient echo), FSPGR (fast spoiled gradient echo), FLASH (fast low angle shot), FFE (fast field echo), TOMROP (T1 by multiple read out pulses), FSE (fast spin echo), VIBE (volumetric interpolated breath-hold examination), TAPIR (T1 mapping with partial inversion recovery), THRIVE (T1 high resolution isotropic volume examination)

Table A.3.: Complete list of K^{Trans} values reported for different tissue types and tracer kinetic models. Given values are the cohort averages as reported in the included articles (where results were reported for several groups, the range of group averages is given). For normal-appearing tissues, information about the patient's pathology is given in brackets. Where necessary, units were converted assuming unity tissue density and values were transferred from whole blood to blood plasma notation assuming a haematocrit of 0.45. Please note that some subjects included in these studies (e.g. high grade glioma patients) underwent treatment before entering the study. Hence, the reported baseline parameters might be influenced by interventions that were not the focus in the study.

Tissue type	Publication	K^{Trans} ($\cdot 10^{-2}$ min^{-1})	Model
Normal-appearing tissues			
WM	Cramer and Larsson (2014)	0.043 (healthy controls)	Modified Tofts
	Song et al. (2011)	5.000 (healthy controls) to 16.000 (multiple system atrophy)	
	Cramer et al. (2014)	0.040 (healthy controls) to 0.090 (MS)	Patlak
	Cramer and Larsson (2014)	0.048 (healthy controls)	
	Larsen et al. (2013)	0.165 (tumour)	
	Larsson et al. (2009)	0.440 (tumour)	
	Montagne et al. (2015)	0.175 (young healthy controls) to 0.253 (MS)	
	Taheri et al. (2011a)	0.180 (healthy controls) to 0.200 (ischaemic stroke)	
	Taheri et al. (2011b)	0.180 (healthy controls) to 0.240 (MS)	
	Cramer and Larsson (2014)	0.051 (healthy controls)	Other
	Sourbron et al. (2009)	−0.030 (tumour)	
GM	Cramer and Larsson (2014)	0.053 (healthy controls)	Modified Tofts
	Cramer et al. (2014)	0.030 (healthy controls) to 0.080 (MS)	Patlak
	Cramer and Larsson (2014)	0.155 (healthy controls)	
	Larsson et al. (2009)	0.495 (tumour)	
	Montagne et al. (2015)	0.070 (young healthy controls) to 0.185 (mild cognitive impairment)	
	Cramer and Larsson (2014)	0.063 (healthy controls)	Other
	Sourbron et al. (2009)	−0.009 (tumour)	

Continued on next page

Table A.3 — *Continued from previous page*

Tissue type	Publication	K^{Trans} ($\cdot 10^{-2}$ min^{-1})	Model
Mixed tissue types	Noseworthy and Bray (2000)	0.000 (normoxic controls) to 4.300 (hyperoxic, zinc-deficient)	Conventional Tofts
	Ali et al. (2010)	3.000 (tumour)	Modified Tofts
	Cao et al. (2009)	3.100 (tumour)	
	Wei et al. (2011)	0.400 (traumatic injury)	
	Zhang et al. (2012)	0.300 (grade I glioma) to 0.500 (grade IV glioma patients)	
	Aksoy et al. (2013)	0.000 (haemorrhagic stroke)	Patlak
	Engelhorn et al. (2013)	2.000 (tumour)	
	Ewing et al. (2003)	6.200 (ischaemic stroke)	
	Kassner et al. (2005)	−0.243 (ischaemic stroke not proceeding to haemorrhage) to 0.010 (proceeding to haemorrhage)	
	Kassner et al. (2009)	0.320 (ischaemic stroke)	
	Taheri et al. (2009)	0.000 (ischaemic stroke)	
	Thornhill et al. (2010)	−0.390 (ischaemic stroke)	
Stroke lesions			
Ischaemic strokes	Abo-Ramadan et al. (2009)	0.350	Patlak
	Durukan et al. (2009)	0.400	
	Ewing et al. (2003)	0.410	
	Kassner et al. (2005)	−0.123 (not proceeding to haemorrhage) to 3.100 (proceeding to haemorrhage)	
	Kassner et al. (2009)	0.780	
	Nagaraja et al. (2010)	0.240 (striatum) to 0.370 (parietal-insular cortex)	
	Thornhill et al. (2010)	0.840	
	Taheri et al. (2009)	0.100 (subcortical) to 0.150 (cortical)	
Hemmorrhagic strokes	Aksoy et al. (2013)	5.500	Patlak
MS lesions	Jelescu et al. (2011)	9.240	Conventional Tofts
	Larsson et al. (1990)	3.534	Other
Tuberculomas	Haris et al. (2008b)	204.000	Conventional Tofts
	Singh et al. (2007)	281.000	

Continued on next page

Table A.3 — *Continued from previous page*

Tissue type	Publication	K^{Trans} ($\cdot 10^{-2}$ min^{-1})	Model
Traumatic injuries	Wei et al. (2011)	0.400 (mild) to 4.900 (severe)	Modified Tofts
Infective lesions	Haris et al. (2008c)	210.000	Conventional Tofts
Neurocysticercosis	(Gupta et al., 2012)	2.000 (asymptomatic) to 5.000 (symptomatic)	Conventional Tofts
Tumour tissues			
Gliomas	Ahn et al. (2014)	5.300 (unmethylated) to 9.100 (methylated)	Conventional Tofts
	Cha et al. (2006)	5.500	
	Ferl et al. (2010)	4.900 (3 days prior to treatment) to 5.300 (1 day prior to treatment)	
	Haris et al. (2008a)	75.000 (low grade) to 124.000 (high grade)	
	Haris et al. (2008c)	8.000 (grade I) to 111.000 (grade IV)	
	Harrer et al. (2004)	2.000 to 136.000 (range within population given only)	
	Jia et al. (2013)	2.800 (grade II) to 14.300 (grade IV)	
	Roberts et al. (2000)	−0.200 (grade I) to 7.080 (grade IV)	
	Roy et al. (2013)	4.000 (low grade) to 24.000 (high grade)	
	Singh et al. (2007)	40.000 (low grade) to 109.000 (high grade)	
	Zhu et al. (2000)	16.600	
	Abe et al. (2015)	0.340 (low grade) to 31.000 (high grade)	Modified Tofts
	Ali et al. (2010)	12.600 (periphery) to 13.800 (centre)	
	Aryal et al. (2014)	2.090 (aggressive)	
	Awasthi et al. (2012)	11.000	
	Bagher-Ebadian et al. (2012)	1.9 (aggressive)	
	Bergamino et al. (2013)	1.100 (grade II) to 5.100 (grade IV)	
	Bergamino et al. (2015)	3.300 (grade I-II) to 22.000 (grade IV)	
	Choi et al. (2013)	1.000 (low grade) to 5.000 (high grade)	
	Chwang et al. (2014)	2.500 (contrast: Gadofosveset) to 4.600 (contrast: Gadopentetate)	
	Ferrier et al. (2007)	6.300 (centre)	
	Harrer et al. (2004)	2.800 to 14.200 (range within population given only)	
	Larsson et al. (2013)	4.000 (high grade)	
	Sahoo et al. (2013)	0.100 (low grade) to 83.000 (high grade)	
	Zhang et al. (2012)	16.600	

Continued on next page

Table A.3 — *Continued from previous page*

Tissue type	Publication	K^{Trans} ($\cdot 10^{-2}$ min^{-1})	Model
	Bagher-Ebadian et al. (2012)	0.190 (less aggressive)	Patlak
	Bergamino et al. (2013)	1.000 (grade II) to 3.900 (grade IV)	
	Engelhorn et al. (2013)	4.200 (periphery) to 6.400 (centre)	
	Krueck et al. (1994)	0.976	
	Larsen et al. (2013)	0.660 (regressing) to 1.980 (progressing)	
	Larsson et al. (2009)	1.650	
	Harrer et al. (2004)	0.700 to 6.500 (range within population given only)	Other
	Larsson et al. (1990)	9.150	
	Li et al. (2010)	13.000	
	Quarles et al. (2012)	1.700 (gliosarcoma) to 6.200 (other glioma)	
	Sahoo et al. (2013)	9.000 (low grade) to 109.000 (high grade)	
Brain metastases	Almeida-Freitas et al. (2014)	13.000	Conventional Tofts
	Abe et al. (2015)	38.000	Modified Tofts
Brain lymphomas	Abe et al. (2015)	44.000	Modified Tofts
Meningeomas	Cha et al. (2006)	47.000	Conventional Tofts
	Zhu et al. (2000)	27.800	
Schwannomas	Zhu et al. (2000)	22.800	Conventional Tofts
	Li et al. (2012a)	8.300	Modified Tofts
Mixed tumour types	Thompson et al. (2012)	25.000	Conventional Tofts
	Chu et al. (2012)	34.000	Modified Tofts

B. Copies of publications

This section provides copies of the following publications that are related to the work presented in this thesis:

1. Heye, A. K., Culling, R. D., Valdés Hernández, M. D. C., Thrippleton, M. J. and Wardlaw, J. M. (2014). Assessment of blood-brain barrier disruption using dynamic contrast-enhanced MRI. A systematic review. *NeuroImage Clinical*, 6:262–274.

2. Heye, A. K., Thrippleton, M. J., Armitage, P. A., Valdés Hernández, M. D. C., Makin, S., Glatz, A., Sakka, E. and Wardlaw, J. M. (2016). Tracer kinetic modelling for DCE-MRI quantification of subtle blood-brain barrier permeability. *NeuroImage*, 125:446-455.

3. Heye, A. K.[†], Thrippleton, M. J.[†], Chappell, F., Valdés Hernández, M. D. C., Armitage, P. A., Makin, S., Muñoz Maniega, S., Sakka, E., Flatman, P. W., Dennis, M. S. and Wardlaw, J. M. (2016). Blood pressure and sodium: association with MRI markers in cerebral small vessel disease. *Journal of Cerebral Blood Flow and Metabolism*, 36(1):264-274.

[†] The first two authors contributed equally to this work

NeuroImage: Clinical 6 (2014) 262–274

Contents lists available at ScienceDirect

NeuroImage: Clinical

journal homepage: www.elsevier.com/locate/ynicl

Review Article

Assessment of blood–brain barrier disruption using dynamic contrast-enhanced MRI. A systematic review

Anna K. Heye[a], Ross D. Culling[b], Maria del C. Valdés Hernández[a], Michael J. Thrippleton[a], Joanna M. Wardlaw[a,*]

[a] Neuroimaging Sciences, University of Edinburgh, Edinburgh, UK
[b] College of Medicine and Veterinary Medicine, University of Edinburgh, Edinburgh, UK

ARTICLE INFO

Article history:
Received 18 July 2014
Received in revised form 4 September 2014
Accepted 5 September 2014
Available online 10 September 2014

Keywords:
Dynamic contrast-enhanced MRI
Permeability
Perfusion
Blood–brain barrier

ABSTRACT

There is increasing recognition of the importance of blood–brain barrier (BBB) disruption in aging, dementia, stroke and multiple sclerosis in addition to more commonly-studied pathologies such as tumors. Dynamic contrast-enhanced MRI (DCE-MRI) is a method for studying BBB disruption in vivo. We review pathologies studied, scanning protocols and data analysis procedures to determine the range of available methods and their suitability to different pathologies. We systematically review the existing literature up to February 2014, seeking studies that assessed BBB integrity using T1-weighted DCE-MRI techniques in animals and humans in normal or abnormal brain tissues. The literature search provided 70 studies that were eligible for inclusion, involving 417 animals and 1564 human subjects in total. The pathologies most studied are intracranial neoplasms and acute ischemic strokes. There are large variations in the type of DCE-MRI sequence, the imaging protocols and the contrast agents used. Moreover, studies use a variety of different methods for data analysis, mainly based on model-free measurements and on the Patlak and Tofts models. Consequently, estimated K^{Trans} values varied widely. In conclusion, DCE-MRI is shown to provide valuable information in a large variety of applications, ranging from common applications, such as grading of primary brain tumors, to more recent applications, such as assessment of subtle BBB dysfunction in Alzheimer's disease. Further research is required in order to establish consensus-based recommendations for data acquisition and analysis and, hence, improve inter-study comparability and promote wider use of DCE-MRI.

Contents

* Corresponding author at: Brain Research Imaging Centre, Neuroimaging Sciences, University of Edinburgh, Western General Hospital, Crewe Road, Edinburgh EH4 2XU, UK.
E-mail address: joanna.wardlaw@ed.ac.uk (J.M. Wardlaw).

http://dx.doi.org/10.1016/j.nicl.2014.09.002

1. Introduction

The blood–brain barrier (BBB) separates the parenchyma of the central nervous system from the blood. Quantitative information about the functional integrity of the BBB can be gained by performing dynamic contrast-enhanced MRI (DCE-MRI). DCE-MRI has proven valuable in the assessment of many brain pathologies that cause an opening of the BBB, such as tumors (Singh et al., 2007), multiple sclerosis (Jelescu et al., 2011) and acute ischemic strokes (Kassner et al., 2009). While these diseases show relatively large abnormalities in BBB functionality, there is also growing interest in the application of DCE-MRI to pathologies associated with more subtle and chronic BBB disruption, such as cerebral small vessel disease (Wardlaw et al., 2008; Wardlaw et al., 2009), diabetes (Starr et al., 2003) and Alzheimer's disease (Starr et al., 2009).

Although DCE-MRI has been widely used to study pathological changes in BBB functionality, studies differ in their MR imaging procedures and have been performed using a variety of different MRI sequences, contrast agents and time courses. Furthermore, there is no standard method for analyzing the data. Established analysis approaches include relatively simple non-model based methods (Topakian et al., 2010) as well as a range of pharmacokinetic models (Tofts, 1991). Several previous reviews have focused on specific applications such as oncology (Türkbey et al., 2010; Jain, 2013; Barnes et al., 2012) and on methodological aspects of DCE-MRI (Sourbron and Buckley, 2012, 2013); as far as we are aware, there are no reviews that cover the application of DCE-MRI in aging, microvascular disease or dementia. The aim of this work is to provide an overview of all applications and scanning protocols used in DCE-MRI of the brain by performing a systematic review of the literature. First, we describe the important components of the BBB and available permeability models, then review available data on BBB permeability imaging. Furthermore, we aim to identify the most commonly used methods for data analysis and provide an overview of the resulting parameter ranges.

2. Background

2.1. Blood–brain barrier functionality

The BBB is formed by endothelial cells that line brain capillaries and are sealed by tight junctions, which are unique to the brain microvasculature. The endothelium of the BBB interacts with several cellular and non-cellular elements, such as astrocytes, pericytes, microglial cells and basement membranes, that provide both functional support and structural support to the BBB (Abbott and Friedman, 2012; Obermeier et al., 2013). Together they form an interactive cellular complex, the 'neurovascular unit' (NVU). A schematic drawing of the NVU is shown in Fig. 1. The BBB regulates the passage of essential molecules such as glucose, while restricting the diffusion of potentially harmful substances.

Many brain pathologies are known to cause a disruption of the BBB. The mechanisms that cause BBB opening are many and differ between diseases. In meningitis, for example, damage to the BBB is initiated by extrinsic systemic factors, such as infections and autoimmune processes. Other diseases, including Alzheimer's disease and ischemic stroke, are thought to activate intrinsic cellular mechanisms secondary to the neuroinflammatory injury and other as yet unknown processes (Rosenberg, 2012). Several comprehensive reviews provide detailed information on the molecular biology of BBB disruption in disease (Abbott and Friedman, 2012; Obermeier et al., 2013; Rosenberg, 2012).

2.2. Measurement of blood–brain barrier disruption using DCE-MRI

Disruption of the BBB can enable the extravasation of low-molecular weight MRI contrast agents. This accumulation of contrast material in the extravascular extracellular space (EES) of affected tissues leads to increased longitudinal relaxation rate and, therefore, increased signal intensity in T1-weighted images. DCE-MRI exploits this T1 enhancement in order to detect and evaluate regions of BBB disruption. The DCE-MRI procedure typically consists of intravenous injection of contrast agent followed by the repeated acquisition of T1-weighted images (see Fig. 2), providing measurements of signal enhancement as a function of time. The enhancement kinetics can be used to extract quantitative or semi-quantitative information regarding BBB integrity.

MR signal changes caused by contrast agent extravasation are determined by several factors, including tissue perfusion and capillary permeability. In the brain, DCE-MRI is considered to be the standard MRI approach for assessing permeability, while dynamic susceptibility contrast MRI (DSC-MRI) is the method of choice for perfusion imaging (Sourbron and Buckley, 2013). However, it has been shown that DCE-MRI can combine perfusion and permeability measurements by using a sufficiently long acquisition time (to capture slow interstitial uptake) with high temporal resolution early on (to capture the first pass of the contrast bolus) (Li et al., 2000; Li et al., 2012; Sourbron et al., 2009; Larsson et al., 2009).

2.3. Analysis of DCE-MRI data

Different approaches have been used to analyze DCE-MRI data, ranging from relatively simple visual assessment of enhancement curves to more complex fitting to pharmacokinetic models. Heuristic analysis of the signal enhancement curves provides semi-quantitative measures

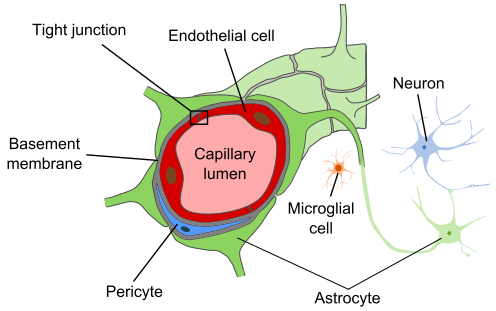

Fig. 1. Schematic drawing of the neurovascular unit. The BBB is formed by endothelial cells that line brain capillaries and are sealed by tight junctions. Astrocytes, pericytes, microglial cells and basement membranes interact with the endothelium of the BBB, providing functional and structural support.

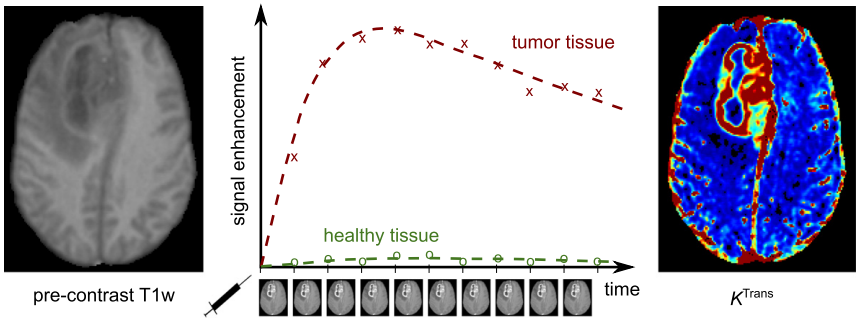

Fig. 2. Illustration of DCE-MRI in a patient with a glioma. The repeated acquisition of T1-weighted images after contrast agent injection allows the calculation of signal enhancement as a function of time (middle) when compared to the pre-contrast signal intensity (left). These curves can be used to calculate maps of quantitative pharmacokinetic parameters (e.g. K^{Trans}, right).

of BBB disruption, such as the area under the curve (AUC) and the time to maximum enhancement. Such measurements are easy to obtain but difficult to interpret (Budde et al., 2012). Quantitative analysis on the other hand aims to provide a link between the tissue signal enhancement and physiologically relevant parameters such as microvascular permeability, blood flow, blood volume fraction and interstitial volume fraction.

In order to relate the measured signal enhancement to the contrast agent concentration, an appropriate signal model is required. While early DCE-MRI studies assumed a linear relationship between signal enhancement and contrast uptake, it is well known that the signal enhancement is highly dependent on intrinsic tissue and acquisition parameters (Armitage et al., 2005; Armitage et al., 2011). Consequently, more complex approaches were developed in order to control for the effect of tissue characteristics such as the pre-contrast longitudinal relaxation time and the longitudinal and transverse relaxivities of the contrast agent (Armitage et al., 2005).

Pharmacokinetic modeling was first introduced for the analysis of DCE-MRI in the early 1990s by Brix et al. (1991), Larsson et al. (1990), and Tofts (1991), followed by a consensus paper on the notation (Tofts et al., 1999). Since then, improvement of the imaging techniques (e.g. higher temporal resolution and contrast-to-noise ratio) and a better understanding of the underlying physiology have promoted the development of several more complex pharmacokinetic models. Detailed reviews of tracer kinetic modelling approaches in DCE-MRI have been published by Sourbron and Buckley (2012, 2013). In the following, we will briefly describe a basic tissue model and the three most commonly used pharmacokinetic models in DCE-MRI.

Fig. 3A displays a general tissue model with exchange of contrast agent between blood plasma and the EES. Target parameters of pharmacokinetic modeling in DCE-MRI are the fractional plasma volume v_p, the fractional interstitial volume v_e, the plasma flow F_p and the permeability-surface area product PS, which measures the rate at which contrast agent particles leak out of the plasma and into the EES per unit tissue volume and plasma concentration. An important physiological parameter that is widely reported in DCE-MRI studies is the volume transfer constant K^{Trans}, which is the rate at which contrast agent is delivered to the EES per volume of tissue and contrast agent concentration in the arterial blood plasma. While the terms PS and K^{Trans} are sometimes used interchangeably in the literature, PS represents the clearance for contrast agent leaking from the capillary plasma into the EES, i.e. the flux of contrast agent across the BBB normalized to the tissue plasma concentration and tissue volume; in contrast, K^{Trans} (as implicitly defined by Tofts et al., 1999), is the contrast clearance normalized to the *arterial* plasma concentration and therefore depends on the plasma flow F_p supplying the capillaries in addition to PS (the mathematical form of this relationship is model-dependent). K^{Trans} is necessarily equal to the product of plasma flow F_p and the extraction fraction E (i.e. the fraction of contrast agent molecules that leak into the EES).

Most pharmacokinetic models require the arterial input function (AIF) to be known, which describes the tracer concentration in blood plasma over time. There are several strategies for determining the AIF (Calamante, 2013), including the use of a standard function (Weinmann et al., 1984), experimentally derived population-averaged AIFs (Parker et al., 2006) and simultaneous individual measurement of the AIF in a feeding vessel close to the tissue of interest (Sourbron et al., 2009).

The conventional Tofts model (Tofts, 1991) considers isodirectional flux of tracer between the two well-mixed blood plasma and EES compartments with the volume transfer constant K^{Trans}. The plasma compartment is assumed to have negligible volume ($v_p \approx 0$), which makes the classic Tofts model a one-compartment model for weakly vascularized tissues. This model is illustrated in Fig. 3B and characterized by the working Eq. (1):

$$C_t(t) = K^{Trans} \int_0^t C_p(\tau) \exp\left[-\frac{K^{Trans}(t-\tau)}{v_e}\right] d\tau, \quad (1)$$

where $C_p(t)$ is the AIF.

Tofts et al. extended their classic model by introducing the blood plasma as a second well-mixed and highly perfused compartment (Tofts et al., 1999; see Fig. 3C). In addition to the two parameters K^{Trans} and v_e, the model allows the fractional plasma volume v_p to be estimated and, hence, separates enhancement effects due to contrast leakage from those due to intravascular contrast:

$$C_t(t) = v_p C_p(t) + K^{Trans} \int_0^t C_p(\tau) \exp\left[-\frac{K^{Trans}(t-\tau)}{v_e}\right] d\tau. \quad (2)$$

If the model fits the data well with a non-negligible v_p value, then the tissue must be highly perfused ($F_p = \infty$) and the system is permeability-limited with $K^{Trans} = PS$ (Sourbron and Buckley, 2013).

Finally, the Patlak model also describes a highly perfused two-compartment tissue but considers unidirectional transport from the blood plasma into the EES (see Fig. 3D). The tracer concentration in tissue is given by

$$C_t(t) = v_p C_p(t) + K^{Trans} \int_0^t C_p(\tau) d\tau. \quad (3)$$

When first introducing this approach, Patlak and colleagues proposed a linear graphical analysis method, which is often used as it

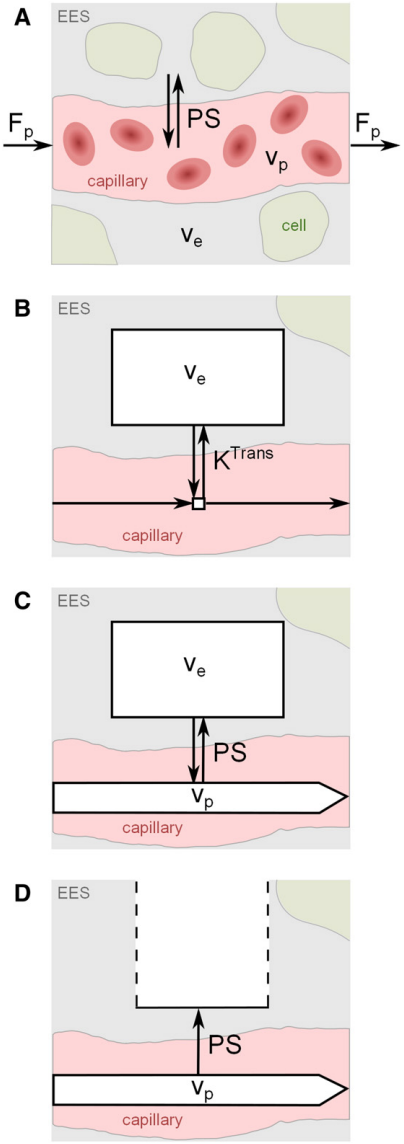

Fig. 3. Schematic illustrations of common pharmacokinetic models and target parameters. The exchange between the extravascular extracellular space (EES, volume fraction v_e) and capillary blood plasma (volume fraction v_p) is determined by the plasma flow F_p and the permeability-surface area product PS. (A) Generic tissue model. (B) Conventional Tofts model (with negligible blood volume and volume transfer constant K^{Trans}). (C) Modified Tofts model with non-negligible blood compartment. (D) Patlak model with non-negligible plasma compartment and one-way transport of contrast agent across the BBB. For the latter two models, it may be assumed that $K^{Trans} = PS$ for any solution fitting the data well with a non-negligible v_p.

permits simple and fast fitting. In this analysis, the ratio $C_t(t)/C_p(t)$ is regressed against $\int_0^t C_p(\tau)d\tau/C_p(t)$, yielding a straight line with slope K^{Trans} and y-intercept v_p.

3. Methods

3.1. Search strategy

The existing literature was systematically reviewed up to February 2014 by performing an electronic search in PubMed, EMBASE, MEDLINE and Web of Knowledge databases. Multiple combinations of the following search terms were used: 'permeability', 'brain', 'blood–brain barrier', 'MRI', 'dynamic', 'DCE-MRI' and 'contrast enhancement'. English as well as non-English literature was sought. The electronic search was supplemented by hand searching the reference lists of review papers.

One reviewer performed the primary literature search, removed duplicates and screened all papers' titles and abstracts in order to identify those relevant for full assessment. Before final inclusion or exclusion of studies, a second reviewer continued the search, read the full text of the selected articles, extracted the relevant data and performed the analysis. Disagreements between reviewers about inclusion or exclusion of papers were resolved through discussion with a third reviewer. The third, fourth and fifth reviewers complemented the search and assisted with the data analysis.

3.2. Eligibility criteria

We sought studies which assessed BBB integrity using dynamic contrast-enhanced MRI techniques. We included studies on humans and animals in all diseases known or thought to affect BBB function. Consequently, we excluded other applications of DCE-MRI such as breast or prostate cancer as well as publications that focus on theoretical aspects of image processing or modeling without testing them in a clinical setting (e.g. Gal et al., 2008). Furthermore, we accepted only primary research articles which were available as full-text, but checked review articles for additional primary references.

We excluded studies using non-dynamic MRI methods, DSC-MRI or non-MRI methods in order to decrease variability between studies, which is already considerable between DCE-MRI studies. The literature search yielded several papers that focused on therapeutic BBB disruption for novel anti-cancer drugs. Since these mainly addressed pharmaceutical or technical aspects of the disruption method on a molecular level, these studies were rejected. An excellent review on DCE-MRI in clinical trials of antivascular therapies can be found in O'Connor et al. (2012). However, we did include studies that focused on the clinical effect of treatment strategies and its link with BBB disruption if they provided baseline DCE-MRI parameters. Moreover, we rejected single case reports and articles in which substantial information about the MRI procedure or the data analysis was lacking.

3.3. Data extraction and analysis

One reviewer independently extracted the data from each included study and cross-checked information with preliminary extracted data. Disagreements were resolved by consensus. We noted the studied disease or pathology, sample size and subjects' ages (in the case of human studies). Moreover, we extracted details of the DCE-MRI protocol, noting scanner field strength, MRI sequence with repetition time (TR) and echo delay time (TE), field of view, matrix size, slice thickness, overall duration and temporal resolution. Extracted data also included the type and dose of contrast agent and the injection protocol. Furthermore, we noted whether post-processing techniques were applied prior to data analysis, the analysis method used and the tissues/locations analyzed. Where

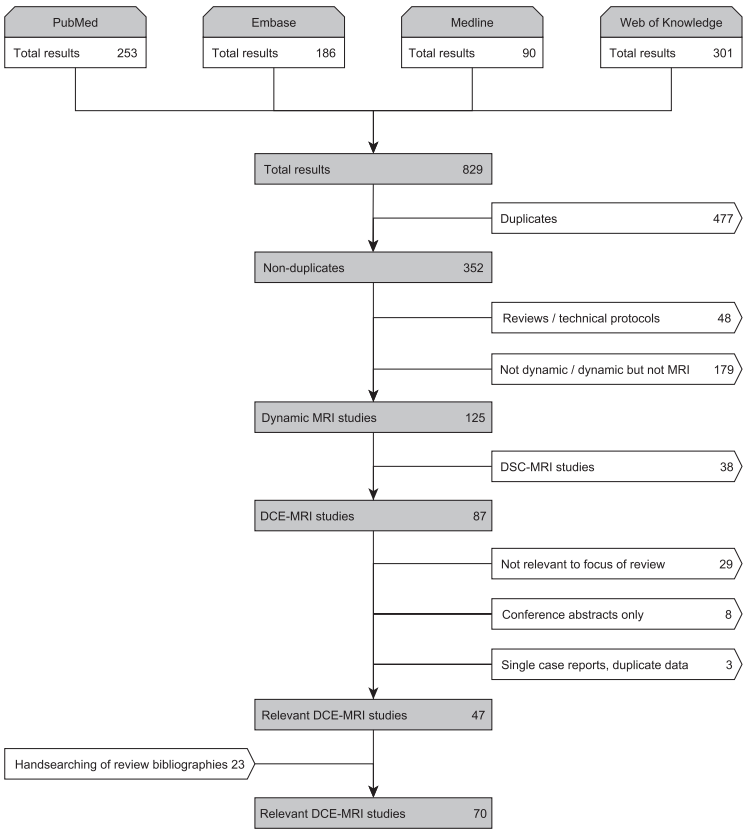

Fig. 4. Flow diagram summarizing the literature search and inclusion process.

given, quantitative measurements were extracted. We noted the main study purpose and the overall conclusion of the study.

In consequence of the large heterogeneity of included studies, quality assessment using standardized criteria as recommended in Guyatt et al. (2008) was difficult. However, we extracted limitations of the methodology where stated and whether any patients had been imaged but then excluded from further analysis, so as to assess the feasibility and applicability of the technique.

4. Results

4.1. Systematic literature search results

The electronic search yielded 829 results, 31 of which were in non-English languages. After removing duplicates, 352 publications were further analyzed for inclusion (see Fig. 4). After scanning abstracts and titles, we excluded studies using non-dynamic and non-MRI methods ($n = 179$). We also excluded review papers ($n = 46$), technical protocols ($n = 2$) and DSC-MRI studies ($n = 38$), leaving 87 articles for full-text assessment. At this stage, we identified 29 studies that were not relevant to the focus of this review. Moreover, we excluded conference abstracts that were not detailed enough for full data extraction and that had not subsequently been published in full ($n = 8$), single-case reports and publications with missing information on the imaging methodology ($n = 2$) and duplicate publications ($n = 1$). In addition to the resulting 47 relevant DCE-MRI studies, 23 relevant articles were identified by hand searching the bibliographies of review papers. Overall, the full literature search to February 2014 provided 70 DCE-MRI studies that were eligible for inclusion in this review, published between February 1990 (Kermode et al., 1990) and December 2013 (Cramer et al., 2014).

4.2. Subjects and sample sizes

Table 1 summarizes the main study sample characteristics and scanning protocols related to each pathology. Of the 70 included studies, 17 used animals (i.e. rodents (Budde et al., 2012; Abo-Ramadan et al., 2009; Ali et al., 2010; Durukan et al., 2009; Ewing et al., 2003; Ferrier et al., 2007; Nagaraja et al., 2010; Taheri et al., 2009; Hoff et al., 2012; Krueck et al., 1994; Li et al., 2010; Noseworthy and Bray, 2000; Quarles et al., 2012; Aryal et al., 2014; Brandt et al., 2008), apart from one study of beagle dogs (Su et al., 1998) and one of rabbits (Wei et al., 2011)). The sample size was not made available in one of these publications (Ewing et al., 2003). The mean sample size of the remaining animal studies was 25 animals, with a total number of 417 animals (including 19 healthy controls; 336/417 were rodents). The largest included study involved 113 rats (Abo-Ramadan et al., 2009), whereas

Table 1
Study sample characteristics and scanning protocols related to pathology. 'Mean age' displays the average of study mean ages for studies investigating the same pathology.

Pathology	Sample				Scanning protocol		References
	Subjects	Number of studies	Number of subjects	Mean age (years)	Median imaging duration (min)	Median temporal resolution (sec)	
Intracranial neoplasms	Humans	30	716	48.4	5.5	5.3	Singh et al. (2007); Li et al. (2000); Li et al. (2012); Sourbron et al. (2009); Larsson et al. (2009); Larsson et al. (1990); Haris et al. (2008a,c); Thompson et al. (2012); Miyati et al. (1997); Awasthi et al. (2012); Roberts et al. (2000); Bagher-Ebadian et al. (2012); Manuchehri et al. (2007); Cao et al. (2009); Cha et al. (2006); Chu et al. (2012); Harrer et al. (2004); Ludeman et al. (2002); Lüdemann et al. (2009); Lüdeman et al. (2000); Mills et al. (2009); Provenzale et al. (2006); Zhu et al. (2000); Ferl et al. (2010); Jia et al. (2013); Larsen et al. (2013); Wilkinson et al. (2006); Zhang et al. (2012); Larsson et al. (2013)
	Animals	8	140	–	15.0	11.5	Budde et al. (2012); Ali et al. (2010); Ferrier et al. (2007); Hoff et al. (2012); Krueck et al. (1994); Li et al. (2010); Quarles et al. (2012); Aryal et al. (2014)
Stroke / cerebrovascular disease	Humans	11	482	65.9	9.0	14.0	Kassner et al. (2009); Wardlaw et al. (2008); Wardlaw et al. (2009); Topakian et al. (2010); Armitage et al. (2011); Aksoy et al. (2013); Vidarsson et al. (2009); Kassner et al. (2005); Thornhill et al. (2010); Taheri et al. (2011a,b)
	Animals	5	154	–	25.0	150.0	Abo-Ramadan et al. (2009); Durukan et al. (2009); Ewing et al. (2003); Nagaraja et al. (2010); Taheri et al. (2009)
Multiple sclerosis	Humans	8	186	41.3	21.8	34.8	Jelescu et al. (2011); Larsson et al. (1990); Kermode et al. (1990); Cramer et al. (2014); Taheri et al. (2011b); Gaitán and Shea (2011); Shinohara et al. (2011); Ingrisch et al. (2012)
Pneumococcal meningitis	Animals	1	42	–	n/a	n/a	Brandt et al. (2008)
Zinc deficiency	Animals	1	36	–	36.0	240.0	Noseworthy and Bray (2000)
Neurocysticercosis	Humans	1	35	n/a	3.0	5.7	Gupta et al. (2012)
Traumatic head injuries	Animals	1	30	–	7.5	15.0	Wei et al. (2011)
Alzheimer's disease	Humans	1	30	73.7	34.4	229.0	Starr et al. (2009)
Multiple system atrophy	Humans	1	29	59.0	6.0	7.7	Song et al. (2011)
Infective brain lesions	Humans	1	26	26.6	2.8	5.3	Haris et al. (2008a)
Mild cognitive impairment	Humans	1	22	47.0	6.8	25.5	Wang et al. (2006)
Diabetes	Humans	1	20	68.2	90.0	900.0	Starr et al. (2003)
Brain tuberculomas	Humans	2	18	23.2	2.8	5.3	Singh et al. (2007); Haris et al. (2008b)
Normal aging	Animals	1	15	–	12.0	15.0	Su et al. (1998)

two studies used a sample size smaller than ten (Ferrier et al., 2007; Li et al., 2010).

The remaining 53 studies were in humans, including 1564 subjects in total (163 of which were healthy controls). The mean sample size for human studies was 27. Only one study involved more than 100 subjects (Haris et al., 2008a) and six studies were based on fewer than ten humans (Jelescu et al., 2011; Larsson et al., 1990; Kermode et al., 1990; Thompson et al., 2012).

Information regarding patient age was not provided in seven of the 53 studies (Li et al., 2000; Li et al., 2012; Sourbron et al., 2009; Larsson et al., 1990; Aksoy et al., 2013; Miyati et al., 1997; Awasthi et al., 2012). A further seven publications stated only the age range of the study subjects (Awasthi et al., 2012; Haris et al., 2008b; Roberts et al., 2000; Vidarsson et al., 2009; Bagher-Ebadian et al., 2012; Kassner et al., 2005; Manuchehri et al., 2007). Mean age as stated in the remaining 39 human studies was highly dependent on the studied pathology, ranging between 9 years (Thompson et al., 2012) (pediatric brain tumors) and 74 years (Wang et al., 2006) (mild cognitive impairment).

4.3. Pathologies studied

The majority of animal studies concerned intracranial neoplasms (Budde et al., 2012; Ali et al., 2010; Ferrier et al., 2007; Hoff et al., 2012; Krueck et al., 1994; Li et al., 2010; Quarles et al., 2012; Aryal et al., 2014) including a total of 140/417 animals. Five publications investigated changes in the BBB caused by induced focal cerebral ischemia in 154/417 animals overall (Abo-Ramadan et al., 2009; Durukan et al., 2009; Ewing et al., 2003; Nagaraja et al., 2010; Taheri et al., 2009). Moreover, one study each focused on the influence of pneumococcal meningitis (Brandt et al., 2008), normal aging (Su et al., 1998), zinc deficiency (Noseworthy and Bray, 2000) or traumatic head injuries (Wei et al., 2011) on the BBB.

The pathology most studied in humans was intracranial neoplasms (30 publications, 716/1564 subjects), including primary brain tumors and brain metastases (Li et al., 2012; Sourbron et al., 2009; Larsson et al., 2009; Larsson et al., 1990; Haris et al., 2008a,c; Thompson et al., 2012; Miyati et al., 1997; Awasthi et al., 2012; Roberts et al., 2000; Bagher-Ebadian et al., 2012; Manuchehri et al., 2007; Cao et al., 2009; Cha et al., 2006; Chu et al., 2012; Harrer et al., 2004; Ludemann et al., 2002; Lüdemann et al., 2009; Lüdemann et al., 2000; Mills et al., 2009; Provenzale et al., 2006; Zhu et al., 2000; Ferl et al., 2010; Jia et al., 2013; Larsen et al., 2013; Wilkinson et al., 2006; Zhang et al., 2012). Eleven studies investigated changes in BBB integrity caused by stroke and/or cerebrovascular disease (Kassner et al., 2009; Wardlaw et al., 2008; Wardlaw et al., 2009; Topakian et al., 2010; Armitage et al., 2011; Aksoy et al., 2013; Vidarsson et al., 2009; Kassner et al., 2005; Thornhill et al., 2010; Taheri et al., 2011a,b) with a total of 482/1564 subjects. Eight studies focused on multiple sclerosis (Jelescu et al., 2011; Larsson et al., 1990; Kermode et al., 1990; Cramer et al., 2014; Taheri et al., 2011b; Gaitán and Shea, 2011; Shinohara et al., 2011; Ingrisch et al., 2012) including a total of 186/1564 subjects. Other pathologies included Alzheimer's disease (Starr et al., 2009), mild cognitive impairment (Wang et al., 2006), brain tuberculomas (Singh et al., 2007; Haris et al., 2008b), infective brain lesions (Haris et al., 2008a), multiple system atrophy (Song et al., 2011), diabetes (Starr et al., 2003) and neurocysticercosis (Gupta et al., 2012).

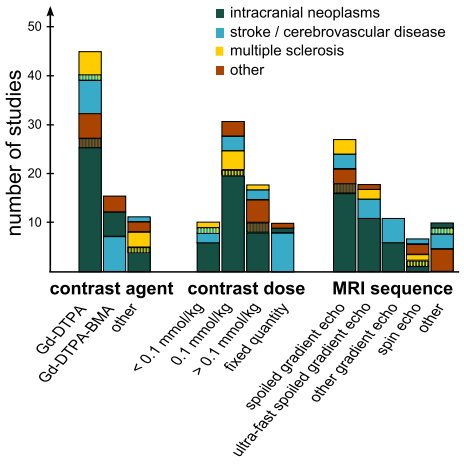

Fig. 5. Summary of contrast agents, contrast agent doses and MRI sequences. The bar height indicates the number of studies using a particular method, subdivided by pathology.

4.4. Blood–brain barrier changes in disease

Thirteen of the 70 included studies aimed to investigate the correlation between a particular disease and BBB dysfunction. For this purpose, BBB disruption was quantified in order to test for a significant difference between diseased subjects and healthy controls. Significant differences compared to control subjects or healthy tissue were found in eight studies, investigating acute ischemic stroke (Abo-Ramadan et al., 2009), pneumococcal meningitis (Brandt et al., 2008), brain metastases (Budde et al., 2012), multiple system atrophy (Song et al., 2011), type-II diabetes (Starr et al., 2003), vascular cognitive impairment (Taheri et al., 2011a), normal-appearing and lesion tissue in multiple sclerosis patients (Cramer et al., 2014; Taheri et al., 2011b), mild cognitive impairment (Taheri et al., 2011b), zinc deficiency (Noseworthy and Bray, 2000) and small vessel disease (Topakian et al., 2010). Moreover, Starr et al. observed differences in signal intensity profiles over time between Alzheimer's disease patients and controls (Starr et al., 2009). Increased BBB disruption without statistical significance was observed in patients with mild cognitive impairment (Wang et al., 2006). Su et al. showed a non-significant increase in BBB permeability with normal aging in beagle dogs (Su et al., 1998).

16 studies performed DCE-MRI in order to distinguish between different types or grades of pathology. Seven of those studies showed statistical significance that DCE-MRI derived parameters differentiate primary brain tumor types and grades (Roberts et al., 2000; Ludemann et al., 2002; Lüdemann et al., 2000; Mills et al., 2009; Zhu et al., 2000; Jia et al., 2013; Zhang et al., 2012). Furthermore, significant differences were found between infective vs. neoplastic brain lesions (Haris et al., 2008a), asymptomatic vs. symptomatic neurocysticercosis (Gupta et al., 2012), severe and moderate vs. mild traumatic brain injuries (Wei et al., 2011), and radiation necrosis vs. tumor recurrence (Larsen et al., 2013). Wardlaw et al. showed that post-contrast signal enhancement was higher in cerebrospinal fluid and white matter in lacunar (i.e. small vessel disease stroke) than in cortical (i.e. large artery atherothromboembolic stroke) patients (Wardlaw et al., 2008; Wardlaw et al., 2009). Kassner et al. found significantly different permeability scores between stroke patients who proceeded to hemorrhage and those who did not with and without thrombolytic therapy (Kassner et al., 2009; Kassner et al., 2005). Furthermore, Aksoy et al. (2013) reported significantly different DCE-MRI parameters for hemorrhagic strokes depending on their size and location.

4.5. Contrast agent and dose

The type and dose of contrast agents used in the included publications are summarized in Fig. 5. In most studies, the contrast agent used was Gd-DTPA (gadopentetate dimeglumine, 45/70 studies) or its variant Gd-DTPA-BMA (gadodiamide, 15/70 studies), given as an intravenous bolus injection. In 31 studies, this contrast agent was given in the standard dose of 0.1 mmol/kg body weight. However, delivered

doses ranged from 0.02 mmol/kg (Awasthi et al., 2012) to 0.5 mmol/kg (Ferrier et al., 2007). Ten studies delivered a fixed quantity of contrast agent, ranging between 7.5 mmol (Kassner et al., 2009; Vidarsson et al., 2009; Thornhill et al., 2010) and 20 mmol (Wardlaw et al., 2008; Wardlaw et al., 2009; Armitage et al., 2011) in humans. Single studies employed different gadolinium-based agents such as Gd-DOTA (gadoterate meglumine) (Li et al., 2000; Chu et al., 2012), gadobutrol (Gd-BT-DO3A) (Jelescu et al., 2011; Cramer et al., 2014; Wilkinson et al., 2006; Ingrisch et al., 2012; Song et al., 2011; Larsson et al., 2013), gadoteriol (Thompson et al., 2012) and albumin-labeled Gd-DTPA (Ali et al., 2010). We did not find any study that investigated the influence of different contrast agent types or concentrations, though Abo-Ramadan et al. state that different doses lead to an increase or decrease in signal-to-noise ratio (Abo-Ramadan et al., 2009).

4.6. Scanning techniques and field strength

The MRI pulse sequence types used are summarized in Fig. 5. The technique most frequently used was a spoiled gradient echo sequence (27 studies) and its ultra-fast variants (18 studies). Further protocols include 11 other gradient recalled echo sequences (Kassner et al., 2009; Larsson et al., 2009; Budde et al., 2012; Abo-Ramadan et al., 2009; Durukan et al., 2009; Hoff et al., 2012; Quarles et al., 2012; Kassner et al., 2005; Cao et al., 2009; Thornhill et al., 2010; Larsson et al., 2013), six spin-echo methods (Larsson et al., 1990; Kermode et al., 1990; Taheri et al., 2009; Krueck et al., 1994; Noseworthy and Bray, 2000; Su et al., 1998) and two unspecified T1-weighted imaging sequences (Starr et al., 2003; Song et al., 2011). Furthermore, two studies used a TOMROP (T-One by Multiple Read-Out Pulses) pulse sequence (Ewing et al., 2003; Nagaraja et al., 2010), two studies used T1 mapping of partial inversion recovery (TAPIR) (Taheri et al., 2011a,b), and one study each used a THRIVE (Wei et al., 2011), RF-FAST (Wang et al., 2006) and TWIST (Jia et al., 2013) sequence.

Four publications focused on introducing new scanning methods. A scanning procedure for combined and consecutive DSC- and DCE-MRI measurement was introduced by Miyati et al. (1997) and Thompson et al. (2012) respectively. Moreover, Jelescu et al. (2011) and Li et al. (2012) presented a dual-temporal resolution scanning method with high temporal resolution during the bolus first pass and high spatial resolution during the later phase.

The majority of human studies (35/53) were performed with a magnetic field strength of 1.5 T, while 16 studies used a 3 T scanner; one study each was performed using a 0.5 T (Kermode et al., 1990) and a 1.9 T scanner (Starr et al., 2003). A wider range of magnetic field strengths from 1.5 T (Krueck et al., 1994) to 11.75 T (Li et al., 2010) were found in animal studies, with the majority of studies using 4.7 or 7 T scanners. Two studies did not provide this information (Li et al., 2012; Wei et al., 2011).

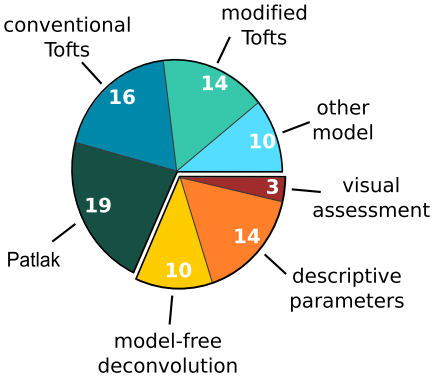

Fig. 6. Data analysis methods used in the included studies. Numbers indicate the count of studies using the particular method. (Note that some studies used more than one approach. Consequently, the numbers of studies do not add up to the 70 included studies.).

4.7. Duration and temporal resolution of DCE-MRI

The duration of data collection following contrast injection varied widely with values from 2.1 min (Miyati et al., 1997) to 155 min (Shinohara et al., 2011). The median DCE-MRI imaging durations (not stated in five publications (Larsson et al., 1990; Li et al., 2010; Brandt et al., 2008; Chu et al., 2012; Provenzale et al., 2006)) according to pathology studied are shown in Table 1, together with the median temporal resolution (not stated in three publications (Brandt et al., 2008; Chu et al., 2012; Provenzale et al., 2006)). The highest temporal resolution of 1 s was found in tumor studies (Larsson et al., 2009; Quarles et al., 2012), whereas one study on diabetes used the longest intervals, in the range of 10–30 min (Starr et al., 2003).

Vidarsson et al. (2009) and Larsson et al. (2013) investigated the influence of the temporal resolution and/or overall scan time on the quantification of BBB disruption, finding that reducing the overall scanning time and sampling with a lower temporal resolution result in increased uncertainty of the pharmacokinetic parameters K^{Trans}, v_e and v_p. As shown in Table 1, the overall scanning duration and the temporal resolution vary significantly between applications. In general, the highest temporal resolution is used in brain tumors. This is necessary to measure the fast kinetics typically seen in malignant neoplasms, but may limit spatial resolution and coverage. Conversely, studies that assess tissues with slow leakage rates (e.g. healthy appearing tissue in MS patients, aging or dementia) often use lower temporal resolutions that allow for better spatial resolution and coverage.

4.8. Use of post-processing techniques

42 of the 70 included studies (60%) did not report the use or method of image post-processing. The most commonly used technique reported was image registration, aligning the DCE-MRI images to a pre-contrast acquisition and/or anatomic images, in order to remove patient movement (Jelescu et al., 2011; Kassner et al., 2009; Wardlaw et al., 2008; Wardlaw et al., 2009; Starr et al., 2003; Starr et al., 2009; Topakian et al., 2010; Budde et al., 2012; Armitage et al., 2011; Taheri et al., 2009; Haris et al., 2008a,b,c; Aksoy et al., 2013; Lüdemann et al., 2009; Zhu et al., 2000; Ferl et al., 2010; Zhang et al., 2012; Thornhill et al., 2010; Taheri et al., 2011a; Gaitán and Shea, 2011; Shinohara et al., 2011; Larsson et al., 2013). Several studies reported a lack of precision of quantitative values due to limited spatial resolution or poor signal-to-noise ratio (Kassner et al., 2009; Ferrier et al., 2007; Cha et al., 2006; Gaitán and Shea, 2011), but only four studies report the use of image processing techniques for noise reduction, including Gaussian smoothing (Lüdemann et al., 2009), Kalman filtering (Taheri et al., 2011a,b) and unspecified smoothing of the signal enhancement curves (Ferl et al., 2010). In addition, three studies corrected DCE-MRI data for scanner signal intensity drift using phantoms. Only one study investigated the effect of scanner noise and drift on signal enhancement data (Armitage et al., 2011), concluding that studies should investigate and if necessary correct for these influences in order to prevent systematic errors.

4.9. Data analysis methods and pharmacokinetic models

A wide variety of approaches to data analysis were used in the included studies (Fig. 6). Model-free methods included the visual assessment of spatiotemporal enhancement patterns in multiple sclerosis lesions (Kermode et al., 1990; Gaitán and Shea, 2011; Shinohara et al., 2011), calculation of semi-quantitative parameters from the signal

Table 2
K^{Trans} values reported for different tissue types and pharmacokinetic models. Given values are the median [range] of reported study sample means from human (in black) and animal (in orange) studies. Please note that some subjects included in these studies (e.g. high grade glioma patients) underwent treatment before entering the study. Hence, the reported baseline parameters might be influenced by interventions that were not the focus in the study.

Pathology	K^{Trans} ($\cdot 10^{-2}$ min^{-1})			
	Conventional Tofts	Modified Tofts	Patlak	Other
Normal appearing tissue				
Mixed gray and white matter	–	0.40/1.70 [0.30 - 0.50]/[0.40 - 3.00]	0.39/0.03 [0.00 - 0.06]	0.01 [0.00 - 0.32]
White matter	–	1.60	0.20 [0.04 - 0.84]	0.04
Gray matter	–	–	0.08 [0.05 - 0.89]	–
Tumor tissue				
Mixed	6.00 [-0.37 - 25.00]	34.00	–	–
Glioma	16.60 [2.00 - 124.00]	7.95/12.60 [1.90 - 21.40]/[2.09 - 13.80]	3.10/0.97 [1.20 - 3.60]	0.70/6.25 [1.70 - 13.00]
Meningeoma	37.40 [27.80 - 47.00]	–	–	–
Astrocytoma	14.30 [2.80 - 111.00]	–	–	–
Stroke lesion				
Ischemic	–	–	0.84/0.35 [0.15 - 0.41]	1.94 [0.78 - 3.10]
Hemorrhagic	–	–	–	5.50
Multiple sclerosis lesion	2.23 [0.92 - 3.53]	–	–	0.98
Neurocysticercosis	3.50 [2.00 - 5.00]	–	–	–
Tuberculoma	242.50 [204.00 - 281.00]	–	–	–
Infective lesion	210.00	–	–	–
Traumatic injury	–	3.80 [0.19 - 4.90]	–	–

enhancement (Wardlaw et al., 2008; Wardlaw et al., 2009; Starr et al., 2003; Starr et al., 2009; Topakian et al., 2010; Brandt et al., 2008; Su et al., 1998; Miyati et al., 1997; Wang et al., 2006; Mills et al., 2009; Provenzale et al., 2006; Wilkinson et al., 2006) and/or contrast agent concentration (Budde et al., 2012; Armitage et al., 2011) curves, and model-free deconvolution (Singh et al., 2007; Larsson et al., 2009; Cramer et al., 2014; Haris et al., 2008a,c; Awasthi et al., 2012; Ferl et al., 2010; Larsen et al., 2013; Gupta et al., 2012). The most commonly used pharmacokinetic models were the conventional Tofts model (Singh et al., 2007; Jelescu et al., 2011; Li et al., 2000; Noseworthy and Bray, 2000; Haris et al., 2008a,b,c; Thompson et al., 2012; Manuchehri et al., 2007; Cha et al., 2006; Harrer et al., 2004; Zhu et al., 2000; Ferl et al., 2010; Jia et al., 2013; Gupta et al., 2012), the modified Tofts model (Li et al., 2012; Ali et al., 2010; Hoff et al., 2012; Aryal et al., 2014; Wei et al., 2011; Awasthi et al., 2012; Bagher-Ebadian et al., 2012; Cao et al., 2009; Chu et al., 2012; Harrer et al., 2004; Zhang et al., 2012; Ingrisch et al., 2012; Song et al., 2011; Larsson et al., 2013), the Patlak model (Larsson et al., 2009; Cramer et al., 2014; Abo-Ramadan et al., 2009; Durukan et al., 2009; Ewing et al., 2003; Nagaraja et al., 2010; Taheri et al., 2009; Krueck et al., 1994; Vidarsson et al., 2009; Bagher-Ebadian et al., 2012; Larsen et al., 2013; Thornhill et al., 2010; Taheri et al., 2011a,b) and a simplified approach based on the Patlak model (Kassner et al., 2009; Ferrier et al., 2007; Aksoy et al., 2013; Roberts et al., 2000; Kassner et al., 2005) as introduced by Shames et al. (1993) and Iannotti et al. (1987). Other modeling approaches included a variant of the conventional Tofts model that considers only the first pass of the contrast bolus (Li et al., 2000; Harrer et al., 2004), a two-compartment exchange (Sourbron et al., 2009; Larsson et al., 2009) and uptake (Sourbron et al., 2009; Ingrisch et al., 2012) model, and a modified two-compartment exchange model that includes two EES compartments (one in slow and one in fast exchange with the blood compartment) (Ludemann et al., 2002; Lüdemann et al., 2009; Lüdemann et al., 2000). Furthermore, one study each applied an AIF-free reference region model introduced by Yankeelov et al. (2005) in rat gliomas (Quarles et al., 2012) and a shutter-speed model considering three-site equilibrium water exchange (Li et al., 2010). Table 2 summarizes the range of K^{Trans} estimates for different tissue types and pharmacokinetic models as reported in the included publications.

Several studies aimed primarily at comparing different approaches for data analysis. Li et al. (2000) introduced a variant of the conventional Tofts model that only considers the first pass of the contrast bolus. They evaluated this method in $n = 11$ patients with primary brain neoplasms, finding that the results were visually comparable with those of the conventional Tofts model but less noisy and less susceptible to large vessel contributions. Harrer et al. (2004) evaluated the same model in $n = 18$ patients with high-grade gliomas, reporting a good correlation with the modified Tofts model but no correlation with the conventional Tofts method, though it should be noted that the AIFs used differed between the models due to software limitations. Values obtained with the conventional Tofts model were considerably higher, indicating an overestimation of quantitative parameters due to vessel contributions. Larsson et al. (2009) used simulated data in order to investigate the accuracy of the two-compartment exchange and Patlak models. As expected, they found that the Patlak method is accurate for

low values of K^{Trans}, whereas the two-compartment exchange model provides more accurate results for high K^{Trans} values (Larsson et al., 2009). Li et al. (2010) considered the effect of water exchange, finding the Patlak model to significantly underestimate the fractional blood volume when compared to their three-site equilibrium shutter-speed model. A non-parametric method for evaluating DCE-MRI in $n = 16$ glioma patients was presented by Ferl et al. (2010), who showed that their resulting parameters closely approximate the conventional Tofts model parameters. Finally, Bagher-Ebadian et al. (2012) presented a method for quantifying BBB disruption in heterogeneous glioblastoma based on a voxel-by-voxel selection from a set of nested models: the most complex model with three parameters was required to fit the data in regions of aggressive tumor growth, while simpler models predominated in less aggressive tumor portions and in healthy tissues.

5. Discussion

Our systematic review of the literature revealed 70 studies involving methods to assess BBB disruption in 15 pathologies in 417 animals and 1564 humans. These studies showed considerable heterogeneity with regard to image acquisition and analysis methods. This is partly a consequence of the wide range of tissues, pathologies and study objectives. For example, tumor studies used higher temporal resolution and shorter imaging duration on average compared with studies of less permeable tissue such as multiple sclerosis, ischemic stroke and normal appearing brain. However, it should be noted that a minority of the articles explicitly justified the methodology used. The factors influencing inter-study comparability and implications for futures studies are discussed in the following paragraphs.

5.1. Inter-study comparability of quantitative DCE-MRI parameters

Due to the wide range of analysis techniques used and their strong dependence on underlying assumptions and acquisition parameters, a lack of inter-study comparability represents a major problem. Care must be taken when comparing results from different studies as shown by the wide parameter ranges in Table 2. Some of this variability is inevitable due to the heterogeneity of the study populations (e.g. subjects' age) and study designs. Since most articles did not explicitly justify the analytical method employed, differences in the choice of pharmacokinetic model may account for some of the variation. Biased parameter estimates are likely to be obtained when the assumptions of the model are not met in the tissue or when the data acquired are inadequate to determine a unique solution. For example, several studies (e.g. Ali et al., 2010, Zhang et al., 2012) apply the same model to tumor tissue and contralateral healthy tissue, although the underlying tissue physiology is very different and one model is unlikely to be valid in both situations. The importance of appropriate model selection has been demonstrated both theoretically (Sourbron and Buckley, 2011) and experimentally in gliomas (Harrer et al., 2004) and low-permeability brain tissue (Larsson et al., 2009; Cramer and Larsson, 2014) and is discussed further in Section 5.2. Several additional factors may also influence the results of DCE-MRI studies.

Firstly, the calculation of contrast agent concentration from signal enhancement requires reliable estimation of intrinsic tissue parameters such as the pre-contrast longitudinal relaxation time $T1_0$. There are several methods of estimating $T1_0$, with variable flip angle (Brookes et al., 1999) and variable saturation time delay (Larsson et al., 1988) being the most common. The effect of uncertainty in $T1_0$ estimation on the calculation of contrast agent concentrations has been investigated by Schabel and Parker (Schabel and Parker, 2008). They demonstrate that $T1_0$ produces a significant concentration bias, which shows the importance of accounting for $T1_0$ when assessing BBB disruption in different tissue types (Armitage et al., 2011). It should also be noted that, unless T1 is measured at each time point, drifts in signal intensity may introduce further errors in pharmacokinetic parameters; as noted above, the issue of scanner stability was seldom addressed in the included articles.

Secondly, most pharmacokinetic models require the AIF to be known. Hence, determination of AIF represents a key issue in the reliable estimation of pharmacokinetic parameters. As mentioned above, there are several strategies for AIF selection and the optimal method varies according to pathology, study aims and clinical requirements (Calamante, 2013). In most applications, direct measurement of the AIF is generally considered preferable to standard or averaged AIFs (Lavini and Verhoeff, 2010). However, this method is not always possible and is susceptible to partial volume and in-flow artefacts; uncertainty remains regarding which vessel should be sampled and how, with approaches ranging from manual region of interest selection to methods for automatic vessel detection (Chen et al., 2008). There is also disagreement on whether to describe the capillary bed in terms of blood concentration or plasma concentration by correcting for the hematocrit (Hct). In the latter case, Hct should ideally be determined for every subject, but a standard value such as $Hct = 0.45$ is often assumed (Sourbron and Buckley, 2013). In theory, all model equations and resulting parameter values can easily be converted between conventions. However, several studies did not report this and other details, impeding reliable comparison of parameter values from different studies.

Other sources of uncertainty rarely considered in DCE-MRI studies may arise due to a lack of available data. For example, relaxivity values specific to a contrast agent, field strength and tissue/pathology are rarely known, with the consequence that uniform relaxivity across tissues and compartments is generally assumed. A further common assumption is that of fast water exchange between compartments; the influence of restricted water exchange has been described in the literature (see 100 and references therein) but models accounting for this effect have received relatively little attention.

5.2. Implications for future DCE-MRI studies of BBB disruption

Given the diversity of DCE-MRI applications in the brain, it is impossible to prescribe a universal "recipe" for future studies, though attempts have been made to better standardize methodology and reporting (Tofts et al., 1999; DCE MRI Technical Committee, 2012; Leach et al., 2012). Instead, it is essential to recognise that the optimal method is highly dependent on the specific application. An extensive body of primary DCE-MRI literature and a number of excellent review articles should help to facilitate optimal study design in the future. In the following paragraphs we discuss some of the key aspects of acquisition protocol design and data analysis. In addition to these technical aspects, it should be noted that the overall design of a study (e.g. large sample size, appropriate control group) will be particularly important given the limitations of present DCE-MRI methods. We recommend that for most applications, changes in the longitudinal relaxation rate rather than signal intensity should be measured, since the former more accurately reflects contrast agent concentration, required for quantitative pharmacokinetic analysis. A range of pulse sequences are available to obtain this data, and the optimal choice may be a compromise between speed, accuracy, spatial coverage and other factors. Two of the most critical acquisition parameters to determine are the temporal resolution and total duration of the scan, since the optimal values depend on the nature of the tissue being investigated and the quantities to be measured (Sourbron and Buckley, 2012). For example, temporal resolution of the order of a second is required to quantify tissue plasma flow; even if this quantity is of no interest, it may be necessary to account for flow in order to accurately assess permeability. The likely influence of blood flow may be determined using computer simulations, providing plausible tissue parameter ranges are available and relevant to the subjects and tissues being studied (Sourbron et al., 2009; Larsson et al., 2009). Temporal resolution must also be set against requirements for *spatial* resolution and coverage, which differ markedly between applications (e.g. focal vs. diffuse pathology). For accurate

measurement of the permeability-surface area product *PS*, the scan duration should be long enough for significant contrast extravasation to occur: this may be on the order of a few minutes in tissues such as brain tumors, but longer scans are required in less permeable tissues such as normal-appearing brain. If the EES volume fraction v_e is to be accurately measured then imaging should continue well into the "washout" phase, when the EES contrast agent concentration begins to fall. Further research is needed to investigate how variations in contrast agent types and doses affect pharmacokinetic parameters.

A wide range of pharmacokinetic models have been proposed for fitting DCE-MRI data, the most popular of which divide the tissue into well-mixed compartments. It is essential to recognize the assumptions built into these models and to assess their likely validity for a given application (Sourbron and Buckley, 2013). The original Tofts model, for example, is strictly valid only in weakly vascularized tissues, where contrast agent in the capillaries can be neglected; furthermore, the fitted K^{Trans} is equal to *PS* only when the blood flow is sufficiently high. For tissues where the vascular contribution is significant, the Patlak or extended Tofts models may be more appropriate, provided again that plasma flow is high. The choice of model should also reflect the MRI protocol: if the acquisition duration is short and BBB leakage is slow then models that do not allow back-diffusion (e.g. Patlak and tissue-uptake models) may be suitable, while application of a model that does include back-diffusion (e.g. extended Tofts model) can result in increased uncertainty in the fitted parameters. Similarly, application of a model that includes flow (e.g. tissue-uptake and two-compartment exchange models) is counterproductive if the acquired temporal resolution is insufficient. These and other considerations have been investigated theoretically by Sourbron and Buckley (2011) and are summarized accessibly in their recent review (Sourbron and Buckley, 2013). A recent investigation by Cramer et al. further emphasized the importance of appropriate model selection in the context of subtle BBB permeability (Cramer and Larsson, 2014). If it is unclear which model to select *a-priori* then data-driven approaches, e.g. use of Akaike information criteria, can be used to determine the most suitable model (Ewing and Bagher-Ebadian, 2013), although this does not guarantee that the model assumptions are met.

As most current data apply to tumors, more data are required for assessing low-level BBB abnormalities. The relative lack of methodological assessments to determine the best methods of measuring low level BBB disruption in normal or abnormal appearing brain in aging, dementia or brain microvascular disease, argue for substantially more work to determine the optimum contrast and dose, acquisition parameters, and data analysis methods.

6. Conclusion

This systematic review has highlighted the wide range of applications where DCE-MRI has been used to assess BBB integrity. We found large variations in studied pathologies, MRI procedures and data analysis methods resulting in widely varying estimates of permeability parameters. Nevertheless, DCE-MRI has been shown to provide valuable information in a growing field of applications, ranging from the grading of primary brain tumors to the assessment of healthy-appearing tissue in multiple sclerosis patients or dementia. In methodological terms, DCE-MRI is a relatively mature technique, but the lack of agreed standards for image acquisition, data modeling and study reporting hinders inter-study comparison and meta-analysis. Improved reliability of DCE-MRI, especially in subtle permeability states, is required. Where feasible, further technical development should be accompanied by attempts to establish consensus-based recommendations for data acquisition and analysis in order to improve inter-study comparability and promote wider use of DCE-MRI both clinically and in research (Tofts et al., 1999; DCE MRI Technical Committee, 2012; Leach et al., 2012).

Acknowledgments

This work was funded by the Row Fogo Charitable Trust (Ref. AD.ROW4.35), SINAPSE (Scottish Imaging Network: A Platform for Scientific Excellence - Scottish Funding Council, Ref. HR07020) and supported by NHS Lothian Research & Development.

References

Abbott, N.J., Friedman, A., 2012. Overview and introduction: the blood–brain barrier in health and disease. Epilepsia 53 (Suppl 6), 1–6. http://dx.doi.org/10.1111/j.1528-1167.2012.03696.x23134489.

Abo-Ramadan, U., Durukan, A., Pitkonen, M., Marinkovic, I., Tatlisumak, E., Pedrono, E., et al., 2009. Post-ischemic leakiness of the blood–brain barrier: a quantitative and systematic assessment by Patlak plots. Experimental Neurology 219, 328–333. http://dx.doi.org/10.1016/j.expneurol.2009.06.00219520075.

Aksoy, D., Bammer, R., Mlynash, M., Venkatasubramanian, C., Eyngorn, I., Snider, R.W., et al., 2013. Magnetic resonance imaging profile of blood–brain barrier injury in patients with acute intracerebral hemorrhage. Journal of the American Heart Association 2, e000161. http://dx.doi.org/10.1161/JAHA.113.00016123709564.

Ali, M.M., Janic, B., Babajani-Feremi, A., Varma, N.R.S., Iskander, A.S.M., Anagli, J., et al., 2010. Changes in vascular permeability and expression of different angiogenic factors following anti-angiogenic treatment in rat glioma. PLoS ONE 5, e8727. http://dx.doi.org/10.1371/journal.pone.000872720090952.

Armitage, P., Behrenbruch, C., Brady, M., Moore, N., 2005. Extracting and visualizing physiological parameters using dynamic contrast-enhanced magnetic resonance imaging of the breast. Medical Image Analysis 9, 315–329. http://dx.doi.org/10.1016/j.media.2005.01.00115950895.

Armitage, P.A., Farrall, A.J., Carpenter, T.K., Doubal, F.N., Wardlaw, J.M., 2011. Use of dynamic contrast-enhanced MRI to measure subtle blood–brain barrier abnormalities. Magnetic Resonance Imaging 29, 305–314. http://dx.doi.org/10.1016/j.mri.2010.09.00221030178.

Aryal, M.P., Nagaraja, T.N., Keenan, K.A., Bagher-Ebadian, H., Panda, S., Brown, S.L., et al., 2014. Dynamic contrast enhanced MRI parameters and tumor cellularity in a rat model of cerebral glioma at 7 T. Society of Magnetic Resonance in Medicine 71, 2206–2214. http://dx.doi.org/10.1002/mrm.2487323878070.

Awasthi, R., Pandey, C.M., Sahoo, P., Behari, S., Kumar, V., Kumar, S., et al., 2012. Dynamic contrast-enhanced magnetic resonance imaging-derived kep as a potential biomarker of matrix metalloproteinase 9 expression in patients with glioblastoma multiforme: a pilot study. Journal of Computer Assisted Tomography 36, 125–130. http://dx.doi.org/10.1097/RCT.0b013e31823f6c5922261782.

Bagher-Ebadian, H., Jain, R., Nejad-Davarani, S.P., Mikkelsen, T., Lu, M., Jiang, Q., et al., 2012. Model selection for DCE-T1 studies in glioblastoma. Magnetic Resonance in Medicine: Official Journal of the Society of Magnetic Resonance in Medicine / Society of Magnetic Resonance in Medicine 68, 241–251. http://dx.doi.org/10.1002/mrm.2321122127934.

Barnes, S.L., Whisenant, J.G., Loveless, M.E., Yankeelov, T.E., 2012. Practical dynamic contrast enhanced MRI in small animal models of cancer: data acquisition, data analysis, and interpretation. Pharmaceutics 4, 442–478. http://dx.doi.org/10.3390/pharmaceutics403044223105959.

Brandt, C.T., Simonsen, H., Liptrot, M., Søgaard, L.V., Lundgren, J.D., Ostergaard, C., et al., 2008. In vivo study of experimental pneumococcal meningitis using magnetic resonance imaging. BMC Medical Imaging 8, 1. http://dx.doi.org/10.1186/1471-2342-8-118194516.

Brix, G., Semmler, W., Port, R., 1991. Pharmacokinetic parameters in CNS Gd-DTPA enhanced MR imaging. Journal of Computer Assisted Tomography 15, 621–628. http://dx.doi.org/10.1097/00004728-199107000-000182061479.

Brookes, J.A., Redpath, T.W., Gilbert, F.J., Murray, A.D., Staff, R.T., 1999. Accuracy of T1 measurement in dynamic contrast-enhanced breast MRI using two- and three-dimensional variable flip angle fast low-angle shot. Journal of Magnetic Resonance Imaging: JMRI 9, 163–171. http://dx.doi.org/10.1002/(SICI)1522-2586(199902)9:2<163::AID-JMRI3>3.0.CO;2-L10077009.

Budde, M.D., Gold, E., Jordan, E.K., Frank, J.A., 2012. Differential microstructure and physiology of brain and bone metastases in a rat breast cancer model by diffusion and dynamic contrast enhanced MRI. Clinical & Experimental Metastasis 29, 51–62. http://dx.doi.org/10.1007/s10585-011-9428-222042553.

Calamante, F., 2013. Arterial input function in perfusion MRI: a comprehensive review. Progress in Nuclear Magnetic Resonance Spectroscopy 74, 1–32. http://dx.doi.org/10.1016/j.pnmrs.2013.04.00224083460.

Cao, Y., Tsien, C.I., Sundgren, P.C., Nagesh, V., Normolle, D., Buchtel, H., et al., 2009. Dynamic contrast-enhanced magnetic resonance imaging as a biomarker for prediction of radiation-induced neurocognitive dysfunction. Clinical Cancer Research: an Official Journal of the American Association for Cancer Research 15, 1747–1754. http://dx.doi.org/10.1158/1078-0432.CCR-08-142019223506.

Cha, S., Yang, L., Johnson, G., Lai, A., Chen, M.H., Tihan, T., et al., 2006. Comparison of microvascular permeability measurements, K Trans, determined with pass T2*-weighted MR imaging methods in gliomas and meningiomas. AJNR. American Journal of Neuroradiology 27, 409–41716484420.

Chen, J., Yao, J., Thomasson, D., 2008. Automatic determination of arterial input function for dynamic contrast enhanced MRI in tumor assessment. Medical Image Computing and Computer-Assisted Intervention: MICCAI ... International Conference on Medical Image Computing and Computer-Assisted Intervention 11, 594–60118979795.

Chu, J.-P., Mak, H.K.-F., Yau, K.K.-W., Zhang, L., Tsang, J., Chan, Q., et al., 2012. Pilot study on evaluation of any correlation between MR perfusion (Ktrans) and diffusion

(apparent diffusion coefficient) parameters in brain tumors at 3 Tesla. Cancer Imaging: the Official Publication of the International Cancer Imaging Society 12, 1–6. http://dx.doi.org/10.1102/1470-7330.2012.000122275724.
Cramer, S.P., Larsson, H.B.W., 2014. Accurate determination of blood–brain barrier permeability using dynamic contrast-enhanced T1-weighted MRI: a simulation and in vivo study on healthy subjects and multiple sclerosis patients. Journal of Cerebral Blood Flow and Metabolism: Official Journal of the International Society of Cerebral Blood Flow and Metabolism 1–11 http://dx.doi.org/10.1038/jcbfm.2014.12625074746.
Cramer, S.P., Simonsen, H., Frederiksen, J.L., Rostrup, E., Larsson, H.B.W., 2014. Abnormal blood–brain barrier permeability in normal appearing white matter in multiple sclerosis investigated by MRI. NeuroImage. Clinical 4, 182–189. http://dx.doi.org/10.1016/j.nicl.2013.12.00124371801.
DCE MRI Technical Committee, 2012. DCE MRI Quantification Profile, Quantitative Imaging Biomarkers AllianceVersion 1.0. Reviewed Draft. Available from: http://rsna.org/QIBA.aspx.
Durukan, A., Marinkovic, I., Strbian, D., Pitkonen, M., Pedrono, E., Soinne, L., et al., 2009. Post-ischemic blood–brain barrier leakage in rats: one-week follow-up by MRI. Brain Research 1280, 158–165. http://dx.doi.org/10.1016/j.brainres.2009.05.02519450568.
Ewing, J.R., Bagher-Ebadian, H., 2013. Model selection in measures of vascular parameters using dynamic contrast-enhanced MRI: experimental and clinical applications. NMR in Biomedicine 26, 1028–1041. http://dx.doi.org/10.1002/nbm.299623881857.
Ewing, J.R., Knight, R.A., Nagaraja, T.N., Yee, J.S., Nagesh, V., Whitton, P.A., et al., 2003. Patlak plots of Gd-DTPA MRI data yield blood–brain transfer constants concordant with those of 14C-sucrose in areas of blood–brain opening. Magnetic Resonance in Medicine: Official Journal of the Society of Magnetic Resonance in Medicine / Society of Magnetic Resonance in Medicine 50, 283–292. http://dx.doi.org/10.1002/mrm.1052412876704.
Ferl, G.Z., Xu, L., Friesenhahn, M., Bernstein, L.J., Barboriak, D.P., Port, R.E., 2010. An automated method for nonparametric kinetic analysis of clinical DCE-MRI data: application to glioblastoma treated with bevacizumab. Magnetic Resonance in Medicine: Official Journal of the Society of Magnetic Resonance in Medicine / Society of Magnetic Resonance in Medicine 63, 1366–1375. http://dx.doi.org/10.1002/mrm.2233520432307.
Ferrier, M.C., Sarin, H., Fung, S.H., Schatlo, B., Pluta, R.M., Gupta, S.N., et al., 2007. Validation of dynamic contrast-enhanced magnetic resonance imaging-derived vascular permeability measurements using quantitative autoradiography in the RG2 Rat brain tumor model. Neoplasia (New York, N.Y.) 9, 546–555. http://dx.doi.org/10.1593/neo.0728917710157.
Gaitán, M.I., Shea, C.D., 2011. Evolution of the blood–brain barrier in newly forming multiple sclerosis lesions. Annals of Neurology 70, 22–29. http://dx.doi.org/10.1002/ana.2247221710622.
Gal, Y., Mehnert, A., Bradley, A., McMahon, K., Kennedy, D., Crozier, S., 2008. A new denoising method for dynamic contrast-enhanced MRI. Annual International Conference of the IEEE Engineering in Medicine and Biology Society 847–850.
Gupta, R.K., Awasthi, R., Rathore, R.K.S., Verma, A., Sahoo, P., Paliwal, V.K., et al., 2012. Understanding epileptogenesis in calcified neurocysticercosis with perfusion MRI. Neurology 78, 618–625. http://dx.doi.org/10.1212/WNL.0b013e318248deae22302547.
Guyatt, G.H., Oxman, A.D., Vist, G.E., Kunz, R., Falck-Ytter, Y., Alonso-Coello, P., et al., 2008. GRADE: an emerging consensus on rating quality of evidence and strength of recommendations. BMJ (Clinical Research Ed.) 336, 924–926. http://dx.doi.org/10.1136/bmj.39489.470347.AD18436948.
Haris, M., Gupta, R.K., Singh, A., Husain, N., Husain, M., Pandey, C.M., et al., 2008a. Differentiation of infective from neoplastic brain lesions by dynamic contrast-enhanced MRI. Neuroradiology 50, 531–540. http://dx.doi.org/10.1007/s00234-008-0378-618379766.
Haris, M., Husain, N., Singh, A., Awasthi, R., Singh Rathore, R.K., Husain, M., et al., 2008b. Dynamic contrast-enhanced (DCE) derived transfer coefficient (ktrans) is a surrogate marker of matrix metalloproteinase 9 (MMP-9) expression in brain tuberculomas. Journal of Magnetic Resonance Imaging: JMRI 28, 588–597. http://dx.doi.org/10.1002/jmri.2149118777539.
Haris, M., Husain, N., Singh, A., Husain, M., Srivastava, S., Srivastava, C., et al., 2008c. Dynamic contrast-enhanced derived cerebral blood volume correlates better with Leak correction than with No correction for vascular endothelial growth factor, microvascular density, and grading of astrocytoma. Journal of Computer Assisted Tomography 32, 955–965. http://dx.doi.org/10.1097/RCT.0b013e31816200d119204461.
Harrer, J.U., Parker, G.J.M., Haroon, H.A., Buckley, D.L., Embelton, K., Roberts, C., et al., 2004. Comparative study of methods for determining vascular permeability and blood volume in human gliomas. Journal of Magnetic Resonance Imaging: JMRI 20, 748–757. http://dx.doi.org/10.1002/jmri.2018215503330.
Hoff, B.A., Bhojani, M.S., Rudge, J., Chenevert, T.L., Meyer, C.R., Galbán, S., et al., 2012. DCE and DW-MRI monitoring of vascular disruption following VEGF-Trap treatment of a rat glioma model. NMR in Biomedicine 25, 935–942. http://dx.doi.org/10.1002/nbm.181422190279.
Iannotti, F., Fieschi, C., Alfano, B., 1987. Simplified, noninvasive PET measurement of blood–brain barrier permeability. Journal of Computer Assisted Tomography 11, 390–397. http://dx.doi.org/10.1097/00004728-198705000-000043106433.
Ingrisch, M., Sourbron, S., Morhard, D., Ertl-Wagner, B., Kümpfel, T., 2012. Quantification of perfusion and permeability in multiple sclerosis: dynamic contrast-enhanced MRI in 3D at 3T. Investigative Radiology 47, 252–258. http://dx.doi.org/10.1097/RLI.0b013e31823bfc9722373532.
Jain, R., 2013. Measurements of tumor vascular leakiness using DCE in brain tumors: clinical applications. NMR in Biomedicine 26, 1042–1049. http://dx.doi.org/10.1002/nbm.299423832526.
Jelescu, I.O., Leppert, I.R., Narayanan, S., Araújo, D., Arnold, D.L., Pike, G.B., 2011. Dual-temporal resolution dynamic contrast-enhanced MRI protocol for blood–brain barrier permeability measurement in enhancing multiple sclerosis lesions. Journal of Magnetic Resonance Imaging: JMRI 33, 1291–1300. http://dx.doi.org/10.1002/jmri.2256521590997.
Jia, Z.Z., Geng, D.Y., Liu, Y., Chen, X.R., Zhang, J., 2013. Microvascular permeability of brain astrocytoma with contrast-enhanced magnetic resonance imaging: correlation analysis with histopathologic grade. Chinese Medicine J2013 (126), 1953–195623673117.
Kassner, A., Roberts, T., Taylor, K., Silver, F., Mikulis, D., 2005. Prediction of hemorrhage in acute ischemic stroke using permeability MR imaging. AJNR. American Journal of Neuroradiology 26, 2213–221716219824.
Kassner, A., Roberts, T.P.L., Moran, B., Silver, F.L., Mikulis, D.J., 2009. Recombinant tissue plasminogen activator increases blood–brain barrier disruption in acute ischemic stroke: an MR imaging permeability study. AJNR. American Journal of Neuroradiology 30, 1864–1869. http://dx.doi.org/10.3174/ajnr.A177419661169.
Kermode, A.G., Tofts, P.S., Thompson, A.J., MacManus, D.G., Rudge, P., Kendall, B.E., et al., 1990. Heterogeneity of blood–brain barrier changes in multiple sclerosis: an MRI study with gadolinium-DTPA enhancement. Neurology 40, 229–235. http://dx.doi.org/10.1212/WNL.40.2.2292300240.
Krueck, W.G., Schmiedl, U.P., Maravilla, K.R., Spence, A.M., Starr, F.L., Kenney, J., 1994. MR assessment of radiation-induced blood–brain barrier permeability changes in rat glioma model. AJNR. American Journal of Neuroradiology 15, 625–6328010261.
Larsen, V.A., Simonsen, H.J., Law, I., Larsson, H.B.W., Hansen, A.E., 2013. Evaluation of dynamic contrast-enhanced T1-weighted perfusion MRI in the differentiation of tumor recurrence from radiation necrosis. Neuroradiology 55, 361–369. http://dx.doi.org/10.1007/s00234-012-1127-423262559.
Larsson, C., Kleppestø, M., Rasmussen, I., Salo, R., Vardal, J., Brandal, P., et al., 2013. Sampling requirements in DCE-MRI based analysis of high grade gliomas: Simulations and clinical results. Journal of Magnetic Resonance Imaging: JMRI 37, 818–829. http://dx.doi.org/10.1002/jmri.2386623086710.
Larsson, H.B., Stubgaard, M., Frederiksen, J.L., Jensen, M., Henriksen, O., Paulson, O.B., 1990. Quantitation of blood–brain barrier defect by magnetic resonance imaging and gadolinium-DTPA in patients with multiple sclerosis and brain tumors. Magnetic Resonance in Medicine: Official Journal of the Society of Magnetic Resonance in Medicine / Society of Magnetic Resonance in Medicine 16, 117–131. http://dx.doi.org/10.1002/mrm.19101601112255233.
Larsson, H.B.W., Courivaud, F., Rostrup, E., Hansen, A.E., 2009. Measurement of brain perfusion, blood volume, and blood–brain barrier permeability, using dynamic contrast-enhanced T(1)-weighted MRI at 3 tesla. Magnetic Resonance in Medicine: Official Journal of the Society of Magnetic Resonance in Medicine / Society of Magnetic Resonance in Medicine 62, 1270–1281. http://dx.doi.org/10.1002/mrm.2213619780145.
Larsson, H.B.W., Frederiksen, J., Kjaer, L., Henriksen, O., Olesen, J., 1988. In vivo determination of T1 and T2 in the brain of patients with severe but stable multiple sclerosis. Magnetic Resonance in Medicine: Official Journal of the Society of Magnetic Resonance in Medicine / Society of Magnetic Resonance in Medicine 7, 43–55. http://dx.doi.org/10.1002/mrm.19100701063386521.
Lavini, C., Verhoeff, J.J.C., 2010. Reproducibility of the gadolinium concentration measurements and of the fitting parameters of the vascular input function in the superior sagittal sinus in a patient population. Magnetic Resonance Imaging 28, 1420–1430. http://dx.doi.org/10.1016/j.mri.2010.06.01720817379.
Leach, M.O., Morgan, B., Tofts, P.S., Buckley, D.L., Huang, W., Horsfield, M.A., et al., 2012. Imaging vascular function for early stage clinical trials using dynamic contrast-enhanced magnetic resonance imaging. European Radiology 22, 1451–1464. http://dx.doi.org/10.1007/s00330-012-2446-x22562143.
Li, K.-L., Buonaccorsi, G., Thompson, G., Cain, J.R., Watkins, A., Russell, D., et al., 2012. An improved coverage and spatial resolution — using dual injection dynamic contrast-enhanced (ice-DICE) MRI: a novel dynamic contrast-enhanced technique for cerebral tumors. Magnetic Resonance in Medicine: Official Journal of the Society of Magnetic Resonance in Medicine / Society of Magnetic Resonance in Medicine 68, 452–462. http://dx.doi.org/10.1002/mrm.2325222791559.
Li, K.L., Zhu, X.P., Waterton, J., Jackson, A., 2000. Improved 3D quantitative mapping of blood volume and endothelial permeability in brain tumors. Journal of Magnetic Resonance Imaging: JMRI 12, 347–357. http://dx.doi.org/10.1002/1522-2586(200008)12:2<347::AID-JMRI19>3.3.CO;2-Z10931600.
Li, X., Rooney, W.D., Várallyay, C.G., Gahramanov, S., Muldoon, L.L., Goodman, J.A., et al., 2010. Dynamic-contrast-enhanced-MRI with extravasating contrast reagent: Rat cerebral glioma blood volume determination. Journal of Magnetic Resonance (San Diego, Calif.: 1997) 206, 190–199. http://dx.doi.org/10.1016/j.jmr.2010.07.00420674422.
Lüdemann, L., Hamm, B., Zimmer, C., 2000. Pharmacokinetic analysis of glioma compartments with dynamic Gd-DTPA-enhanced magnetic resonance imaging. Magnetic Resonance Imaging 18, 1201–1214. http://dx.doi.org/10.1016/S0730-725X(00)00223-X11167040.
Lüdemann, L., Warmuth, C., Plotkin, M., Förschler, A., Gutberlet, M., Wust, P., et al., 2009. Brain tumor perfusion: comparison of dynamic contrast enhanced magnetic resonance imaging using T1, T2, and T2* contrast, pulsed arterial spin labeling, and H2(15)O positron emission tomography. European Journal of Radiology 70, 465–474. http://dx.doi.org/10.1016/j.ejrad.2008.02.01218359598.
Ludemann, L., Wurm, R., Zimmer, C., 2002. Pharmacokinetic modeling of Gd-DTPA extravasation in brain tumors. Investigative Radiology 37, 562–570. http://dx.doi.org/10.1097/00004424-200210000-0000512352165.
Manuchehri, A.M., Sathyapalan, T., Lowry, M., Turnbull, L.W., Rowland-Hill, C., Atkin, S.L., 2007. Effect of dopamine agonists on prolactinomas and normal pituitary assessed by dynamic contrast enhanced magnetic resonance imaging (DCE-MRI). Pituitary 10, 261–266. http://dx.doi.org/10.1007/s11102-007-0048-417557207.

Mills, S.J., Soh, C., O'Connor, J.P.B., Rose, C.J., Buonaccorsi, G.A., Cheung, S., et al., 2009. Tumour enhancing fraction (EnF) in glioma: relationship to tumour grade. European Radiology 19, 1489–1498. http://dx.doi.org/10.1007/s00330-008-1288-z19198847.

Miyati, T., Banno, T., Mase, M., Kasai, H., Shundo, H., Imazawa, M., et al., 1997. Dual dynamic contrast-enhanced MR imaging. Journal of Magnetic Resonance Imaging: JMRI 7, 230–235. http://dx.doi.org/10.1002/jmri.1880701369039621.

Nagaraja, T.N., Karki, K., Ewing, J.R., Divine, G.W., Fenstermacher, D., Patlak, C.S., et al., 2010. The MRI-measured arterial input function resulting from a bolus injection of Gd-DTPA in a rat model of stroke slightly underestimates that of Gd-[14C]DTPA and marginally overestimates the blood-to-brain influx rate constant determined by Patlak plots. Magnetic Resonance Imaging 63, 1502–1509.

Noseworthy, M.D., Bray, T.M., 2000. Zinc deficiency exacerbates loss in blood–brain barrier integrity induced by hyperoxia measured by dynamic MRI. Proceedings of the Society for Experimental Biology and Medicine. Society for Experimental Biology and Medicine (New York, N.Y.) 223, 175–182. http://dx.doi.org/10.1111/j.1525-1373.2000.22324.x10654621.

O'Connor, J.P.B., Jackson, A., Parker, G.J.M., Roberts, C., Jayson, G.C., 2012. Dynamic contrast-enhanced MRI in clinical trials of antivascular therapies. Nature Reviews. Clinical Oncology 9, 167–177. http://dx.doi.org/10.1038/nrclinonc.2012.222330689.

Obermeier, B., Daneman, R., Ransohoff, R.M., 2013. Development, maintenance and disruption of the blood–brain barrier. Nature Medicine 19, 1584–1596. http://dx.doi.org/10.1038/nm.340724309662.

Parker, G.J.M., Roberts, C., Macdonald, A., Buonaccorsi, G.A., Cheung, S., Buckley, D.L., et al., 2006. Experimentally-derived functional form for a population-averaged high-temporal-resolution arterial input function for dynamic contrast-enhanced MRI. Magnetic Resonance in Medicine: Official Journal of the Society of Magnetic Resonance in Medicine / Society of Magnetic Resonance in Medicine 56, 993–1000. http://dx.doi.org/10.1002/mrm.2106617036301.

Provenzale, J.M., York, G., Moya, M.G., Parks, L., Choma, M., Kealey, S., et al., 2006. Correlation of relative permeability and relative cerebral blood volume in high-grade cerebral neoplasms. AJR. American Journal of Roentgenology 187, 1036–1042. http://dx.doi.org/10.2214/AJR.04.067616985154.

Quarles, C.C., Gore, J.C., Xu, L., Yankeelov, T.E., 2012. Comparison of dual-echo DSC-MRI- and DCE-MRI-derived contrast agent kinetic parameters. Magnetic Resonance Imaging 30, 944–953. http://dx.doi.org/10.1016/j.mri.2012.03.00822617148.

Roberts, H.C., Roberts, T.P., Brasch, R.C., Dillon, W.P., 2000. Quantitative measurement of microvascular permeability in human brain tumors achieved using dynamic contrast-enhanced MR imaging: correlation with histologic grade. AJNR. American Journal of Neuroradiology 21, 891–899 10815665.

Rosenberg, G.A., 2012. Neurological diseases in relation to the blood–brain barrier. Journal of Cerebral Blood Flow and Metabolism: Official Journal of the International Society of Cerebral Blood Flow and Metabolism 32, 1139–1151. http://dx.doi.org/10.1038/jcbfm.2011.19722252235.

Schabel, M.C., Parker, D.L., 2008. Uncertainty and bias in contrast concentration measurements using spoiled gradient echo pulse sequences. Physics in Medicine and Biology 53, 2345–2373. http://dx.doi.org/10.1088/0031-9155/53/9/01018421121.

Shames, D.M., Kuwatsuru, R., Vexler, V., Mühler, A., Brasch, R.C., 1993. Measurement of capillary permeability to macromolecules by dynamic magnetic resonance imaging: a quantitative noninvasive technique. Magnetic Resonance in Medicine: Official Journal of the Society of Magnetic Resonance in Medicine / Society of Magnetic Resonance in Medicine 29, 616–622. http://dx.doi.org/10.1002/mrm.19102905068505897.

Shinohara, R.T., Crainiceanu, C.M., Caffo, B.S., 2011. Population-wide principal component-based quantification of blood–brain-barrier dynamics in multiple sclerosis. Neuroimage 57, 1430–1446. http://dx.doi.org/10.1016/j.neuroimage.2011.05.03821635955.

Singh, A., Haris, M., Rathore, D., Purwar, A., Sarma, M., Bayu, G., et al., 2007. Quantification of physiological and hemodynamic indices using T(1) dynamic contrast-enhanced MRI in intracranial mass lesions. Journal of Magnetic Resonance Imaging: JMRI 26, 871–880. http://dx.doi.org/10.1002/jmri.2108017896358.

Song, S.K., Lee, S.-K., Lee, J.J., Lee, J.E., Choi, H.S., Sohn, Y.H., et al., 2011. Blood–brain barrier impairment is functionally correlated with clinical severity in patients of multiple system atrophy. Neurobiology of Aging 32, 2183–2189. http://dx.doi.org/10.1016/j.neurobiolaging.2009.12.01720149484.

Sourbron, S., Ingrisch, M., Siefert, A., Reiser, M., Herrmann, K., 2009. Quantification of cerebral blood flow, cerebral blood volume, and blood–brain-barrier leakage with DCE-MRI. Magnetic Resonance in Medicine: Official Journal of the Society of Magnetic Resonance in Medicine / Society of Magnetic Resonance in Medicine 62, 205–217. http://dx.doi.org/10.1002/mrm.2200519449435.

Sourbron, S.P., Buckley, D.L., 2013. Classic models for dynamic contrast-enhanced MRI. NMR in Biomedicine 26, 1004–1027. http://dx.doi.org/10.1002/nbm.294023674304.

Sourbron, S.P., Buckley, D.L., 2011. On the scope and interpretation of the Tofts models for DCE-MRI. Magnetic Resonance in Medicine: Official Journal of the Society of Magnetic Resonance in Medicine / Society of Magnetic Resonance in Medicine 66, 735–745. http://dx.doi.org/10.1002/mrm.2286121384424.

Sourbron, S.P., Buckley, D.L., 2012. Tracer kinetic modelling in MRI: estimating perfusion and capillary permeability. Physics in Medicine and Biology 57, R1–33. http://dx.doi.org/10.1088/0031-9155/57/2/R122173205.

Starr, J.M., Farrall, A.J., Armitage, P., McGurn, B., Wardlaw, J., 2009. Blood–brain barrier permeability in Alzheimer's disease: A case-control MRI study. Psychiatry Research 171, 232–241. http://dx.doi.org/10.1016/j.pscychresns.2008.04.00319211227.

Starr, J.M., Wardlaw, J., Ferguson, K., MacLullich, A., Deary, I.J., Marshall, I., 2003. Increased blood–brain barrier permeability in type II diabetes demonstrated by gadolinium magnetic resonance imaging. Journal of Neurology, Neurosurgery, and Psychiatry 74, 70–76. http://dx.doi.org/10.1136/jnnp.74.1.7012486269.

Su, M.Y., Head, E., Brooks, W.M., Wang, Z., Muggenburg, B.A., Adam, G.E., et al., 1998. Magnetic resonance imaging of anatomic and vascular characteristics in a canine model of human aging. Neurobiology of Aging 19, 479–485. http://dx.doi.org/10.1016/S0197-4580(98)00081-59880050.

Taheri, S., Candelario-Jalil, E., Estrada, E.Y., Rosenberg, G.A., 2009. Spatiotemporal correlations between blood–brain barrier permeability and apparent diffusion coefficient in a rat model of ischemic stroke. PloS One 4, e6597. http://dx.doi.org/10.1371/journal.pone.000659719668371.

Taheri, S., Gasparovic, C., Huisa, B.N., Adair, J.C., Edmonds, E., Prestopnik, J., et al., 2011a. Blood–brain barrier permeability abnormalities in vascular cognitive impairment. Stroke; a Journal of Cerebral Circulation 42, 2158–2163. http://dx.doi.org/10.1161/STROKEAHA.110.61173121719768.

Taheri, S., Gasparovic, C., Shah, N.J., Rosenberg, G.A., 2011b. Quantitative measurement of blood–brain barrier permeability in human using dynamic contrast-enhanced MRI with fast T1 mapping. Magnetic Resonance in Medicine: Official Journal of the Society of Magnetic Resonance in Medicine / Society of Magnetic Resonance in Medicine 65, 1036–1042. http://dx.doi.org/10.1002/mrm.2268621413067.

Thompson, E.M., Guillaume, D.J., Dósa, E., Li, X., Nazemi, K.J., Gahramanov, S., et al., 2012. Dual contrast perfusion MRI in a single imaging session for assessment of pediatric brain tumors. Journal of Neuro-Oncology 109, 105–114. http://dx.doi.org/10.1007/s11060-012-0872-x22528798.

Thornhill, R.E., Chen, S., Rammo, W., Mikulis, D.J., Kassner, A., 2010. Contrast-enhanced MR imaging in acute ischemic stroke: T2* measures of blood–brain barrier permeability and their relationship to T1 estimates and hemorrhagic transformation. AJNR. American Journal of Neuroradiology 31, 1015–1022. http://dx.doi.org/10.3174/ajnr.A200320190209.

Tofts, P.S., Brix, G., Buckley, D.L., Evelhoch, J.L., Henderson, E., Knopp, M.V., et al., 1999. Contrast-enhanced T 1 -Weighted MRI of a diffusible tracer: Standardized quantities and symbols. Journal of Magnetic Resonance Imaging 232, 223–232.

Tofts, P.S., Kermode, A.G., 1991. Measurement of the blood–brain barrier permeability and leakage space using dynamic MR imaging. 1. Fundamental concepts. Magnetic Resonance in Medicine: Official Journal of the Society of Magnetic Resonance in Medicine / Society of Magnetic Resonance in Medicine 17, 357–367. http://dx.doi.org/10.1002/mrm.19101702082062210.

Topakian, R., Barrick, T.R., Howe, F.A., Markus, H.S., 2010. Blood–brain barrier permeability is increased in normal-appearing white matter in patients with lacunar stroke and leucoaraiosis. Journal of Neurology, Neurosurgery, and Psychiatry 81, 192–197. http://dx.doi.org/10.1136/jnnp.2009.17207219710048.

Türkbey, B., Thomasson, D., Pang, Y., Bernardo, M., Choyke, P.L., 2010. The role of dynamic contrast-enhanced MRI in cancer diagnosis and treatment. Diagnostic and Interventional Radiology (Ankara, Turkey) 16, 186–192. http://dx.doi.org/10.4261/1305-3825.DIR.2537-08.119885783.

Vidarsson, L., Thornhill, R.E., Liu, F., Mikulis, D.J., Kassner, A., 2009. Quantitative permeability magnetic resonance imaging in acute ischemic stroke: how long do we need to scan? Magnetic Resonance Imaging 27, 1216–1222. http://dx.doi.org/10.1016/j.mri.2009.01.01919695816.

Wang, H., Golob, E.J., Su, M.-Y., 2006. Vascular volume and blood–brain barrier permeability measured by dynamic contrast enhanced MRI in hippocampus and cerebellum of patients with MCI and normal controls. Journal of Magnetic Resonance Imaging: JMRI 24, 695–700. http://dx.doi.org/10.1002/jmri.2066916878309.

Wardlaw, J.M., Doubal, F., Armitage, P., Chappell, F., Carpenter, T., Muñoz Maniega, S., et al., 2009. Lacunar stroke is associated with diffuse blood–brain barrier dysfunction. Annals of Neurology 65, 194–202. http://dx.doi.org/10.1002/ana.2154919260033.

Wardlaw, J.M., Farrall, A., Armitage, P.A., Carpenter, T., Chappell, F., Doubal, F., et al., 2008. Changes in background blood–brain barrier integrity between lacunar and cortical ischemic stroke subtypes. Stroke; a Journal of Cerebral Circulation 39, 1327–1332. http://dx.doi.org/10.1161/STROKEAHA.107.50012418309161.

Wei, X.-E., Wang, D., Li, M.-H., Zhang, Y.-Z., Li, Y.-H., Li, W.-B., 2011. A useful tool for the initial assessment of blood–brain barrier permeability after traumatic brain injury in rabbits: dynamic contrast-enhanced magnetic resonance imaging. Journal of Trauma 71, 1645–1650. http://dx.doi.org/10.1097/TA.0b013e31823498eb22182873.

Weinmann, H.J., Laniado, M., Mützel, W., 1984. Pharmacokinetics of GdDTPA/dimeglumine after intravenous injection into healthy volunteers. Physiological Chemistry and Physics and Medical NMR 16, 167–1726505043.

Wilkinson, I.D., Jellineck, D.A., Levy, D., Giesel, F.L., Romanowski, C.A.J., Miller, B.-A., et al., 2006. Dexamethasone and enhancing solitary cerebral mass lesions: alterations in perfusion and blood–tumor barrier kinetics shown by magnetic resonance imaging. Neurosurgery 58, 640–646. http://dx.doi.org/10.1227/01.NEU.0000204873.68395.A016575327.

Yankeelov, T.E., Luci, J.J., Lepage, M., Li, R., Debusk, L., Lin, P.C., et al., 2005. Quantitative pharmacokinetic analysis of DCE-MRI data without an arterial input function: a reference region model. Magnetic Resonance Imaging 23, 519–529. http://dx.doi.org/10.1016/j.mri.2005.02.01315919597.

Zhang, N., Zhang, L., Qiu, B., Meng, L., Wang, X., Hou, B.L., 2012. Correlation of volume transfer coefficient Ktrans with histopathologic grades of gliomas. Journal of Magnetic Resonance Imaging: JMRI 36, 355–363. http://dx.doi.org/10.1002/jmri.2367522581762.

Zhu, X.P., Li, K.L., Kamaly-Asl, I.D., Checkley, D.R., Tessier, J.J., Waterton, J.C., et al., 2000. Quantification of endothelial permeability, leakage space, and blood volume in brain tumors using combined T1 and T2* contrast-enhanced dynamic MR imaging. Journal of Magnetic Resonance Imaging: JMRI 11, 575–585. http://dx.doi.org/10.1002/1522-2586(200006)11:6<575::AID-JMRI2>3.0.CO;2-110862055.

NeuroImage 125 (2016) 446–455

Contents lists available at ScienceDirect

NeuroImage

journal homepage: www.elsevier.com/locate/ynimg

Tracer kinetic modelling for DCE-MRI quantification of subtle blood–brain barrier permeability

Anna K. Heye [a], Michael J. Thrippleton [a,*], Paul A. Armitage [a,b], Maria del C. Valdés Hernández [a], Stephen D. Makin [a], Andreas Glatz [a], Eleni Sakka [a], Joanna M. Wardlaw [a]

[a] Neuroimaging Sciences, University of Edinburgh, Chancellors Building, 49 Little France Crescent, Edinburgh EH16 4SB, UK
[b] Department of Cardiovascular Science, University of Sheffield, Medical School, Beech Hill Road, Sheffield S10 2RX UK

ARTICLE INFO

Article history:
Received 16 June 2015
Accepted 7 October 2015
Available online 20 October 2015

Keywords:
Blood–brain barrier
Dynamic contrast-enhanced MRI
Tracer kinetic modelling
Cerebral small vessel disease

ABSTRACT

There is evidence that subtle breakdown of the blood–brain barrier (BBB) is a pathophysiological component of several diseases, including cerebral small vessel disease and some dementias. Dynamic contrast-enhanced MRI (DCE-MRI) combined with tracer kinetic modelling is widely used for assessing permeability and perfusion in brain tumours and body tissues where contrast agents readily accumulate in the extracellular space. However, in diseases where leakage is subtle, the optimal approach for measuring BBB integrity is likely to differ since the magnitude and rate of enhancement caused by leakage are extremely low; several methods have been reported in the literature, yielding a wide range of parameters even in healthy subjects. We hypothesised that the Patlak model is a suitable approach for measuring low-level BBB permeability with low temporal resolution and high spatial resolution and brain coverage, and that normal levels of scanner instability would influence permeability measurements. DCE-MRI was performed in a cohort of mild stroke patients ($n = 201$) with a range of cerebral small vessel disease severity. We fitted these data to a set of nested tracer kinetic models, ranking their performance according to the Akaike information criterion. To assess the influence of scanner drift, we scanned 15 healthy volunteers that underwent a "sham" DCE-MRI procedure without administration of contrast agent. Numerical simulations were performed to investigate model validity and the effect of scanner drift. The Patlak model was found to be most appropriate for fitting low-permeability data, and the simulations showed v_p and K^{Trans} estimates to be reasonably robust to the model assumptions. However, signal drift (measured at approximately 0.1% per minute and comparable to literature reports in other settings) led to systematic errors in calculated tracer kinetic parameters, particularly at low permeabilities. Our findings justify the growing use of the Patlak model in low-permeability states, which has the potential to provide valuable information regarding BBB integrity in a range of diseases. However, absolute values of the resulting tracer kinetic parameters should be interpreted with extreme caution, and the size and influence of signal drift should be measured where possible.

Introduction

Imaging and biochemical investigations suggest that breakdown of the blood–brain barrier (BBB) may be implicated in ageing and the pathophysiology of several diseases, including cerebral small vessel disease, lacunar stroke, vascular dementia and Alzheimer's disease (Farrall and Wardlaw, 2009; Iadecola, 2013; Wardlaw et al., 2013a). Reliable in vivo methods for measuring microvascular integrity are therefore essential to investigate the mechanisms underlying such diseases and to assess potential therapies. The cerebrospinal fluid (CSF) to plasma albumin ratio is a widely accepted in vivo marker of BBB integrity but is non-specific and highly invasive.

The most widely used imaging method for assessing BBB integrity and other microvascular properties is dynamic contrast-enhanced MRI (DCE-MRI), in which a paramagnetic contrast agent is injected and the time dependence of the resulting T_1-weighted image enhancement measured. There are many approaches to analysing such data, from simple heuristic measures to a growing library of tracer kinetic models (Sourbron and Buckley, 2012), which aim to estimate physiological parameters including blood flow, blood volume and the rate of extravascular leakage. These techniques have been developed and applied primarily in neurooncology and body imaging, where contrast uptake in tissue is typically large and rapid. However, the optimal modelling approach for research in diseases where the BBB remains largely intact

* Corresponding author at: Brain Research Imaging Centre, Neuroimaging Sciences, University of Edinburgh, Western General Hospital, Crewe Road, Edinburgh EH4 2XU, UK. Fax: +44 131 537 2661.
E-mail addresses: a.k.heye@sms.ed.ac.uk (A.K. Heye), m.j.thrippleton@ed.ac.uk (M.J. Thrippleton), p.armitage@sheffield.ac.uk (P.A. Armitage), M.Valdes-Hernan@ed.ac.uk (M.C. Valdés Hernández), Stephen.Makin@ed.ac.uk (S.D. Makin), andi.glatz@gmail.com (A. Glatz), eleni.sakka@ed.ac.uk (E. Sakka), Joanna.Wardlaw@ed.ac.uk (J.M. Wardlaw).

http://dx.doi.org/10.1016/j.neuroimage.2015.10.018
1053-8119/

(and extravascular contrast uptake is therefore slow) is unclear. Some groups have applied semi-quantitative approaches, comparing signal enhancement–time curves between patient groups to avoid assumptions inherent in modelling (Wardlaw et al., 2008) or calculating heuristic quantities such as "area under curve" (Topakian et al., 2010). These approaches have the advantage of being straightforward to implement and do not require advanced image processing, but they do not distinguish between intra- and extravascular contrast and may be influenced by the acquisition parameters and other variables. Recently, a number of more complex, model-based approaches to quantifying subtle BBB leakage have been suggested, with applications in cognitive impairment (Montagne et al., 2015; Taheri et al., 2011a), healthy subjects (Cramer and Larsson, 2014), and in the normal-appearing tissue of patients with multiple sclerosis (Cramer et al., 2014), primary brain tumours (Larsson et al., 2009; Sourbron et al., 2009) and acute stroke (Thornhill et al., 2010), involving a range of acquisition and analysis methods.

In this work, we performed DCE-MRI in a large cohort of mild stroke patients with a range of small vessel disease features and severity. We aimed to determine the tracer kinetic modelling approach most suitable for assessing subtle BBB leakage using a data-driven approach, to determine its validity both in theory and experimentally and to obtain tracer kinetic parameters for normal-appearing tissues and lesions. We hypothesised that low temporal resolution data analysed using the Patlak model is appropriate for measuring low-level BBB permeability with high spatial resolution and brain coverage, and that scanner instability causes significant systematic errors in quantitative permeability measurements.

Materials and methods

Clinical cohort

Patients

We recruited 264 patients with first clinically evident mild (i.e., expected to be non-disabling) ischaemic stroke from the local stroke service. Included patients had to be over 18 years old, have a definite diagnosis of ischaemic stroke, be able to consent themselves, have an MRI scan at diagnosis and be medically stable enough to return for a DCE-MRI scan at between 1 and 3 months post-stroke and a follow-up at 1 year. All patients underwent clinical assessment by a stroke physician, diagnostic MR imaging and cognitive testing at presentation. An expert panel of stroke physicians and neuro-radiologists assessed each case in order to confirm the diagnosis of ischaemic stroke and classify the ischaemic stroke subtype. DCE-MRI was performed a minimum of 1 month after the stroke in order to avoid acute effects of the stroke on the local BBB. This study was approved by the Lothian Ethics of Medical Research Committee (REC 09/81101/54) and the NHS Lothian R + D Office (2009/W/NEU/14), and all patients gave written informed consent.

MRI

All imaging was performed on a 1.5 T MRI scanner (Signa HDxt, General Electric, Milwaukee, WI) using an 8-channel phased-array head coil. Diagnostic MR imaging at presentation included axial T_2-weighted (T2W; T_R/T_E = 6000/90 ms, 24 × 24 cm field of view (FoV), 384 × 384 Propeller acquisition, 1.5 averages, 28 × 5 mm slices, 1 mm slice gap), axial fluid-attenuated inversion recovery (FLAIR; $T_R/T_E/T_I$ = 9000/153/2200 ms, 24 × 24 cm FoV, 384 × 224 acquisition matrix, 28 × 5 mm slices, 1 mm slice gap), gradient echo (GRE; T_R/T_E = 800/15 ms, 20° flip angle, 24 × 18 cm FoV, 384 × 168 acquisition matrix, 2 averages, 28 × 5 mm slices, 1 mm slice gap) and sagittal 3D T_1-weighted imaging (T1W; inversion recovery-prepared spoiled gradient echo $T_R/T_E/T_I$ = 7.3/2.9/500 ms, 8° flip angle, 330 × 214.5 cm FoV, 256 × 146 acquisition matrix, 100 × 1.8 mm slices) and diffusion tensor MRI (single-shot echo-planar imaging with 30 diffusion directions (b = 1000 s/mm) and 2 × b_0 acquisitions, T_R/T_E = 7700/82 ms, 24 × 24 cm FoV, 128 × 128 acquisition matrix, 28 × 5 mm slices, 1 mm slice gap). DCE-MRI was performed at approximately 1 month after first presentation and consisted of a 3D T1W spoiled gradient echo sequence with T_R/T_E = 8.24/3.1 ms, 24 × 24 cm FOV, 256 × 192 acquisition matrix and 42 × 4 mm slices. Two pre-contrast acquisitions were carried out at flip angles of 2° and 12° to enable the calculation of pre-contrast longitudinal relaxation times (T_{10}). An intravenous bolus injection of 0.1 mmol/kg of gadoterate meglumine (Gd-DOTA, Dotarem, Guerbet, France) was administered simultaneously with the start of 20 acquisitions with 12° flip angle and a temporal resolution of 73 s, leading to a DCE-MRI duration of approximately 24 minutes.

Image processing

All image analysis was performed blind to clinical and permeability data. All structural and DCE-MRI images were aligned to the 12° pre-contrast image using rigid-body registration (FSL-FLIRT (Jenkinson and Smith, 2001)) in order to correct for bulk patient movement. We defined all small vessel features according to agreed STRIVE standards (Wardlaw et al., 2013b). We used a multispectral MRI data fusion and minimum variance quantisation technique (Valdés Hernández et al., 2010) for the segmentation of white matter hyperintensities (WMH) and normal-appearing white matter (NAWM). Please note that we use the term "WMH" to include hyperintensities in the white and subcortical grey matter. The resulting masks were manually refined and, separately, old stroke lesions and the index (i.e., which had led to patient entry to the study) stroke lesion boundaries were semi-automatically outlined on FLAIR images using the "Region of Interest" tool of Analyze 11.0™ (AnalyzeDirect, KS). Index/recent stroke lesions (RSL) were defined as the hyperintense regions identified on the diffusion weighted image including any corresponding signal changes on FLAIR, T2W and T1W images, associated with swelling or lack of ex vacuo effect, that followed a vascular territory. Stroke lesion masks were checked for accuracy by a neuroradiologist; all other tissue masks were checked visually for accuracy and manually edited as necessary. Subcortical/deep grey matter (DGM) masks were generated automatically by a software pipeline that used FSL-SUSAN (Smith and Brady, 1997) for noise reduction, an age-relevant brain template (Farrell et al., 2009), FSL-FLIRT for aligning the template to each image data set and FSL-FIRST (Patenaude et al., 2011) for extracting the subcortical structures, followed by manual boundary correction. To minimise any residual contamination of the DGM, the mask was eroded by one voxel. An example of a FLAIR image and segmentation masks is shown in Fig. 1.

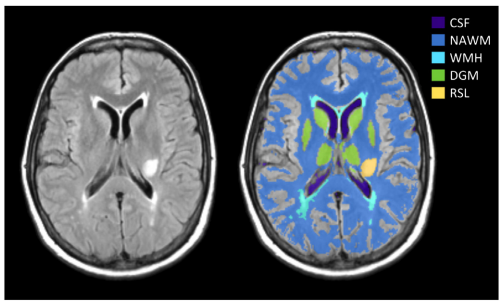

Fig. 1. Representative MRI data and tissue segmentation. FLAIR image (left) and tissue masks superimposed on FLAIR image (CSF: cerebrospinal fluid, NAWM: normal-appearing white matter, WMH: white matter hyperintensities, DGM: deep grey matter, RSL: recent stroke lesion).

DCE-MRI analysis

For each post-contrast time point i, we calculated the median signal intensity over all voxels for each tissue type (S_i). The signal enhancement E_i (representing the fractional signal increase above baseline) was then calculated as $E_i = (S_i - S_0) / S_0$, where S_0 is the signal intensity of the 12° pre-contrast acquisition. T_{10} was calculated based on the variable flip angle method by Brookes et al. (Brookes et al., 1999) using

$$\frac{1}{T_{10}} = \frac{1}{T_R} \ln\left(\frac{S_R \sin\alpha_b \cos\alpha_a - \sin\alpha_a \cos\alpha_b}{S_R \sin\alpha_b - \sin\alpha_a}\right), \quad (1)$$

where $S_R = S_a/S_b$, with S_a and S_b representing the signal intensities of the two pre-contrast acquisitions with flip angles $\alpha_a = 2°$ and $\alpha_b = 12°$. The contrast agent concentration C_i was then estimated by numerical solution of the following equation (Armitage et al., 2005):

$$E_i = \exp(-r_2 C_i T_E) \times \left[\frac{1-\exp(-P-Q)-\cos\alpha_b(\exp(P)-\exp(-2P-Q))}{1-\exp(P)-\cos\alpha_b(\exp(P-Q)-\exp(-2P-Q))}\right]-1, \quad (2)$$

where $P = T_R/T_{10}$, $Q = r_1 C_i T_R$, longitudinal and transverse contrast agent relaxivities r_1 and r_2 with $r_1/r_2 = 4.2/6.7\ s^{-1}mM^{-1}$ (Rohrer et al., 2005).

We obtained a vascular input function (VIF) from a voxel located on the superior sagittal sinus (SS) since partial volume effects and inflow artefact were reduced at that location compared with obtaining the AIF from a feeding artery (Lavini and Verhoeff, 2010); the delay between arterial and venous responses is expected to be very small compared with the temporal resolution (Sourbron et al., 2009; Sourbron and Buckley, 2012). Two observers, independently and blind to each other's results, manually selected a single voxel for VIF extraction, using a slice proximal to the basal ganglia structures and the lateral ventricles. This voxel was chosen to provide a high peak signal enhancement and smooth variation during the DCE-MRI time course. Where the observers selected different voxels, the voxel with the highest peak enhancement was chosen unless the signal curve was significantly noisier (a noise estimate was calculated as the sum of squared differences between the signal curve and a fitted bi-exponential curve). The calculated whole-blood concentration $C_b(t)$ measured in the SS was converted to plasma concentration using the formula $C_p(t) = C_b(t) / (1 - Hct)$, with the most recent available haematocrit measurement in the patient's clinical record (where no haematocrit measurement was available ($n = 3$) we assumed Hct = 0.45).

Tracer kinetic modelling

Tracer kinetic modelling aims to provide a link between the tissue signal enhancement and the physiological parameters, including the fractional plasma volume v_p, the fractional interstitial volume v_e and the permeability-surface area product PS. We fitted the following three models to the tissue concentration curves: (i) the modified Tofts model (Tofts et al., 1999), (ii) the Patlak model (Patlak et al., 1983) and (iii) the steady-state model (Sourbron and Buckley, 2013). A schematic overview of these models and their relationship with the more general two-compartment-exchange model (2CXM) (Sourbron and Buckley, 2013) is shown in Fig. 2.

The modified Tofts model describes a highly perfused ($F_p = \infty$) two-compartment tissue, considering bidirectional transport between the blood plasma and the extracellular extravascular space (EES). The concentration of contrast agent in the tissue is given by

$$C_t(t) = v_p C_p(t) + K^{Trans} \int_0^t C_p(\tau)\ \exp\left[-\frac{K^{Trans}(t-\tau)}{v_e}\right] d\tau, \quad (3)$$

where the volume transfer constant K^{Trans} represents the rate at which contrast agent is delivered to the EES per volume of tissue and contrast agent concentration of the VIF (PS denotes the same transfer constant with respect to capillary plasma concentration); in general, the measured K^{Trans} depends on both the plasma flow F_p and the permeability-surface area product PS; however, if the assumptions of the model are met (i.e., flow is high enough and the rate of contrast extravasation is low enough to ensure equal concentration in the arteries and capillary bed) and the measurement process is accurate, then $K^{Trans} \approx PS$ is a good approximation (Sourbron and Buckley, 2013). In the work that follows, we use the symbol K^{Trans} to indicate experimental or simulated measurements and PS to indicate the permeability-surface area product used to generate simulated data.

The Patlak model can be seen as a special case of the modified Tofts model, which ignores backflux from the EES into the blood plasma compartment. Consequently, it only allows for the estimation of the two parameters K^{Trans} and v_p:

$$C_t(t) = v_p C_p(t) + K^{Trans} \int_0^t C_p(\tau)\, d\tau. \quad (4)$$

If it is further assumed that there is no transfer of contrast to the EES, the one-parameter steady-state model (Sourbron and Buckley, 2013) is obtained:

$$C_t(t) = v_p C_p(t). \quad (5)$$

Model fitting was performed using in-house software programmed in MATLAB (MathWorks, Natick, MA, USA) by non-linear minimisation of the sum of squared residuals. All parameters were restricted to positive values, and $v_p + v_e$ was constrained to be less than or equal to 1; fitting was repeated 25 times with different initial values to reduce the probability of selecting local minima (Ahearn et al., 2005). The first three post-contrast time points of all contrast agent concentration curves were omitted from sum of squares calculation since the rapid concentration changes during and immediately after the first pass are not adequately resolved by the acquisition protocol and are not accurately modelled by any of the three nested models (Larsson et al.,

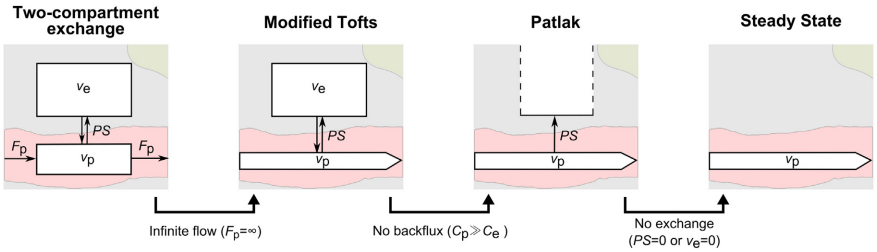

Fig. 2. Set of nested tracer kinetic models. Target parameters of DCE-MRI modelling are the fractional plasma volume v_p, the fractional interstitial volume v_e, the plasma flow F_p and the permeability-surface area product PS. The four models are related by a series of simplifying assumptions.

2009), resulting in biased parameter estimates that depend on F_p; this was confirmed by computer simulations.

Model comparison

The competing models were ranked according to the Akaike information criterion (AIC) (Akaike, 1974), which has been applied in DCE-MRI by several groups (Brix et al., 2009; Ingrisch et al., 2010). The AIC accounts for the trade-off between goodness-of-fit and model complexity, by combining the sum of squared errors SS_m with the number of free parameters K_m associated with the model m:

$$\mathrm{AIC}_m = N\ \ln\left(\frac{SS_m}{N}\right) + 2(K_m + 1), \tag{6}$$

where N denotes the number of data points. For small samples, i.e., $N/K_m < 40$ as in our case, the AIC should be extended with a second-order bias correction term (Burnham and Anderson, 2004), giving the small-sample version

$$\mathrm{AICc}_m = \mathrm{AIC}_m + \frac{2K_m(K_m+1)}{N-K_m-1}. \tag{7}$$

The Akaike weight AW_m describes the probability that the model m is best amongst a set of M models, following the equation (Luypaert et al., 2012)

$$\mathrm{AW}_m = \frac{\exp(-\Delta_m/2)}{\sum_{i=1}^{M}\exp(-\Delta_i/2)} \quad \text{with} \quad \Delta_m = \mathrm{AICc}_m - \min(\mathrm{AICc}_1, \ldots, \mathrm{AICc}_M). \tag{8}$$

For a statistical comparison between tracer kinetic parameters, Wilcoxon's signed rank test (since the data were in general not normally distributed) was used.

Healthy volunteers

To assess signal changes unrelated to the contrast agent, we recruited 15 healthy volunteers that underwent the same DCE-MRI protocol as applied in the clinical cohort but without administration of contrast agent. This study was approved by ACCORD Healthy Volunteer Research Ethics Committee (REC 14/HV/0001), and all volunteers gave written informed consent. We manually placed regions of interest (ROIs) in NAWM and DGM and calculated median signal intensity and enhancement curves for each ROI as described previously. Signal drift was calculated as the overall change in signal intensity per minute and is given as percentage of the time-averaged signal.

In addition to the dynamic sequence, we accurately measured T_1 using the inversion recovery method (Larsson et al., 1988) (IR) in $n = 7$ volunteers. For this purpose, we acquired 2D inversion recovery spin echo echo-planar imaging with multiple inversion times (IR-SE-EPI; $T_R/T_E = 10000/25.4$ ms, 24×24 cm FOV, 256×192 acquisition matrix, 1×4 mm slice, $T_I = [100, 340, 580, 820, 1060, 1300, 2000, 3000]$ ms). T_1 was calculated by fitting the following equation to the median ROI signal intensities (SI):

$$\mathrm{SI} = \left|A + B\ \exp\left(-\frac{T_I}{T_1}\right)\right| \tag{9}$$

T_1 was measured immediately before and after the non-contrast DCE-MRI acquisition, yielding the two measurements $T_{1,\mathrm{pre}}$ (before DCE-MRI) and $T_{1,\mathrm{post}}$ (after DCE-MRI). All values are given as mean and standard deviation.

Simulations

Numerical simulations were performed to systematically investigate model validity. First, we generated a high-resolution ($\Delta t = 0.1$ s) VIF using the function introduced by Parker et al., (2006), which consists of two Gaussians plus an exponential term modulated by a sigmoid function. In order to generate a simulated VIF with realistic first-pass behaviour that also matched our data at longer times post-injection, we introduced an additional exponential term resulting in the following function:

$$C_p(t) = \frac{1}{1-\mathrm{Hct}}\left(\sum n = 12\frac{A_n}{\sigma_n\sqrt{2\pi}}\exp\left(-\frac{(t-T_n)^2}{2\sigma_n^2}\right) + \frac{\sum n = 12\alpha_n\exp(-\beta_n t)}{1+\exp(-s(t-\tau))}\right). \tag{10}$$

For the Gaussian functions and sigmoid modulation, which describe the first and second pass of the VIF, we used the parameters given by Parker et al. (A_n, σ_n, T_n, s, τ). The parameters α_n and β_n were obtained by fitting Eq. (10) to the population-average VIF from our patient data (Supplementary Fig. 1). Simulated tissue concentration curves were generated by convolving this VIF with the impulse response function of the 2CXM, which has four free parameters: F_p, PS, v_p and v_e (Sourbron and Buckley, 2013). PS and v_p values were chosen to represent the range of values obtained in normal-appearing tissue, WMH and stroke lesions; v_e was chosen to be 0.2 (Syková and Nicholson, 2008) and F_p values between 10 and 50 ml/100 g/min were selected to represent typical values for NAWM, WMH and DGM (Brickman et al., 2009). Random noise was added to the curves to give a concentration contrast-to-noise ratio (CNR) similar to that observed in NAWM and DGM in our clinical cohort; the CNR was defined as the peak contrast agent concentration divided by a noise estimate, which was calculated as the standard deviation of the difference between the measured concentration curve and the Patlak model fit ($\mathrm{CNR} = \max[C_t(t)] / \mathrm{std}[C_t(t) - C_{\mathrm{Patlak}}(t)]$). Simulations were repeated, adding a signal drift to both the tissue curve and the VIF. The added drift was of similar magnitude to that found in the healthy volunteer cohort (values given in the results section). We then down-sampled the VIF and tissue concentration curves to the experimental temporal resolution ($\Delta t = 73$ s), and these were fitted to the Patlak model as described above. We also calculated the semi-quantitative parameters $\mathrm{AUC}_{\mathrm{norm}}$ (defined as the area under the tissue enhancement curve divided by the area under the vascular enhancement curve) and the late slope of the enhancement curve (obtained by linear regression of the tissue signal enhancement data). As for the clinical data, the first three post-contrast data points were neglected for calculating the sum of squared residuals during model fitting and for calculation of semi-quantitative parameters. The simulations were repeated 1000 times for every set of parameters to quantify the influence of noise.

Results

Patients

DCE-MRI was performed on average 38 days after first presentation and data suitable for analysis were obtained in 201 patients with mean age of 66.0 ± 11.5 years. Fig. 3 shows the cohort-averaged signal enhancement curves in NAWM, DGM, WMH, RSL and SS. All tissues show a signal enhancement of approximately 2%–8%, with abnormal tissues (WMH and RSL) showing a steeper increase in signal enhancement over time compared with normal-appearing tissues (WM and DGM).

An example of tracer kinetic model fitting for a single patient is shown in Fig. 4A; the Patlak and modified Tofts models provide good fits to the measured signal but the steady-state model is not sufficient to describe the data. This observation is confirmed by analysis of the Akaike weights (Fig. 4B), which shows that the Patlak model best

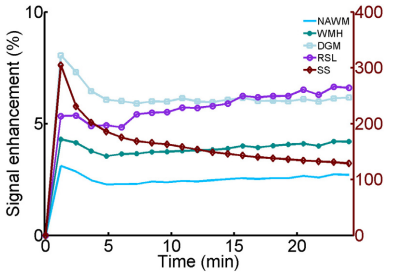

Fig. 3. Cohort average signal enhancement curves. Post-contrast signal enhancement versus time obtained from the median signal intensity in each tissue type (NAWM: normal-appearing white matter, WMH: white matter hyperintensities, DGM: deep grey matter, RSL: recent stroke lesion, SS: sagittal sinus) and averaged over all patients ($n = 201$). *Y*-axis scales for the tissue and sagittal sinus enhancement curves are shown on the left and right, respectively.

represents the data in most subjects for all tissue types, and was selected as the optimum model in 74%–78% of patients for the four tissues measured. The resulting Patlak parameters are listed in Table 1. A comparison between tissue types is shown in Fig. 5; all differences between tissue types were significant ($p < 0.001$) except for K^{Trans} in WMH and DGM and v_p in WMH and RSL. In particular, K^{Trans} and v_p are significantly higher in WMH compared to NAWM; K^{Trans} is significantly higher in RSL compared to all other tissues.

Healthy volunteers

DCE-MRI data without contrast administration was obtained in 15 healthy volunteers with mean age 31.4 ± 7.4 years. Fig. 6A shows the corresponding average signal enhancement curves in NAWM and DGM. The data show an approximately linear drift in signal intensity of 0.10 ± 0.06%/min in DGM and 0.06 ± 0.03%/min in NAWM. To investigate whether part of the drift can be explained by subtle physiological changes, we accurately measured T_1 before and after the DCE-MRI sequence in 8 of the volunteers. T_1 values were in line with previous literature (Vymazal et al., 1999) with $T_{1,pre}/T_{1,post} = 903 \pm 66$ ms / 892 ± 53 ms in DGM and $T_{1,pre}/T_{1,post} = 680 \pm 40$ ms / 674 ± 41 ms in NAWM (see Fig. 6B); the small decrease in T_1 over the period of the DCE-MRI acquisition was not statistically significant ($\Delta T_1 = -11 \pm 20$ ms in DGM and $\Delta T_1 = -7 \pm 14$ ms in NAWM).

Table 1
Fitted Patlak parameters. Values are shown as mean ± standard error in normal-appearing white matter (NAWM), white matter hyperintensities (WMH), deep grey matter (DGM) and recent stroke lesions (RSL). All differences between tissue types were significant ($p < 0.001$) except for K^{Trans} in WMH and DGM and v_p in WMH and RSL.

	K^{Trans} ($\times 10^{-4}$ min^{-1})	v_p ($\times 10^{-2}$)
NAWM	2.96 ± 0.12	0.58 ± 0.02
WMH	3.96 ± 0.13	0.80 ± 0.04
DGM	3.91 ± 0.12	1.21 ± 0.03
RSL	5.77 ± 0.41	0.80 ± 0.05

Simulations

The results of simulations performed to determine the validity of the Patlak model are shown in Fig. 7. These compare fitted parameters with the "true" parameters used to generate synthetic signal-time curves using the 2CXM model. All simulations are based on a CNR of 8 and a T_1 of 969 ms, corresponding to typical NAWM values observed in our patient cohort. In the absence of drift (Fig. 6A), $K^{Trans} \approx PS$ and v_p is accurately estimated when *PS* is low, despite very low temporal resolution and the simplifying assumptions of the Patlak model. At higher *PS* values, K^{Trans} underestimates *PS*, and v_p is slightly overestimated as a result of back-diffusion, which is neglected in the Patlak model. The model is robust to differences in blood flow, with low flow resulting in a slightly greater underestimation of *PS*. To investigate the effect of scanner drift, we included a 0.08%/min signal drift (comparable to that measured in the healthy volunteer group) in the simulations. This leads to systematic underestimation of v_p and overestimation of leakage (Fig. 6B), but K^{Trans} and v_p remain approximately linear functions of the specified values, largely independent of plasma flow and of one another. The magnitude of the systematic error introduced by signal drift is T_1 dependent, with an estimated range across the tissues of approximately $2.2–3.2 \times 10^{-4}$ min^{-1} for K^{Trans} and -2.4 to -1.6×10^{-3} for v_p.

For comparison, Fig. 8 shows the relationship between *PS* and v_p, and the semi-quantitative parameters AUC_{norm} and the late slope of the signal enhancement curve. AUC_{norm} correlates strongly with v_p but is also influenced by *PS*. Similarly, the enhancement slope correlates with *PS* but is not independent of v_p.

Discussion

Analysis of patient DCE-MRI data using the Akaike information criterion revealed the Patlak model to be the most appropriate of the three models for quantification of subtle BBB disruption, in line with our hypothesis. The steady-state model does not adequately fit the data;

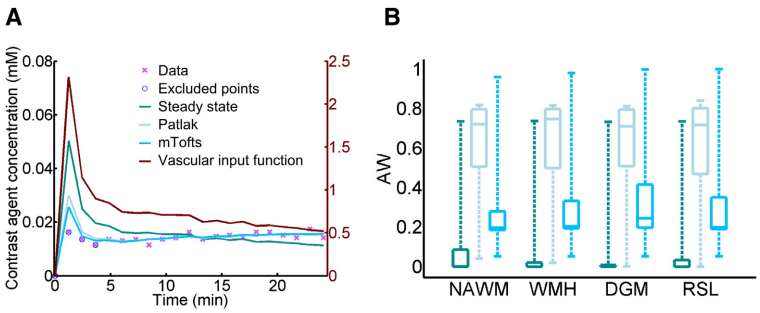

Fig. 4. Comparison of model fits to the patient data. (A) Example concentration–time curve for normal-appearing white matter in a single patient. In general, the steady-state model does not fit the data well; while both the Patlak and modified Tofts (mTofts) models typically fit the data similarly well, the Patlak model has a higher Akaike weight (AW) than the modified Tofts model in most cases due to the lower number of free parameters. (B) Comparison of AW for the three models in normal-appearing white matter (NAWM), white matter hyperintensities (WMH), deep grey matter (DGM) and recent stroke lesions (RSL). In most patients, the Patlak model had the highest AW for all tissue types (legend as in A).

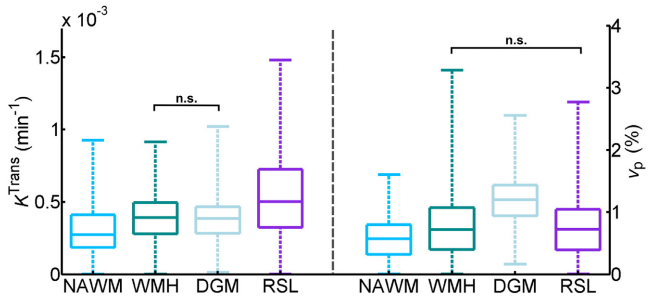

Fig. 5. Comparison of fitted Patlak parameters between tissue types. Box plots showing the distribution of K^{Trans} (left) and v_p (right) in normal-appearing white matter (NAWM), white matter hyperintensities (WMH), deep grey matter (DGM) and recent stroke lesions (RSL). Brackets with n.s. indicate non-significant differences with $p > 0.5$; all other differences between tissue types are significant with $p < 0.001$ (brackets omitted for clarity).

while both the Patlak and modified Tofts models fit the data similarly well, the simpler Patlak model does so using fewer free parameters and is therefore selected. The additional complexity of the modified Tofts model results in over-fitting in the low-permeability regime, consistent with a previous report regarding the behaviour of Tofts parameters in a smaller study of healthy volunteers and MS patients (Cramer and Larsson, 2014). Application of the Patlak model in situations of subtle BBB leakage was further supported by the numerical simulations, confirming that appropriate estimates of PS ($\approx K^{Trans}$), and v_p can be obtained independent of cerebral blood flow (CBF) and despite the use of a temporal resolution much lower than is typically employed in DCE-MRI (Heye et al., 2014); this was consistent with simulations performed by Larsson et al. for a shorter, high temporal resolution acquisition (Larsson et al., 2009). A consequence of this finding is that DCE-MRI protocols for investigating diffuse subtle BBB pathology may benefit from prioritising, as here, spatial resolution, whole-brain coverage and contrast-to-noise ratio over sampling rate to allow for analysis of subtle leakage across all brain structures. In contrast to the fitted tracer kinetic parameters, we found semi-quantitative parameters to reflect a combination of underlying tissue properties.

In our cohort of mild stroke patients, K^{Trans} was greater in WMH than in NAWM. This is consistent with some pathology studies (e.g., Tomimoto et al., 1996; Wharton et al., 2015; Young et al., 2008) and other DCE-MRI studies that reported increased BBB disruption in areas of WMH compared to NAWM (Hanyu et al., 2002; Taheri et al., 2011a; Topakian et al., 2010). In contrast, a recent study by Huisa et al. found increased BBB disruption in NAWM surrounding the WMH rather than in the WMH themselves (Huisa et al., 2015), while others failed to detect any BBB leakage in or around WMH (Wahlund and Bronge, 2000). The exact role of BBB breakdown in SVD pathology remains to be defined. K^{Trans} was greater still in the recent stroke lesion, comparable to findings of Thornhill et al. in acute-phase stroke lesions (Thornhill et al., 2010) and known tissue changes from many pathology examinations. K^{Trans} was greater in GM than in NAWM, which may partly reflect the higher vessel density and vascular surface area of GM (Schlageter et al., 1999), consistent with the higher measured blood plasma volume. WMH, which are often regarded as "ischaemic" lesions and might therefore be expected to have reduced plasma volume, had greater v_p than NAWM. This finding is only partly explained by the T_1 difference between the tissues, which results in a predicted greater underestimation of v_p in NAWM due to scanner drift. Assumptions such as tissue-independent relaxivity and water exchange rates may also influence the values. Another possible explanation is that a few WMH are found in tissue that was originally subcortical grey matter, especially in the head of the caudate nucleus, where baseline blood volume is likely to be higher. Very few studies have measured cerebral blood volume (CBV) and CBF in WMH themselves, as opposed to general CBV and CBF in patients with WMH. While some studies using DSC-MRI have reported reduced CBV in WMH, e.g., Sachdev et al. (2004), Marstrand et al. (2002) found reduced CBF but similar CBV in WMH compared with NAWM. Although DCE-MRI is a more quantitative marker of microvascular properties than DSC-MRI, previous studies applying DCE-MRI in SVD have not reported v_p values for WMH to the best of our knowledge. We suggest therefore that future studies should assess CBF and CBV in WMH as well as normal tissues so as to resolve this issue.

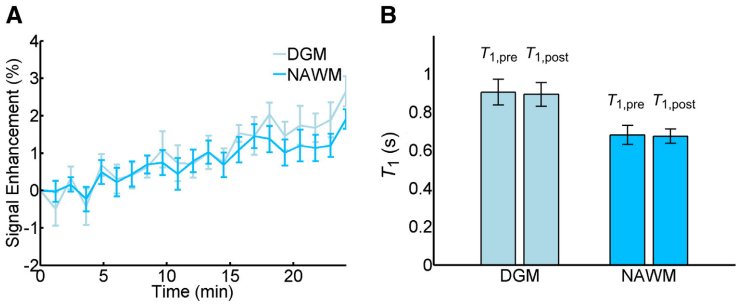

Fig. 6. Contrast-free measurements in healthy volunteers. (A) Average signal enhancement curves ($n = 15$) in normal-appearing white matter (NAWM) and deep grey matter (DGM), showing a drift in signal intensity; error bars indicate the mean ± standard error. (B) T_1 measurements obtained before and after the DCE-MRI sequence using the inversion recovery method ($n = 7$); error bars indicate the mean ± 1.96 standard deviations.

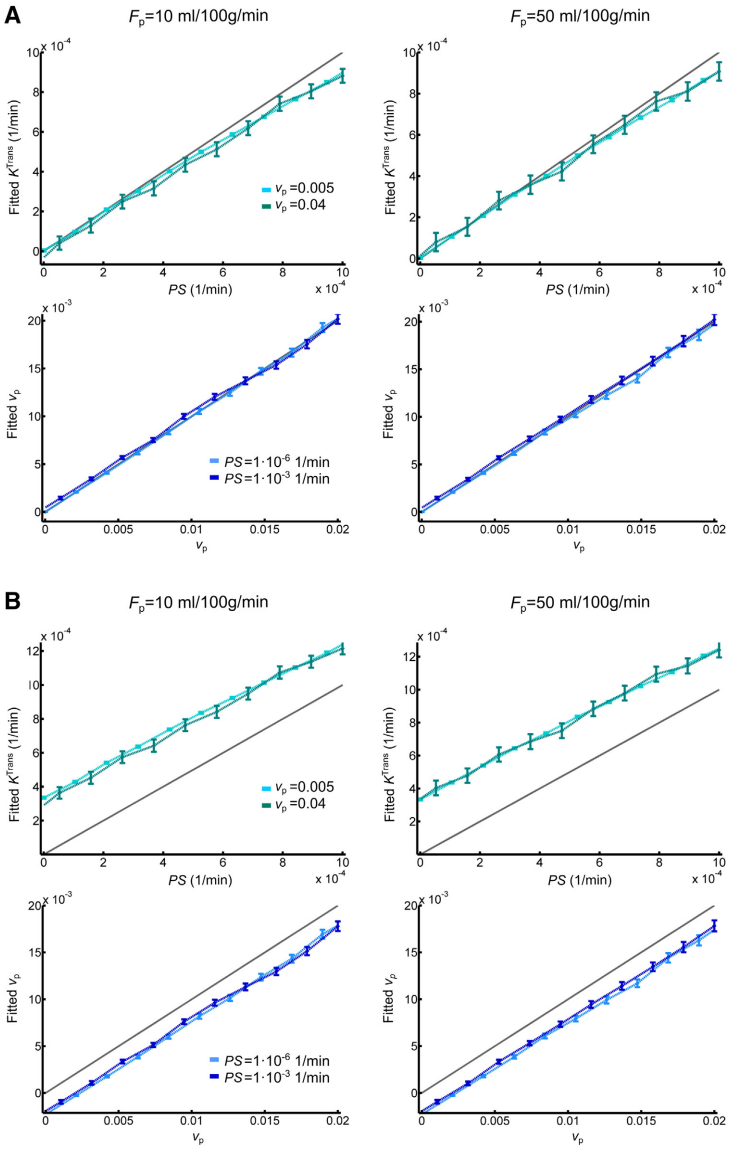

Fig. 7. Simulated accuracy of Patlak parameters. (A) Relationship of permeability-surface area product PS (top row) and blood plasma volume v_p (bottom row) values, with corresponding fitted Patlak parameters. Results are shown for two different blood plasma flow (F_p), PS and v_p values. For all simulations, the interstitial volume was set to 0.2. Error bars indicate the mean ± 1.96 standard deviations; the grey line represents the identity line. (B) As above but including a 0.08%/min signal drift.

In subjects who did not receive contrast, we observed a signal change of approximately 0.08%/min. This level of instability is unlikely to be problematic in typical DCE-MRI applications with larger, more rapid signal enhancements over shorter acquisition times. However, our simulations show that the drift is predicted to cause a substantial upward shift of K^{Trans} measurements in the low-permeability regime, which would account for some of the apparent leakage seen in normal-appearing white matter and other tissues. As a result, attempts to quantify low levels of permeability should be interpreted with caution, unless information regarding scanner drift and its likely effect on the values are available. This finding is consistent with recently reported simulation results (Barnes et al., 2015) and may partly account

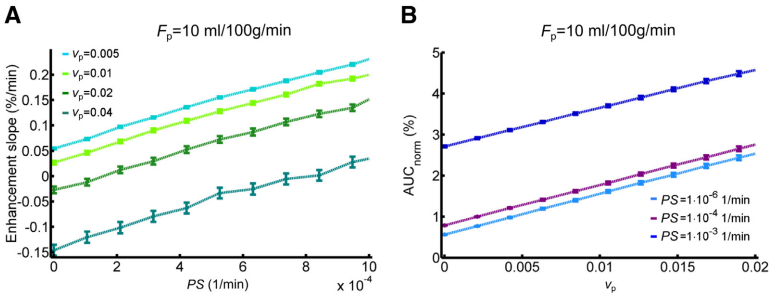

Fig. 8. Relationship between simulated semi-quantitative parameters and tissue properties. (A) Relationship between the signal enhancement slope and the permeability-surface area product *PS* for different blood plasma volumes v_p. (B) Relationship between normalised area under the signal enhancement curve and v_p for different *PS* values. A signal drift of 0.08%/min was added to the synthetic data; results are shown for blood plasma flow $F_p = 10$ ml/100 g/min and interstitial volume $v_e = 0.2$.

for the wide variation in K^{Trans} values reported in the literature for normal-appearing brain tissue (Cramer et al., 2014; Larsson et al., 2009; Montagne et al., 2015; Sourbron et al., 2009; Taheri et al., 2011a, 2011b; Thornhill et al., 2010), which span three orders of magnitude and include negative values (Sourbron et al., 2009). Signal drift measurements are rarely reported in the DCE-MRI literature, an exception being Cramer et al. who reported a drift at 3 T (1%–3% over 15 minutes) comparable to our measurements at 1.5 T (Cramer and Larsson, 2014). The drift behaviour of our scanner was also within the range of values obtained in a multi-centre survey of fMRI quality assurance parameters, which concluded that "stable scanners generally average around 1.0% [signal drift over 6.7 minutes] or less" (Friedman and Glover, 2006). The influence of signal drift in fMRI is much less severe than here since it typically has a lower frequency than the task-related signal change, is suppressed using a high-pass filter and the scans are quicker; in DCE-MRI, it is harder to distinguish between drift and contrast enhancement as both occur on similar timescales. It is worth noting that DCE-MRI methods consisting of repeated T_1 measurements (e.g., Taheri et al., 2011b) should largely self-compensate for signal drifts of instrumental origin and, depending on the pulse sequence used, changes in the radiofrequency field strength. However, the causes of signal drift are not well-understood and may also be influenced by subtle biological changes (Lowe and Russell, 1999), consistent with our (non-significant) observation of T_1 change and by a previous report of tissue-dependent drift on the same scanner as in the present work (Armitage et al., 2011). The effect should also be mitigated by optimising the protocol for sensitivity to changes in contrast agent concentration.

Despite the potentially confounding influence of drift, our simulations indicate that K^{Trans} and v_p estimates remain approximately linear independent functions of the permeability-surface area product and plasma volume, respectively. They provide a valuable if relative indication of blood–brain barrier integrity and blood plasma volume for applications in well-designed studies with appropriate control groups and statistical correction for confounds; such quantities remain easier to interpret than semi-quantitative measurements (Budde et al., 2012).

This and other DCE-MRI studies are limited by additional sources of error, which have been described elsewhere. For example, the variable flip angle method (also known as "DESPOT1") used here and in many other studies (Homer and Beevers, 1985) has the advantage of yielding T_1 maps with whole-brain coverage and adequate SNR within an acceptable acquisition time. However, it is sensitive to flip angle variations across the brain, i.e., deviations of the actual from the operator defined flip angles caused by B_1 field inhomogeneities and the slab excitation profile of the radiofrequency pulse, resulting in errors in T_{10} and other parameters (Armitage et al., 2011; Schabel and Parker, 2010). At 1.5 T and using a radiofrequency transmit volume coil, such flip angle variations should be limited and reasonably consistent within the cohort. In future studies, especially on scanners with higher field strength, it would be prudent to either employ methods that estimate and/or correct for flip angle errors, such as DESPOT1-HIFI (Deoni, 2007). Look–Locker-based methods such as TAPIR (Shah et al., 2001) also provide an alternative approach for T_{10} measurement, permitting faster sampling of the magnetization recovery curve than the conventional inversion recovery method. The sensitivity of these methods to flip angle variations is reduced since the flip angle can be modelled as an unknown parameter during fitting of the inversion recovery curve. It should also be recognised that all tracer kinetic models necessarily make assumptions regarding tissue structure and the transport of blood plasma and contrast agent. For example, as the low temporal resolution of our acquisition protocol does not permit estimation of blood flow, we selected three models that assume the tissue to be highly perfused (i.e., $F_p = \infty$). Although this is not the case in real tissues, it remains a good approximation when the blood flow is sufficient to equalise the arterial and capillary concentrations (requiring $PS \ll F_p$) (Sourbron and Buckley, 2011), with our simulations confirming the validity of this approximation; the choice of models should also be seen in relation to temporal resolution, which in this case is much longer than the transit time of the tissue blood compartment. It should also be emphasised that while *PS* (or K^{Trans}) is commonly used as a marker of "permeability," it is equally influenced by the capillary surface area, which will depend on the anatomy and pathology of micro vessels. Future studies should try to determine vessel density and size so as to include realistic estimates of capillary endothelial surface area in the permeability calculations. Furthermore, a disadvantage of low temporal resolution acquisition is that cerebral blood flow cannot be determined in addition to v_p and *PS*; where knowledge of CBF is required and temporal resolution is adequate, the uptake model may be substituted for the Patlak model in low-permeability tissue (Ingrisch et al., 2012; Sourbron et al., 2009). Finally, the DCE-MRI data in this study has been analysed at the level of ROIs rather than voxels. This approach was selected due to the low contrast-to-noise ratio in single voxels and due to the influence of artefacts (e.g., Gibbs ringing and motion), which, while typically at the level of only a few percent, have a similar magnitude to the small contrast-induced signal *changes* and therefore have a disproportionate influence on voxel-wise pharmacokinetic parameters (Supplementary Fig. 2). Averaging over an ROI reduces the influence of noise and artefact, enabling more robust measurement of background BBB status, especially in normal-appearing tissue where signal changes are small. However, a limitation of this approach is that it does not allow the detection of local variation in BBB function.

In conclusion, the Patlak model is a simple and appropriate method for measuring low-level BBB leakage, and our results, based on a large sample of mild stroke patients, justify its emerging popularity in the

study of disorders involving subtle BBB disruption and of healthy-appearing tissue (Cramer et al., 2014; Montagne et al., 2015; Taheri et al., 2011a). The model is reasonably robust to the assumptions of high blood flow and negligible back-diffusion, but the resulting tracer kinetic parameters are influenced by signal drift particularly at low-permeability states. It is therefore important to optimise study MRI protocols for measurement of low-level permeability and to assess the magnitude and consistency of drift in future studies by performing non-contrast experiments in volunteers as done here or in a subset of patients (Armitage et al., 2011; Cramer and Larsson, 2014) and simulations to predict the likely effect on study findings. These considerations are particularly critical for multi-centre studies.

Supplementary data to this article can be found online at http://dx.doi.org/10.1016/j.neuroimage.2015.10.018.

Acknowledgements

This work was funded by Wellcome Trust (SDM, recruitment and MRI scanning costs; grant 088134/Z/09/A), Row Fogo Charitable Trust (MCVH, AKH), Age UK (SMM), NHS Lothian Research and Development Office (MJT), Scottish Funding Council and the Chief Scientist Office of Scotland for funding the Scottish Imaging Network: A Platform for Scientific Excellence ("SINAPSE"; JMW, radiography staff).

We thank K. Shuler for providing expert administrative support during data collection, analyses and manuscript preparation.

References

Ahearn, T.S., Staff, R.T., Redpath, T.W., Semple, S.I.K., 2005. The use of the Levenberg–Marquardt curve-fitting algorithm in pharmacokinetic modelling of DCE-MRI data. Phys. Med. Biol. 50, N85–N92. http://dx.doi.org/10.1088/0031-9155/50/9/N02.

Akaike, H., 1974. A new look at the statistical model identification. IEEE Trans. Autom. Control 19, 716–723. http://dx.doi.org/10.1109/TAC.1974.1100705.

Armitage, P., Behrenbruch, C., Brady, M., Moore, N., 2005. Extracting and visualizing physiological parameters using dynamic contrast-enhanced magnetic resonance imaging of the breast. Med. Image Anal. 9, 315–329. http://dx.doi.org/10.1016/j.media.2005.01.001.

Armitage, P.A., Farrall, A.J., Carpenter, T.K., Doubal, F.N., Wardlaw, J.M., 2011. Use of dynamic contrast-enhanced MRI to measure subtle blood–brain barrier abnormalities. Magn. Reson. Imaging 29, 305–314. http://dx.doi.org/10.1016/j.mri.2010.09.002.

Barnes, S.R., Ng, T.S.C., Montagne, A., Law, M., Zlokovic, B.V., Jacobs, R.E., 2015. Optimal acquisition and modeling parameters for accurate assessment of low K trans blood–brain barrier permeability using dynamic contrast-enhanced MRI. Magn. Reson. Med. http://dx.doi.org/10.1002/mrm.25793.

Brickman, A.M., Zahra, A., Muraskin, J., Steffener, J., Holland, C.M., Habeck, C., Borogovac, A., Ramos, M.A., Brown, T.R., Asllani, I., Stern, Y., 2009. Reduction in cerebral blood flow in areas appearing as white matter hyperintensities on magnetic resonance imaging. Psychiatry Res. 172, 117–120. http://dx.doi.org/10.1016/j.pscychresns.2008.11.006.

Brix, G., Zwick, S., Kiessling, F., Griebel, J., 2009. Pharmacokinetic analysis of tissue microcirculation using nested models: multimodel inference and parameter identifiability. Med. Phys. 36, 2923. http://dx.doi.org/10.1118/1.3147145.

Brookes, J.A., Redpath, T.W., Gilbert, F.J., Murray, A.D., Staff, R.T., 1999. Accuracy of T1 measurement in dynamic contrast-enhanced breast MRI using two- and three-dimensional variable flip angle fast low-angle shot. J. Magn. Reson. Imaging 9, 163–171.

Budde, M.D., Gold, E., Jordan, E.K., Frank, J.A., 2012. Differential microstructure and physiology of brain and bone metastases in a rat breast cancer model by diffusion and dynamic contrast enhanced MRI. Clin. Exp. Metastasis 29, 51–62. http://dx.doi.org/10.1007/s10585-011-9428-2.

Burnham, K.P., Anderson, D.R., 2004. Multimodel inference: understanding AIC and BIC in model selection. Sociol. Methods Res. 33, 261–304. http://dx.doi.org/10.1177/0049124104268644.

Cramer, S.P., Larsson, H.B.W., 2014. Accurate determination of blood–brain barrier permeability using dynamic contrast-enhanced T1-weighted MRI: a simulation and in vivo study on healthy subjects and multiple sclerosis patients. J. Cereb. Blood Flow Metab. 34, 1655–1665. http://dx.doi.org/10.1038/jcbfm.2014.126.

Cramer, S.P., Simonsen, H., Frederiksen, J.L., Rostrup, E., Larsson, H.B.W., 2014. Abnormal blood–brain barrier permeability in normal appearing white matter in multiple sclerosis investigated by MRI. NeuroImage Clin. 4, 182–189. http://dx.doi.org/10.1016/j.nicl.2013.12.001.

Deoni, S.C.L., 2007. High-resolution T1 mapping of the brain at 3 T with driven equilibrium single pulse observation of T1 with high-speed incorporation of RF field inhomogeneities (DESPOT1-HIFI). J. Magn. Reson. Imaging 26, 1106–1111. http://dx.doi.org/10.1002/jmri.21130.

Farrall, A.J., Wardlaw, J.M., 2009. Blood–brain barrier: ageing and microvascular disease—systematic review and meta-analysis. Neurobiol. Aging 30, 337–352. http://dx.doi.org/10.1016/j.neurobiolaging.2007.07.015.

Farrell, C., Chappell, F., Armitage, P.A., Keston, P., Maclullich, A., Shenkin, S., Wardlaw, J.M., 2009. Development and initial testing of normal reference MR images for the brain at ages 65–70 and 75–80 years. Eur. Radiol. 19, 177–183. http://dx.doi.org/10.1007/s00330-008-1119-2.

Friedman, L., Glover, G.H., 2006. Report on a multicenter fMRI quality assurance protocol. J. Magn. Reson. Imaging 23, 827–839. http://dx.doi.org/10.1002/jmri.20583.

Hanyu, H., Asano, T., Tanaka, Y., Iwamoto, T., Takasaki, M., Abe, K., 2002. Increased blood–brain barrier permeability in white matter lesions of Binswanger's disease evaluated by contrast-enhanced MRI. Dement. Geriatr. Cogn. Disord. 14, 1–6. http://dx.doi.org/10.1159/000058326.

Heye, A.K., Culling, R.D., Valdés Hernández, M.D.C., Thrippleton, M.J., Wardlaw, J.M., 2014. Assessment of blood–brain barrier disruption using dynamic contrast-enhanced MRI. A systematic review. NeuroImage Clin. 6, 262–274. http://dx.doi.org/10.1016/j.nicl.2014.09.002.

Homer, J., Beevers, M.S., 1985. Driven-equilibrium single-pulse observation of T1 relaxation. A reevaluation of a rapid "new" method for determining NMR spin-lattice relaxation times. J. Magn. Reson. 63, 287–297. http://dx.doi.org/10.1016/0022-2364(85)90318-X.

Huisa, B.N., Caprihan, A., Thompson, J., Prestopnik, J., Qualls, C.R., Rosenberg, G.A., 2015. Long-term blood–brain barrier permeability changes in Binswanger disease. Stroke 46, 2413–2418. http://dx.doi.org/10.1161/STROKEAHA.115.009589.

Iadecola, C., 2013. The pathobiology of vascular dementia. Neuron 80, 844–866. http://dx.doi.org/10.1016/j.neuron.2013.10.008.

Ingrisch, M., Sourbron, S., Reiser, M., Peller, M., 2010. Model selection in dynamic contrast enhanced MRI: the Akaike information criterion. World Congr. Med. Phys. Biomed. Eng. 356–358. http://dx.doi.org/10.1007/978-3-642-03882-2-94.

Ingrisch, M., Sourbron, S., Morhard, D., Ertl-Wagner, B., Ku, T., 2012. Quantification of perfusion and permeability in multiple sclerosis. Investig. Radiol. 47, 252–258.

Jenkinson, M., Smith, S., 2001. A global optimisation method for robust affine registration of brain images. Med. Image Anal. 5, 143–156.

Larsson, H.B.W., Frederiksen, J., Kjær, L., Henriksen, O., Olesen, J., 1988. In vivo determination ofT1 andT2 in the brain of patients with severe but stable multiple sclerosis. Magn. Reson. Med. 7, 43–55. http://dx.doi.org/10.1002/mrm.1910070106.

Larsson, H.B.W., Courivaud, F., Rostrup, E., Hansen, A.E., 2009. Measurement of brain perfusion, blood volume, and blood–brain barrier permeability, using dynamic contrast-enhanced T(1)-weighted MRI at 3 tesla. Magn. Reson. Med. 62, 1270–1281. http://dx.doi.org/10.1002/mrm.22136.

Lavini, C., Verhoeff, J.J.C., 2010. Reproducibility of the gadolinium concentration measurements and of the fitting parameters of the vascular input function in the superior sagittal sinus in a patient population. Magn. Reson. Imaging 28, 1420–1430. http://dx.doi.org/10.1016/j.mri.2010.06.017.

Lowe, M.J., Russell, D.P., 1999. Treatment of baseline drifts in fMRI time series analysis. J. Comput. Assist. Tomogr. 23, 463–473.

Luypaert, R., Ingrisch, M., Sourbron, S., de Mey, J., 2012. The Akaike information criterion in DCE-MRI: does it improve the haemodynamic parameter estimates? Phys. Med. Biol. 57, 3609–3628. http://dx.doi.org/10.1088/0031-9155/57/11/3609.

Marstrand, J.R., Garde, E., Rostrup, E., Ring, P., Rosenbaum, S., Mortensen, E.L., Larsson, H.B.W., 2002. Cerebral perfusion and cerebrovascular reactivity are reduced in white matter hyperintensities. Stroke 33, 972–976. http://dx.doi.org/10.1161/01.STR.0000012808.81667.4B.

Montagne, A., Barnes, S.R., Law, M., Zlokovic, B.V., Montagne, A., Barnes, S.R., Sweeney, M.D., Halliday, M.R., Sagare, A.P., Zhao, Z., Toga, A.W., Jacobs, R.E., Liu, C.Y., Amezcua, L., Harrington, M.G., Chui, H.C., 2015. Blood–brain barrier breakdown in the aging human report blood–brain barrier breakdown in the aging human hippocampus. Neuron 85, 296–302. http://dx.doi.org/10.1016/j.neuron.2014.12.032.

Parker, G.J.M., Roberts, C., Macdonald, A., Buonaccorsi, G.A., Cheung, S., Buckley, D.L., Jackson, A., Watson, Y., Davies, K., Jayson, G.C., 2006. Experimentally-derived functional form for a population-averaged high-temporal-resolution arterial input function for dynamic contrast-enhanced MRI. Magn. Reson. Med. 56, 993–1000. http://dx.doi.org/10.1002/mrm.21066.

Patenaude, B., Smith, S.M., Kennedy, D.N., Jenkinson, M., 2011. A Bayesian model of shape and appearance for subcortical brain segmentation. NeuroImage 56, 907–922. http://dx.doi.org/10.1016/j.neuroimage.2011.02.046.

Patlak, C.S., Blasberg, R.G., Fenstermacher, J.D., 1983. Graphical evaluation of blood-to-brain transfer constants from multiple-time uptake data. J. Cereb. Blood Flow Metab. 3, 1–7.

Rohrer, M., Bauer, H., Mintorovitch, J., Requardt, M., Weinmann, H.-J., 2005. Comparison of magnetic properties of MRI contrast media solutions at different magnetic field strengths. Investig. Radiol. 40, 715–724.

Sachdev, P., Wen, W., Shnier, R., Brodaty, H., 2004. Cerebral blood volume in T2-weighted white matter hyperintensities using exogenous contrast based perfusion MRI. J. Neuropsychiatry Clin. Neurosci. 16, 83–92.

Schabel, M.C., Parker, D.L., 2010. Uncertainty and bias in contrast concentration measurements using spoiled gradient echo pulse sequences. Phys. Med. Biol. 53, 2345–2373. http://dx.doi.org/10.1088/0031-9155/53/9/010.Uncertainty.

Schlageter, K.E., Molnar, P., Lapin, G.D., Groothuis, D.R., 1999. Microvessel organization and structure in experimental brain tumors: microvessel populations with distinctive structural and functional properties. Microvasc. Res. 58, 312–328. http://dx.doi.org/10.1006/mvre.1999.2188.

Shah, N.J., Zaitsev, M., Steinhoff, S., Zilles, K., 2001. A new method for fast multislice T(1) mapping. NeuroImage 14, 1175–1185. http://dx.doi.org/10.1006/nimg.2001.0886.

Smith, S.M., Brady, J.M., 1997. SUSAN—a new approach to low level image processing. Int. J. Comput. Vis. 23, 45–78. http://dx.doi.org/10.1023/A:1007963824710.

Sourbron, S.P., Buckley, D.L., 2011. On the scope and interpretation of the Tofts models for DCE-MRI. Magn. Reson. Med. 66, 735–745. http://dx.doi.org/10.1002/mrm.22861.

Sourbron, S.P., Buckley, D.L., 2012. Tracer kinetic modelling in MRI: estimating perfusion and capillary permeability. Phys. Med. Biol. 57, R1–R33. http://dx.doi.org/10.1088/0031-9155/57/2/R1.

Sourbron, S.P., Buckley, D.L., 2013. Classic models for dynamic contrast-enhanced MRI. NMR Biomed. 26, 1004–1027. http://dx.doi.org/10.1002/nbm.2940.

Sourbron, S., Ingrisch, M., Siefert, A., Reiser, M., Herrmann, K., 2009. Quantification of cerebral blood flow, cerebral blood volume, and blood–brain-barrier leakage with DCE-MRI. Magn. Reson. Med. 62, 205–217. http://dx.doi.org/10.1002/mrm.22005.

Syková, E., Nicholson, C., 2008. Diffusion in brain extracellular space. Physiol. Rev. 88, 1277–1340. http://dx.doi.org/10.1152/physrev.00027.2007.

Taheri, S., Gasparovic, C., Huisa, B.N., Adair, J.C., Edmonds, E., Prestopnik, J., Grossetete, M., Shah, N.J., Wills, J., Qualls, C., Rosenberg, G.A., 2011a. Blood–brain barrier permeability abnormalities in vascular cognitive impairment. Stroke 42, 2158–2163. http://dx.doi.org/10.1161/STROKEAHA.110.611731.

Taheri, S., Gasparovic, C., Shah, N.J., Rosenberg, G.A., 2011b. Quantitative measurement of blood–brain barrier permeability in human using dynamic contrast-enhanced MRI with fast T1 mapping. Magn. Reson. Med. 65, 1036–1042. http://dx.doi.org/10.1002/mrm.22686.

Thornhill, R.E., Chen, S., Rammo, W., Mikulis, D.J., Kassner, A., 2010. Contrast-enhanced MR imaging in acute ischemic stroke: T2* measures of blood–brain barrier permeability and their relationship to T1 estimates and hemorrhagic transformation. Am. J. Neuroradiol. 31, 1015–1022. http://dx.doi.org/10.3174/ajnr.A2003.

Tofts, P.S., Brix, G., Buckley, D.L., Evelhoch, J.L., Henderson, E., Knopp, M.V., Larsson, H.B.W., Lee, T., Mayr, N.A., Parker, G.J.M., Port, R.E., Taylor, J., Weisskoff, R.M., 1999. Contrast-enhanced T1-weighted MRI of a diffusable tracer: standardized quantities and symbols. J. Magn. Reson. Imaging 232, 223–232.

Tomimoto, H., Akiguchi, I., Suenaga, T., Nishimura, M., Wakita, H., Nakamura, S., Kimura, J., 1996. Alterations of the blood–brain barrier and glial cells in white-matter lesions in cerebrovascular and Alzheimer's disease patients. Stroke 27, 2069–2074.

Topakian, R., Barrick, T.R., Howe, F.A., Markus, H.S., 2010. Blood–brain barrier permeability is increased in normal-appearing white matter in patients with lacunar stroke and leucoaraiosis. J. Neurol. Neurosurg. Psychiatry 81, 192–197. http://dx.doi.org/10.1136/jnnp.2009.172072.

Valdés Hernández, M. del C., Ferguson, K.J., Chappell, F.M., Wardlaw, J.M., 2010. New multispectral MRI data fusion technique for white matter lesion segmentation: method and comparison with thresholding in FLAIR images. Eur. Radiol. 20, 1684–1691. http://dx.doi.org/10.1007/s00330-010-1718-6.

Vymazal, J., Righini, A., Brooks, R.A., Canesi, M., Mariani, C., Leonardi, M., Pezzoli, G., 1999. T1 and T2 in the brain of healthy subjects, patients with Parkinson disease, and patients with multiple system atrophy: relation to iron content. Radiology 211, 489–495. http://dx.doi.org/10.1148/radiology.211.2.r99ma53489.

Wahlund, L.-O., Bronge, L., 2000. Contrast-enhanced MRI of white matter lesions in patients with blood–brain barrier dysfunction. Ann. N. Y. Acad. Sci. 903, 477–481.

Wardlaw, J.M., Farrall, A., Armitage, P.A., Carpenter, T., Chappell, F., Doubal, F., Chowdhury, D., Cvoro, V., Dennis, M.S., 2008. Changes in background blood–brain barrier integrity between lacunar and cortical ischemic stroke subtypes. Stroke 39, 1327–1332. http://dx.doi.org/10.1161/STROKEAHA.107.500124.

Wardlaw, J.M., Smith, C., Dichgans, M., 2013a. Mechanisms of sporadic cerebral small vessel disease: insights from neuroimaging. Lancet Neurol. 12, 483–497. http://dx.doi.org/10.1016/S1474-4422(13)70060-7.

Wardlaw, J.M., Smith, E.E., Biessels, G.J., Cordonnier, C., Fazekas, F., Frayne, R., Lindley, R.I., O'Brien, J.T., Barkhof, F., Benavente, O.R., Black, S.E., Brayne, C., Breteler, M., Chabriat, H., Decarli, C., de Leeuw, F.-E., Doubal, F., Duering, M., Fox, N.C., Greenberg, S., Hachinski, V., Kilimann, I., Mok, V., van Oostenbrugge, R., Pantoni, L., Speck, O., Stephan, B.C.M., Teipel, S., Viswanathan, A., Werring, D., Chen, C., Smith, C., van Buchem, M., Norrving, B., Gorelick, P.B., Dichgans, M., 2013b. Neuroimaging standards for research into small vessel disease and its contribution to ageing and neurodegeneration. Lancet Neurol. 12, 822–838. http://dx.doi.org/10.1016/S1474-4422(13)70124-8.

Wharton, S.B., Simpson, J.E., Brayne, C., Ince, P.G., 2015. Age-associated white matter lesions: the MRC cognitive function and ageing study. Brain Pathol. 25, 35–43. http://dx.doi.org/10.1111/bpa.12219.

Young, V.G., Halliday, G.M., Kril, J.J., 2008. Neuropathologic correlates of white matter hyperintensities. Neurology 71, 804–811. http://dx.doi.org/10.1212/01.wnl.0000319691.50117.54.

Original Article

JCBFM

Journal of Cerebral Blood Flow & Metabolism
2016, Vol. 36(1) 264–274

DOI: 10.1038/jcbfm.2015.64
jcbfm.sagepub.com
SAGE

Blood pressure and sodium: Association with MRI markers in cerebral small vessel disease

Anna K Heye[1,*], Michael J Thrippleton[1,*], Francesca M Chappell[1], Maria del C Valdés Hernández[1], Paul A Armitage[1,2], Stephen D Makin[1], Susana Muñoz Maniega[1], Eleni Sakka[1], Peter W Flatman[3], Martin S Dennis[1] and Joanna M Wardlaw[1]

Abstract

Dietary salt intake and hypertension are associated with increased risk of cardiovascular disease including stroke. We aimed to explore the influence of these factors, together with plasma sodium concentration, in cerebral small vessel disease (SVD). In all, 264 patients with nondisabling cortical or lacunar stroke were recruited. Patients were questioned about their salt intake and plasma sodium concentration was measured; brain tissue volume and white-matter hyperintensity (WMH) load were measured using structural magnetic resonance imaging (MRI) while diffusion tensor MRI and dynamic contrast-enhanced MRI were acquired to assess underlying tissue integrity. An index of added salt intake ($P = 0.021$), pulse pressure ($P = 0.036$), and diagnosis of hypertension ($P = 0.0093$) were positively associated with increased WMH, while plasma sodium concentration was associated with brain volume ($P = 0.019$) but not with WMH volume. These results are consistent with previous findings that raised blood pressure is associated with WMH burden and raise the possibility of an independent role for dietary salt in the development of cerebral SVD.

Keywords

Blood pressure, salt, sodium, small vessel disease, white-matter hyperintensities

Received 15 January 2015; Revised 13 March 2015; Accepted 13 March 2015

Introduction

Cerebral small vessel disease (SVD) accounts for 20% to 25% of strokes and causes cognitive impairment, disability, and dementia. The pathogenesis of SVD is poorly understood but hypertension and other vascular risk factors have been identified. Previous work in our group revealed associations between blood pressure and white-matter hyperintensity (WMH) burden and between blood pressure and previsible white-matter damage assessed by diffusion tensor imaging.[1,2]

The influence of dietary salt intake on stroke incidence and mortality is well known[3] but may be only partly mediated by its effect on blood pressure.[4] Plasma sodium concentration is assumed to be tightly regulated but there is some evidence to suggest that even small variations can affect physical and mental health in the elderly population.[5,6] The role of dietary and plasma sodium in cerebral SVD is unclear.

In this work, we assessed a cohort of patients with recent nondisabling stroke and exhibiting a spectrum of SVD severity. We performed magnetic resonance

[1]Neuroimaging Sciences, University of Edinburgh, Edinburgh, UK
[2]Department of Cardiovascular Science, University of Sheffield, Sheffield, UK
[3]Centre for Integrative Physiology, University of Edinburgh, Edinburgh, UK
[*]These authors contributed equally to this work

Corresponding author:
Joanna M Wardlaw, Brain Research Imaging Centre, Neuroimaging Sciences, University of Edinburgh, Western General Hospital, Crewe Road, Edinburgh EH4 2XU, UK.
Email: joanna.wardlaw@ed.ac.uk

imaging (MRI) scans to assess WMH volume, brain tissue volume, diffusion tensor MRI (DT-MRI) measures of tissue integrity, and T1-weighted imaging of contrast uptake. Blood pressure, an index of added dietary salt intake, and plasma sodium concentration were assessed and tested for associations with imaging findings.

Materials and methods

Participants

Participants were 264 adult patients who presented to our in- and out-patient stroke service. We recruited consecutive patients with first clinically evident nondisabling lacunar or mild cortical ischemic stroke, including those with diabetes, hypertension, and other vascular risk factors. We excluded patients with unstable hypertension or diabetes, other neurologic disorders and major medical conditions including renal failure that would preclude use of intravenous gadolinium contrast agents. We excluded patients unable to give consent, with contraindications to MRI or intravenous contrast, who had hemorrhagic stroke or those whose symptoms resolved within 24 hours (i.e., transient ischemic attack). The study was approved by the Lothian Research Ethics Committee (REC 09/81101/54) and the NHS Lothian R&D Office (2009/W/NEU/14) and conducted according to the principles expressed in the Declaration of Helsinki. All patients gave written informed consent.

Clinical data, diet and smoking history, WMH volume, brain tissue volume, and DT-MRI were obtained at presentation. Participants returned approximately 1 to 3 months after presentation for dynamic contrast-enhanced MRI (DCE-MRI), the delay being to avoid acute effects of the stroke on the local blood–brain barrier.

Clinical and Laboratory Measurements

On presentation, a clinician trained in stroke obtained the clinical details of the presenting stroke and determined the clinical stroke subtype (lacunar and cortical) using the Oxfordshire Community Stroke Project (OCSP) classification.[7] The same clinical researcher also recorded age, demographic details, past medical history of hypertension, previous stroke, previous transient ischemic attack, ischemic heart disease, peripheral vascular disease, diabetes mellitus, atrial fibrillation, hypercholesterolemia, heart failure, smoking and alcohol use, as well as all medications used and obtained blood biochemistry, brain MRI and other stroke investigations. We defined hypertension as blood pressure of 140/90 mmHg or greater on presentation or a previous diagnosis; smokers were defined as currently smoking or having given up within the previous 12 months and nonsmokers as having never smoked or having given up more than 12 months previously.

An experienced neuroradiologist assessed acute stroke subtype (lacunar or cortical) on MR diffusion-weighted imaging (generated from DT-MRI), fluid-attenuated inversion recovery (FLAIR), T2 and T1-weighted diagnostic imaging. Acute lacunar infarcts were required to be less than 20 mm in maximum axial diameter and in the deep white or gray matter (GM) of the cerebral hemispheres or brainstem. Infarcts involving the cortex, or subcortical infarcts larger than 20 mm diameter (i.e., a large striatocapsular infarct) were classed as 'cortical', likely to be due to large artery atherothromboembolism. All scans and clinical details were then reviewed by an expert panel of neurologists, stroke physicians, and neuroradiologists to establish the final stroke subtype using all clinical and imaging information. If no lesion was present on imaging, then the stroke was classified based on the clinical findings alone using the Bamford classification.[7]

We measured systolic and diastolic blood pressure (SBP and DBP, respectively) from the brachial artery in the stroke clinic or stroke ward using hospital blood pressure devices, which were checked and maintained by technical staff. Pulse pressure (PP) and mean arterial pressure (MAP) were calculated as SBP−DBP and DBP, respectively. Plasma sodium concentration was measured from blood samples taken during clinic assessment and measured in the NHS Lothian Biochemistry Department.

Participants were also asked to describe their addition of salt to food during cooking and at the dining table using the following salt intake score: 1 = always, 2 = often, 3 = occasionally, 4 = rarely, and 5 = never; the mean of the two scores was subtracted from 6 to give an ordinal categorical variable in the range of 1 (minimum use of salt) to 5 (maximum use of salt) for use in statistical analyses.

Magnetic Resonance Imaging

Magnetic resonance imaging was performed with a 1.5 Tesla MRI scanner (Signa HDxt, General Electric, Milwaukee, WI, USA) using an 8-channel phased-array head coil. Diagnostic MRI was acquired at presentation, including axial T2-weighted (T2W; repetition time (TR)/echo time (TE) = 6,000/90 ms, 24 × 24 cm field of view (FoV), 384 × 384 Propeller acquisition, 1.5 averages, 28 × 5 mm slices, 1 mm slice gap), axial FLAIR (TR/TE/inversion time (TI) = 9,000/153/2,200 ms, 24 × 24 cm FoV, 384 × 224 acquisition matrix, 28 × 5 mm slices, 1 mm slice gap), axial GRE (gradient echo; TR/TE = 800/15 ms, 20° flip angle, 24 × 18 cm

FoV, 384×168 acquisition matrix, 2 averages, 28×5 mm slices, 1 mm slice gap) and sagittal 3D T1-weighted imaging (T1W; inversion recovery-prepared SPGR (spoiled gradient echo) TR/TE/TI = 7.3/2.9/500 ms, 8° flip angle, 330×214.5 cm FoV, 256×146 acquisition matrix, 100×1.8 mm slices) and DT-MRI (single-shot echo-planar imaging with 30 diffusion directions ($b = 1{,}000$ s/mm^2) and $2 \times b_0$ acquisitions, TR/TE = 7,700/82 ms, 24×24 cm FoV, 128×128 acquisition matrix, 28×5 mm slices, 1 mm slice gap). The DCE-MRI was performed between 1 and 3 months after first presentation (median 38, interquartile range (31,54) days) and consisted of 20 consecutive 3D T1W SPGR acquisitions (TR/TE = 8.2/3.1 ms, 12° flip angle, 24×24 cm FoV, 256×192 acquisition matrix, 42×4 mm slices, 73 seconds acquisition time) with a total acquisition time of approximately 24 minutes, initiated simultaneously with an intravenous bolus injection of 0.1 mmol/kg gadoterate meglumine (Gd-DOTA, Dotarem, Guerbet, France). Two additional SPGR acquisitions were obtained before contrast administration with flip angles of 2° and 12°, respectively for calculation of the precontrast longitudinal relaxation time $T_{1,0}$.

Image Processing and Analysis

Preprocessing. Magnetic resonance images were converted from DICOM to Analyze 7.5 format. Structural and DCE-MRI images were aligned to the precontrast T1W image using rigid-body registration (FSL-FLIRT[8]); for participants who did not receive DCE-MRI, images were instead coregistered to the T2W image.

Tissue segmentation. The FLAIR and GRE images were processed using in-house software ('MCMxxxVI'[9]) to extract WMH in the brain parenchyma; these were manually refined and, separately, old stroke lesions or index stroke lesions were manually outlined using Analyze 11.0 (AnalyzeDirect, Stilwell, KS, USA). White-matter hyperintensity was identified as punctate or diffuse areas in the white matter and deep GM of the cerebral hemispheres or in the brainstem that were 3 mm or larger in diameter and hyperintense with respect to normal-appearing white matter and GM on T2W and FLAIR images; some hypointensity on T1W MRI was allowed as long as not less intense than cerebrospinal fluid (CSF). White-matter hyperintensity included 'dirty' or ill-defined diffuse hyperintensities with varying and erratic intensity patterns emerging from the lateral ventricle wall[10,11] provided such regions had outstanding intensity differences with respect to the normal-appearing white matter (NAWM) identified on T1W images. Index stroke lesions were defined as the hyperintense regions identified on the diffusion-weighted image generated from the DT-MRI scan including any corresponding signal changes on FLAIR, T2W, and T1W images, associated with swelling or lack of *ex vacuo* effect, that followed a vascular territory. Old stroke lesions were wedge-shaped hyperintense regions on the FLAIR or T2W images, and hypointense on the T1W image including cortex and/or subcortical tissues, with or without cavitation, and with *ex vacuo* effect reflecting tissue loss. The NAWM masks were generated using MCMxxxVI as described in Valdés Hernández et al.[12] Subcortical GM masks were generated automatically by a software pipeline that used FSL-SUSAN[13] for noise reduction, an age-relevant brain template,[14] FSL-FLIRT for aligning the template to each image data set, and FSL-FIRST[15] for extracting the subcortical structures, followed by manual boundary correction. To minimize any residual contamination of the subcortical GM, the mask was eroded by one voxel. An example of MR images and segmentation masks is shown in Figure 1.

Brain tissue volume. Intracranial volume (ICV), defined as contents within the inner skull table including brain tissue, CSF, veins, and dura, and limited inferiorly by the tip of the odontoid peg at the foramen magnum, was extracted using the GRE image and the Object Extraction Tool in Analyze 11.0, followed by manual editing. Nonbrain tissue (CSF, venous sinuses, and meninges) was extracted using MCMxxxVI. The volume of the resulting 'nonbrain' binary masks was subtracted from the ICV to provide a measure of total brain tissue volume. For statistical analysis, the brain tissue volume as a percentage of ICV (%BTV) and the WMH volume as a percentage of ICV (%WMH) were also calculated.

Diffusion tensor magnetic resonance imaging processing. The DTI images were processed using in-house software, which removed bulk motion and eddy current induced distortions using FSL FLIRT[8] and generated a directionally averaged diffusion-weighted image, mean diffusivity (MD), and fractional anisotropy (FA) parametric images using standard methods based on multivariate linear regression. For each data set nonlinear registration[16] was used to align the tissue masks in the structural space (T2W) with the parametric maps in the diffusion space using the NiftyReg tool (http://sourceforge.net/projects/niftyreg/) applied using TractoR software (http://www.tractor-mri.org.uk/diffusion-processing) to obtain the transformation between the brain extracted structural T2W image and the b_0 diffusion volume. To avoid partial volume averaging with CSF due to registration inaccuracies, the CSF mask was dilated by one voxel in each direction and

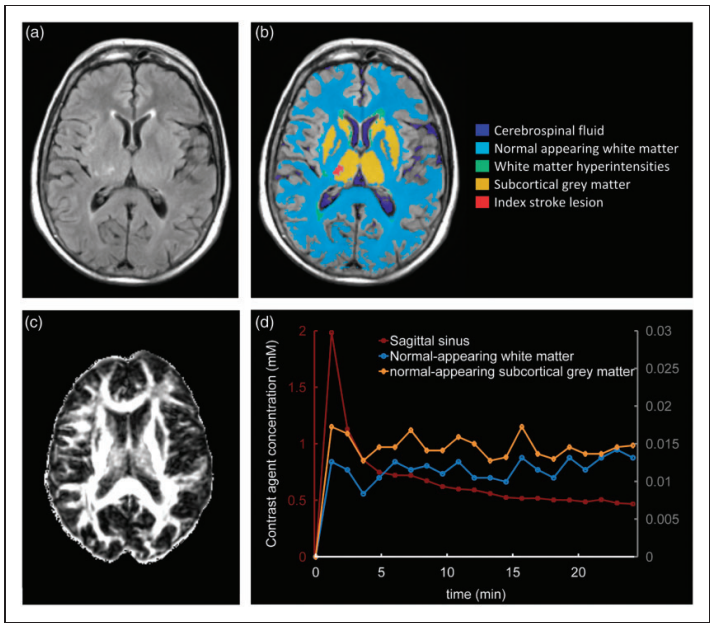

Figure 1. Representative magnetic resonance imaging (MRI) data and tissue segmentation. (A) Fluid-attenuated inversion recovery (FLAIR) image, (B) tissue masks superimposed on FLAIR image, (C) fractional anisotropy map, (D) contrast agent concentration curves obtained from dynamic contrast-enhanced MRI (DCE-MRI); y-axes scales for the sagittal sinus plasma concentration and normal-appearing tissue concentration curves are shown on the left and the right, respectively.

then subtracted from the NAWM, WMH, and subcortical GM masks in the diffusion space. Median MD and FA were extracted for NAWM and subcortical GM in each patient.

Dynamic contrast-enhanced magnetic resonance imaging. Median signal intensities for normal-appearing subcortical GM and white matter masks were extracted from the coregistered precontrast and postcontrast T1W images. A vascular input function was also determined by manual selection of a voxel in the superior sagittal sinus, using a slice proximal to the basal ganglia structures and the lateral ventricles. This voxel was chosen to provide a high peak signal enhancement and smooth variation during the DCE-MRI time course and was chosen independently by two observers; where the observers selected different voxels, the voxel with the highest peak enhancement was chosen unless the signal curve was significantly noisier (a noise estimate was calculated as the sum of squared differences between the signal curve and a fitted biexponential curve). $T_{1,0}$ was calculated using the median signal intensities in the two precontrast images with flip angles 2° and 12° and used to derive time-concentration curves for each tissue as described in Armitage et al.;[17] contrast agent concentration in the sagittal sinus was converted to plasma concentration using the factor 1/(1–Hct) and the most recent available hematocrit measurement in the patient's clinical record (if no hematocrit measurement was available ($n = 3$) we assumed Hct = 0.45). To semiquantitatively assess contrast uptake in tissue, we calculated the normalized area under curve (nAUC) defined as the area under the tissue concentration curve divided by the area under the superior sagittal sinus plasma concentration curve.

Statistical Analysis

Descriptive statistics in the text are given as mean ± standard deviation. Regressions were assessed by examination of the differences between the data and model predictions, and collinearity by variance inflation factors using SPSS version 19 (IBM Corp., Armonk, NY, USA) and Matlab (MathWorks, Inc., Natick, MA, USA). Predictors of %WMH and %BTV were investigated using multiple linear

regression models with correction for age, smoking status, stroke subtype, and additional factors given in the text and tables. Residuals for the %WMH model were not approximately normally distributed; to correct for this, the transformed outcome variable ln(0.005 + %WMH) was regressed instead. Subcortical GM MD (units $10^{-6}\,mm^2/s$) was also transformed to ln(−700 + MD) for this reason.

Results

Subjects

A total of 264 subjects were recruited into the study with mean age 66.9 ± 11.8 years and a ratio of 45:55 for diagnosis of lacunar-to-cortical stroke; 39% of patients were smokers and 72% had hypertension (Table 1). Reasons for exclusion are shown in Figure 2. After withdrawals and rejection of imaging data on quality grounds, DT-MRI and DCE-MRI data suitable for analysis were obtained in 262 and 201 patients, respectively.

White-Matter Hyperintensity and Brain Tissue Volume

Mean WMH volume as a percentage of ICV was 1.5 ± 1.6% with a positively skewed distribution. Pulse pressure ($\beta = 0.0092$/mm Hg, $P = 0.036$) and a diagnosis of hypertension ($\beta = 0.46$, $P = 0.0093$) were significant predictors of increased WMH volume as a percentage of ICV with correction for age, stroke subtype, and smoking status (Table 2 and Figure 3). Repetition of the analysis with replacement of PP and MAP with DBP and SBP showed that SBP but not DBP was positively associated with transformed %WMH ($\beta = 0.0079$/mm Hg, $P = 0.040$). Salt intake score was also positively associated with WMH volume ($\beta = 0.14$, $P = 0.021$; Figure 3); further analyses using the separate scores for cooking and table salt usage were consistent with this finding ($\beta = -0.11/-0.067$; $P = 0.020/0.18$ for cooking/table salt—note that the coefficient sign change is expected, since the combined score was inverted). Regression analysis of brain tissue volume (mean: 71 ± 5% of ICV) with the same covariates revealed a positive association between plasma sodium concentration and %BTV corresponding to an increase in brain tissue volume of 2% ICV per 10 mmol/L sodium ($P = 0.019$). Age was the most significant factor in the analyses of both %WMH and %BTV ($P < 0.0001$).

Diffusion Tensor Magnetic Resonance Imaging

The DT-MRI data were obtained in 262 subjects (DT-MRI data for two subjects were rejected due to failure of the nonlinear image registration). Mean diffusivity was distributed with mean values of 801 ± 52 and $787 \pm 32 \times 10^{-6}\,mm^2/s$ in subcortical GM and NAWM, respectively, with corresponding FA of 0.234 ± 0.021 and 0.256 ± 0.022. The influence of blood pressure, added salt intake, and plasma sodium concentration on these variables was modelled with correction for smoking, stroke subtype, and age, as well as normalized WMH volume to account for SVD severity (Table 3). Plasma sodium concentration was negatively associated with MD in NAWM ($\beta = -1.2 \times 10^{-6}\,(mm^2\,L)/(s\,mmol)$; $P = 0.011$) and FA in subcortical GM ($\beta = -0.9 \times 10^{-3}$ L/mmol; $P = 0.021$). Salt intake score was negatively associated with FA in subcortical GM ($\beta = -3.4 \times 10^{-3}$ L/mmol; $P = 0.0012$); additional analyses using the separate scores for salt usage during cooking and at the table were consistent with this finding ($\beta = 2.0/2.5$; $P = 0.016/0.0052$ for cooking/table salt). In WM, there were

Table 1. Descriptive statistics for demographic, clinical, and imaging variables including DT-MRI and DCE-MRI parameters in normal-appearing white matter and subcortical gray matter.

Parameter	N	*Mean (s.d.)*
Age (years)	264	66.9 (11.8)
Sex (% female)	264	42
Stroke subtype (% lacunar)	264	45
Hypertension (%)	264	72
Smoker[a] (%)	262	39
Diabetes (%)	264	11
Pulse pressure (mm Hg)	264	63 (20)
Mean arterial pressure (mm Hg)	264	103 (15)
Salt intake score	250	2.7 (1.3)
Plasma sodium concentration (mmol/L)	260	139 (3)
Structural MRI		
%WMH (%)	264	1.5 (1.6)
%BTV (%)	264	71 (5)
DT-MRI		
MD ($10^{-6}\,mm^2/s$)		
GM	262	801 (52)
NAWM	262	787 (32)
FA		
GM	262	0.234 (0.021)
NAWM	262	0.256 (0.022)
DCE-MRI		
nAUC (10^{-3})		
GM	201	16.8 (4.3)
NAWM	201	9.9 (3.7)

Abbreviations: BTV, brain tissue volume; DCE-MRI, dynamic contrast-enhanced MRI; DT-MRI, diffusion tensor MRI; FA, fractional anisotropy; GM, gray matter; MD, mean diffusivity; MRI, magnetic resonance imaging; nAUC, normalized area under curve; NAWM, normal-appearing white matter. [a]Currently smoking or had given up within the previous 12 months.

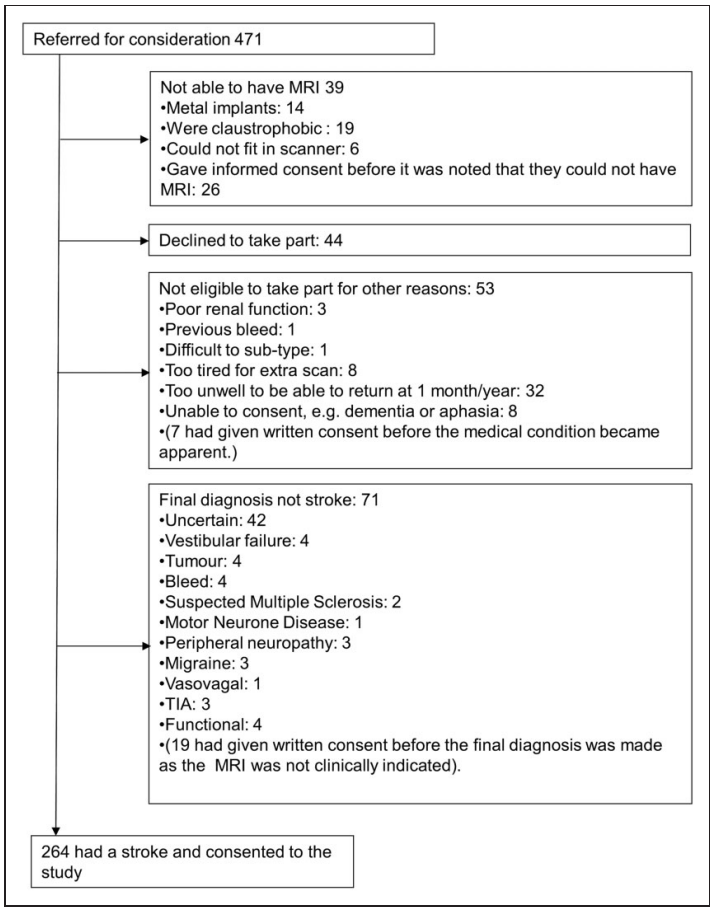

Figure 2. Flow chart showing recruitment to the Mild Stroke Study 2. MRI, magnetic resonance imaging; TIA, transient ischemic attack.

corresponding trends for reduced FA with increasing salt score ($\beta = -1.3 \times 10^{-3}$; $P = 0.19$) and lower plasma sodium ($\beta = 0.62 \times 10^{-3}$ L/mmol; $P = 0.090$) but these were not significant at the two-tailed 5% type 1 error level.

Dynamic Contrast-Enhanced Magnetic Resonance Imaging

Of the 264 patients recruited, 56 did not undergo DCE-MRI at 1-month follow-up due to decline in renal function (3), being too unwell (7), lack of venous access (4), and declining to have the scan (42). Of the 208 patients that underwent DCE-MRI, data suitable for analysis was obtained in 201 (data for seven subjects were rejected due to 'tissueing' of contrast, technical faults during the scan or unacceptable data quality caused by patient movement). The DCE-MRI parameters were modelled using the same covariates as for DT-MRI data (Table 4). Plasma sodium concentration was positively associated with nAUC in NAWM ($\beta = 0.18 \times 10^{-3}$; $P = 0.019$) but blood pressure, hypertension, and salt intake score were not significant predictors. The most significant covariate in these analyses was age, which was negatively associated with nAUC in both NAWM and subcortical GM ($P < 0.0001$).

Table 2. Multiple linear regression analysis of %WMH and %BTV.

	ln(0.005 + %WMH)		*%BTV*	
	β *(95% CI)*	*P*	β *(95% CI)*	*P*
PP (mm Hg)	0.0092 (0.00059, 0.018)	0.036	−0.022 (−0.054, 0.011)	0.20
MAP (mm Hg)	−0.0037 (−0.015, 0.0073)	0.51	0.013 (−0.029, 0.055)	0.55
Hypertension	0.46 (0.11, 0.81)	0.0093	−0.68 (−2.0, 0.65)	0.31
Salt intake score	0.14 (0.021, 0.25)	0.021	0.26 (−0.19, 0.70)	0.26
Plasma sodium (mmol/L)	−0.029 (−0.072, 0.014)	0.18	0.20 (0.033, 0.36)	0.019
Smoking	0.31 (−0.0033, 0.63)	0.052	−1.2 (−2.4, 0.039)	0.058
Stroke subtype (cortical = 0, lacunar = 1)	0.27 (−0.023, 0.57)	0.070	−0.40 (−1.5, 0.73)	0.49
Age (years)	0.053 (0.039, 0.067)	<0.0001	−0.25 (−0.30, −0.20)	<0.0001

Abbreviations: BTV, brain tissue volume; CI, confidence interval; PP, pulse pressure; MAP, mean arterial pressure; WMH, white-matter hyperintensity.

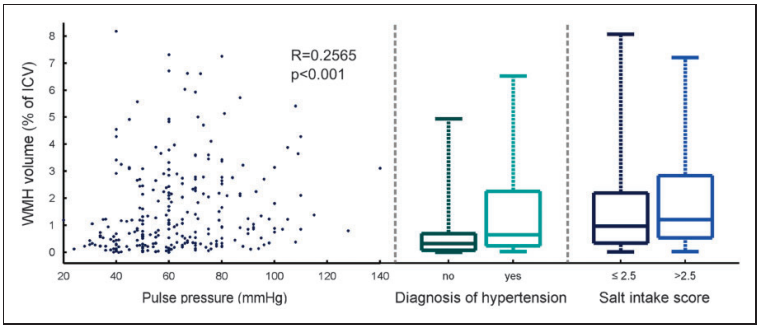

Figure 3. Relationship between white-matter hyperintensity (WMH) volume and pulse pressure (PP), diagnosis of hypertension, and salt intake score. The association between WMH volume and PP (Spearman's $R = 0.26$, $P < 0.001$) survived correction for age and all other factors listed in Table 2. ICV, Intracranial volume.

Discussion

Our finding that arterial blood pressure is associated with increased WMH volume is broadly consistent with the results of previous studies[1,2,18–21] and with the hypothesis that sustained pressure elevation and pressure fluctuations in the small cerebral vessels result in microvascular damage.[22] The independent association with clinical diagnosis of hypertension, additional to that of BP, likely reflects the historical effect of blood pressure elevation on vasculature and end organs in addition to that at the time of the study. Others have shown that WMH volume is also predicted by increased large artery stiffness, which may be one cause of increased pressure fluctuations in the small cerebral vessels.[23,24]

A novel finding of this study is that routinely adding more salt to food, which likely increases overall dietary salt intake in addition to the amounts of salt already present in food, is associated with greater WMH volume. There was also a highly significant negative association between the salt intake score and FA in normal-appearing subcortical GM, suggestive of 'previsible' reduced tissue integrity.[25] The interactions between salt intake, blood pressure, and cerebrovascular disease are not fully understood: it is widely accepted that sodium intake increases blood pressure[26] and that hypertension leads to cardiovascular disease including stroke[27,28] and there is indirect evidence to support the beneficial effects of reducing the salt intake on the incidence of cardiovascular disease.[28,29] Furthermore, epidemiologic studies indicate that salt intake is associated with increased risk of stroke and cardiovascular disease independently of blood pressure.[4,30,31] Our findings, which are corrected for blood pressure (both PP and MAP), hypertension, and age (as much as one can), suggest this might also be the case in cerebral SVD. Studies in the literature addressing the

Table 3. Multiple linear regression analysis of DT-MRI measurements in normal-appearing white matter and subcortical gray matter.

	$ln(-700 + MD_{GM}\ [10^{-6}\ mm^2/s])$		$MD_{NAWM}\ (10^{-6}\ mm^2/s)$		$FA_{GM}\ (10^{-3})$		$FA_{NAWM}\ (10^{-3})$	
	β (95% CI)	P	β (95% CI)	P	β (95% CI)	P	β (95% CI)	P
PP (mm Hg)	0.00079 (−0.0018, 0.0033)	0.54	0.16 (−0.021, 0.34)	0.083	0.056 (−0.095, 0.21)	0.47	−0.030 (−0.17, 0.11)	0.68
MAP (mm Hg)	0.0020 (−0.0013, 0.0052)	0.24	−0.14 (−0.38, 0.090)	0.23	−0.094 (−0.29, 0.10)	0.34	−0.041 (−0.22, 0.14)	0.66
Hypertension	0.046 (−0.058, 0.15)	0.39	0.64 (−6.7, 8.0)	0.86	−3.7 (−9.8, 2.4)	0.23	−2.1 (−7.9, 3.7)	0.48
Salt intake score	0.013 (−0.022, 0.048)	0.46	0.54 (−1.9, 3.0)	0.66	−3.4 (−5.5, −1.4)	0.0012	−1.3 (−3.2, 0.63)	0.19
Plasma sodium (mmol/L)	−0.0027 (−0.015, 0.010)	0.68	−1.2 (−2.1, −0.28)	0.011	−0.90 (−1.7, −0.14)	0.021	0.62 (−0.096, 1.3)	0.090
Smoking	0.016 (−0.078, 0.11)	0.74	3.8 (−2.9, 10.)	0.27	2.0 (−3.6, 7.6)	0.48	−1.5 (−6.8, 3.7)	0.57
Stroke subtype (cortical = 0, lacunar = 1)	0.096 (0.0079, 0.18)	0.033	0.60 (−5.7, 6.9)	0.85	−9.8 (−15., −4.5)	0.00029	−0.047 (−5.0, 4.9)	0.98
Age (years)	0.014 (0.0095, 0.018)	<0.0001	1.2 (0.89, 1.5)	<0.0001	0.088 (−0.18, 0.35)	0.51	−0.53 (−0.77, −0.28)	<0.0001
%WMH (%)	0.15 (0.12, 0.18)	<0.0001	4.9 (2.8, 7.0)	<0.0001	−2.3 (−4.0, −0.56)	0.0097	−4.5 (−6.1, −2.9)	<0.0001

Abbreviations: CI, confidence interval; DT-MRI, diffusion tensor MRI; MD, mean diffusivity; FA, fractional anisotropy; GM, gray matter; MAP, mean arterial pressure; NAWM, normal-appearing white matter; PP, pulse pressure; WMH, white-matter hyperintensity.

role of sodium in SVD are lacking and the pathophysiologic mechanism of any harm is unclear. A possible direct effect of salt on the endothelium, in addition to any effect via elevated BP, might account for the increased stroke risk due to salt beyond that accounted for by hypertension alone: for example, salt-sensitive (versus salt-resistant) hypertension is associated with peripheral endothelial dysfunction[32] which, if also present in the brain, might account for the dynamic cerebral and systemic endothelial dysfunction seen in several studies of SVD[33] and the increased level of WMH seen here. However, although the linear model used here fitted our data well, the significance of salt intake score as an independent predictor of WMH could also be influenced by complex nonlinear interactions between salt intake, blood pressure, and vascular disease, which become steeper with advancing age, in hypertensives and high salt intake.[28]

In contrast to dietary sodium consumption, plasma sodium concentration did not predict WMH volume but was associated with brain tissue volume, corresponding to an increase of 2% of ICV per 10 mmol/L sodium. Lower plasma sodium was also associated with increased MD in NAWM and increased FA in subcortical GM. The explanations for these associations are unknown and should be explored in future studies. Changes in brain volume may occur after acute changes in osmolality, but are thought to be temporary and rapidly reversed after changes in solute balance.[34] Furthermore, none of our participants were either hypernatremic (defined as [Na] > 146 mmol/L) or severely hyponatremic ([Na] < 125 mmol/L), though 13% were mild to moderately hyponatremic (125[Na]135 mmol/L). These findings may reflect transient changes related to hydration state, diet, time of day, or other factors. Most of our patients were managed as outpatients, not being ill enough to require hospital admission, and were mobile, cognitively competent outpatients with no clinical evidence of dehydration. However, plasma sodium was also associated with contrast uptake at DCE-MRI measured 1 month later, corresponding to a relative increase in nAUC in NAWM of 20% per 10 mmol/L sodium; this suggests that part of the association with brain volume may be accounted for by differences in blood volume. Age was a strong negative predictor of nAUC in GM and NAWM, consistent with literature reports of a reduction in the cerebral blood supply with age.[35] We note that, although contrast uptake in normal-appearing brain tissue is likely to be primarily intravascular, increased blood–brain barrier permeability in patients with SVD may result in an extracellular contribution to the nAUC particularly at older ages;[36] indeed, the positive association of nAUC with WMH volume may indicate such a contribution. Quantitative assessment of

Table 4. Multiple linear regression analysis of DCE-MRI measurements in normal-appearing white matter and subcortical gray matter.

	$nAUC_{GM}$ (10^{-3})		$nAUC_{NAWM}$ (10^{-3})	
	β (95% CI)	P	β (95% CI)	P
PP (mm Hg)	0.016 (−0.018, 0.050)	0.34	0.0068 (−0.022, 0.036)	0.65
MAP (mm Hg)	−0.0095 (−0.054, 0.035)	0.67	−0.0069 (−0.045, 0.032)	0.72
Hypertension	−0.44 (−1.9, 1.0)	0.55	−0.32 (−1.6, 0.93)	0.62
Salt intake score	0.14 (−0.33, 0.61)	0.56	0.015 (−0.39, 0.42)	0.94
Plasma sodium (mmol/L)	0.010 (−0.16, 0.18)	0.91	0.18 (0.030, 0.33)	0.019
Smoking	−0.36 (−1.7, 0.96)	0.59	−1.2 (−2.3, −0.034)	0.044
Stroke subtype (cortical = 0, lacunar = 1)	−0.028 (−1.2, 1.2)	0.96	−0.39 (−1.4, 0.63)	0.45
Age (years)	−0.18 (−0.24, −0.11)	<0.0001	−0.14 (−0.19, −0.082)	<0.0001
%WMH (%)	0.40 (0.0018, 0.80)	0.049	0.40 (0.053, 0.74)	0.024

Abbreviations: CI, confidence interval; DCE-MRI, dynamic contrast-enhanced magnetic resonance imaging; GM, gray matter; MAP, mean arterial pressure; nAUC, normalized area under curve; NAWM, normal-appearing white matter; PP, pulse pressure; WMH, white-matter hyperintesity.

contrast extravasation in this patient group will be considered in future work.

All analyses presented in this work were corrected for whether subjects were smokers. In line with the previous literature, smokers had both greater WMH volume[37] and lower brain volume[38] corresponding to a total brain volume difference of approximately 1% of ICV.

Our results concerning added dietary salt are limited by the qualitative and self-reported nature of these data. The index, based on a simple questionnaire, was designed for use in our clinical setting and did not attempt to assess total salt intake, an acknowledged complex task due to problems with accurate recall, and by the highly variable amounts of salt present in food or added by manufacturers during processing. However, our index may better reflect salt appetite and long-term exposure to salt. There is no gold-standard way to assess the salt intake of these patients retrospectively, and even the validity of a 24-hour urine collection, which is not practical in this cohort, has been questioned.[39] More complex questionnaires given by a dietician can provide a measure of intake but also depend on self-report and would not have been appropriate with this cohort of patients. A disadvantage of both detailed dietary questionnaires and biochemical tests is that they provide a snapshot of salt consumption, which may not reflect long-term exposure and habits, particularly during recovery from a stroke where intake may have been influenced by the recent stroke and lifestyle advice. Future work might focus on a more quantitative assessment of salt intake in patients presenting with mild stroke. Despite these reservations, our index correlated well with WMH volume and the trend was preserved when assessed using our two separate salt scores.

A second limitation is that our blood tests, while quantitative, measured plasma sodium concentration at a single point in time contemporaneous with measurement of WMH volume, %BTV, FA, and MD but not nAUC. As plasma sodium concentration shows strong individuality, it is unlikely to vary much unless the patient is over or under hydrated.[40] It should also be noted that the plasma sodium concentration can be influenced by kidney function, glucose level, and medication (13.3% of patients had reduced kidney function (estimated glomerular filtration rate $< 60\,mL/min/1.73\,m^2$) and 19.3% of patients took the diuretic medications Bendrofluimethiazide or Furosemide). However, correcting for these potential confounds made little difference to our results. Finally, we note that the age range of participants in this study was wide (34 to 96 years) and findings may be confounded by age-related effects not fully eliminated by the model; it is therefore desirable to replicate the findings in a larger study or in a sample with narrower age range.

In conclusion, arterial PP and diagnosis of hypertension predict WMH volume in patients with mild stroke. Added dietary salt intake was also independently associated with WMH. Plasma sodium concentration, while not associated with WMH volume, was a significant predictor of brain tissue volume and of gadolinium contrast agent uptake in NAWM.

Funding

The author(s) received no financial support for the research, authorship, and/or publication of this article.

Acknowledgement

This work was funded by Wellcome Trust (SDM and MRI scanning costs; grant 088134/Z/09/A), Row Fogo Charitable Trust (MCVH, AKH), Age UK (SMM), NHS Lothian

Research and Development Office (MJT), Scottish Funding Council and the Chief Scientist Office of Scotland for funding the Scottish Imaging Network: A Platform for Scientific Excellence ('SINAPSE'; JMW, radiography staff). The authors thank K Shuler for providing expert administrative support during data collection, analyses, and manuscript preparation.

Declaration of conflicting interests

The author(s) declared no potential conflicts of interest with respect to the research, authorship, and/or publication of this article.

Authors' contributions

AKH contributed to DCE-MRI analysis, statistical analysis. MJT and FMC contributed to manuscript preparation and statistical analysis. MVH contributed to processing and analysis of structural MRI and DT-MRI. PAA contributed to design of imaging protocol and to DCE-MRI and DT-MRI processing. SDM contributed to patient recruitment and assessment, collection of demographic data. SMM contributed to DT-MRI analysis. ES contributed to structural MRI analysis. PWF contributed advice regarding physiology and manuscript preparation. MSD contributed to oversight of patient clinical assessment and stroke subtyping. JMW contributed to study conception, funding and supervision, diagnostic MRI assessment, and manuscript preparation.

References

1. Aribisala BS, Morris Z, Eadie E, Thomas A, Gow A, Valdes Hernandez MC, et al. Blood pressure, internal carotid artery flow parameters, and age-related white matter hyperintensities. *Hypertension* 2014; 63: 1011–1018.
2. Maclullich AM, Ferguson KJ, Reid LM, Deary IJ, Starr JM, Seckl JR, et al. Higher systolic blood pressure is associated with increased water diffusivity in normal-appearing white matter. *Stroke* 2009; 40: 3869–3871.
3. Li XY, Cai XL, Bian PD and Hu LR. High salt intake and stroke: meta-analysis of the epidemiologic evidence. *CNS Neurosci Ther* 2012; 18: 691–701.
4. Strazzullo P, D'Elia L, Kandala NB and Cappuccio FP. Salt intake, stroke, and cardiovascular disease: meta-analysis of prospective studies. *Brit Med J* 2009; 339: b4567.
5. Decaux G. Is asymptomatic hyponatremia really asymptomatic? *Am J Med* 2006; 119: S79–S82.
6. Schrier RW. Does 'asymptomatic hyponatremia' exist? *Nat Rev Nephrol* 2010; 6: 185.
7. Bamford J, Sandercock P, Dennis M, Burn J and Warlow C. Classification and natural history of clinically identifiable subtypes of cerebral infarction. *Lancet* 1991; 337: 1521–1526.
8. Jenkinson M, Bannister P, Brady M and Smith S. Improved optimization for the robust and accurate linear registration and motion correction of brain images. *NeuroImage* 2002; 17: 825–841.
9. Hernandez MDV, Ferguson KJ, Chappell FM and Wardlaw JM. New multispectral MRI data fusion technique for white matter lesion segmentation: method and comparison with thresholding in FLAIR images. *Eur Radiol* 2010; 20: 1684–1691.
10. Filippi M and Rocca MA. Dirty-appearing white matter: a disregarded entity in multiple sclerosis. *Am J Neuroradiol* 2010; 31: 390–391.
11. Moore GR, Laule C, Mackay A, Leung E, Li DK, Zhao G, et al. Dirty-appearing white matter in multiple sclerosis: preliminary observations of myelin phospholipid and axonal loss. *J Neurol* 2008; 255: 1802–1811. (discussion 1812.
12. Valdes Hernandez Mdel C, Gallacher PJ, Bastin ME, Royle NA, Maniega SM, Deary IJ, et al. Automatic segmentation of brain white matter and white matter lesions in normal aging: comparison of five multispectral techniques. *Magn Reson Imaging* 2012; 30: 222–229.
13. Smith SM and Brady JM. SUSAN - A new approach to low level image processing. *Int J Comput Vis* 1997; 23: 45–78.
14. Farrell C, Chappell F, Armitage PA, Keston P, Maclullich A, Shenkin S, et al. Development and initial testing of normal reference MR images for the brain at ages 65–70 and 75–80 years. *Eur Radiol* 2009; 19: 177–183.
15. Patenaude B, Smith SM, Kennedy DN and Jenkinson M. A Bayesian model of shape and appearance for subcortical brain segmentation. *NeuroImage* 2011; 56: 907–922.
16. Modat M, Ridgway GR, Taylor ZA, Lehmann M, Barnes J, Hawkes DJ, et al. Fast free-form deformation using graphics processing units. *Comput Methods Programs Biomed* 2010; 98: 278–284.
17. Armitage PA, Farrall AJ, Carpenter TK, Doubal FN and Wardlaw JM. Use of dynamic contrast-enhanced MRI to measure subtle blood-brain barrier abnormalities. *Magn Reson Imaging* 2011; 29: 305–314.
18. Liu WH, Liu R, Sun W, Peng Q, Zhang WW, Xu E, et al. Different impacts of blood pressure variability on the progression of cerebral microbleeds and white matter lesions. *Stroke* 2012; 43: 2916–U253.
19. Shrestha I, Takahashi T, Nomura E, Ohtsuki T, Ohshita T, Ueno H, et al. Association between central systolic blood pressure, white matter lesions in cerebral MRI and carotid atherosclerosis. *Hypertens Res* 2009; 32: 869–874.
20. Verhaaren BFJ, Vernooij MW, de Boer R, Hofman A, Niessen WJ, van der Lugt A, et al. High blood pressure and cerebral white matter lesion progression in the general population. *Hypertension* 2013; 61: 1354–1359.
21. Waldstein SR, Wendell CR, Lefkowitz DM, Siegel EL, Rosenberger WF, Spencer RJ, et al. Interactive relations of blood pressure and age to subclinical cerebrovascular disease. *J Hypertens* 2012; 30: 2352–2356.
22. O'Rourke MF and Safar ME. Relationship between aortic stiffening and microvascular disease in brain and kidney - Cause and logic of therapy. *Hypertension* 2005; 46: 200–204.
23. Brisset M, Boutouyrie P, Pico F, Zhu YC, Zureik M, Schilling S, et al. Large-vessel correlates of cerebral small-vessel disease. *Neurology* 2013; 80: 662–669.
24. Poels MMF, Zaccai K, Verwoert GC, Vernooij MW, Hofman A, van der Lugt A, et al. Arterial stiffness and

cerebral small vessel disease The Rotterdam Scan Study. *Stroke* 2012; 43: 2637–2642.
25. Aribisala BS, Royle NA, Maniega SM, Valdes Hernandez MC, Murray C, Penke L, et al. Quantitative multi-modal MRI of the Hippocampus and cognitive ability in community-dwelling older subjects. *Cortex* 2014; 53: 34–44.
26. Mente A, O'Donnell MJ, Rangarajan S, McQueen MJ, Poirier P, Wielgosz A, et al. Association of urinary sodium and potassium excretion with blood pressure. *N Engl J Med* 2014; 371: 601–611.
27. He FJ, Li J and Macgregor GA. Effect of longer term modest salt reduction on blood pressure: Cochrane systematic review and meta-analysis of randomised trials. *Brit Med J* 2013; 346: f1325.
28. O'Donnell M, Mente A, Rangarajan S, McQueen MJ, Wang X, Liu L, et al. Urinary sodium and potassium excretion, mortality, and cardiovascular events. *N Engl J Med* 2014; 371: 612–623.
29. Cappuccio FP and Ji C. Less salt and less risk of stroke further support to action. *Stroke* 2012; 43: 1195–1196.
30. Aburto NJ, Ziolkovska A, Hooper L, Elliott P, Cappuccio FP and Meerpohl JJ. Effect of lower sodium intake on health: systematic review and meta-analyses. *BMJ* 2013; 346: f1326.
31. Gardener H, Rundek T, Wright CB, Elkind MSV and Sacco RL. Dietary sodium and risk of stroke in the Northern Manhattan Study. *Stroke* 2012; 43: 1200–1205.
32. Bragulat E, de la Sierra A, Antonio MT and Coca A. Endothelial dysfunction in salt-sensitive essential hypertension. *Hypertension* 2001; 37: 444–448.
33. Stevenson SF, Doubal FN, Shuler K and Wardlaw JM. A systematic review of dynamic cerebral and peripheral endothelial function in lacunar stroke versus controls. *Stroke* 2010; 41: e434–e442.
34. Verbalis JG. Brain volume regulation in response to changes in osmolality. *Neuroscience* 2010; 168: 862–870.
35. Aanerud J, Borghammer P, Chakravarty MM, Vang K, Rodell AB, Jonsdottir KY, et al. Brain energy metabolism and blood flow differences in healthy aging. *J Cereb Blood Flow Metab* 2012; 32: 1177–1187.
36. Farrall AJ and Wardlaw JM. Blood-brain barrier: ageing and microvascular disease—systematic review and meta-analysis. *Neurobiol Aging* 2009; 30: 337–352.
37. Staals J, Makin SD, Doubal FN, Dennis MS and Wardlaw JM. Stroke subtype, vascular risk factors, and total MRI brain small-vessel disease burden. *Neurology* 2014; 83: 1228–1234.
38. Swan GE and Lessov-Schlaggar CN. The effects of tobacco smoke and nicotine on cognition and the brain. *Neuropsychol Rev* 2007; 17: 259–273.
39. Titze J, Dahlmann A, Lerchl K, Kopp C, Rakova N, Schroder A, et al. Spooky sodium balance. *Kidney Int* 2014; 85: 759–767.
40. Zhang Z, Duckart J, Slatore CG, Fu Y, Petrik AF, Thorp ML, et al. Individuality of the plasma sodium concentration. *Am J Physiol Renal Physiol* 2014; 306: F1534–F1543.